Understanding the molecular pharmacology of vascular calcium-activated chloride channels



Ria Dinsdale

St John's College

University of Oxford

Thesis submitted for the degree of Doctor of Philosophy

Hilary 2021

Abstract

Calcium-activated chloride channels (CaCCs) are a class of ion channel involved in a multitude of cellular functions. The role of CaCCs is especially well recognised in vascular smooth muscle cells (VSMCs), where CaCCs are activated by agonist-induced Ca^{2+} release and their opening triggers depolarisation leading to vasoconstriction. CaCCs have been proposed as new potential therapeutic targets for diseases of altered blood vessel tone including systemic and pulmonary hypertension, as well hypotension and shock. Selective and potent CaCC modulators, however, are currently missing. Our lab has previously demonstrated that anthracene-9-carboxylic acid (A9C) has a biphasic effect on TMEM16A currents, producing both activation and inhibition depending on the concentration range and membrane potential. Defining the mode of action of this test compound can therefore help the design of both synthetic inhibitors and activations. Patch-clamp electrophysiology of cloned and native ion channels was used in conjunction with single point mutagenesis and wire myography to gain insights on the molecular pharmacology of TMEM16A-CaCCs. The main findings of this thesis are:

1. The selectivity of two of the most potent modulators of TMEM16A currently available 2-(4'-chloro-2'-methylphenoxy)-*N*-[(2''-methoxyphenyl)methylideneamino]-acetamide (Ani9) and *N*-((4'-methoxy)-2'-naphthyl)-5-nitroanthranilic acid (MONNA) was studied on isolated mouse VSMCs and isolated aortic rings. Ani9 potently blocked cloned and native TMEM16A channels, without interfering with other conductance's in mouse aortic SMCs. MONNA was found to inhibit cloned and native TMEM16A channels. However, MONNA also activated BK_{Ca} channels and inhibited Ca_V channels,

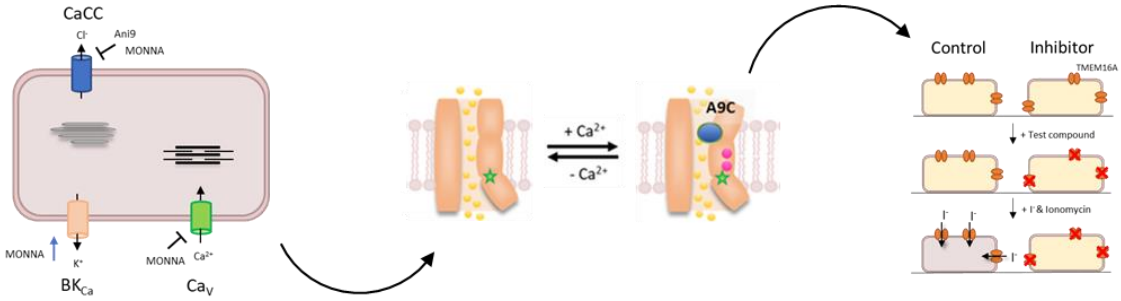
significantly affecting the tone of aortic rings through a combined action of multiple conductance's.

2. The mode of action of A9C on the TMEM16A channel was elucidated. TMEM16A channels with the activation gate constitutively open were used to dissect the mechanism of A9C inhibition and activation. These channels were found to be entirely insensitive to A9C in the absence of intracellular Ca^{2+}. However, when intracellular Ca^{2+} was presence, the mutant channels regained their sensitivity to extracellular A9C. Thus, intracellular Ca^{2+} is mandatory for the channel response for extracellular A9C. The underlying mechanism is an unanticipated conformational change in the outer pore, revealing a novel aspect of Ca^{2+}-gating in the TMEM16A channel, and its implication for channel pharmacology.

3. A fluorescence-based screening cellular system was developed to enable a higher through-put evaluation of possible compounds that modulate TMEM16A function. This method was tested using known modulators of the TMEM16A channel. This cell system may help future drug screening exercises.

To conclude, the research in this thesis has led to the determination of the binding site of A9C on the TMEM16A channel and revealed that the binding site become accessible to A9C only when intracellular Ca^{2+} is present; this indicates a possible site for therapeutic drug targets that can become accessible during stimulation of the cell by factors that trigger Ca^{2+} release (such as stimulation of VSMCs by vasoactive agonists). The pharmacology of TMEM16A was also systematically studied and the selectivity of two of the most commonly used tool compounds defined, which enables a more in-depth interpretation of published results involving these modulators. Collectively, these

data advance our understanding of the pharmacology of the TMEM16A channel. The definition of a ligand binding site may form the basis for the rational design of small molecules acting at this site.



Acknowledgements

First and foremost, I would like to thank Paolo Tammaro for giving me the opportunity to undertake my DPhil within his lab, and for introducing me to patch-clamp electrophysiology. His commitment and inspiration to training me to be a great scientist has made my DPhil an extremely rewarding experience. I would like to thank Professor Angela Russell for her continued support throughout my academic career, your guidance and support has been invaluable. Huge thanks Professor Phillip Stansfeld for supporting me through my DPhil and together with Tanadet Pipatpolkai working on the computational component of my DPhil to make this work complete.

A highlight of my time in the Department of Pharmacology is having met some amazing friends. Thank you so much Kathryn Acheson, Abigail Wilson, Lara Scofano, Razik Mu-u-Min and Claire Pearson for their friendship and many baked goods. Within the Russel group I have made some amazing friendships, thank you Isabel Wilkinson and Alice Kennett for all the fun nights and coffees we have had.

To my wonderful Mum, Dad, Sister, and Niece, thank you for your unwavering love and support during my academic career and being my biggest supporters. Thank you to all my wonderful friends for being a constant source of encouragement, and particularly Alex Picksley, for your care and understanding every step along the way. Thank you for everything.

Finally, I would like to thank the British Heart Foundation for their funding.

Abstract 1
Acknowledgements 4
List of Figures 9
List of Tables 12
List of Abbreviations 13
1 Introduction 17
1.1 Vascular structure and function 17
1.1.1 Basic principles of vascular haemodynamics 18
1.1.2 Regulation of vascular tone 21
1.2 Vascular smooth muscle cells 23
1.2.1 Vascular excitation-contraction coupling 24
1.2.2 Electrical properties of vascular SMC 26
1.2.3 Ion channels in vascular SMC 28
1.3 CaCCs 32
1.3.1 TMEM16x family 33
1.3.2 Biophysical properties of CaCCs 35
1.4 TMEM16A in health and disease 36
1.4.1 TMEM16A in cancer cells 37
1.4.2 TMEM16A in airway and intestinal epithelial cells 39
1.4.3 TMEM16A in vascular disease 42
1.5 The interplay of TMEM16A gating and pharmacology 46
1.5.1 TMEM16A gating 47
1.5.2 Pharmacology of TMEM16A 49
1.6 Hypothesis and aims 55
2 Chapter 2: Materials and Methods 58
2.1 Chemicals and reagents 58
2.2 Cell preparation 58
2.2.1 Cell culture and transfection 58
2.2.2 Generation of stable line 59
2.2.3 Isolation of native SMCs 60
2.3 Molecular biology 61
2.3.1 Amplification, extraction, and purification of plasmid DNA 61
2.3.2 Single point mutagenesis 62
2.4 Electrophysiology 64
2.4.1 Basic theoretical principles 65

2.4.2 Patch-clamp set-up 66
2.4.3 Patch-clamp configurations 68
2.5 Electrophysiological solutions 70
2.5.1 Solutions for measurement of I_{CaCC} 70
2.5.2 Drug preparations and perfusion system 76
2.5.3 Stimulation protocols 76
2.5.4 Noise Analysis 79
2.5.5 Liquid Junction Potential measurements 81
2.6 Isometric tension measurements 82
2.6.1 Myography experimental design 82
2.6.2 Mounting of vessels 82
2.6.3 Normalisation 83
2.7 Premo™ Halide Sensor kit 88
2.8 Data and statistical analysis 89
2.9 Contribution to work 90
3 Chapter 3: Fundamental characterisation of cloned and native TMEM16A pharmacology 92
3.1 TMEM16A and TMEM16B calcium sensitivity 94
3.2 TMEM16A I-V relationship 96
3.3 Whole cell-current recording for other cloned vascular channels: TMEM16B and TMEM16F 99
3.3.1 TMEM16B I-V relationship 99
3.3.2 TMEM16F I-V relationship 101
3.4 Defining the sensitivity of TMEM16A to Cl^- channel modulators 102
3.4.1 Inhibitors 102
3.4.2 Activators 104
3.4.3 Biphasic Modulators 105
3.5 Effect of MONNA on other TMEM16x family members: TMEM16B and TMEM16F 108
3.5.1 Effect of inhibitors on TMEM16B 108
3.5.2 Effect of inhibitors on TMEM16F 109
3.6 Competition with extracellular Cl^- 110
3.7 Effect of NFA on TMEM16A's single channel current and open probability as examined by noise analysis 112
3.8 Effect of Ani9 and MONNA on isolated aortic rings 114
3.8.1 Effect of reducing $[Cl^-]_{ext}$ in VSMCs on isolated aortic rings 117
3.8.2 Effect of Ani9 and MONNA on K^+-mediated depolarisation of aortic rings 121

3.9 Native currents in isolated VSMCs 123
3.9.1 TMEM16A currents in isolated VSMCs 124
3.9.2 Effect on inhibitors on native TMEM16A in VSMCs 125
3.9.3 Effect of inhibitors on cationic current 127
3.9.4 Exploration of MONNA's modulation of VSMC ion channels 129
3.10 Effect of inhibitors on Ca_V currents in VSMCs 133
3.11 Discussion 135
3.11.1 Cloned TMEM16A channels 136
3.11.2 Action of inhibitors on TMEM16A and towards identification of binding modality 136
3.11.3 Action of activators on TMEM16A 138
3.11.4 Action of biphasic modulators on TMEM16A and elucidation of mechanism of action 139
3.11.5 Modulation of TMEM16x family members by potent TMEM16A inhibitors 140
3.11.6 TMEM16A in VSMC agonist induced contraction 140
3.11.7 TMEM16A in isolated VSMC currents 141
3.12 Physiological significance 143
4 Chapter 4: Molecular basis of modulation of the TMEM16A channel by A9C and NFA: Insights into channel gating 145
4.1 A9C: TMEM16A modulator with biphasic effect 148
4.2 Exploration of constitutively active TMEM16A channels 150
4.2.1 Electrophysiological characterisation of constitutively active mutations 150
4.2.2 A9C effect on constitutively active channels in 0 and ~0.1 µM $[Ca^{2+}]_i$ 155
4.3 Assessing the influence of the electrostatic gate of the effect of A9C 160
4.3.1 Ca^{2+} sensitivity of TMEM16A-E650A 161
4.3.2 Assessing the influence of the electrostatic gate on the effect of A9C 162
4.4 Separation of inhibiting and activating effects of A9C and NFA on TMEM16A using a rapid perfusion system 164
4.4.1 Effect of 300 µM A9C on TMEM16A, TMEM16A-Q645A and TMEM16A-I637A 164
4.5 Assessing the effect of Ca^{2+} on Cl^- permeation: evidence for a structural rearrangement of the outer pore region 167
4.6 Molecular dynamics simulations offer insights into the structural rearrangement of the outer pore region 171
4.6.1 Identification of the A9C binding site 174
4.7 Effect of biphasic modulator, NFA, on TMEM16A current 177
4.7.1 NFA effect on constitutively active channels in 0 and ~0.1 µM $[Ca^{2+}]_i$ 178

4.7.2 Assessing the influence of the electrostatic gate on the effect of NFA 181
4.7.3 Effect of 30 µM NFA on TMEM16A, TMEM16A-Q645A and TMEM16A-I637A 182
4.8 Discussion..... 183
4.8.1 Gating mechanisms of the TMEM16x channels and scramblases..... 185
4.8.2 Identification of A9C binding site in the TMEM16A channel 187
5 Chapter 5: Developing a system to test new small molecules acting on TMEM16A channels..... 190
5.1 Creation of TMEM16A stable HEK-293 cell line 190
5.2 TMEM16A current response to Ionomycin..... 194
5.2.1 Effect of TMEM16A inhibitors on ionomycin elicited TMEM16A currents 199
5.3 Use of Premo™ Halide Sensor to assess modulation of TMEM16A 202
5.4 Discussion..... 203
6 Chapter 6: Concluding remarks 207
Publications, presentations, and posters 211
References 213

List of Figures

Figure 1.1 Organisation and dimensions of the blood vessels in the human circulatory system 20
Figure 1.2 Vascular smooth muscle cell contraction. 25
Figure 1.3 Ion channels and transporters expressed in VSMCs. 31
Figure 1.4 Effect of possible pharmacological effects of TMEM16A. 37
Figure 1.5 Role of TMEM16A in airway epithelium. 41
Figure 1.6 Proposed role of TMEM16A in smooth muscle cell contraction. 44
Figure 1.7 General CaCC inhibitors 50
Figure 1.8 Selective TMEM16A inhibitors 52
Figure 1.9 TMEM16A activators 53
Figure 1.10 Biphasic modulators of TMEM16A 54
Figure 2.1 Diagrammatic representative of single point mutagenesis 64
Figure 2.2 The cell membrane as a simple electrical circuit. 66
Figure 2.3 Schematic demonstrating the whole-cell patch-clamp experimental set up. 68
Figure 2.4 Patch-clamp electrophysiology recording configuration. 70
Figure 2.5 Patch-clamp recording voltage stimulation protocols. 79
Figure 2.6 Wire myography setup 83
Figure 2.7 Normalisation of tension 85
Figure 3.1 Ca^{2+} sensitivity of TMEM16A and TMEM16B channels. 95
Figure 3.2 Properties of the cloned TMEM16A IV-relationship 98
Figure 3.3 Properties of TMEM16B IV-relationship 100
Figure 3.4 Properties of TMEM16F IV-relationship 102
Figure 3.5 The effects of inhibitors on whole-cell TMEM16A currents 104
Figure 3.6 The effects of E_{act} on whole-cell TMEM16A currents 105
Figure 3.7 The effects of biphasic modulators on whole-cell TMEM16A currents 107
Figure 3.8 The effect of MONNA on whole-cell TMEM16B currents 109
Figure 3.9 The effect of MONNA on whole-cell TMEM16F currents 110
Figure 3.10 The effect of varying $[Cl^-]_{ext}$ on Ani9 and MONNA-mediated inhibition of TMEM16A currents. 112
Figure 3.11 Non-stationary noise analysis for whole-cell TMEM16A currents in the presence and absence of NFA activation. 114
Figure 3.12 PE-mediated contraction of aortic rings in the presence of Ani9 and MONNA. 117
Figure 3.13 Diagram depicting the effect of electrochemical gradient in VSMCs 118
Figure 3.14 PE-mediated contraction of aortic rings in the presence of low $[Cl^-]_{ext}$ and Ani9 or MONNA 120
Figure 3.15 K-MES-mediated contraction of aortic rings in the presence of Ani9 and MONNA. 123
Figure 3.16 Properties of TMEM16A IV-relationship in isolated aortic VSMCs. 125

Figure 3.17 MONNA effect on TMEM16A current in VSMCs. 126
Figure 3.18 Ani9 effect on TMEM16A current in VSMCs. 127
Figure 3.19 Effect of MONNA on cationic currents from isolated VSMCs. 128
Figure 3.20 Effect of Ani9 on cationic currents from isolated VSMCs. 129
Figure 3.21. Effect of MONNA on isolated VSMCs in the presence of a variety of ion channel blockers. 132
Figure 3.22 Effect of MONNA on Ca_V currents from isolated VSMCs. 134
Figure 3.23 Effect of Ani9 on Ca_V currents from isolated VSMCs. 135
Figure 4.1 Gating mechanisms of wild-type and mutant (TMEM16A-Q645A and TMEM16A-I637A) channels. 148
Figure 4.2 Effect of extracellular A9C and NFA on whole-cell TMEM16A current amplitudes. 149
Figure 4.3 Ca^{2+} sensitivity of TMEM16A-Q645A and TMEM16A-I637A channels. 151
Figure 4.4 Characterisation of IV-relationship of TMEM16A-Q645A and TMEM16A-I637A in the presence or absence of intracellular Ca^{2+}. 154
Figure 4.5 Effect of extracellular A9C on whole-cell TMEM16A, TMEM16A-Q645A, and TMEM16A-I637A current amplitudes in the absence or presence of Ca^{2+}. 157
Figure 4.6 Effects of various $[A9C]_{ext}$ on whole-cell TMEM16A, TMEM16A-Q645A and TMEM16A-I637A current amplitude 159
Figure 4.7 TMEM16A structure with Q654 and E650 resides highlighted. 160
Figure 4.8 Ca^{2+} sensitivity of TMEM16A-Q645AE650A channels. 161
Figure 4.9 Effect of extracellular A9C on whole-cell TMEM16A-Q645A-E650A current amplitudes in the presence or absence of Ca^{2+} 162
Figure 4.10 Effect of alternative cations on TMEM16A electrostatic gate 163
Figure 4.11 Separation of inhibiting and activating effects of A9C on TMEM16A, TMEM16A-Q645A and TMEM16A-I637A channels. 166
Figure 4.12 Saturation and binding of Cl^- with the TMEM16A-Q645A channel pore. . 168
Figure 4.13 Occupancy of water molecules inside the TMEM16A pore. 173
Figure 4.14 Relative position of the A9C molecule in the TMEM16A channel with the presence and absence of Ca^{2+}. 175
Figure 4.15 Experimental validation of the putative A9C binding site 176
Figure 4.16 Effect of extracellular NFA on whole-cell TMEM16A current amplitudes. 178
Figure 4.17 Effect of extracellular NFA on whole-cell TMEM16A, TMEM16A-Q645A, and TMEM16A-I637A current amplitudes in the presence or absence of Ca^{2+}. 180
Figure 4.18 Effect of extracellular NFA on whole-cell TMEM16A-Q645A-E650A current amplitudes in the presence or absence of Ca^{2+}. 181
Figure 4.19 Separation of inhibiting and activating effects of NFA on TMEM16A, TMEM16A-Q645A, and TMEM16A-I637A channels. 183
Figure 5.1 Diagrammatic representation of fluorescence quenching assay. 192
Figure 5.2 IV-relationship of stably transfected TMEM16A HEK-293 cell line 194
Figure 5.3 Structure of Ionomycin 194
Figure 5.4 Effect of ionomycin on TMEM16A currents in HEK-293 cells. 198
Figure 5.5 Effect of inhibitors and ionomycin on TMEM16A currents in HEK-293 cells. 201

Figure 5.6 Fluorescence assay with I^- supplemented CaCC extracellular solution 203
Figure 6.1 Proposed mechanism of Ca^{2+}-dependent gating and A9C modulation of channel activity. 209

List of Tables

Table 1.1 Ionic composition of vascular smooth muscle 28
Table 2.1 Primers designed for construction of TMEM16A mutant channels. 63
Table 2.2 Standard CaCC Extracellular Solutions 71
Table 2.3 Standard CaCC Intracellular Solutions 71
Table 2.4 Ca^{2+} concentrations for Standard CaCC extracellular solutions 72
Table 2.5 Low Cl^- Extracellular Solution 72
Table 2.6 0 Ca^{2+} Extracellular Solution 73
Table 2.7 Low EGTA Intracellular Solution 73
Table 2.8 Cationic extracellular solution 73
Table 2.9 Cationic intracellular solution 74
Table 2.11 Cl^- dose response extracellular solution 74
Table 2.12 Concentration of NaCl 74
Table 2.13 Cl^- dose response intracellular solution 75
Table 2.14 Dissociation medium (DM) 75
Table 2.15 Physiological salt solution (PSS) 86
Table 2.16 Low Cl^- physiological salt solution 86
Table 2.17 I^- supplemented extracellular solution 89
Table 3.1 Hill-fit parameters (EC_{50}, max and h) (Eq. 19) for aortic ring tension versus [PE] relationships obtained in the absence (control) and presence of Ani9 or MONNA 116
Table 3.2 The effect of TMEM16A inhibitors on aortic contraction in conditions of low $[Cl^-]_{ext}$ 119
Table 3.3 Effect of TMEM16A inhibitors on aortic contraction in the presence of 100 mM K-MES 122
Table 3.4 Cationic currents evoked in VSMCs in the presence of ion channel blockers and MONNA. 131
Table 4.1 Ca^{2+} sensitivity of TMEM16A-Q645A and TMEM16A-I637A channels. 152
Table 5.1 Effect of ionomycin on TMEM16A currents in HEK-293 cells 197
Table 5.2 Effect of inhibitors and ionomycin on TMEM16A currents in HEK-293 cells. 200

List of Abbreviations

$[Ca^{2+}]_i$	Intracellular free Ca^{2+} concentration
$[Cl^-]_{ext}$	Extracellular Cl^- concentration
$[K^+]_{ext}$	Extracellular K^+ concentration
A9C	Anthracene-9-carboxylic acid
AACTs	2-acylaminocycloalkylthiophene-3-carboxylic acid arylamides
ADP	Adenosine diphosphate
Ani9	2-(4-chloro-2-methylphenoxy)-N- [(2-methoxyphenyl)methylideneamino]-acetamide
ATP	Adenosine triphosphate
BK_{Ca}	Big conductance K^+ channel
bp	Base pairs
CaCC	Ca^{2+}-activated chloride channel
cAMP	Cyclic adenosine monophosphate
Ca_V	Voltage-gated Ca^{2+} channels
CD8	Cluster of differentiation 8
cDNA	Complementary DNA
CF	Cystic fibrosis
CFTR	Cystic fibrosis transmembrane receptor
ClC	Voltage-gated Cl^- channels
C_m	Capacitance
cryo-EM	Cryogenic electron microscopy
DAG	Diacylglycerol
ddH2O	Double-distilled H2O
DIDS	4,4'-Diisothiocyano-2,2'-stilbenedisulfonic acid
DM	Dissociation medium
DMSO	Dimethyl sulfoxide
D-PBS	Dulbecco's Phosphate-Buffered Saline solution
DTT	Dithiothreitol

E_{act}	N-aroylaminothiazole
EDHF	Endothelium-derived hyperpolarizing factor
E_K	Potassium reversal potential
E_{rev}	Reversal potential
F_{act}	Tetrazolylbenzamide
FRT	Fisher rat thyroid
GPCR	G protein coupled receptors
GWAS	Genome-wide association study
HEK-293	Human embryonic kidney 293
HEK-293T	Human embryonic kidney 293T
I_{CaCC}	CaCC current
IM	Ionomycin
I_{max}	Maximal current
IP_3	Inositol-1,4,5-triphosphate
I_{peak}	Peak current
I_{ss}	Steady-state current
K2P	Two-pore domain potassium channels
K_{ATP}	ATP-dependent K^+ channel
K_{ir}	Inwardly rectifying K^+ channel
KO	Knock-out
LB	Lysogeny broth
MES	Methanesulfonate
MLC	Myosin light chain
MLCK	Myosin light-chain kinase
MONNA	N-((4-methoxy)-2-naphthyl)-5-nitroanthranilic acid
mRNA	Messenger ribonucleic acid
NA	Noradrenaline
NFA	Niflumic acid
NKCC1	$Na^+/K^+/2Cl^-$ cotransporter
NO	Nitric oxide
NPPB	5-Nitro-2-(3-phenylpropylamino)benzoic acid

NSAIDs	Nonsteroidal anti- inflammatory drugs
NSCCs	Non-selective cation channels
NT	Non-transfected
PAH	Pulmonary arterial hypertension
PASMC	Pulmonary Artery Smooth Muscle Cells
PCR	Polymerase chain reaction
PE	Phenylephrine
PIP_2	Phosphatidylinositol 4,5-bisphospate
P_o	Open probability
PSS	Physiological salt solution
ROCs	Receptor-operated channels
SAR	Structure activity relationship
siRNA	small interference RNA
SITS	4- acetamido-4'-isothiocyanatostilbene-2,2'-disulfonic acid
SMCs	Smooth muscle cells
SOCs	Store-operated channels
SR	Sarcoplasmic reticulum
STICs	Spontaneous transient inward currents
STOCs	Spontaneous transient outward currents
SV40	Simian Virus 40
TRP	Transient receptor potential
VGCC	Voltage-gated cation channels
V_m	Membrane potential
VRAC	Volume-regulated anion channel
VSMCs	Vascular smooth muscles cells

Chapter 1

Introduction

1 Introduction

1.1 Vascular structure and function

Blood vessels regulate the flow of blood within the body. These vessels are made up of three main layers: *tunica intima* (innermost coat), *tunica media* (middle coat) and *tunica adventitia* (outer coat) (Herring, Paterson & Levick, 2018; Klabunde, 2011).

The *tunica intima* is a monolayer of endothelial cells and basal lamina. The endothelial cells are orientated along the flow and provide a smooth surface that favours blood flow. The *tunica intima* also secretes a range of vasoactive compounds, such as antithrombotic vasodilator nitric oxide (NO), endothelin, lamin and collagens (Herring, Paterson & Levick, 2018; Klabunde, 2011).

The *tunica media* is the thickest layer of the vessel and provides the mechanical strength and contractile power. This layer is made up of vascular smooth muscle cells (VSMCs) and a matrix of elastin and collagen fibres. Within elastic arteries the amount of elastin is greater than those of muscular arteries. Two sheets of elastin (internal and external lamina) delimit the *tunica media*. The *tunica media* interacts with the *tunica intima* through myo-endothelial junctions, where the endothelial cells protrude through the internal lamina, contacting the smooth muscle cells and sending processes through. Within arteries the *tunica media* and *intima* are more developed than in veins. The tunica media is found in all but the smallest blood vessels, the capillaries and venules (Herring, Paterson & Levick, 2018; Klabunde, 2011).

The *tunica adventitia* is the outermost layer and is made up of connective tissue, which is arrange longitudinally with adipose tissue, and tethers the vessel to the surrounding tissue. There is no distinct border to this layer, it blends into the surrounding tissue. In

large arteries, the *tunica media* contains small blood vessels (the *vasa vasorum*) that provide oxygen and nutrients to the smooth muscle layer. The *tunica adventitia* may encompass sympathetic nerve terminals which release transmitters (such as noradrenaline and adenosine triphosphate (ATP)) and are important regulators of muscle tone (Herring, Paterson & Levick, 2018; Klabunde, 2011).

1.1.1 Basic principles of vascular haemodynamics

Vascular haemodynamics is the study of how blood flows through the cardiovascular system. In the simplest approximation, blood flow (F) in a single blood vessel depends on the difference in pressure at the end of the vessel (ΔP) and the resistance to blood flow provided by the vessel (R):

$$F = \frac{\Delta P}{R} \qquad [1]$$

The resistance of a single vessel is well described by Poiseuille's law which defines R as a function of blood viscosity (η), vessel length (L), and radius (r):

$$R = \frac{8\eta L}{\pi r^4} \qquad [2]$$

Combining equations 1 and 2 can therefore describe how blood flow relates to the pressure gradient (ΔP), vessel radius (r) and length (L), alongside blood viscosity (η):

$$F = \frac{\Delta P \pi r^4}{8\eta L} \qquad [3]$$

While this is a useful equation to analyse blood flow in a single vessel, it is based on several assumptions, such as that the vessels are straight, rigid tubes, blood viscosity is

constant and does not depend on blood flow, and that the flow is under ideal lamina conditions (Herring, Paterson & Levick, 2018; Klabunde, 2011).

The radius of the vessel is regulated by smooth muscle cells and, according to equation 2, a small reduction in vascular tone greatly increases local blood flow. It should be noted that the resistance of a given part of the circulation strongly depends on the arrangement of the vessels either in parallel or series. Thus, capillary beads generally produce low resistance to blood flow because in spite of capillaries having individually small diameters, their large number (hence large total cross-sectional area) and their arrangement in parallel lowers their overall resistance to blood flow (Fig. 1.1).

$$\frac{1}{R_{parallel}} = \frac{1}{R_1} + \frac{1}{R_2} + \frac{1}{R_3} + \cdots \frac{1}{R_n}$$

Where $R_{parallel}$ is the total parallel resistance, and R_X are the resistance of the individual blood vessels.

In contrast, the resistance of large vessels is arranged in series and therefore the total resistance is the sum of the individual vessel resistances. Leading to large overall implications if there is a small change in an individual vessel (Fig. 1.1).

$$R_{series} = R_1 + R_2 + R_3 + \ldots R_n$$

Where R_{series} is the total series resistance, and R_X are the resistance of the individual blood vessels (Herring, Paterson & Levick, 2018; Klabunde, 2011).

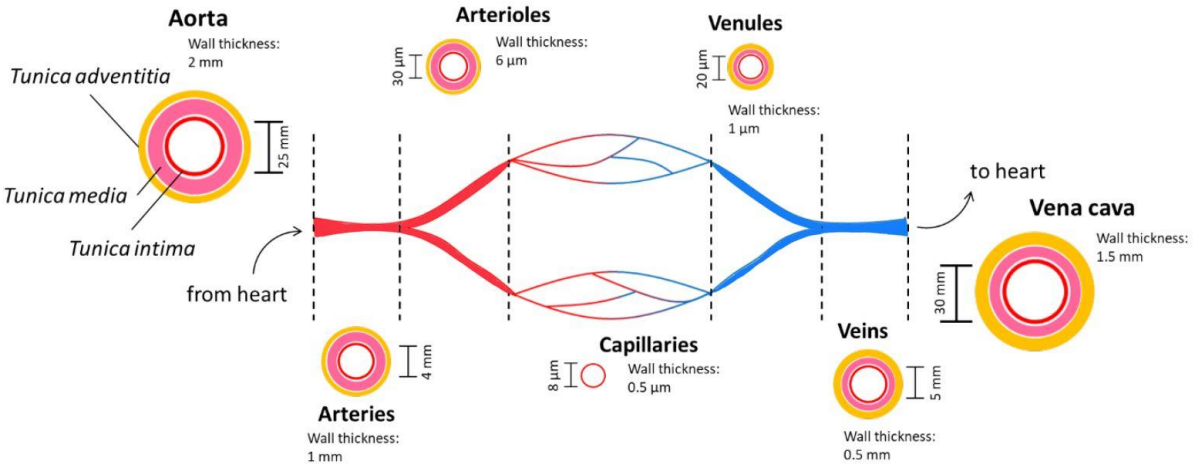


Figure 1.1 Organisation and dimensions of the blood vessels in the human circulatory system

Diagrammatic representation of the circulatory system demonstrating blood vessels in series from the aorta and arteries separating into arterioles, which then separate into a parallel network of capillaries. Vessels then converge into venules and veins as they return to the heart via the vena cava. Vessel dimensions taken from (Burton, 1954).

Muscular arteries control the resistance in the circulatory system but also the compliance. The compliance is defined as the degree to which the arterial system distends as the pressure increases (Rang, 2007). As the rate of volume ejected by the left ventricle is greater than the rate it can drain to the small resistance arteries the excess volume of blood is accommodated in the elastic arteries, such as the aorta. They are high in elastin when compared to other vessels and therefore play a major role in elastic recoil during diastole (Klabunde, 2011). Muscular arteries are smaller than the aorta, measuring ~4 mm in diameter in man, with a wall thickness of ~1 mm (Burton, 1954). The distendability of these vessels is defined by the arterial compliance:

$$C = \frac{\Delta V}{\Delta P} \qquad [4]$$

where ΔV is the increase in blood volume in the arterial system required to produce unit increase in arterial pressure, ΔP (Herring, Paterson & Levick, 2018).

1.1.2 Regulation of vascular tone

Vascular tone regulates regional blood flow, arterial blood pressure, capillary filtration rate and central venous pressure. Vascular tone is controlled by the interplay between the action of vasodilator and vasoconstrictor stimuli; these signals are integrated by VSMCs and ultimately determine artery tone and diameter (Herring, Paterson & Levick, 2018; Webb, 2003). Vascular tone is controlled by intrinsic and extrinsic factors. Intrinsic (within an organ or tissue) factors are the main causes of local blood flow and include Bayliss myogenic response, endothelial secretions, vasoactive metabolites, autacoids and temperature (Herring, Paterson & Levick, 2018). The Bayliss myogenic effect is a major intrinsic effect of the change of vessel tone following an increase in blood pressure, and it originates from within the vessel itself (Bevan & Laher, 1991; Herring, Paterson & Levick, 2018; Klabunde, 2011). It is believed that this effect involves the activity of stretch or volume regulated channels in SMCs (Di & Malik, 2010; Earley, 2013), activation of these channels has an influence over the membrane potential and can effect many downstream pathways causing SMC contraction (Herring, Paterson & Levick, 2018).

Extrinsic (outside the organ) factors are the main stimuli that control systemic vascular resistance and include vasomotor nerves and vasoactive hormones (Herring, Paterson & Levick, 2018). Neurotransmitters, for example noradrenaline, are released from sympathetic nerve terminals and bind to receptors on the plasma membrane of VSMCs.

Majority of these transmitters bind to a panel of GPCRs giving rise to a variety of responses by activating different receptors. Three types of adrenoceptors (α1, α2 and β2) are expressed on the plasma membrane of VSMCs. Activation of the G_q coupled α1 receptors leads to vasoconstriction via the activation of the IP_3 signalling cascade (described below in more detail, section 1.4.3) (Klabunde, 2011). Activation of the G_i coupled α2 receptors cause vasoconstriction via reducing the formation of cAMP therefore leading to higher MLCK concentration (Wettschureck & Offermanns, 2005). Activation of GPCRs also cause vasodilation. Specifically, activation of the G_s coupled β2 receptor increases the activity of adenylyl cyclase and in turn the concentration of MLCK, causing relaxation of the muscle (Henry & Goldie, 1990; Herring, Paterson & Levick, 2018). Gap junctions electrically couple the SMCs and therefore activity from one SMC will spread to its neighbours causing a synchronised response, allowing multiple SMCs to be controlled via a single neurone (Greger, 1996; Herring, Paterson & Levick, 2018).

Endothelial cells also have a function to modulate vascular tone. The endothelium secretes a series of vasoactive compounds, these compounds tend to be released as they are synthesised rather than being stored for later use (Herring, Paterson & Levick, 2018). Prostacyclin was the first vasodilator to be discovered (Moncada & Vane, 1979). Prostacyclin receptors on smooth muscle cells are G_s-coupled receptors and lead to increase in cAMP synthesis (Kuo & Ehrlich, 2015; Moncada & Vane, 1979). Nitric oxide (NO) was then found to be a potent vasodilator when the action of an acetylcholine analogue, carbachol, was reversed from a vasodilator to a vasoconstrictor on removal of the endothelium. From this NO was found to be a factor responsible for endothelium-derived relaxation (Furchgott & Zawadzki, 1980; Palmer, Ferrige & Moncada, 1987). In

some small vessels the vasodilation was found to persist when the production of NO and prostacyclin had been inhibited. While the exact compound causing this action has not yet been identified is involves the hyperpolarization of vascular smooth muscles cells, therefore it has been coined the 'endothelium-derived hyperpolarizing factor' (EDHF) (Herring, Paterson & Levick, 2018). The endothelium also secretes vasoconstrictors e.g. the peptide endothelin-1. Endothelin-1 binds to G_q-PCRs on the surface of smooth muscle cells and triggers the IP_3 signalling cascade, triggering a long-lasting constriction (Klabunde, 2011).

Among the key factors that modulate VSMCs tone are the ionic compositions of the intracellular and extracellular environment. A feature of VSMCs is their elevated intracellular Cl^- concentration ($[Cl^-]_i$). This is due to the action of the Na^+-K^+-$2Cl^-$ co-transporter (NKCC) (Schroeder, Cheng, Jan & Jan, 2008) and the Cl^-/HCO_3^- exchanger AE2 (Matchkov, Aalkjaer & Nilsson, 2005) on the VSMCs plasma membrane (Bulley & Jaggar, 2014; Chipperfield & Harper, 2000). As a result, the Cl^- equilibrium potential is raised above the resting membrane potential in VSMCs. Opening of Cl^- channels within the plasma membrane of VSMCs is therefore associated with Cl^- efflux and membrane depolarisation (Herring, Paterson & Levick, 2018; Webb, 2003).

1.2 Vascular smooth muscle cells

Vascular smooth muscle cells are spindle shaped cells which are between 8-10 µm in diameter and 80-200 µm in length. These cells contain contractile proteins, actin, and myosin, which are regulated by the concentration of $[Ca^{2+}]_i$. These cells are connected by ion-permeable electrically conductive gap junctions formed of connexin proteins

(Herring, Paterson & Levick, 2018). Gap junctions allows the transmission of depolarising ionic current from cell to cell to initiate a coordinated contraction of the smooth muscle. Smooth muscle cells also contain many indentations in the cell membrane called caveolae. Caveolae in the cell surface increase the total membrane area by up to 75 % (Herring, Paterson & Levick, 2018) are also thought to act as signalling domains that play a role in the growth and contraction of SMCs.

Mechanical, electrical, and chemical stimuli can all initiate contraction in vascular smooth muscle cells. Mechanical stimuli such as a change in transluminal pressure on the vessel wall will cause contraction without any electrical or chemical stimuli, this is termed the myogenic response (Johansson, 1989; Johnson, 1989). Electrical depolarisation of the smooth muscle cell membrane activates voltage-gated cation channels (VGCC) which causing an increase in $[Ca^{2+}]_i$ and therefore contraction. Chemical stimuli cause contraction by binding to specific receptors on the plasma membrane and elicits smooth muscle cell contraction (Herring, Paterson & Levick, 2018).

1.2.1 Vascular excitation-contraction coupling

In large blood vessels, contraction and relaxation is determined by cytosolic Ca^{2+} and is regulated by changes in Ca^{2+} sensitivity. Influx of Ca^{2+} through ion channels on the plasma membrane or release of Ca^{2+} from internal stores, such as the sarcoplasmic reticulum (SR) cause an increase in $[Ca^{2+}]_i$ (Fig. 1.2) (Somlyo & Himpens, 1989). This elevation in $[Ca^{2+}]_i$ enables contraction of VSMCs after an excitatory stimulus (Herring, Paterson & Levick, 2018).

This leads to the creation of a Ca^{2+}-calmodulin complex, calmodulin being a cytoplasmic protein which binds 4 Ca^{2+} ions, this complex then activates a serine/threonine kinase called myosin light chain kinase (MLCK) (Herring, Paterson & Levick, 2018; Webb, 2003). The light chain part of the myosin head then binds to the actin forming a crosslink. For this process to occur the light chain myosin head must be phosphorylated. MLCK transfers a phosphate group from ATP to the myosin light chain which then goes on to from the crosslink with actin. The myosin head then rotates to generate tension, remaining in place to maintain this contracted state (Herring, Paterson & Levick, 2018; Webb, 2003).

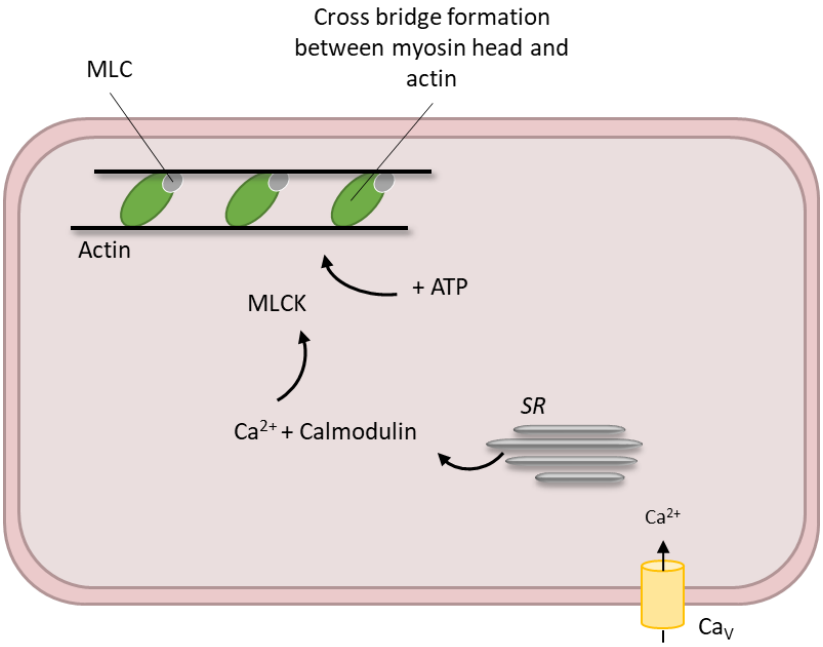


Figure 1.2 Vascular smooth muscle cell contraction.

Contraction of vascular smooth muscle is started by an increase in $[Ca^{2+}]_i$ by activation of Ca_V or release from the sarcoplasmic reticulum (SR). This leads to the creation of Ca^{2+}-calmodulin complex which activates MLCK. MLCK transfers a phosphate group from ATP to the myosin light chain which forms the crosslink with actin and causes SMC contraction.

As described above, Ca^{2+} and its regulation are crucial factors in the regulation of vascular tone, and changes in $[Ca^{2+}]_i$ serve as a principle mechanism for contraction and relaxation. When the muscle is at rest the $[Ca^{2+}]_i$ in VSMCs is low (~100 nM) (Herring, Paterson & Levick, 2018; Hill-Eubanks, Werner, Heppner & Nelson, 2011) compared to the $[Ca^{2+}]_{ext}$ and within intracellular Ca^{2+} stores (Somlyo & Himpens, 1989). This difference creates an electrochemical gradient for influx of Ca^{2+} into the cytoplasm. Extracellular Ca^{2+} which enters through Ca^{2+} conducting channels in the plasma membrane (Amberg & Navedo, 2013; Hill-Eubanks, Werner, Heppner & Nelson, 2011; Marks, 1992). These channels are also responsible for the small extracellular Ca^{2+} influx which contributes to basal tone (Herring, Paterson & Levick, 2018). Stored Ca^{2+} in the cells are released from the sarcoplasmic reticulum (SR) store via IP_3-dependant Ca^{2+} release which is activated by noradrenaline (Amberg & Navedo, 2013). Ca^{2+}-ATPase pumps in the plasma and SR membrane continuously pumps Ca^{2+} out of the cytoplasm, along with an Na^{+}-Ca^{2+} exchanger which continuously pumps Ca^{2+} out of the cell (Levitsky, 2007; McCarron, Walsh & Fay, 1994). Therefore Ca^{2+} channels and membrane potential are major factors influencing VSM contraction, in the next section the ion channels and electrical properties of the cells are described.

1.2.2 Electrical properties of vascular SMC

The hydrophobic nature of the plasma membrane constitutes a barrier to ion diffusion. The presence of ion channels and transporters allow selective (active or passive) transport of different ion species (Hille, 2007; Huang & Keynes, 2021).

The combined existence of an inequal ionic distribution at the two sides of the membrane and the unequal permeability of the membrane to various ions lead to the generation of a membrane potential. The magnitude and direction of the flux for each individual ion type will depend on the corresponding electrochemical gradient, which is given by the difference between the membrane potential and the equilibrium potential of the ion. The Nernst equation defines the equilibrium potential (E_X) for a given ion (X) as:

$$E_X = \frac{RT}{z_x F} ln \frac{[X]_{out}}{[X]_{in}} \quad [5]$$

where $[X]_{in}$ and $[X]_{out}$ are the intracellular or extracellular concentration of the ion, respectively, R is the universal gas constant, T is the temperature in Kelvin, z_X is the charge of the ion and F is Faraday's constant (Hille, 2007).

Therefore, the overall resting membrane potential of the cell (V_m) is a function of the concentration of ions inside and outside the cell and their permeability through the membrane. The resting membrane potential is well described by the "constant field" equation developed by Goldman-Hodgkin-Katz (the 'GHK voltage equation'). This equation allows the calculation of E_{rev} as:

$$E_{rev} = \frac{RT}{F} \ln \left(\frac{p_k[K]_{out} + p_{Na}[Na]_{out} + p_{Cl}[Cl]_{in}}{p_k[K]_{in} + p_{Na}[Na]_{in} + p_{Cl}[Cl]_{out}}\right) \quad [6]$$

where p_{ion} is the relative permeability of the ion (Table 1.1 for VSMCs). For mixtures of permeant anions with different valences it is more complicated and more complete expressions have been derived (Huang & Keynes, 2021).

Table 1.1 Ionic composition of vascular smooth muscle

Ion	Intracellular (mM)	Extracellular (mM)	Nernst Equilibrium potential (mV)
K^+	165	5	-89
Na^+	9	137	+69
Ca^{2+}	0.0001	1.2	+124
Cl^-	54	134	-23
HCO_3^-	7.3	15.5	-19
H^+	8.7×10^{-8} (pH 7.06)	4.0×10^{-8} (pH 7.4)	-20

Data taken from (Herring, Paterson & Levick, 2018). Muscle is measured in a relaxed state and it is assumed $[Ca^{2+}]_i$ is in a free, unbound state.

1.2.3 Ion channels in vascular SMC

In this section, I will provide an account of the main ion channels found in VSM. The ion channel distribution may vary depending on the vascular bed and possibly the species difference may also exist (Jackson, 2000; Tykocki, Boerman & Jackson, 2017).

There are four main types of ion channel expressed in VSMC: K^+, Ca^{2+}, non-selective cation and Cl^-. These alongside transporters, co-transports and exchangers maintain the resting membrane potential which deviation from can elicit vasoconstriction or vasodilation (Herring, Paterson & Levick, 2018).

The K^+ channels are especially important in the generation of the resting membrane potential of VSMCs due to the high intracellular K^+ concentration, generated by the action of the active Na^+-K^+ pump (Jackson, 2017).

There are four main types of K^+ channels in VSMCs: K_{ir}, inward rectifying, K_{ATP}, ATP-dependant, K_v, voltage dependent and K_{Ca}, Ca^{2+}-dependent. The properties of these K^+ channels differ however they all have a specific contribution to vascular tone (Herring, Paterson & Levick, 2018).

Inwardly rectifying K^+ channels sense extracellular K^+ and contributes to vasodilation in exercising muscle, myocardium, and the brain (Nelson & Quayle, 1995). The open probability (P_o) increases with a rise in extracellular K^+, in the range of 5-25 mM. This increased K^+ conductance shifts the resting membrane potential towards the equilibrium potential of K^+ which hyperpolarises the membrane and leads to vasodilation.

ATP-dependent K^+ channel is also inwardly rectifying is regulated by ATP and nucleotide diphosphatases such as ADP (Reimann & Ashcroft, 1999; Teramoto, 2006). The channel has been implicated in hypoxic vasodilation (Quayle, Turner, Burrell & Kamishima, 2006).

K_v and K_{Ca} channels contribute to the resting membrane potential (Ko, Burg, Platoshyn, Msefya, Firth & Yuan, 2007; Lara, Acevedo & Onetti, 1999; Nelson & Quayle, 1995). K_v channels are activated by membrane depolarisation once the potential has reached ~-30 mV and contribute to the basal membrane potential (Nelson & Quayle, 1995). K_{Ca} channels expressed in VSMCs are the "Big Conductance" isoform (Herring, Paterson & Levick, 2018). At resting membrane potentials BK_{Ca} is activated by spontaneous Ca^{2+} sparks generating spontaneous transient outward currents (STOCs) which also contribute to the resting membrane potential making it more negative, reducing vascular excitability and reducing the P_o of VGCC (Herring, Paterson & Levick, 2018). Constitutively active ("leak") two-pore (K2P) channels play an important role in stabilizing the negative V_m and counterbalancing depolarization (Olschewski et al., 2017).

VGCCs mediate depolarisation-dependent contraction (Bers, 2002; Tsien, 1983). These channels are highly selective of divalent cations (Ca^{2+} and Ba^{2+}), which open on depolarisation of the membrane. The predominant VGCC in VSMCs are L-type Ca^{2+} channels (Catterall, 2011; Knot & Nelson, 1998), and the P_o is a continuous function of membrane V_m, where at resting V_m there is a low but finite P_o (Herring, Paterson & Levick, 2018). These channels along with the constitutively active transient receptor potential (TRP) channels allow a small influx of Ca^{2+} and this low cytosolic Ca^{2+} activates myosin heads to generate basal vascular tone (Klabunde, 2011).

In addition to influx via VGCCs Ca^{2+} also enters the cell through non-selective cation channels (NSCCs), which mediate depolarization-independent contraction and contribute to agonist-induced electrical excitation (Putney et al., 2017). There are two major types of NSCC expressed in VSMCs, receptor-operated channels (ROCs) and store-operated channels (SOCs) (Large, 2002; Thorneloe & Nelson, 2005), both being activated by agonist induced, pharmacomechanical contraction, via activation of the G_q-PLCβ-DAG pathway (Herring, Paterson & Levick, 2018). This is typical of large arteries where few L-type Ca^{2+} channels are expressed, this pathway is important in this thesis where the main blood vessel studied is the aorta.

In VSM $[Cl^-]_i$ is unusually high at ~54 mM due to the $Na^+K^+2Cl^-$ co-transporters and Cl^- HCO_3^- exchangers (Herring, Paterson & Levick, 2018; Madden, Ray, Keller & Kleinman, 2001). The Cl^- equilibrium of the cell leads to addition of -20 mV to the resting membrane potential, so at rest the Cl^- are closed. The main Cl^- channels expressed are calcium-activated chloride channels which are they main channel of study in this thesis and their role in smooth muscle in described in further depth in section 1.5. In brief, on

opening of CaCCs by an increase in $[Ca^{2+}]_i$ the resting membrane potential of -50 mV drives Cl^- out of the cell, this efflux of Cl^- depolarizes the V_m towards the Cl^- equilibrium potential and also increases the P_o of VGCC leading to an influx of Ca^{2+} into the cell evoking agonist-induced contraction of the smooth muscle and therefore altering the blood vessel tone (Hartzell, Putzier & Arreola, 2005; Large & Wang, 1996; Saleh & Greenwood, 2005).

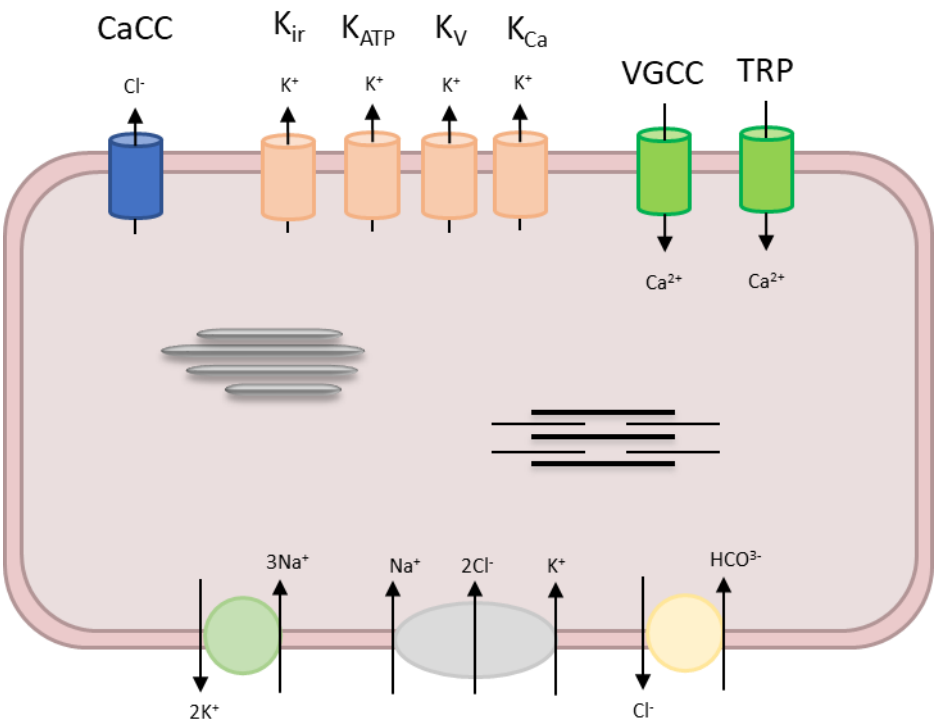


Figure 1.3 Ion channels and transporters expressed in VSMCs.

Calcium-activated chloride channels, depicted in blue, are activated by intracellular Ca^{2+} causing membrane depolarisation. Potassium channels, depicted in orange, generate the negative resting membrane potential due to the high $[K^+]_i$. Ca^{2+} channels, depicted in bright green, allow influx of Ca^{2+} which facilitates contraction. Sodium-potassium pump, depicted in light green, maintains the high $[K^+]_i$. $Na^+K^+2Cl^-$ co-transporter, depicted in grey, and $Cl^-HCO_3^-$ exchangers, depicted in yellow, maintain the high $[Cl^-]_i$.

1.3 CaCCs

While there is a wealth of knowledge and modulators of VGCC there is much less known about CaCCs in VSMCs. CaCCs are proposed depolarising channels within VSMCs. In the sections below I will describe the biophysical, pharmacological, and physiological properties of the channels, which are the focus of my DPhil project. Therefore, looking to understand the molecular pharmacology and towards targeting CaCCs for therapeutic benefit.

CaCC currents were observed for the first time in the 1980s (Bader, Bertrand & Schwartz, 1982; Barish, 1983; Miledi, 1982) but their molecular identity has only been resolved in 2008 when three separate research groups discovered that the *TMEM16A* gene was responsible for this current (Caputo et al., 2008; Schroeder, Cheng, Jan & Jan, 2008; Yang et al., 2008).

Yang et al. (2008) discovered TMEM16A while searching among proteins that has multiple transmembrane segments. While expressing TMEM16A they found it gave Cl^- currents activated by receptor mediated intracellular Ca^{2+} mobilization. For example, TMEM16A was co-expressed with endothelin, angiotensin, muscarinic, histamine or purinergic receptors and actuate stimulation with the corresponding agonist gave large CaCC currents. TMEM16A activation by direct Ca^{2+} application on the cytosolic side was also studied. The currents elicited resemble native CaCCs in terms of Ca^{2+} sensitivity, voltage-dependence, and response to inhibitors.

Schroeder et al. (2008) used expression cloning in their study after they discovered that oocytes from axolotl salamander had no CaCC current while oocytes from *Xenopus laevis* frogs show CaCC currents. Physiologically as the CaCC currents in *Xenopus* oocytes

are responsible for the block of polyspermia (Schroeder, Cheng, Jan & Jan, 2008). Axolotl oocytes lack CaCC current since their fertilization is polyspermic by nature (Schroeder, Cheng, Jan & Jan, 2008). Axolotl oocytes were used for expression cloning that lead to identification of TMEM16A as a CaCC-coding gene. Heterologous expression in a variety of mammalian cell lines of TMEM16A gave rise to Cl^- currents with voltage and Ca^{2+} sensitivity analogues to that of native CaCCs in *Xenopus* oocytes. TMEM16A channels were also found to be sensitive to CaCC blockers such as, 4,4'-Diisothiocyano-2,2'-stilbenedisulfonic acid (DIDS), niflumic acid (NFA) and 5-Nitro-2-(3-phenylpropylamino)benzoic acid (NPPB) (Schroeder, Cheng, Jan & Jan, 2008).

Caputo et al. (2008) used the knowledge that treating human bronchial epithelial cells with IL-4 or IL-13 increases CaCC activity. Gene expression microarrays were used to identify genes upregulated by IL-4 in epithelial cells. It was discovered that downregulation of *TMEM16A* resulted in a significant reduction of CaCC current in pancreatic CFPAC-1 cells. Both purinergic receptors and Ca^{2+} ionophore activation was used to activate *TMEM16A*, demonstrating it is not an indirect regulator of CaCCs but is responsible for it.

The TMEM16A sequence had no similarities to any other known ion channel and so became the founding member of the TMEM16x family.

1.3.1 TMEM16x family

The TMEM16 family of proteins comprised of 10 members defined by a letter from A to J (with I missing). The TMEM16x proteins serve as ion channels or lipid scramblases. Phospholipid scramblases allow for the movement of lipids between the inner and outer

leaflet by lowering the energy barrier to permeation (Williamson, 2016). This changes the composition of the membrane and therefore effects fluidity and cell signalling pathways (Malvezzi et al., 2013; Suzuki, Umeda, Sims & Nagata, 2010).

TMEM16A and TMEM16B function as CaCCs while TMEM16C, TMEM16D, TMEM16E, TMEM16F, TMEM16G, TMEM16J are proposed phospholipid scramblases and non-selective channels (Gyobu et al., 2016; Suzuki, Fujii, Imao, Ishihara, Kuba & Nagata, 2013). TMEM16H, TMEM16J are poorly understood and are poorly or not expressed on the plasma membrane and are thought to have intracellular functions (Tian, Schreiber & Kunzelmann, 2012). TMEM16K has recently been identified as a scramblase expressed intracellularly (Bushell et al., 2019) and has been proposed as a swell activated Cl^- channel in macrophages, controlling cellular volume and therefore macrophage function (Hammer et al., 2015).

Various studies have looked at the expression profiles of this family within the vasculature. For example, TMEM16A, TMEM16F and TMEM16K being most abundant in rat Pulmonary Artery Smooth Muscle Cells (PASMCs) (Manoury, Tamuleviciute & Tammaro, 2010).

Thus far, only a few mutations in TMEM16x have been unequivocally linked to human disease. However, mutations in TMEM16F cause Scott syndrome, a bleeding disorder resulting from dysfunctional phospholipid scrambling in platelets (Suzuki, Umeda, Sims & Nagata, 2010; Yang et al., 2012). One patient was also found to have a mutation in the TMEM16A gene, the patient identified was male and suffered from orthostatic hypotension, atrial fibrillation and subsequent systolic arrhythmia (Brookfield, 2014). It is possible that the rapid growth of Genome-wide association study (GWAS) will

elucidate new genetic associations between TMEM16x and human disease. For example, a recent study linked TMEM16A with cardiac abnormalities (Wild et al., 2017). Although genetic analysis of TMEM16x still at its infancy, dysregulation of TMEM16x function/expression has been clearly linked to disease (as outlined in greater detail in section 1.4).

1.3.2 Biophysical properties of CaCCs

TMEM16A channels mediate outwardly rectifying Cl^- currents with complex activation kinetics. TMEM16A and TMEM16B are both CaCCs with ~60 % homology and display similar electrophysiological properties (Scudieri, Sondo, Caci, Ravazzolo & Galietta, 2013). The selectivity sequence of TMEM16A and TMEM16B is $SCN^- > NO_3^- > I^- > Br^- > Cl^- > F^-$ (Adomaviciene, Smith, Garnett & Tammaro, 2013), however due to the high concentration of Cl^- compared to other ions in a physiological setting CaCCs mediated predominantly Cl^- currents in vivo. In addition, the EC_{50} of TMEM16A and TMEM16B currents *versus* $[Ca^{2+}]_i$ relationship at +70 mV were rather similar, being equal ~1.3 and 1.8 µM, respectively (Adomaviciene, Smith, Garnett & Tammaro, 2013). The single channel conductance of TMEM16A has been reported to be ~3-8 pS (Adomaviciene, Smith, Garnett & Tammaro, 2013; Yang et al., 2008) depending on the expression system and that of TMEM16B is ~2-3 pS (Adomaviciene, Smith, Garnett & Tammaro, 2013; Yang et al., 2008).

TMEM16A and TMEM16B are gated by V_m, $[Ca^{2+}]_i$ and external permeant anions (Contreras-Vite et al., 2016). Two components of CaCCs gating has been detected: fast and slow (Hartzell, Putzier & Arreola, 2005). The slow gating component is strongly

dependent on V_m, residues in the first intracellular loop and extracellular [Cl^-] under physiological conditions (Cruz-Rangel, De Jesús-Pérez, Contreras-Vite, Pérez-Cornejo, Hartzell & Arreola, 2015).

At low Ca^{2+} (<< 1 μM) the TMEM16A and TMEM16B current displays a time dependence with outward rectification (Adomaviciene, Smith, Garnett & Tammaro, 2013). Whereas as Ca^{2+} increases that time dependant activation is reduced, and current-voltage relationship becomes almost linear. In the sections below, I will focus on TMEM16A since it is the predominant form isoform found in VSMC and it is the channel studied in this project.

1.4 TMEM16A in health and disease

TMEM16A widely expressed in various tissues and is involved in several physiological process, so upregulation and abnormal expression of these channels have been linked to several diseases. Both activators and inhibitors have been suggested to be therapeutically beneficial.

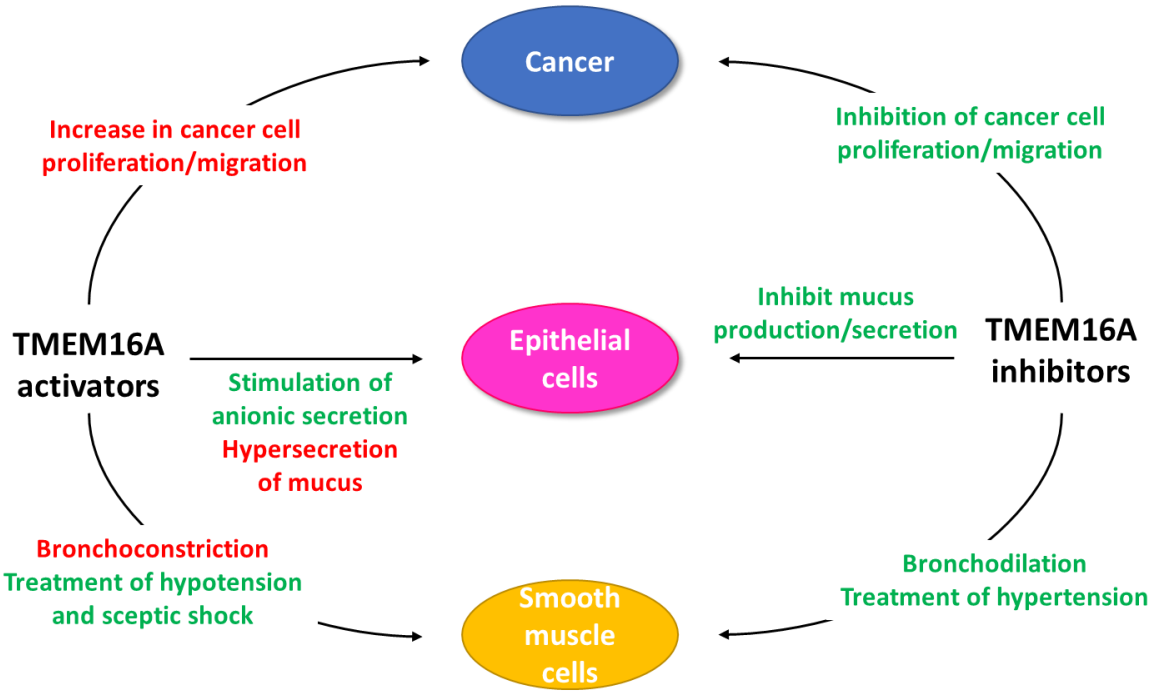


Figure 1.4 Effect of possible pharmacological effects of TMEM16A.

Diagrammatic summary of possible pharmacological effects (green: therapeutic effects; red: potential off target side effect) of TMEM16A activators and inhibitors. Activation of TMEM16A in the epithelial cells of the airways could improve mucociliary clearance by enhancing the secretion of anions, while also causing hypersecretion. However, as TMEM16A in abundantly expressed in smooth muscle cells of the bronchus, TMEM16A activators may also cause bronchoconstriction. Inhibition of TMEM16A cells could a decrease cell proliferation/migration in cancer cells, however activation would cause the opposite effect and have a detrimental effect. Inhibition of TMEM16A could be potentially beneficial to induce relaxation of smooth muscle cells in the vasculature for treatment of diseases such as hypertension.

1.4.1 TMEM16A in cancer cells

Before the discovery of TMEM16A as a CaCC, anoctamins have been found to be upregulated in a variety of human cancers (Britschgi et al., 2013; Dixit et al., 2015; Kashyap et al., 2009; Sauter, Novak, Pedersen, Larsen & Hoffmann, 2015; Sui et al., 2014). Whether increased expression of TMEM16A is a cause or consequence of carcinogenic cellular phenotype remains to be elucidated. TMEM16A has been found to

be highly expressed in gastrointestinal cancer (West et al., 2004), amplified and overexpressed in oral squamous cell carcinomas (Huang, Godfrey, Gooding, McCarty & Gollin, 2006), and upregulated in head and neck squamous cell carcinomas, gastrointestinal stromal tumours (Ruiz et al., 2012) and breast cancers (Britschgi et al., 2013).

TMEM16A expression has been associated with reduced survival and increased metastatic potential (Ayoub et al., 2010; Duvvuri et al., 2012; Ruiz et al., 2012). It has been reported that cancers high with TMEM16A expression are associated with a median 23-month survival time while cancers without TMEM16A expression are typically associated with a longer (56-month) survival time (Ruiz et al., 2012).

In *in vitro* studies, cultured cell lines with high TMEM16A expression had higher cell proliferation compared to cells in which TMEM16A expression was suppressed with small interference RNA (siRNA) (Britschgi et al., 2013; Duvvuri et al., 2012; Liu, Lu, Liu, Huang & Wang, 2012) or the TMEM16A current inhibited pharmacologically (Britschgi et al., 2013; Mazzone et al., 2012; Stanich et al., 2011) have shown reduced cell growth.

In cell lines in which TMEM16A was overexpressed there was an increase in phosphorylation of ERK1/2 and in cyclin D1 levels. A mutated TMEM16A (K610A) which abolishes Cl^- transport was used to probe this effect. Expressing these mutant channels shows no ERK1/2 phosphorylation, demonstrating that Cl^- transport is important for the cell cycle and proliferation (Wang et al., 2012).

The studies described above indicate that TMEM16A might has a role in cancer progression and it may serve as a diagnostic and prognostic marker for cancer, as well as serving as a potential drug target.

1.4.2 TMEM16A in airway and intestinal epithelial cells

Cystic fibrosis (CF) is an inflammatory disease caused by dysfunctional cystic fibrosis transmembrane conductance regulator (CFTR) chloride channel (Galietta, 2013; Kunzelmann et al., 2019). Loss of function of the CFTR channel leads to a defect in epithelial ion transport and therefore the condition is characterised by airway obstruction due to mucus hypersecretion, airway plugging, and bronchoconstriction.

TMEM16A has been shown to be highly expressed in human and rodent airway epithelial cells (Ousingsawat, Martins, Schreiber, Rock, Harfe & Kunzelmann, 2009; Rock et al., 2009) therefore it has been postulated that TMEM16A activators could be used a drug target for the treatment of cystic fibrosis. As a Cl^- channel expressed in airway epithelial cells it has been thought that it could be activated to compensate for the loss of CFTR Cl^- efflux, and consequently the associated Na^+ and fluidification of mucus associate with Cl^- and Na^+ accumulation in the airways lumen (Galietta, 2013).

The suggestion is further validated by the observation that TMEM16A has been shown to be upregulated in cystic fibrosis, and this upregulation is particularly seen in mucus producing cells with little expression in ciliated cells (Genovese et al., 2019).

Activation of alternate Cl^- channels is thought to theoretically improve hydration of the airway mucus and to increase mucociliary clearance. As TMEM16A is also expressed in the smooth muscle a possible safety concern is that the use of a TMEM16A activators for CF may promote bronchoconstriction. Therefore, it has been discussed whether activation or inhibition of TMEM16A is most beneficial to treat CF (Kunzelmann et al., 2019). Thus, it can be speculated that a potential use of TMEM16A activators in CF may need to be associated with β2 agonists (e.g. salbutamol) to maintain airways smooth

muscle relaxed. Furthermore, upregulated TMEM16A in mucus producing cells and airway smooth muscle cells during inflammation. This might potentially lead to hypersecretion of mucus and airway contraction (Kunzelmann et al., 2019). It has also been suggested that Inhibitors of TMEM16A would have a minimal effect on the few TMEM16A channels expressed in the fluid secreting epithelial cells but inhibition of TMEM16A channels in the mucus producing cells and airway smooth muscle would inhibit mucus production/secretion and induce bronchodilation. Therefore inhibition appears as it would restore balance between mucus and fluid in CF airways (Kunzelmann et al., 2019).

Unfortunately, it has been shown that TMEM16A activators have limited effect on cystic fibrosis in clinical trials. An earlier clinical trial was performed using stabilized dinucleotides (Denufosol) to induce purinergic Ca^{2+} dependent Cl^- secretion and to restore airway surface liquid with the goal of improving lung function in CF. However, the clinical trial failed to demonstrate any benefit of denufosol (Moss, 2013; Ratjen et al., 2012). It may be speculated that denufosol may have induced additional mucus secretion and even additional airway obstruction.

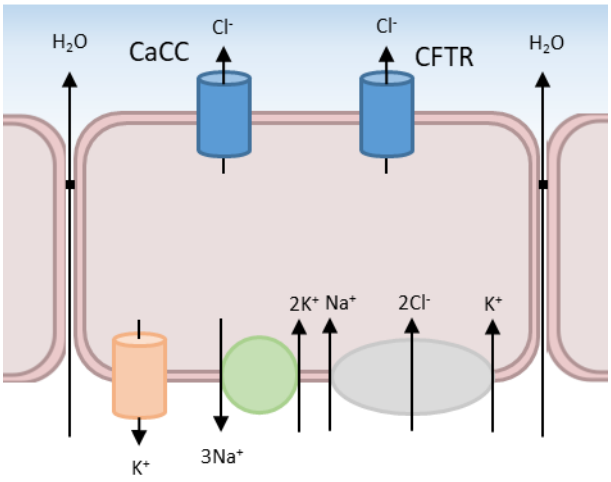


Figure 1.5 Role of TMEM16A in airway epithelium.

Chloride channels, depicted in blue, are responsible for anion secretion form the airway. Potassium channels, depicted in orange, generate the negative resting membrane potential due to the high $[K^+]_i$. Sodium-potassium pump, depicted in light green, maintains the high $[K^+]_i$. $Na^+K^+2Cl^-$ co-transporter, depicted in grey, maintains the high $[Cl^-]_i$.

CaCC currents have also been recorded in intestinal epithelial cells (Huang et al., 2009; Hwang et al., 2009), however TMEM16A has been shown to be a minor component of calcium-activated chloride conductance in these cells (Namkung, Phuan & Verkman, 2011). By using general CaCC inhibitors, specifically $CaCC_{inh}$-A01 and tannic acid, CaCC current was inhibited completely in human intestinal cells. Using a fluorescence-based assay more selective TMEM16A inhibitors were identified and characterised, namely $T16A_{inh}$-A01. $T16A_{inh}$-A01 and digallic acid were found to inhibit CaCC currents only partially in intestinal cells but fully in salivary gland epithelium. siRNA knockdown of TMEM16A reduced expression by ~40 % which was the same reducing as seen by $T16A_{inh}$-A01. The results suggest that TMEM16A carries most of the CaCC current in the salivary gland and only a small fraction of CaCC current in airway and intestinal epithelium (Namkung, Phuan & Verkman, 2011). However, the selectivity of these

compounds has not been fully established. The selectivity of $T16A_{inh}$-A01 has recently been questioned (Boedtkjer, Kim, Jensen, Matchkov & Andersson, 2015) therefore these results should be analysed with this knowledge in mind.

1.4.3 TMEM16A in vascular disease

CaCCs have been shown to be involved in the regulation of myogenic tone and also contraction on stimulation by agonists (Hartzell, Putzier & Arreola, 2005).

CaCC activation is triggered by a rise in the intracellular free Ca^{2+} concentration ($[Ca^{2+}]_i$), as the result of agonist-induced Ca^{2+} release from intracellular stores (Hill-Eubanks, Werner, Heppner & Nelson, 2011). As the E_{Cl} is more positive than the resting membrane potential this results in Cl^- efflux leading to membrane depolarisation, Ca^{2+} influx via voltage-gated Ca^{2+} channels (mainly L-type), and ultimately vasoconstriction. TASK-1 (KCNK3) K^+ channels are part of the K2P family which might oppose this effect, however activation of GPCR leads to an increase in diacylglycerol (DAG) which inhibits TASK-1 (Olschewski et al., 2017). This inhibition facilitates TMEM16A mediated contraction via membrane depolarisation. Down regulation of KCNK3 has also been demonstrated as novel channelopathy leading to the development and progression of pulmonary hypertension (Lambert et al., 2019).

Common Cl^- channel blockers have also been used to demonstrate the role of Cl^- channels in the contraction of VSMCs (Criddle, de Moura, Greenwood & Large, 1996; Criddle, de Moura, Greenwood & Large, 1997; Jones, Shmygol, Kupittayanant & Wray, 2004; Lamb & Barna, 1998; Saleh & Greenwood, 2005; Yuan, 1997). For example NFA and anthracene-9-carboxylic acid (A9C) blocks noradrenaline mediated contraction is

reduced ~50 % (Hartzell, Putzier & Arreola, 2005). Both compounds have also previously been shown to have a biphasic effect on native CaCCs (Piper & Greenwood, 2003a; Piper, Greenwood & Large, 2002) and also cloned TMEM16A (Ta, Adomaviciene, Rorsman, Garnett & Tammaro, 2016). However, as A9C and NFA have also been shown to act of a wide panel of ion channels the results should be taken with caution as the effect could be due to a CaCC independent mechanism. Therefore, in this thesis we will look at off target effects of TMEM16A inhibitors to determine the CaCC component of this response.

CaCCs in VSMCs are also activated by spontaneous Ca^{2+} release from the sarcoplasmic reticulum, resulting in spontaneous transient inward Cl^- currents (STICs) (Large & Wang, 1996; Leblanc et al., 2005) (Fig. 1.4).

TMEM16A was shown to mediate CaCC current in resistance-size arteries and therefore may contribute to the regulation of blood pressure (Thomas-Gatewood et al., 2011). The TMEM16A-KO (knock-out) VSM indicated a major role for TMEM16A in blood pressure regulation (Heinze et al., 2014).

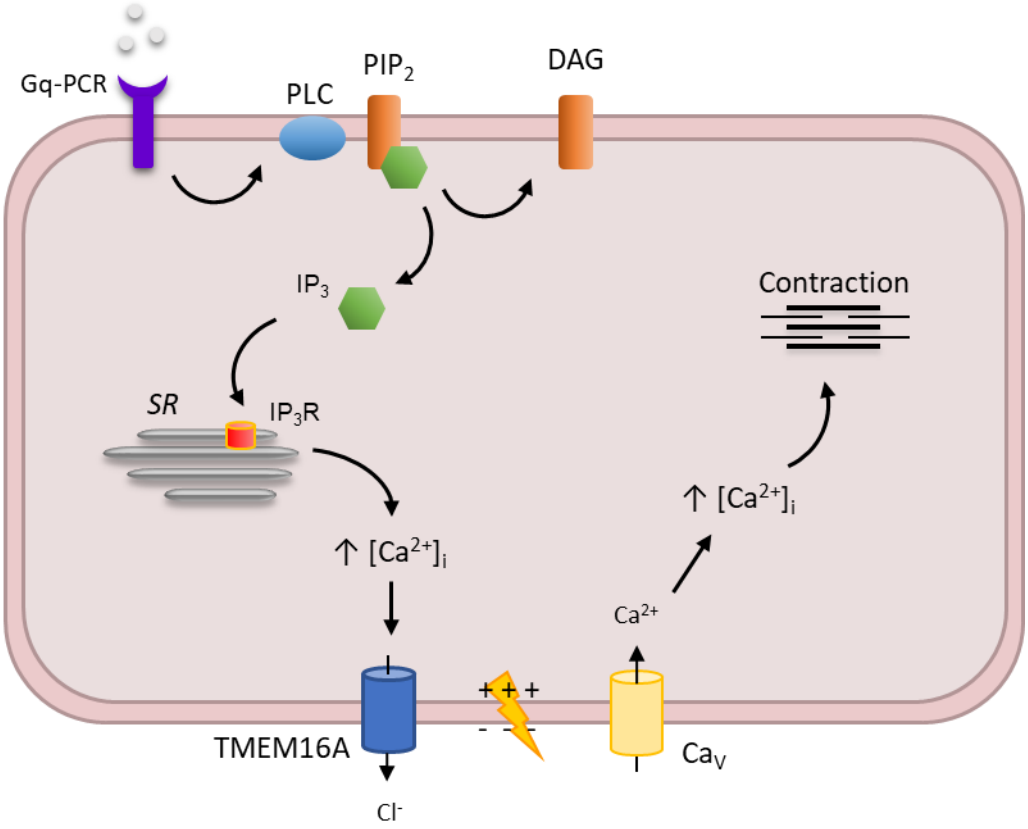


Figure 1.6 Proposed role of TMEM16A in smooth muscle cell contraction.

Noradrenaline (NA) binds to α1-adrenoreceptors on the plasma membrane of VSMCs causing activation of G_q-protein coupled receptors (GPCR) and subsequent Ca^{2+} release from the sarcoplasmic reticulum (SR) via the inositol trisphosphate (IP_3) pathway. This rise in $[Ca^{2+}]_i$ is predicted to activate TMEM16A channels, causing Cl^- efflux and consequently membrane depolarisation and opening of Ca_V channels which leads to cell contraction.

Many studies have explored at the role of TMEM16A in hypertension including pulmonary arterial hypertension (PAH) and systemic hypertension. PAH is characterized by elevated blood pressure in the lung vasculature and can lead to right sided heart failure and death (Archer, Weir & Wilkins, 2010). Increased TMEM16A expression and CaCC current is observed in pulmonary arteries of chronic-hypoxic pulmonary hypertensive rat model (Wang, Li, Huai & Qu, 2015). Upregulation of TMEM16A has

been shown at both the mRNA and protein level (Forrest et al., 2012) with an increase in CaCC current. Contractility was found to be antagonised by CaCC inhibitors niflumic acid (NFA) and $T16A_{inh}$-A01 (Sun, Xia, Paudel, Yang & Sham, 2012). Previous work within the lab has also shows that TMEM16A is the CaCC component of human and rodent pulmonary VSMCs (Manoury, Tamuleviciute & Tammaro, 2010). Loss in TMEM16A from VSMCs resulted in reduced systemic blood pressure, indicating a role for TMEM16A in long term control of blood pressure (Heinze et al., 2014).

Abnormal proliferation of the cells of the *tunica media* of resistance arteries is a hallmark feature of PAH and systemic hypertension (Montani et al., 2013; Tuder, Marecki, Richter, Fijalkowska & Flores, 2007). This cell proliferation leads to vascular remodelling, thickening of arterial walls, blood flow restrictions and increased vascular pressure (Montani et al., 2013). The TMEM16x family has been implicated in cell proliferation (Britschgi et al., 2013; Duvvuri et al., 2012; Liu, Lu, Liu, Huang & Wang, 2012) and thus TMEM16A may participate in the vascular remodelling.

TMEM16A may also be a therapeutic target for septic shock during sepsis. Sepsis occurs when the regulation of the body's immune responses becomes abnormal and this damages many of the organ systems (Gotts & Matthay, 2016). In septic shock, itself a precursor to multi-organ failure and death, there is a large vasodilatation that triggers sympathetic signals to the heart, which is forced to work at much higher rate in the attempt to restore blood pressure and blood perfusion (Rello, Valenzuela-Sánchez, Ruiz-Rodriguez & Moyano, 2017). A compound that could activate the TMEM16A channel and therefore trigger small artery constriction could be very useful therapeutically. Another area of potential application is orthostatic hypotension (Namkung, Thiagarajah,

Phuan & Verkman, 2010), a condition for which current medications have varying degree of success and for which the side effects contribute to poor patient compliance.

1.5 The interplay of TMEM16A gating and pharmacology

The pharmacology and gating of TMEM16A is a complex process and the research into it is still in its infancy. Known modulators of TMEM16A have been shown to act by changing the gating of the channel, specifically A9C where previously in the lab there has been an in-depth study into how the compound affects the gating (Ta, Adomaviciene, Rorsman, Garnett & Tammaro, 2016).

TMEM16A has been shown to be a dimeric protein with two ion conduction pores that are independently activated by Ca^{2+} (Jeng, Aggarwal, Yu & Chen, 2016; Lim, Lam & Dutzler, 2016). Single-particle electron cryomicroscopy (cryo-EM) elucidated the structure of mTMEM16A and therefore provided direct evidence for the structure/function relationship (Dang et al., 2017; Paulino, Kalienkova, Lam, Neldner & Dutzler, 2017). TMEM16A is made up of ten α-helix transmembrane domains, with the N- and C- terminal domains being cytosolic (Paulino, Kalienkova, Lam, Neldner & Dutzler, 2017). The ion conduction pore was shown to be formed by helices α3-α8 (Dang et al., 2017; Paulino, Kalienkova, Lam, Neldner & Dutzler, 2017). These helices also define a negatively charged Ca^{2+} binding site, which binds 2 Ca^{2+} ions (Dang et al., 2017; Paulino, Kalienkova, Lam, Neldner & Dutzler, 2017).

1.5.1 TMEM16A gating

The gating of TMEM16A requires the simultaneous influence of V_m, $[Ca^{2+}]_i$ and the permeant ion. Each subunit of the channel has an independent pore, each subunit binds two Ca^{2+} in a V_m dependent process which is coupled to V_m dependent binding of an external Cl^- ion (Contreras-Vite et al., 2016). This dynamic process opens the channel to a fully conductive state. At low Ca^{2+} the channel is outwardly rectifying and at high Ca^{2+} the current voltage relationship becomes linear (Adomaviciene, Smith, Garnett & Tammaro, 2013; Ferrera, Zegarra-Moran & Galietta, 2011). TMEM16A can be opening at strongly depolarising membrane potentials even in the absence of Ca^{2+} (Contreras-Vite et al., 2016; Cruz-Rangel, De Jesús-Pérez, Contreras-Vite, Pérez-Cornejo, Hartzell & Arreola, 2015; Ta, Adomaviciene, Rorsman, Garnett & Tammaro, 2016; Xiao, Yu, Perez-Cornejo, Cui, Arreola & Hartzell, 2011).

One of the major gating components of the TMEM16A channel is made up of the vacant Ca^{2+} binding site (Lam & Dutzler, 2018). This site is made up of 4 acidic residues: E650, E698, E701, and E730, alongside D734 (Tien et al., 2014). These negatively charged residues make up a barrier to anion permeation, and on binding of Ca^{2+} the barrier is relieved (Lam & Dutzler, 2018). When two Ca^{2+} ions are bound the high positive charge density creates interactions with residues on the alpha 6 domain therefore shifting the conformational equilibrium and stabilises the fully conducting conformation. This binding of Ca^{2+} and conformational change couples the ligand binding and pore opening (Lam & Dutzler, 2018).

The sixth transmembrane domain has also been identified as another major gating component of the TMEM16A channel (Peters et al., 2018). Residues on this domain are

both pore forming and make up part of the Ca^{2+} binding site. This paper uses alanine scanning to determine important residues on this helix which links the gating modes of the channel.

The permeant anion has also been shown to be important in TMEM16A gating. At low Cl^- a monoexponential fit can describe the kinetics of the channel whereas at higher Cl^- a double exponential is required as the Cl^- induces the slow gating component of the current (Cruz-Rangel, De Jesús-Pérez, Contreras-Vite, Pérez-Cornejo, Hartzell & Arreola, 2015). Single channel Cl^- conductance is also reduced when $[Cl^-]_{ext}$ is reduced. Extracellular Cl^- stabilises the Ca^{2+} free close state which favours the transition to open and stabilises the open conformation induced by Ca^{2+} contributing to the V_m dependence of activation.

KCNE-1 has been shown to be an auxiliary unit of TMEM16A acting to shift TMEM16A from a Ca^{2+}-dependant to a voltage-dependant channel (Ávalos Prado et al., 2021). Co-expression of TMEM16A and KCNE-1 in HEK-293 cells produces voltage-dependant Cl- currents in the absence of a rise in $[Ca^{2+}]_i$, and these currents are sensitive to TMEM16A inhibitors, NFA, T16Ainh-A01 and Ani9 (Ávalos Prado et al., 2021).

In the fungal nhTMEM16 there has been shown to be an outer gating component which on binding of Ca^{2+} there is a dynamic rearrangement of the channel which leads to opening the pore by a conformational change in the outer pore (Lee, Khelashvili, Falzone, Menon, Weinstein & Accardi, 2018). While this has been discovered in the fungal nhTMEM16 no movement in the outer pore has been detected by cryo-EM in mTMEM16A (Dang et al., 2017; Lam & Dutzler, 2018; Paulino, Kalienkova, Lam, Neldner & Dutzler, 2017).

1.5.2 Pharmacology of TMEM16A

Potent and selective modulators of TMEM16A could constitute an invaluable resource for scientific research as well as having therapeutic potential as outlined in section 1.4. Currently, selective and potent TMEM16A modulators are not yet available.

The most commonly used CaCC blockers include the fenamates, especially NFA, a group of nonsteroidal anti-inflammatory drugs (NSAIDs). However NFA may also affect other channels such as volume-regulated anion channels (VRAC) (Greenwood & Large, 1998; Xu, Kim, So, Kang, Rhee & Kim, 1997), K^+ channels (Doughty, Miller & Langton, 1998; Wang, Dixon & McKinnon, 1997) and intracellular Ca^{2+} stores (Cruickshank, Baxter & Drummond, 2003).

DIDS and SITS are other compounds that have shown to block CaCC currents but with low potency and low specificity. DIDS has been tested on a few other channels and while it was not found to block CFTR-mediated Cl^- currents, it does inhibit the Cl^- currents mediated by the voltage gated Cl^- channel-3 (ClC-3) channel (Matchkov, Secher Dam, Bødtkjer & Aalkjær, 2013), and also found to antagonise VRAC activity (Best, 1997; Best, Brown, Sheader & Yates, 2000).

A more selective CaCC blocker, $CaCC_{inh}$-A01 was found to block native CaCC currents in intestinal epithelial cells and also found to block ionomycin induced currents (De La Fuente, Namkung, Mills & Verkman, 2007).

Since the cloning of *TMEM16A*, high through put screening has been used to develop more potent and selective compounds. $T16A_{inh}$-A01 was found to block TMEM16A

currents expressed in FRT cells, and this compound was used to study TMEM16A currents in epithelial cells (Namkung, Yao, Finkbeiner & Verkman, 2011a). The vasodilatory effect of $T16A_{inh}$-A01 was studied and it was found that $T16A_{inh}$-A01 blocks CaCCs in vascular smooth muscle cells, and relaxes murine and human blood vessels (Davis et al., 2013). However the selectivity of this compound has now been questioned (Boedtkjer, Kim, Jensen, Matchkov & Andersson, 2015) therefore conclusions made using $T16A_{inh}$-A01 as a selective CaCC blocker should be taken with caution.

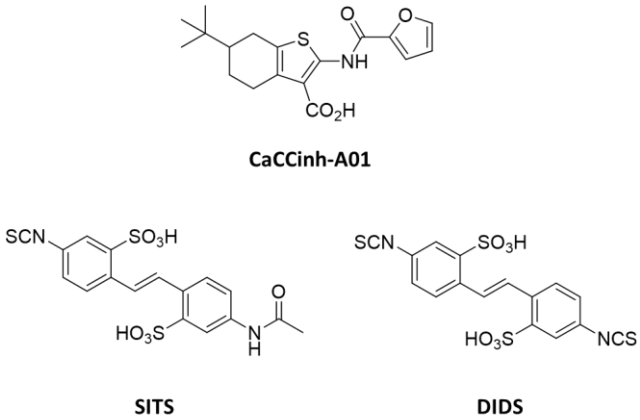


Figure 1.7 General CaCC inhibitors

Chemical structure of general CaCC inhibitors, $CaCC_{inh}$-A01, SITS and DIDS.

In 2013 (Oh et al., 2013) screened compounds for TMEM16A inhibition using native CaCCs in *Xenopus Oocytes*. From several hit compounds they produced a structure-activity relationship (SAR) study of a variety of anthranilic acid derivatives and studied the relationship between the biological activity and the nature and position of the substituents. This study revealed the most potent compound, *N*-((4'-methoxy)-2'-naphthyl)-5-nitroanthranilic acid MONNA, which fully blocked CaCC currents < 1 µM (Oh et al., 2013). Selectivity tests revealed that other chloride channels such as

bestrophin-1, chloride channel protein 2, and CFTR were not appreciably blocked by 10-30 μM MONNA (Oh et al., 2013).

More promisingly a compound with selectivity for TMEM16A over TMEM16B was identified, 2-(4'-chloro-2'-methylphenoxy)-*N*-[(2''-methoxyphenyl)methylideneamino]-acetamide Ani9 (Seo et al., 2016). Ani9 was found to block TMEM16A current expressed in FRT cells fully at sub micromolar potency and also blocks endogenous CaCC currents in PC3, Capan-1 and NHNE cells (Seo et al., 2016). Ani9 did not affect the intracellular Ca^{2+} signalling and CFTR chloride channel activity (Seo et al., 2016), this suggests Ani9 is a useful pharmacological tool for the study of TMEM16A currents in a variety of systems.

In 2017 a compound with ~3.6-fold more potency that Ani9 was reported (Truong et al., 2017). This compound was found in a family of 2-acylaminocycloalkylthiophene-3-carboxylic acid arylamides (AACTs) as inhibitors of TMEM16A, where 48 analogues were synthesised. 10bm was found to be the most potent with a IC_{50} of ~30 nM and found to have a > 10-fold metabolic stability when compared to Ani9 (Truong et al., 2017). AACTs may be useful to study TMEM16A function and as potential drug development candidates however not much research has been done using this a pharmacological tool compound (Truong et al., 2017).

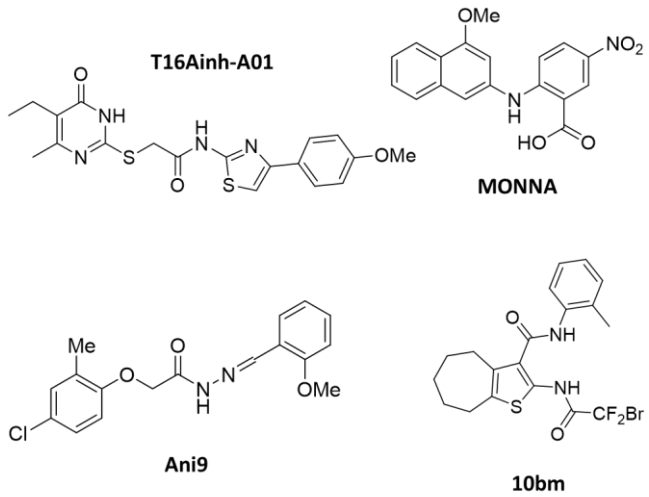


Figure 1.8 Selective TMEM16A inhibitors

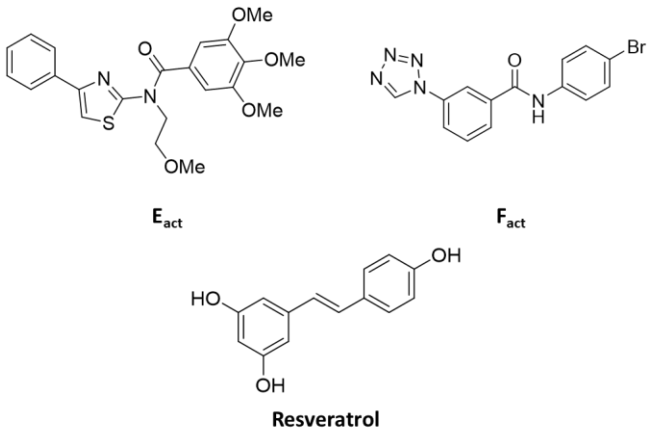
Chemical structure of selective TMEM16A inhibitors, $T16A_{inh}$-A01, MONNA, Ani9 and 10bm.

The need for TMEM16A activators compared to TMEM16A inhibitors has been researched but it's not fully understood which are more beneficial for diseases such as cystic fibrosis (Kunzelmann et al., 2019). There are far more compounds known to inhibit TMEM16A current, but activators are elusive.

Many compounds have been shown to activate TMEM16A indirectly, via increasing intracellular $[Ca^{2+}]_i$. Resveratrol has been demonstrated to activate TMEM16A in an Ca^{2+}-independent manner however it has also been found to modulate a wide panel of other ion channels (Chai et al., 2017).

In 2011 (Namkung, Yao, Finkbeiner & Verkman, 2011a) small molecules, E_{act} and F_{act} were found to increase TMEM16A current. E_{act} was found to activate TMEM16A in the absence of Ca^{2+} in TMEM16A expressing FRT cells while F_{act} was found to potentiate TMEM16A currents only in the presence of high intracellular Ca^{2+} (Namkung, Yao, Finkbeiner & Verkman, 2011a). These compounds were initially thought to directly act

on TMEM16A rather than via an indirect mechanism. However recently it has been discovered that E_{act} activates TMEM16A indirectly via activation of TRPV4 and therefore increase in intracellular Ca^{2+} (Genovese et al., 2019). This effect has been shown to be tissue type specific within airway epithelium (Genovese et al., 2019). F_{act} has increased TMEM16A current in low Ca^{2+} but no affect is seen in high Ca^{2+} and F_{act} does not affect contraction of VSMCs alone (Davis et al., 2013).



E_{act} **F_{act}**

Resveratrol

Figure 1.9 TMEM16A activators

Chemical structure of TMEM16A activators E_{act}, F_{act} and Resveratrol.

Recently a novel TMEM16A potentiator has been published as a treatment for cystic fibrosis by enhancing non–CFTR mediated anion secretion (Danahay et al., 2020). This paper found that enhancing the activity of TMEM16A increases epithelial fluid secretion and enhances mucus clearance independent of CFTR function. This compound was recently sold to Roche for £75 million, demonstrating that TMEM16A in an extremely important therapeutic drug target.

This lack of activators means we need to reassess the results and conclusions made using these tool compounds and highlights the real need for TMEM16A activators, for both science and pharmacologically.

Common chloride channel blockers A9C and NFA have been found to have a biphasic effect on native CaCC current. NFA was found to activate inward currents at negative potentials in rabbit PASMC but blocked the outward current. Therefore, the modulation depends on current flow. NFA also increased current on wash out consistent with the idea that the NFA-induced wash out current is due to a large increase in the probability of chloride channel opening and suggest that reversal of the inhibitory effect of NFA occurs more rapidly than the reversal of the potentiating effects (Piper, Greenwood & Large, 2002). This effect was also seen with A9C in that it increased currents at negative potentials but blocked them at positive potentials again in rabbit PASMC (Piper & Greenwood, 2003a).

The biphasic effect of A9C has been studied in detail on cloned TMEM16A current in the lab. It was found that A9C had an extremely complex effect on A9C at a variety of concentrations and membrane potentials (Ta, Adomaviciene, Rorsman, Garnett & Tammaro, 2016).

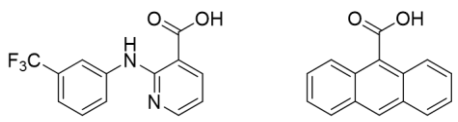


Figure 1.10 Biphasic modulators of TMEM16A

Chemical structure of modulators with a biphasic effect on TMEM16A niflumic acid and A9C.

A9C has been used previously as a pharmacological tool to identify binding sites in the ClC family of chloride channels. By exploiting different binding affinities to different family members and a chimeric strategy to identify binding sites. Using this approach they identified and characterized a binding pocket in ClC-1 (Estévez, Schroeder, Accardi, Jentsch & Pusch, 2003).

1.6 Hypothesis and aims

Based on the discovery that TMEM16A form CaCCs in VSMCs, it is hypothesised that TMEM16A channels represent an important pharmaceutical target to control VSMCs tone. In the longer term, TMEM16A blockers could be used in patients suffering from hypertension (both systemic and pulmonary) while TMEM16A activators have the potential to be therapeutically employed to treat conditions such as hypotension and shock.

Previous exciting pharmacological results indicate that A9C produces a biphasic effect on TMEM16A channel activity. A9C is therefore an excellent candidate for commencing virtual screening in search for specific inhibitors and activators of the channel. We believe there is a realistic possibility of obtaining selective, drug-like compounds that could form the basis of new therapies for a range of vascular disorders. The specific objectives are:

- Systematically study the current modulators of TMEM16A on cloned channels and on native CaCC channels to probe compound selectivity.

- To identify the binding sites for these compounds on the TMEM16A channel and exploit this knowledge for the design and synthesis of additional novel and more potent compounds.
- Begin to establish a system to test new small molecules acting on TMEM16A channels using a commercially available kit.

Chapter 2

Materials and Methods

2 Chapter 2: Materials and Methods

2.1 Chemicals and reagents

All chemicals and reagents were brought from Sigma Aldrich, UK, unless otherwise stated. Ani9 was synthesised by Dr Carole Bataille. Primers were purchased from IDT Technologies, Belgium, and are summarised below. Sequencing was performed by GATC Biotech, Germany.

2.2 Cell preparation

2.2.1 Cell culture and transfection

HEK-293 cells used for generation of a stable line expressing TMEM16A described in Chapter 5. HEK-293T cells were used for the transient expression of TMEM16x. These cells are characterised by a Simian Virus 40 (SV40) large T antigen, which makes transfection of viral plasmids containing SV40 origin of replication more efficient (Lin et al., 2014).

HEK-293 and HEK-293T cells were cultured using the same procedure. Dulbecco's Modified Eagle's Medium F-12 (SigmaAldrich, UK) supplemented with 10 % Foetal Bovine Serum (FBS) (Sigma-Aldrich, UK) and 0.5 % Gentamicin (Sigma-Aldrich, UK) at 37 ˚C in a humid incubator with 5 % CO_2. Cell media was changed every 2-3 days and cells were split when they reached ~70-80 %. The passage procedure was as followed: cells were washed with DPBS then incubated with Trypsin at 37 ˚C for 30 seconds. Once cells had detached from the flask, culture media was used to neutralise the trypsin enzyme (4:1). Cells were dispersed and then centrifuged at 0.2 G for 3 minutes. Continuation

flasks were seeded between 1:3 and 1:10 and cells were seeded 50,000 cells in 35 mm tissue culture dishes for patch-clamp experiments, 24 hours prior to transfection.

HEK-293T cells were transfected 24 hours after seeding with 0.6-0.8 µg DNA constructs and 0.2 µg CD8 complimentary DNA (cDNA) using FUGENE HD (Promega, UK) transfection reagent 1.5 µL/ug of DNA transfected. The transfection reagent comprises a lipid-based mechanism of transfection, during which the DNA is enveloped in a monolayer of lipids and is taken up into the cell by endocytosis (Jacobsen, 2004). After 14-20 hours, cell media was replaced with the appropriate extracellular solution and used for electrophysiological experiments.

0.75 µL Dynabeads were added to each dish, these are anti-CD8 antibody coated beads (Invitrogen, UK). These beads bind to cells expressing the CD8 membrane antigen, it is assumed that if a cell expresses CD8, it will also have incorporated the DNA construct of interest.

2.2.2 Generation of stable line

A stable line expressing TMEM16A was generated for optical screening studies described in Chapter 5. The complete mTMEM16A construct (isoform *a*), subcloned in pcDNA3.1. pcDNA3.1 vectors are 5.4kb vectors designed for high-level stable transfection and contain the neomycin resistance gene, enabling effective selection of stable cell lines. HEK-293 cells were transfected with 2 µg mTMEM16A pcDNA3.1 using FUGENE HD. 24 hours post- transfection cells were selected for antibiotic resistance using Geneticin (G418; 800 µg/ml; Sigma-Aldrich, UK). Medium containing G418 (800 µg/ml) was replaced every 2-3 days. After 2-3 weeks, single-cell–derived clones were obtained by trypsinization of colonies. Each clone was transferred into a well of a

multiwell plate and left to reach ~70% confluence in selection media. Once 70% confluent cells were trypsinsed and transferred to a T25 cell culture flask as well as two 35 mm culture dishes. The T25 flask was used to grow the cell lines up while the smaller dishes were used to assess the expression of mTMEM16A. Although each colony will express the neomycin resistance protein, not all the cells may express mTMEM16A. Successful transfection of mTMEM16A was assessed using whole-cell patch clamp electrophysiology. The clone used in subsequent experiments was selected on the basis that every cell tested produced characteristic CaCC currents with amplitudes > 1 nA. Once selected for, resistance pressure was reduced by decreasing G418 concentration to 400 µg/ml.

2.2.3 Isolation of native SMCs

Wild-type C57BL/6 mice aged 5-8 weeks were culled by a Schedule 1 method in accordance with UK Home Office guidelines. The chest was opened at the diaphragm, and the rib cage opened at the sternum. The heart and lungs were removed, and the descending aorta was removed then immediately submerged in ice-cold PSS. The isolated aorta was then freed of connecting tissue and perivascular fat. Arteries were cut open longitudinally and into small sections to increase the surface area available for enzymatic digestion. The pieces of aorta were then washed with ice-cold PSS and transferred to dissociation media.

Sections of aorta were incubated at 4 °C in DM containing papain (1.5 mg/ml) to ensure diffusion into the tissue. Papain is a cysteine protease which is activated on reduction of sulphydryl groups. Reducing agent dithiothreitol (DTT) (0.5 mg/ml) was used to activate the papain by incubation for 4-minutes at 37 °C. Vessel sections were then

added to DM containing 1.4 mg/ml of collagenase (Type 1 from Clostridium histolyticum) for 2.5-minutes at 37 °C. Collagen in the connective tissue is broken down by the endopeptidase activity of collagenase. Vessel segments were then washed twice in room temperature DM and triturated using a polishing glass pipette to release the aortic VSMCs. Cells were used on the same day as isolated and stored in DM on ice for use in electrophysiology experiments. A drop of DM containing VSMCs were placed on a 35 mm tissue culture dish (Corning, UK) and the appropriate extracellular solution was added after 2 minutes. VMCS were studied in patch-clamp electrophysiology experiments.

2.3 Molecular biology

2.3.1 Amplification, extraction, and purification of plasmid DNA

Each DNA was subcloned into a vector containing an antibiotic-resistance construct to allow selection of bacteria that have incorporated the DNA-vector of interest. Then ~100 ng of plasmid DNA was then added to a 50 µL aliquot of Subcloning Efficient DH5α Competent Cells, (Invitrogen, UK). This strain of *Escherichia Coli* was used as it has been modified to become non-infectious to humans (Hanahan, 1983). Cells were incubated on ice for 30 minutes, then heat shocked at 42 °C for 20 seconds and returned to ice for 2 minutes. This allows uptake of the DNA by the bacteria. Super optimal broth with catabolite repression (SOC medium) (900 µL) was added to the transformed bacterial cells and incubated in a shaker at 3000 rpm and 37 °C for 1 hour. Cells were then spread on lysogeny broth (LB)-ampicillin agar plates, using glass beads, and incubated at 37 °C overnight. Due to the antibiotic-resistance construct only cells that have incorporated the plasmid grew on the plates. Single colonies of bacteria were inoculated into 6

(miniprep) or 50 (midiprep) mL of LB-broth, containing ampicillin and incubated in a shaker at 3000 rpm and 37 °C overnight.

Plasmid DNA was then extracted from the LB-broth and purified using the Qiaprep Spin Miniprep kit (Qiagen, UK) or HiSpeed Plasmid Midi Kit (Qiagen, UK) according to the manufacturer's instructions. Bacterial cells were pelleted via contribution and resuspended in solution containing alkaline detergents to lyse the cells. Lysed cells were then pelleted via contribution and the lysate containing DNA was neutralised and absorbed onto a silica membrane. Ethanol was used to wash the membrane, then eluted with a buffer containing Tris and EDTA to solubilise DNA and to inhibit nuclease, respectively. The DNA concentration was measured in spectrophotometer (Nanodrop 2000cTM, Thermo Scientific) which is based on the amount of light that the DNA can absorbed. The optical density (OD) of 1 measured at 260 nm wavelength indicates 50 µg/ml of DNA (Green & Sambrook, 2012). The ratio of OD measured at 260 nm wavelength over that measured at 280 nm or 230 nm wavelength indicates purity of the DNA.

2.3.2 Single point mutagenesis

A Quikchange® Lightning Site-directed Mutagenesis kit (Agilent Technologies, UK) was used for single point mutagenesis. The mutagenesis reaction was performed as detailed in the manufacturer's instructions. In brief, 5 µl 10x reaction buffer, 1.25 µl (125 ng) of each primer, 1 µl dNTP mix, 1.5 µl QuikSolution reagent, 1 µl Quikchange® Lightning enzyme and ddH2O to a total volume of 50 µL were added to 10-100 ng mTMEM16A DNA. The PCR reaction protocol was; 95°C for 2 minutes, 95°C for 20 seconds, 60°C for

10 seconds, 68°C for 3 minutes (based on a plasmid size of 5.4 kbp, 30 seconds/kb of plasmid length) and a final extension step of 68°C for 5 minutes. The temperature cycling allowed the primers to anneal to the DNA template and extend the length of the new DNA constructs with the desired mutation. The original parental methylated DNA template was digested by adding 2 µl Dpn I, a restriction enzyme, for 5 minutes at 37 °C.

Table 2.1 Primers designed for construction of TMEM16A mutant channels.

	Forward Primer	Reverse Primer
K641A	catcattatgctgggcgcccagctaatccagaac	gttctggattagctgggcgcccagcataatgatg
K584A	aaggccttcctgctcgcctttgtgaactcttac	gtaagagttcacaaaggcgagcaggaaggcctt
F649A	atccagaacaatctcgccgagattggcatcccg	cgggatgccaatctcggcgagattgttctggat
I547A	aacctcgtggtcatcgccctgctggatgaagtt	aacttcatccagcagggcgatgaccacgaggtt
I653A	ctcttcgagattggcgccccgaagatgaaaaag	ctttttcatcttcggggcgccaatctcgaagag
F649A	atccagaacaatctcgccgagattggcatcccg	cgggatgccaatctcggcgagattgttctggat
P679A	ttcgccggcctcacggccgagtacatggaaatg	catttccatgtactcggccgtgaggccggcgaa
Q645A	ggcaagcagctaatcgccaacaatctcttcgag	ctcgaagagattgttggcgattagctgcttgcc
I637A	tgtatccagctgagcgccattatgctgggcaag	cttgcccagcataatggcgctcagctggataca
E650A	cagctaatcgccaacaatctcttcgccattggcatcccg	cgggatgccaatggcgaagagattgttggcgattagctg

Mutant DNA was amplified by transforming into XL10-Gold® ultracompetent cells (Qiagen, UK). XL10-Gold® ultracompetent cells have a high transformation efficiency phenotype (average efficiency ≥ 5 x 10^9 transformants/µg of supercoiled DNA) which allows them to transform large DNA molecules with high efficiency. The transformation protocol was repeated as described for DH5α competent cells, however prior to the addition of DNA. 2 µl Dpn I restriction enzyme was added to each amplification reaction and incubated at 37 ˚C for 5 minutes with gentle shaking. The Dpn I enzyme digests parental, nonmutated, supercoiled DNA. Also, 2 µl β-mercaptoethanol was added to 45

µl XL-10-Gold® ultracompetent cells and incubated on ice for 2 minutes. The β-mercaptoethanol provides conditions which increases the efficiency of transformation. To ensure the single-point mutation had been successful mutant DNA was sequenced and amplified further via transformation in DH5α competent cells as described above.

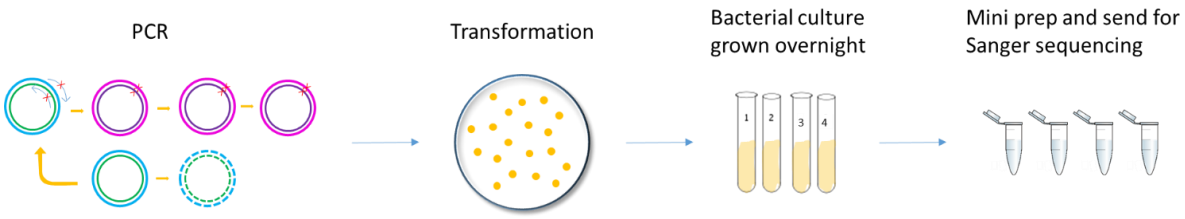


Figure 2.1 Diagrammatic representative of single point mutagenesis

Single point mutation is inserted into the template DNA (blue circle) using complimentary forward and reverse primers. The DNA is then transformed into DH5α cells and grown overnight on ampicillin-LB plates. Four individual colonies are then selected and grown overnight in ampicillin-LB broth. The DNA is then extracted and purified using Qiaprep Spin Miniprep kit (Qiagen, UK), and send for Sanger sequencing.

2.4 Electrophysiology

Patch-clamp electrophysiology is a technique that involves the use of microelectrodes (a glass pipette and a reference electrode) to study the electrical properties of cell membranes (Hamill, Marty, Neher, Sakmann & Sigworth, 1981). The experiments for this thesis were carried out in whole-cell and inside-out patch-clamp techniques in the voltage-clamp configuration. The voltage-clamp technique allows the electrical current arising from the flow of ions, through ion channels present expressed in cell membranes, to be measured. The technique involves the membrane being held at a specific V_m. This provides a method in which the biophysical properties of ion channel associated currents to be studied.

2.4.1 Basic theoretical principles

It is possible to understand the electrical properties of the cell by considering it as a simple electrical circuit like the one shown in figure 2.2. The phospholipid bilayer (an insulator) surrounded each side by ionic solutions (conductors) can be described as a capacitor – two conducting surfaces separated by an insulator – and thus can store charge. The capacitance (C, measured in farads, F) is defined by:

$$C = \frac{\Delta Q}{\Delta V} \qquad [7]$$

where ΔV is the voltage change and Q is the charge. It is important to note that capacitance is proportional to surface area, indicating that the larger cells have larger capacitance. Ion channels within in the plasma membrane act as variable resistors (R) – they control the flow of ionic current (I_i) by only permitting ions to flow across the membrane when open. The total current (I_t) flowing through the circuit can be written as a sum of both the ion current and the capacitor current. Denoting capacitor current as:

$$C\frac{dV}{dt}$$

it follows that,

$$I_t = I_i + C\frac{dV}{dt} \qquad [8]$$

Applying a voltage pulse to the cell causes the cell membrane to become temporarily charged, and a transient cell capacitance current is observed. The change in membrane

potential always takes place after a delay as a result of the cell's capacitance. After this brief charging period, a steady state is reached (dV/dt = 0), the capacitor current becomes zero and the total current is only made up of the ionic current. Thus, the current flowing across the membrane is proportional only to the conductance, i.e. the number of open ion channels. Due to the voltage-dependent nature of ion channels, the voltage-clamp technique allows for a direct measurement of ionic currents by controlling the voltage, thus the opening and closing of voltage-gated ion channels.

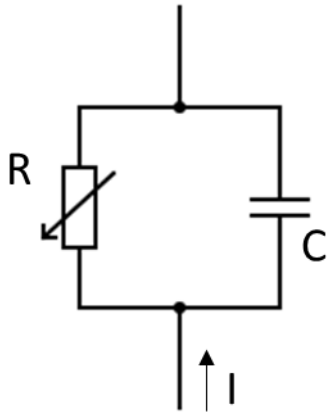


Figure 2.2 The cell membrane as a simple electrical circuit.

Diagrammatic representation of the cell membrane depicted as a simple electrical circuit, made up of a resistor (R) and capacitance (C) in parallel.

2.4.2 Patch-clamp set-up

An inverted Olympus IX51 microscope (Olympus, UK) and a micromanipulator (Scientifica, UK) were positioned on an anti-vibration air table (Newport, USA) and surrounded by a Faraday cage to provide mechanical stability and electrical shielding (Molleman, 2008). All components within the Faraday cage were connected to a single

ground point and the Axopatch 200B amplifier (Axon Instruments, USA) used as the ground source, to enhance electrical shielding.

All recordings were performed at 20-22 °C using an Axopatch 200B amplifier controlled by GePulse software (http://users.ge.ibf.cnr.it/pusch/programs-mik.htm) with an analog-to-digital and digital-to-analog (AD/DA) converter (USB-6221, National Instruments, UK). Pipettes were pulled daily from borosilicate glass capillaries using a two-stage vertical puller (Narishege, UK) and had resistances between 2 and 5 MΩ in the working solutions. Currents were filtered at 2 kHz or 5 kHz and sampled at 10 kHz.

The bath solution was grounded through an Ag–AgCl reference electrode. An AgCl electrode was also used for the pipette electrode and connected to a head stage controlled by the micromanipulator. The AgCl electrodes consist of a silver wire (0.01 mm thick) that has an outer coat of AgCl. The ionic current from the cell is converted to an electrical current within the metal wire according to the following reaction,

$$Cl^- + Ag \leftrightarrow AgCl + e^-$$

which occurs at the interface between the liquid and the metal.

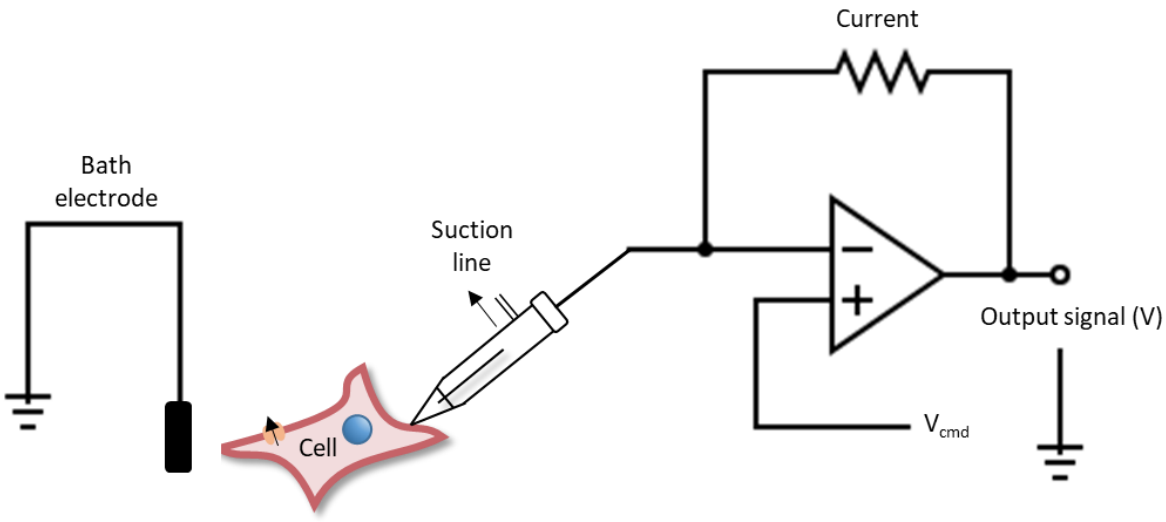


Figure 2.3 Schematic demonstrating the whole-cell patch-clamp experimental set up.

Diagrammatic representation of the whole-cell patch-clamp experimental circuit. Once whole-cell configuration is attained, the intracellular solution diffuses from the pipette into the cell. The pipette is now in contact with the intracellular solution. A current is then injected via the pipette electrode to clamp the membrane potential. The bath electrode records any change in membrane potential which allows an output of the membrane current caused by ion channel activity.

2.4.3 Patch-clamp configurations

To establish whole-cell and inside-out patch-clamp configurations, the tip of the pipette is pushed on to cell membrane and suction is applied to obtain a high resistance (>1 GΩ) seal (GΩ seal).

The whole-cell patch-clamp configuration can be achieved by applying suction once the GΩ seal is formed to punch a small hole in the membrane allowing the pipette and bath solutions to meet (Fig 2.4). This configuration allows investigation of the global activity of all ion channels present on the cell plasma membrane. To allow for equilibration of the pipette solution with the cell interior, whole-cell recordings started >3 min after establishing the whole-cell configuration (Manoury, Tamuleviciute & Tammaro, 2010).

The inside-out configuration can be achieved by excising the patch of membrane contained in the tip of the pipette on formation of the GΩ seal. To remove this patch. the pipette is pulling diagonally away from the cell. In this configuration the cytosolic side of the membrane is exposed to the solution contained within the bath, and therefore it was used to study the effect of ligands applied to the intracellular side of the membrane.

In the whole-cell configuration, the cell membrane can store charge and act as a capacitor which must be compensated. A series resistance is also present arising from the access resistance and pipette resistance which is in series with the membrane capacitance (Molleman, 2008) which also must be compensated to control the V_m. The cell capacitance reflects the size of the cell as the larger the membrane the more charge it can store. To compare currents from cells of different sizes, the current (expressed in pA) was normalised for cell capacitance (expressed in pF) and thus, the current density data is given as pA/pF.

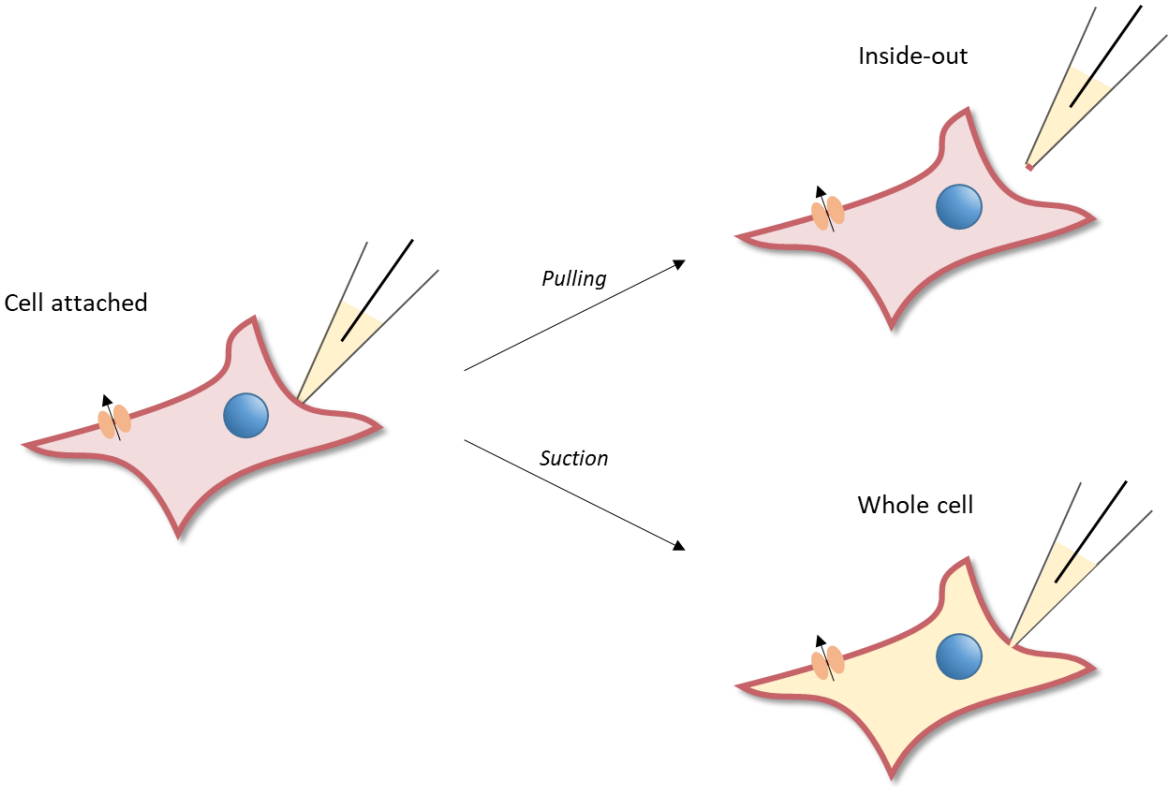


Figure 2.4 Patch-clamp electrophysiology recording configuration.

Diagrammatic representation of patch-clamp recording configurations. The cell membrane is indicated in pink. The blue circle represents the nucleus of the cell. The intracellular solution is indicated in yellow.

2.5 Electrophysiological solutions

2.5.1 Solutions for measurement of I_{CaCC}

Electrophysiological solutions were specifically designed to isolate the Ca^{2+} activated chloride current (I_{CaCC}). Replacement of K^+ with Cs^+ prevented endogenous K^+ currents in HEK-293T cells (Adomaviciene, Smith, Garnett & Tammaro, 2013; Tammaro, Smirnov & Moran, 2005). Osmolarity was maintained at ~300 $mosmolkg^{-1}$ for the intracellular solution and ~330 $mosmolkg^{-1}$ for extracellular solutions and adjusted as required with D-Mannitol. EGTA or HEDTA was used to buffer Ca^{2+}, which allowed free intracellular Ca^{2+} ($[Ca^{2+}]_i$) to be tightly controlled. These two different chelators were used because they have different affinities for Ca^{2+} and are suitable for obtaining different degrees of

free $[Ca^{2+}]_i$ (McGuigan & Stumpff, 2013). HEPES was used to buffer pH which is maintained at 7.3 for intracellular solution and 7.4 for extracellular solution.

The specific recipes for intracellular and extracellular solutions were outlined in Table's below. The amount of free $[Ca^{2+}]_i$ in intracellular solution was calculated using Patcher's Power tool (Dr Mendez and Dr Wurriehausen, Max-Planck Institute – https://www3.mpibpc.mpg.de/groups/neher/index.php?page=aboutppt). In some experiments aimed to examine Cl^- competition with Ani9 and MONNA (Chapter 3), NaCl was reduced to 34 mM, and D-mannitol proportionally increased to ensure the osmolarity of extracellular solution was unchanged.

Table 2.2 Standard CaCC Extracellular Solutions

Reagent	Concentration (mM)
NaCl	150
$CaCl_2$	1
$MgCl_2$	1
Glucose	10
D-Mannitol	10
HEPES	10
pH to 7.4 with NaOH	

Table 2.3 Standard CaCC Intracellular Solutions

Reagent	Concentration (mM)
CsCl	130
EDTA or HEDTA	10
$MgCl_2$	1
HEPES	10
$CaCl_2$	See Table 2.4
pH to 7.3 with NaOH	

Table 2.4 Ca^{2+} concentrations for Standard CaCC extracellular solutions

Free $[Ca^{2+}]_i$ (µM)	Concentration Ca^{2+} (mM)	Chelator
0	-	EDTA
0.007	1	EDTA
0.056	4.5	EDTA
0.103	6	EDTA
0.206	7.5	EDTA
0.274	8	EDTA
0.605	2.1	HEDTA
1.04	3.1	HEDTA
2.27	4.8	HEDTA
12.46	7.8	HEDTA
78.07	9	HEDTA

Table 2.5 Low Cl^- Extracellular Solution

Reagent	Concentration (mM)
NaCl	30
$CaCl_2$	1
$MgCl_2$	1
Glucose	10
D-Mannitol	200
HEPES	10
pH to 7.4 with NaOH	

Experiments the effect of TMEM16A activation by using the ionophore ionomycin to increase intracellular Ca^{2+} we designed solutions with 0 Ca^{2+} in the extracellular solution and low EGTA intracellular solution. EGTA was used to replace $CaCl_2$, compared to the standard intracellular solution, to chelate any Ca^{2+} in the system. This formulation results in a CaCC solution containing 0.21 µM free $[Ca^{2+}]_i$ (Table 2.7).

Table 2.6 0 Ca^{2+} Extracellular Solution

Reagent	Concentration (mM)
NaCl	150
$MgCl_2$	1
Glucose	10
D-Mannitol	10
HEPES	10
EDTA	1
pH to 7.4 with NaOH	

Table 2.7 Low EGTA Intracellular Solution

Reagent	Concentration (mM)
CsCl	130
EGTA	1.5
$MgCl_2$	1
HEPES	10
$CaCl_2$	0 or 1
pH to 7.3 with NaOH	

Experiments designed to study cationic currents of VSMCs (Chapter 1) required intracellular and extracellular solutions containing ionic components in concentrations typically found in VSMCs (tables 2.8 and 2.9). In the intact cell, the $[Ca^{2+}]_i$ was <10 nM to prevent activation of CaCC currents in VSMCs.

Table 2.8 Cationic extracellular solution

Reagent	Concentration (mM)
NaCl	140
KCl	5.4
$MgCl_2$	1
$CaCl_2$	1.8
HEPES	10
D-glucose	10
pH to 7.4 with NaOH	

Table 2.9 Cationic intracellular solution

Reagent	Concentration (mM)
NaCl	10
K-Aspartate	80
KCl	50
$MgCl_2$	1
EGTA	10
HEPES	10
$CaCl_2$	3
pH to 7.4 with NaOH	

Solutions were designed with varying extracellular chloride to detect the dominant binding site of the Cl^- in the absence and presence of $[Ca^{2+}]_i$. Extracellular solution was analogous to the standard I_{CaCC} solution but with varying Cl^- concentrations. The intracellular solution used Cs-MES in place of CsCl to prevent flux of Cl^- from the intracellular side to the extracellular side of the membrane, in order to favour unidirectional flux through the pore.

Table 2.10 Cl^- dose response extracellular solution

Reagent	Concentration (mM)
NaCl	See Table 2.11
$CaCl_2$	1
$MgCl_2$	1
Glucose	10
HEPES	10
pH to 7.3 with NaOH	

Where osmolarity was adjusted to 320 $mOsmolkg^{-1}$ with D-mannitol.

Table 2.11 Concentration of NaCl

$[Cl^-]_o$ (mM)	Concentration of NaCl (mM)

10	6
14	10
34	30
74	70
164	160
366	362

Table 2.12 Cl^- dose response intracellular solution

Reagent	Concentration (mM)
Cs-methanosulphate	130
EDTA	10
$MgCl_2$	1
HEPES	10
$CaCl_2$	0 or 6
pH to 7.3 with NaOH	

Aortic SMCs were isolated and stored in dissociation medium (DM) (table 2.14), as described fully in section 2.7.

Table 2.13 Dissociation medium (DM)

Reagent	Concentration (mM)
NaCl	110
KCl	5
HEPES	10
KH_2PO_4	0.5
NaH_2PO_4	0.5
Taurine	10
EDTA	10
D-glucose	10
$CaCl_2$	0.2
$MgCl_2$	2
Phenol red	0.03
pH to 7.3 with NaOH	

2.5.2 Drug preparations and perfusion system

A9C was dissolved in dimethyl sulfoxide to obtain a stock solution of 0.1 M. Ani9, MONNA and NFA were dissolved in dimethyl sulfoxide to obtain a stock solution of 50 mM. E_{act} was dissolved in dimethyl sulfoxide to obtain a stock solution of 50 mM. Serial dilutions of modulators were made fresh every day in the appropriate extracellular solution.

A local perfusion system consisted of 8 tubes (1.2 mm diameter) filled with different solutions. The cells were lifted and inserted into the tube. Changes in solution were achieved by manually moving tubes. In some experiments (figures 3.6 and 4.15), ultra-rapid changes (≤5 ms) of solutions ("concentrations jump") were achieved by using a computer-controlled system (Warner Instruments) that controlled the rapid movement of the tubes.

2.5.3 Stimulation protocols

IV relationship of TMEM16A (IV ramp protocol): A ramp protocol was used to study TMEM16A current within a broad range of V_m. Ramps of 1 s duration ran between -100 mV and +100 mV.

TMEM16A current *versus* ligand (Ani9, MONNA, A9C or NFA) relationship: A voltage step from 0 to +70 mV for 1.5 s then down from +70 mV to -70 mV for 1 s before returning to 0 was used to assess the current in the presence of increasing ligand (Ani9, MONNA, A9C or NFA). The steady state current at +70 mV measured at increasing concentration of ligand was normalised to the current measured in the absence of

ligand and plotted *versus* [ligand]. The resulting dose response relationships were fitted with modified Hill equations.

$$\frac{I_{ligand}}{I_0} = \frac{1}{1 + \left(\frac{[ligand]}{K_D}\right)^h} \quad [9]$$

Where K_D is the apparent dissociation constant and h is the Hill coefficient.

Current *versus* voltage relationship "IV_CaCC": Current *versus* V_m relationships were constructed by measuring currents in response to V_m steps of 1 s duration (test pulses) from -100 mV to +100 mV in 20 mV increments and succeeded by a step to -60 mV, in order to assess the comparison of mutant I-V relationship to wild type. Pulses were elicited every 2 s from a holding V_m of 0 mV.

Current *versus* Vm relationship (IV-tail protocol): Current *versus* V_m relationships were constructed by measuring currents in response to V_m steps of 1 s duration (test pulses) from −100 to +140 mV in 40 mV increments. Each test pulse was preceded by a V_m step to +70 mV of 1.5 s duration (pre-pulse). Pulses were elicited every 2 s from a holding V_m of 0 mV. Steady-state currents were measured at the end of the test pulses. For determination of the current reversal potential (E_{rev}), instantaneous currents were estimated from extrapolation of single exponential fits of the test-pulse currents to the beginning of each test pulse. These instantaneous current values were plotted as a function of the V_m. Evaluation of the A9C elicited tail pulses the maximal/peak current of the test pulses were measured. Peak and steady state currents were normalised to the steady state current of the +70 mV pre-pulse.

Cl^- binding and saturation experiments: The apparent affinity and electrical distance of the Cl^- the binding site(s) within the pore of the TMEM16A channel was determined with a stimulation protocol and solutions that favours unidirectional Cl^- flux through the pore of the channel. Current was recorded in response to 1 s V_m steps from +70 to +140 mV in 10 mV increments and pulses were elicited every 3.5 s from a holding V_m of 0 mV and in the presence of various extracellular Cl^- concentrations $[Cl^-]_o$.

The current *versus* $[Cl^-]_o$ relationship at various V_m was fitted with a Hill equation of the form:

$$I = Base + \frac{Max - Base}{1 + (\frac{[Cl^-]}{K_d})^h} \qquad [10]$$

where *I* is current normalised to the cell capacitance, *Base* is the pedestal of the curve, *Max* is the maximal asymptotic value of the curve, K_d is the apparent dissociation constant for the ion and *h* is the Hill coefficient.

Ca_V current voltage protocol: The current *versus* voltage relationship for Ca_V channels was obtained by applying 0.2 s pulses from -70 mV to 60 mV in 10 mV steps from a holding potential of -60 mV. The peak current (divided by C_m) at each V_m was measured and plotted *versus* V_m.

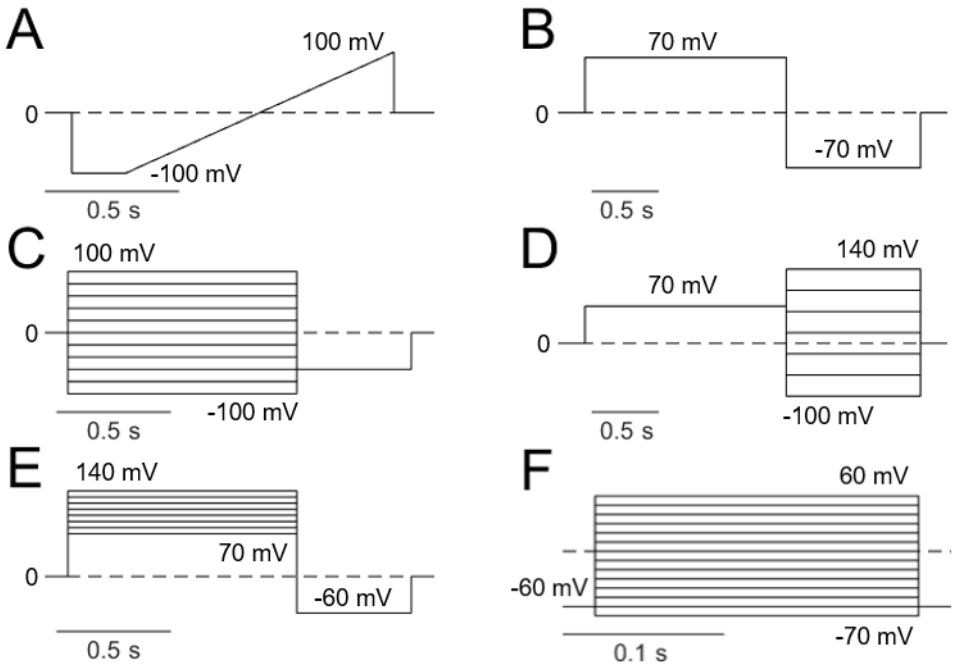


Figure 2.5 Patch-clamp recording voltage stimulation protocols.

(A) IV-ramp voltage protocol; (B) IV-steps voltage protocol; (C) IV-CaCC voltage protocol; (D) IV-tail voltage protocol; (E) Pore Depth Voltage Protocol; (F) Ca_V voltage protocol. Dashed lines represent 0 mV level.

2.5.4 Noise Analysis

Steady state current is underlined by a population of individual channels opening and closing randomly and showing fluctuation (or noise) around the mean current level. Noise analysis is therefore a method in which you can determine the single channel conductance (i) and open probability (P_o) of a channel by assessing the mean and variance of the steady-state macroscopic current (Hille, 2007).

For non-stationary noise analysis (Heinemann & Conti, 1992; Tammaro & Ashcroft, 2007), a voltage step protocol was applied repeatedly with 2 s between steps to ensure that each step starts in identical conditions. The mean current at a certain time point

from the start of each step (I(t)) was calculated from summing the currents elicited by each step at a time point divided by the number of steps:

$$\mathrm{I(t)} = \frac{1}{n}\sum_{k=1}^{n} I_k(t) \qquad [\ 11\ ]$$

Where I(t) is the mean current at time t from the start of each step, n is the number of steps, and I_k(t) is the current amplitude elicited by the kth step at the time, t.

The variance at time t (σ^2(t)) is the sum of squared difference between I_k(t) and I(t) divided by the number of steps:

$$\sigma^2 = \frac{1}{n}\sum_{k=1}^{n} (I_k(t) - I(t))^2 \qquad [\ 12\ ]$$

The macroscopic current (I) through the number (N) of identical and independent ion channels is determined by the following equation:

$$I = iNP_o \qquad [\ 13\ ]$$

and the variance (σ^2) is:

$$\sigma^2 = Ni^2P_o(1 - P_o) \qquad [\ 14\ ]$$

Where (1-P_o) is the probability of the channels being closed. Combing the previous 2 equations we can get:

$$\sigma^2 = iN - \frac{I^2}{N} \qquad [\ 15\ ]$$

The values of I and σ^2 were calculated by equation 15. Background variance and current at 0 mV were subtracted. σ^2 *versus* I relationship was fitted with equation 16 which gives an estimation of i and N. Substitution of these values unto equation 14 will give you a value of P_o.

2.5.5 Liquid Junction Potential measurements

Liquid junction potentials cause deviation from the exact V_m measurement in electrophysiology experiments and therefore introduce error into the analysis, so must be corrected for. In patch-clamp experiments liquid junction potentials occur when liquid-liquid and metal-liquid junction potentials are presence. Metal-liquid junction potentials occur from the potential difference between the pipette and reference electrode. This is due to a redox reaction occurring between the metal of the reference electrode and the salt in the bath solution. To reduce this difference electrodes with identical surface area and material are used. Silver is used for our experiments due to a small redox potential of the metal. Liquid-liquid junction potential occur from the difference in ionic composition of the pipette and bath solutions. This junction potential creates a pipette offset and is controlled for on the patch-clamp amplifier, following the insertion of the pipette into the bath solution. In experiments where the bath solution is altered the liquid junction potentials were calculated using the Patcher's Power Tool

(Dr. Francisco Mendez, Department of Membrane Biophysics at MPI Biophysical Chemistry in Göttingen, Germany; http://www3.mpibpc.mpg.de/groups/neher/index.php?page=software) and corrected offline. In these experiments the bath was grounded through a 3 M KCl agar bridge connected to an Ag-AgCl reference electrode.

2.6 Isometric tension measurements

2.6.1 Myography experimental design

Wire myography is an *in vitro* technique that is a useful and reliable technique to study vascular function, vasodilation and vasoconstriction, in response to various solutions, compounds and or procedures. The technique was first described by (Mulvany & Halpern, 1977).

2.6.2 Mounting of vessels

Directly following cervical dislocation, the vessel was dissected and immediately placed in ice-cold PSS. The perivascular fat was removed, and the vessel was cut unto ~2 mm sections. These were then mounted through the lumen using 2 x 40 µm (gold-plated tungsten wire, Goodfellow, UK) (figure 2.6). In brief, one of mounting pins/arms remains in a fixed position and is attached to a force transducer, while the other is attached to a micrometer and allows for the adjustment in vessel diameter. The force transducer, which can detect changes in force, as small as 0.01 mN, is connected to a computer via an analogue to digital interface (National Instruments, USB-6221-BNC). Data acquisition was executed using Intracept-Chart V4.8.7 software (copyright J Dempster, University

of Strathclyde, UK). During all experiments the vessels were maintained in an organ bath of a small vessel dual wire myograph 410A system (Danish MyoTechnology, DMT, Denmark) containing 5 mL PSS at 37 ˚C. The myograph is split into two independent bath chambers which allows the study of two sections of artery simultaneously.

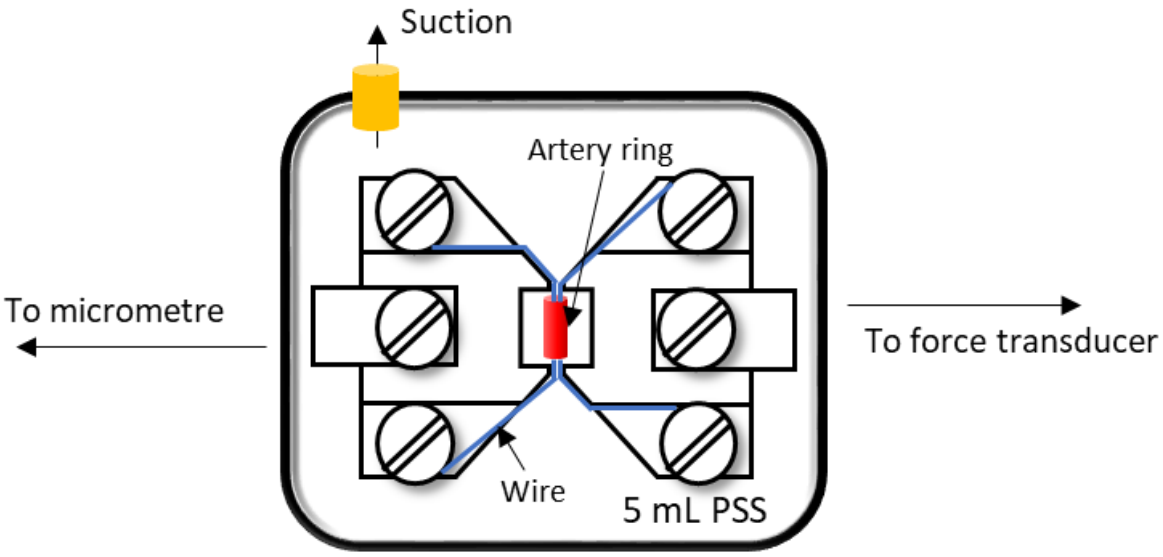


Figure 2.6 Wire myography setup

Diagrammatic representation of the wire-myography setup. The blue lines represent the wire while the red cylinder represents the artery ring.

2.6.3 Normalisation

2.6.3.1 Theory

The magnitude of contraction and sensitivity of the vessel to agonists varies depending on the extent of the stretch applied to the vessel. Therefore, an equal amount of stretch should be applied to all vessels regardless of vessel length or animal sex, for the vessel

to respond accurately compared to other vessels (Mulvany & Halpern, 1977). The aim of the normalisation procedure is to ensure that the micrometer reading (distance between the jaws) produces the internal circumference (IntCir) that the vessel would have if it was relaxed under 90 % of 100 mmHg transmural pressure, this pressure is termed $IntCir_{100}$ (Mulvany & Halpern, 1977). The protocol to calculate the stretch to apply to the vessel was written by Dr Paolo Tammaro using the IGOR (Wavemetrics, USA) platform. The programme implements the algorithm determined by (Mulvany & Halpern, 1977), and is underpinned by the LaPlace law in the form of:

$$P_i = \frac{Tension}{(\frac{IC}{2\pi})} \qquad [\ 16\ ]$$

Where P_i is the effective pressure for each vessel segment, IC is the internal circumference and Tension is as below:

$$Tension = \frac{Force\ (mM)}{2(vessel\ length)(mm)} \qquad [\ 17\ ]$$

The P_i is an estimate of the pressure needed to stretch the vessel to the measured $IntCir_{100}$.

2.6.3.2 Procedure

Vessel length was measured via visual inspection using a BestScope camera (China), inbuilt graticule and Nikon SMZ645 microscope (Nikon Instruments, UK). To acclimatise

the artery rings to the wire myograph, ice cold PSS was replaced with PSS warmed to 37 °C immediately after mounting and vessels left to stabilise for ~30 minutes. The stretch of the vessel was then increased stepwise by increasing the distance between the myograph jaws in small increments (100 µm). The normalisation procedure script takes the jaw measurement and tension values at each step as inputs, alongside the vessel length and wire thickness to calculate the jaw measurement that must be applied to create the desired transmural pressure (90 % of measured $IntCir_{100}$ for aorta) for each artery segment, see Figure 2.7.

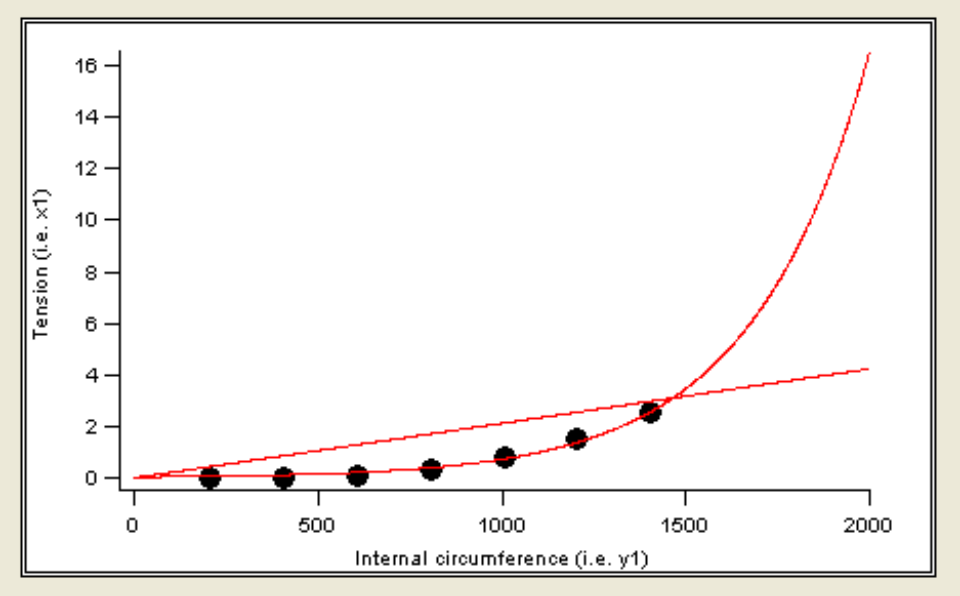


Figure 2.7 Normalisation of tension

Screen shot of normalisation procedure for representative data in IGOR (WaveMetrics, USA), made by Dr Paolo Tammaro. The program calculates the internal circumference of the vessel over a range of jaw measurements. These values are then plotted *versus* the tension and fitted with an exponential (curved red line). The straight red line represents the values of the La Place equation at 100 mmHg. At the point where the two lines cross gives the internal circumference of 100 mmHg for the vessel. The program then uses this value to

determine the jaw measurement that must be applied to create the desired transmural pressure.

2.6.3.3 Solutions used in wire-myography experiments

Isolated aortic rings were dissected, stored, and studied using myography in physiological salt solution (PSS), Table 2.14. Experiments to study the selectivity of common TMEM16A blockers to chloride channels used conditions of low $[Cl^-]_o$ PSS. In these experiments [NaCl] was reduced in PSS and replaced with equimolar Na-methanesulfonate (Na-MES), Table 2.15. This was used to maintain the $[Na^+]$ however MES is TMEM16A impermeant.

Table 2.14 Physiological salt solution (PSS)

Reagent	Concentration (mM)
NaCl	122
KCl	5
HEPES	10
KH_2PO_4	0.5
NaH_2PO_4	0.5
$MgCl_2$	1
D-Glucose	11
$CaCl_2$	1.8
pH to 7.4 with NaOH	

Table 2.15 Low Cl^- physiological salt solution

Reagent	Concentration (mM)
NaCl	22
KCl	5
HEPES	10
KH_2PO4	0.5
NaH_2PO4	0.5
$MgCl_2$	1

D-Glucose	11
$CaCl_2$	1.8
Na-MES	100
pH to 7.4 with NaOH	

2.6.3.4 Experimental procedures for each experiment

For each vessel, functional viability was assessed 5 minutes after normalisation by measuring the contractile response to 50 mM KCl and ensuring it remained consistent over three repeats. Each treatment lasted 6 minutes, after which the vessel was washed with PSS pre-warmed to 37 °C and left for 7 minutes after situation to relax back to baseline.

2.6.3.5 [PE]-tension relationship analysis

The contractility of aortic rings was measured as a function of increasing doses of L-phenylephrine hydrochloride (PE), which was carried out through cumulative additions of the drug (diluted in PSS) to the bath solution. TMEM16A modulators, such as Ani9 or MONNA, were pre-incubated with the aortic rings for 25 minutes prior to adding the first dose of PE. Each data was normalised to the third 50 mM KCl contractile response to accommodate variation in overall contractile force.

Following this, the tension *versus* [PE] relationship in both the absence and presence of TMEM16A modulators for each experiment was fitted to the Hill equation (Equation 19). For each case, the fitted EC_{50} values extracted. Results from each set of experiments were collected and their mean concentration response data were plotted. In each case, a curve was fitted to the mean of the data using the Hill equation:

$$T = \frac{T_{max}}{1 + \left(\frac{[PE]}{EC_{50}}\right)^{h}} \quad [18]$$

where T_{max} is the maximal asymptotic force reached, *[PE]* is the concentration of PE and *h* is the Hill coefficient.

2.6.3.6 High extracellular K^+ experiments

For experiments requiring removal of the Cl^- component of vessel contractility, K-methanesulfonate (K-MES) was used to induce aortic ring contraction in the presence and absence of other modulators. In this case, KCl was still used to assess viability of vessels and for normalisation of data.

2.7 Premo™ Halide Sensor kit

Premo™ Halide Sensor Kit (Invitrogen, UK) was used to transfect cells with a YFP (Venus) biosensor using Baculovirus (BacMam system) delivery.

In brief, TMEM16A_HEK-293 cells were grown to ~80 % confluency in a 25 cm^3 flask. The media was aspirated and replaced with Premo™ Halide sensor transduction solution (1.3:3.5) in D-PBS and incubated at room temperature for 3 hours with gentle rocking. Solution was then aspirated and replaced with media containing BacMam enhancer (1 µL/mL) and incubated for 2 hours at 37 ˚C and 5 % CO_2. The media was then aspirated and replaced with supplemented media and incubated overnight at 37 ˚C and 5 % CO_2. Cells were then trypnised and plated into 96 well plates (Invitrogen, UK) incubated 6-16 hours at 37 ˚C and 5 % CO_2. The media was then aspirated, cells were washed with 200

µL D-PBS and replaced with appropriated extracellular solution. Cells were visualised using a FLUOstar microplate reader (Omega). Baseline fluorescence was recorded for 2 seconds before injection of an equal volume 2X Premo™ halide stimulus buffer containing NaI and fluorescence was recorded for 10 seconds.

Table 2.16 I^- supplemented extracellular solution

Reagent	Concentration (mM)
NaI	150
$CaCl_2$	1.8
$MgCl_2$	1
KCl	2.5
HEPES	10
pH to 7.4 with NaOH	

2.8 Data and statistical analysis

All data was analysed by software written in the IGOR environment (Wavemetrics, USA) by Dr Paolo Tammaro or written in Matlab (USA) by Ria Dinsdale. Unless otherwise stated, the two-tailed Student's T test or ANOVA with Bonferroni post-hoc test was used for statistical analysis with a statistical significance of $P<0.05$. Data is presented as mean ± S.E.M (standard error of the mean) and n is the number of experiments, unless otherwise stated.

2.9 Contribution to work

Unless otherwise stated, all experiments in this thesis were designed by Ria Dinsdale and Dr Paolo Tammaro and executed and analysed by Ria Dinsdale. Tanadet Pipatpolkai and Dr Phillip Stansfeld ran all simulations and did the data collection and analysis for figures 4.16 and 4.17. Dr Kathryn Acheson contributed to the collection of data for figures 3.18, 3.20 and 3.23.

Chapter 3

Fundamental characterisation of cloned and native TMEM16A pharmacology

3 Chapter 3: Fundamental characterisation of cloned and native TMEM16A pharmacology

Research within the Tammaro group has demonstrated that TMEM16A is the major component of CaCC current in VSMCs (Manoury, Tamuleviciute & Tammaro, 2010). The lab, and others, have proposed that TMEM16A current in VSMCs serves as a key depolarising mechanism that enables vessel contraction in response to a rise in intracellular Ca^{2+} triggered by G_qPCR stimulation (Askew Page et al., 2019; Bulley & Jaggar, 2014; Heinze et al., 2014).

As outlined in the Introduction, TMEM16A has been a proposed target to treat a variety of vascular conditions including systemic and pulmonary hypertension. To expedite the therapeutic exploitation of this potential drug target it is essential to gain insight into the mechanism of modulation of the channel by currently available test compounds.

The work presented in this chapter constitutes a systematic characterisation of the mode of action and selectivity of current available blockers. Initially the potency of Ani9 (Seo et al., 2016) and MONNA (Oh et al., 2013), two newly identified TMEM16A inhibitors, on both cloned and native (vascular) TMEM16A channels was characterized. These inhibitors have attracted significant interest in the academic and industrial communities, but their mode of action and effects on native tissue are still poorly understood. Due to the interest in TMEM16A activators, as described in the Introduction we also studied a known activator of TMEM16A, E_{act}, which is commercially available and thus easy to procure. A9C and NFA were known to have a biphasic effect on TMEM16A (Piper & Greenwood, 2003b; Piper, Greenwood & Large, 2002; Ta, Adomaviciene, Rorsman, Garnett & Tammaro, 2016) and have been also considered in

the study because it was argued that gaining an understanding of their mechanisms of action can offer insights into both the process of channel activation and inhibition.

The compound described have been previously tested by other groups (Bradley et al., 2014; Liu, Feng, Luo, Yang, Brett & Hu, 2016; Ni, Kuan & Chen, 2014) to dissect the role of TMEM16A in native tissue. These published reports involved the use of different cell systems and stimulation protocols. Systematic analysis of the effects of these test compounds has never been conducted in parallel on cloned TMEM16A channels, which has therefore been an objective of this chapter.

TMEM16A and TMEM16B are the only two members of the TMEM16x family to form plasma membrane localised CaCCs (Hartzell, Yu, Xiao, Chien & Qu, 2009; Pedemonte & Galietta, 2014). TMEM16B has been shown to be expressed in the vasculature albeit at lower levels than TMEM16A (Davis et al., 2010; Manoury, Tamuleviciute & Tammaro, 2010; Thomas-Gatewood et al., 2011). In this chapter the biophysical properties of TMEM16B was studied and compared to that of TMEM16A. TMEM16A inhibitors were then tested on the TMEM16B channel in order to study the selectivity as Ani9 has previously been shown to modulate TMEM16A over TMEM16B (Seo et al., 2016). TMEM16F is a TMEM16 protein that works both as a channel and scramblase (Scudieri et al., 2015). TMEM16F channels have a characteristic whole-cell Cl^- current that increases in amplitude over time (Scudieri et al., 2015). Mutations in TMEM16F cause Scott syndrome, a bleeding disorder resulting from dysfunctional phospholipid scrambling in platelets (Suzuki, Umeda, Sims & Nagata, 2010; Yang et al., 2012). TMEM16F sensitivity to Cl^- channel modulators were also tested in this chapter with the

rationale that this may help gaining insights on both ion channel and scramblase pharmacology.

In this chapter it is demonstrated that phenylephrine-mediated contractility of isolated aortic smooth muscle rings was drastically reduced in the presence of either Ani9 or MONNA. However, concentrations of Ani9 and MONNA that led to the same degree of inhibition of the heterologous TMEM16A current resulted in different extent of aortic relaxation (being much more pronounced with MONNA than with Ani9). It was hypothesised that this was due to interaction of MONNA with additional ion channels. Patch-clamp experiments involving isolated aortic smooth muscle cell were used to study the effect of Ani9 and MONNA on individual current types (K^+, non-selective cation currents and Ca_v).

Overall, this chapter demonstrates the potential of Ani9 and the limitations of MONNA. This knowledge establishes Ani9 as the best tool compound currently available, which has the potential to be exploited for future drug design research. We also determine that NFA also modulates TMEM16A by a change in gating, a similar mechanism to that of A9C and so define concentrations of A9C and NFA to be used in later chapters.

3.1 TMEM16A and TMEM16B Ca^{2+} sensitivity

To define appropriate $[Ca^{2+}]_i$ for experiments presented in later chapters of my thesis, this study started by testing the Ca^{2+}-sensitivity of cloned TMEM16A and TMEM16B, using the inside-out patch-clamp technique. Patches were excised from HEK-293T cells expressing TMEM16A or TMEM16B and were subsequently held at +70 mV. Current (I) was measured in the presence of various $[Ca^{2+}]_i$. The current was then normalised to an

average current elicited at the two highest $[Ca^{2+}]_i$, 12 and 78 µM $[Ca^{2+}]_i$ (I_{max}). The I/I_{max} relationship was plotted against $[Ca^{2+}]_i$ and fitted with the Hill equation (Eq. 9, Fig. 3.1). TMEM16A currents were characterised by an EC_{50} value of 0.7 ± 0.1 µM and an h value of 2.8 ± 0.1 (n=10). TMEM16B currents were characterised by an EC_{50} value of 1.9 ± 0.3 µM and an h value of 1.4 ± 0.2 (n=4).

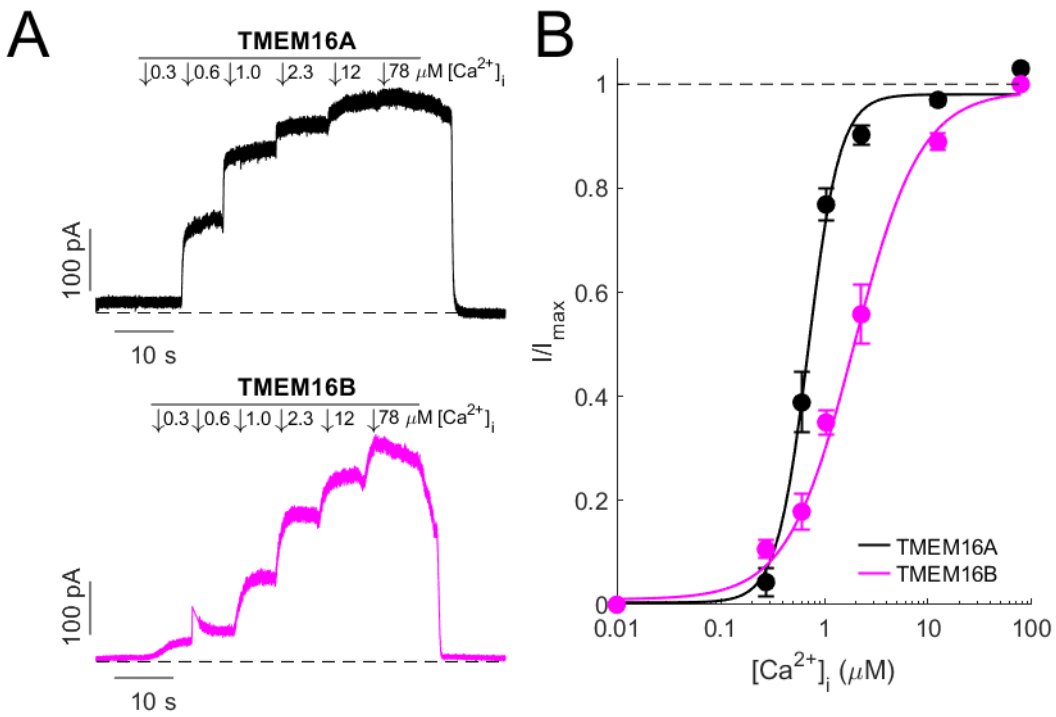


Figure 3.1 Ca^{2+} sensitivity of TMEM16A and TMEM16B channels.

(A) Currents recorded from inside-out patches excised from HEK-293T cells expressing TMEM16A (top) or TMEM16B (bottom) in response to various $[Ca^{2+}]_i$ (µM), as indicated. The voltage was maintained at +70 mV for the whole duration of the recordings. (B) Mean current *versus* $[Ca^{2+}]_i$ relationship measured at +70 mV and normalised to the current measured in the two highest $[Ca^{2+}]_i$ concentrations for TMEM16A (n=10) and TMEM16B (n=4). The smooth curves are best fits of data using equation 9.

3.2 TMEM16A I-V relationship

Experiments in the previous section assessed the extent to which TMEM16A responds to $[Ca^{2+}]_i$. The next experiment aimed to study the response of these channels to varying V_m at a fixed $[Ca^{2+}]_i$.

In the absence or presence of ~0.1 μM $[Ca^{2+}]_i$, the currents recorded from cells transfected with TMEM16A were indistinguishable from the very small currents observed from non-transfected cells (Adomaviciene, Smith, Garnett & Tammaro, 2013) (Fig 3.2). In the presence of 0.3 μM $[Ca^{2+}]_i$, hyperpolarising and depolarising steps showed instantaneous TMEM16A currents, followed by time-dependent relaxations towards new steady-state levels. Currents recorded from cells dialysed with 0.3 μM $[Ca^{2+}]_i$ reached a maximum steady-state current density of 296 ± 37 pA/pF (n=11) at +100 mV. The current density immediately after the voltage changed was measured and represented the instantaneous current component. A nearly linear relationship between the instantaneous current and V_m was observed. However, the relationship between steady-state current (measured at the end of a 1 s voltage step) and the V_m was outwardly rectifying (Fig. 3.2). This phenomenon was expressed as the ratio between the steady-state current and instantaneous current at +100 mV (I_{ss}/I_{inst}), gives a fraction of 5.1 ± 0.3 (n=11). The extent of outward rectification was quantified as the ratio between the steady state current measured at +100 mV (I_{100}) and the current measured at -100 mV (I_{-100}). The I_{100}/I_{-100} (rectification index) was -28.8 ± 3.1 (n=11) for TMEM16A in ~0.3 μM $[Ca^{2+}]_i$. The reversal potential for the TMEM16A currents was approximately 0 mV, close to the estimated Cl^- equilibrium potential for the recording solutions used.

The time-course of the V_m dependent current increase was calculated as the time required to reach the half-maximal current ($\tau_{0.5}$) at the different V_m (Fig 3.2). As the voltage increased, $\tau_{0.5}$ also increased, equalling 59.9 ± 1.5 ms (n=8) at +40 mV and 68.3 ± 2.4 ms (n = 8) at +100 mV (Fig. 3.2). The tail currents measured upon repolarisation to −60 mV were quantified in the same way, $\tau_{0.5}$ did not show a significant change with voltage over the range of +40 mV to +100 mV (Fig. 3.2). The $\tau_{0.5}$ for the deactivating tail current was 43.1 ± 2.8 ms (n=8) when preceded by a pre-pulse to +40 mV and 46.8 ± 1.5 (n=8) when preceded by a pre-pulse to +100 mV.

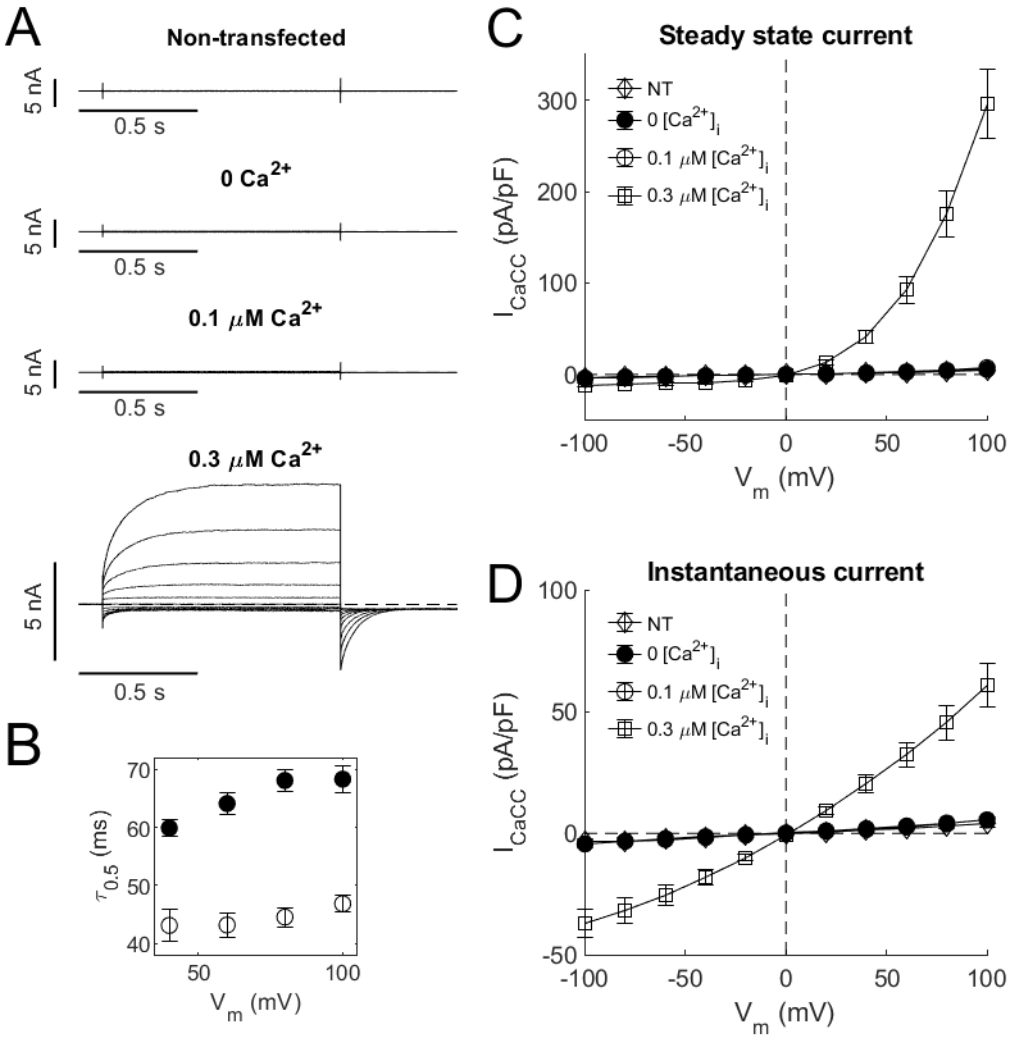


Figure 3.2 Properties of the cloned TMEM16A IV-relationship

(A) Representative whole-cell currents recorded from HEK-293T cells expressing TMEM16A channels, in the absence or presence of Ca^{2+}, as indicated. Dashed horizontal lines represent zero current level. (B) Mean $\tau_{0.5}$ of current activation (filled symbols) and deactivation (open symbols) at various V_m (C) Mean whole-cell current *versus* V_m relationships in the presence of various $[Ca^{2+}]_i$, measured at the end of the test pulses (n=9-11 for each $[Ca^{2+}]_i$) (D) Mean whole-cell current *versus* V_m relationships in the presence of various $[Ca^{2+}]_i$, measured at the beginning of the test pulses.

3.3 Whole cell-current recording for other cloned vascular channels: TMEM16B and TMEM16F

3.3.1 TMEM16B I-V relationship

In addition to the TMEM16A CaCC we also studied the whole cell Cl^- current of TMEM16B, another CaCC channel in the TMEM16x family endogenously expressed in the vasculature. As above the IV-CaCC voltage protocol was used to assess the current-voltage relationship of HEK-293T cells transiently expressing TMEM16B. TMEM16A currents were recorded in the presence of 0.3 μM $[Ca^{2+}]_i$. Conversely, TMEM16B currents were recorded in the presence of 0.6 μM $[Ca^{2+}]_i$. Based on data presented in figure 3.1, different $[Ca^{2+}]_i$ were used to ensure the same extent of activation for the two channels.

In the presence of 0.6 μM $[Ca^{2+}]_i$, hyperpolarising and depolarising steps showed instantaneous TMEM16B currents, followed by time-dependent relaxations towards new steady-state levels. Currents recorded from cells dialysed with ~0.6 μM $[Ca^{2+}]_i$ reached a maximum steady-state current density of 356.5 ± 65.1 pA/pF (n=10) at +100 mV. The current density immediately after the voltage changed was measured and represented the instantaneous current component. There was a nearly linear relationship between the instantaneous current and V_m. However, the relationship between steady-state current and the V_m was outwardly rectifying (Fig. 3.2). Analogues to that seen for TMEM16A. The I_{ss}/I_{inst} at +100 mV gives a fraction of 2.6 ± 0.2 (n=10) and the I_{100}/I_{-100} (rectification index) was -11.3 ± 1.0 (n=10) for TMEM16B in 0.6 μM $[Ca^{2+}]_i$. The reversal potential for the TMEM16B currents was approximately 0 mV, the estimated Cl^- equilibrium potential for the recording solutions used.

The time of half current was measure as described in section 3.2. As the voltage increased, $\tau_{0.5}$ also increased, equalling 4.9 ± 0.2 ms (n=10) at +40 mV and 6.9 ± 0.2 ms (n=10) at +100 mV for TMEM16B channels (P<0.05) (Fig. 3.2). The tail currents measured upon repolarisation to −60 mV were quantified in the same way, $\tau_{0.5}$ did not show a significant change with voltage over the range of +40 mV to +100 mV (Fig. 3.2). The $\tau_{0.5}$ for the deactivating tail current was 1.8 ± 0.2 ms (n=10) when preceded by a pre-pulse to +40 mV and 3.0 ± 0.3 (n=10) when preceded by a pre-pulse to +100 mV. Overall, TMEM16B activation was found to occur ~9.9-fold faster than TMEM16A at +100 mV. Deactivation of TMEM16B was also faster than TMEM16A, by ~15.6-fold.

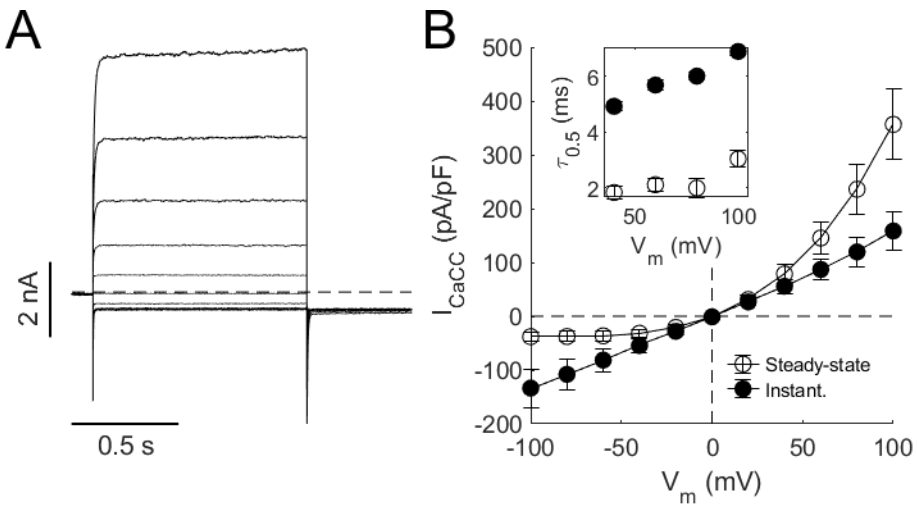


Figure 3.3 Properties of TMEM16B IV-relationship

(A) Whole-cell current recording from HEK-293T cells transiently expressing TMEM16B and dialysed with ~0.6 µM $[Ca^{2+}]_i$. Dotted line represents zero-current level. (B) Mean whole-cell current *versus* V_m relationship, measured at the beginning of the test pulses filled circles and at the end of the test pulses (empty circles) (n=10). Inset in (B) show mean $\tau_{0.5}$ of current activation (filled symbols) and deactivation (open symbols) at various V_m.

3.3.2 TMEM16F I-V relationship

TMEM16F currents were assessed to then enable characterisation of their sensitivity to TMEM16A channel modulators. TMEM16F channels have a characteristic whole-cell Cl^- current that gradually increases in amplitude after establishing whole-cell configuration (Acheson, 2016; Hartzell, Yu, Xiao, Chien & Qu, 2009; Pedemonte & Galietta, 2014). The time course of the development of the whole-cell TMEM16F current was therefore characterised at this stage of the project before any pharmacological testing was carried out.

TMEM16F is far less sensitive to Ca^{2+} than TMEM16A and TMEM16B therefore high intracellular Ca^{2+}, ~78 µM, was used to observe the current, as has been shown previously (Scudieri et al., 2015). Whole-cell currents were recorded from HEK-293T cells transiently expressing TMEM16F and examined using the IV-CaCC voltage protocol.

The IV-CaCC protocol was performed every 2 minutes from the establishment of the whole cell configuration (defined as t=0 minutes). TMEM16F current increased over time (Fig. 3.4), with an outwardly-rectifying IV relationship like that of the TMEM16A and TMEM16B currents described above (Fig. 3.2 and Fig. 3.3). At 100 mV TMEM16F current was 32.3 ± 11.1 pA/pF at t=0 min, increasing to 82.0 ± 31.0 pA/pF at t=2 min, 97.8 ± 32.3 pA/pF at t=4 min, and 107.1 ± 25.5 pA/pF at t=6 min (n=8) (Fig. 3.4).

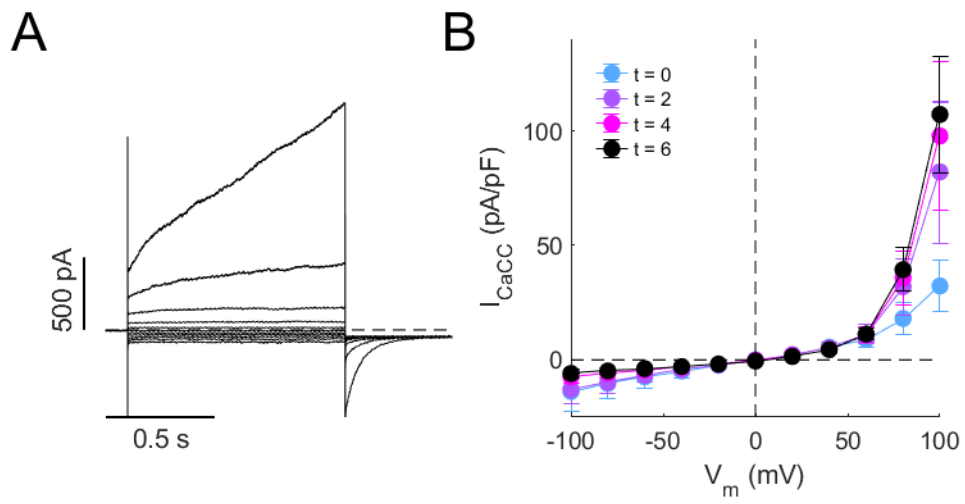


Figure 3.4 Properties of TMEM16F IV-relationship

(A) Whole-cell current recording from HEK-293T cells transiently expressing TMEM16F and dialysed with ~78 µM $[Ca^{2+}]_i$. Dotted line represents zero-current level. (B) Mean whole-cell current *versus* V_m relationship, measured at the end of the test pulses (n=8).

3.4 Defining the sensitivity of TMEM16A to Cl^- channel modulators

To define the relative potency of the TMEM16A blockers, whole-cell currents were recorded in the response to the "step protocol" while the cell was exposed to increasing concentrations of the compounds. In these experiments, the current was measured a two V_m (+70 mV and -70 mV). The current at +70 mV was examined because TMEM16A channels are activated by depolarised V_m: the resulting large current allows an accurate assessment of the effect of the compounds. The compounds were also assessed at -70 mV as this V_m is closer to physiological V_m for VSMCs (Herring, Paterson & Levick, 2018; Rorsman, Ta, Garnett, Swietach & Tammaro, 2018).

3.4.1 Inhibitors

From literature the IC_{50} of Ani9 is 77 nM for apical membrane current in FRT-ANO1 cells (Seo et al., 2016). The effect of Ani9 on cloned TMEM16A was tested using

concentrations within the range of 0.01 - 1 µM (Fig 3.5). Ani9 caused an inhibition of TMEM16A which did not vary at +70 mV and -70 mV. Fits of data to the Hill equation yielded an IC_{50} of 0.05 ± 0.01 µM (n=8) and 0.04 ± 0.01 (n=8) at +70 mV and -70 mV, respectively. The maximum inhibition extrapolated from the Hill equation was 90 ± 3 % (n=8) and 83 ± 5 % (n=8) for +70 mV and -70 mV respectively. When statistically compared, the IC_{50} values, as well as the maximum inhibition, were not significantly different at the two potentials.

The reported IC_{50} of TMEM16A inhibition by MONNA is 0.08 µM (assessed on endogenous TMEM16A currents in *X. laevis* oocytes). The effect of MONNA on cloned TMEM16A was tested using concentrations within the range of 0.01-10 µM (Fig 3.5). Like Ani9, MONNA caused an inhibition of TMEM16A which did not exhibit any voltage dependency. Fits of data to the Hill equation yielded an IC_{50} of 0.47 ± 0.07 µM (n=5) and 0.52 ± 0.07 (n=5) at +70 mV and -70 mV, respectively. The maximum inhibition extrapolated from the Hill equation was 88 ± 3 % (n=5) and 85 ± 4 % (n=5) for +70 mV and -70 mV respectively. When statistically compared, the IC_{50} values, as well as the maximum inhibition, were not significantly different at the two potentials.

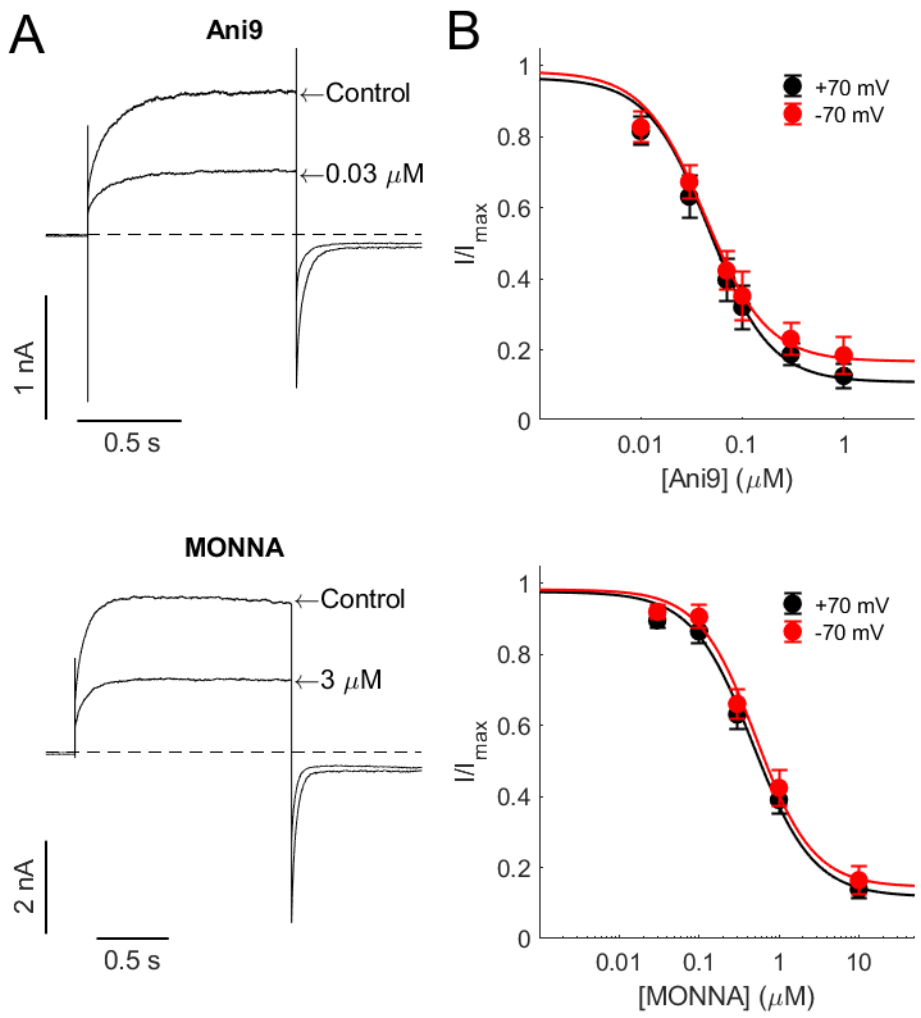


Figure 3.5 The effects of inhibitors on whole-cell TMEM16A currents

(A) Sample whole-cell currents in the absence and presence of inhibitors at the concentrations indicated. Currents were evoked by a 1 s voltage step from a holding potential of 0 to +70 mV and deactivated by a repolarising step to -70 mV. Intracellular solution containing ~0.3 µM $[Ca^{2+}]_i$ was used for all experiments. (B) Concentration-response curves for the inhibition of TMEM16A currents by Ani9, and MONNA at +70 and -70 mV, n=8 (Ani9) and n=5 (MONNA). The curves represent fit of the data to the Hill equation.

3.4.2 Activators

The next step was to examine the TMEM16A response to E_{act}, a commercially available activator (Namkung, Yao, Finkbeiner & Verkman, 2011b) . E_{act} resulted in a small block

of the current at both positive (+70 mV) and negative (-70 mV) V_m. The extent of block was 25.7 ± 10.1 % and 20.6 ± 22.6 % (n=4) at 10 µM and 17.8 ± 7.7 % and 11.7 ± 27.5 % (n=3) at 50 µM, measured at +70 mV and -70 mV respectively in each case (Fig. 3.6). These results are in accordance with published results showing that E_{act} is an indirect activator of TMEM16A (Genovese et al., 2019).

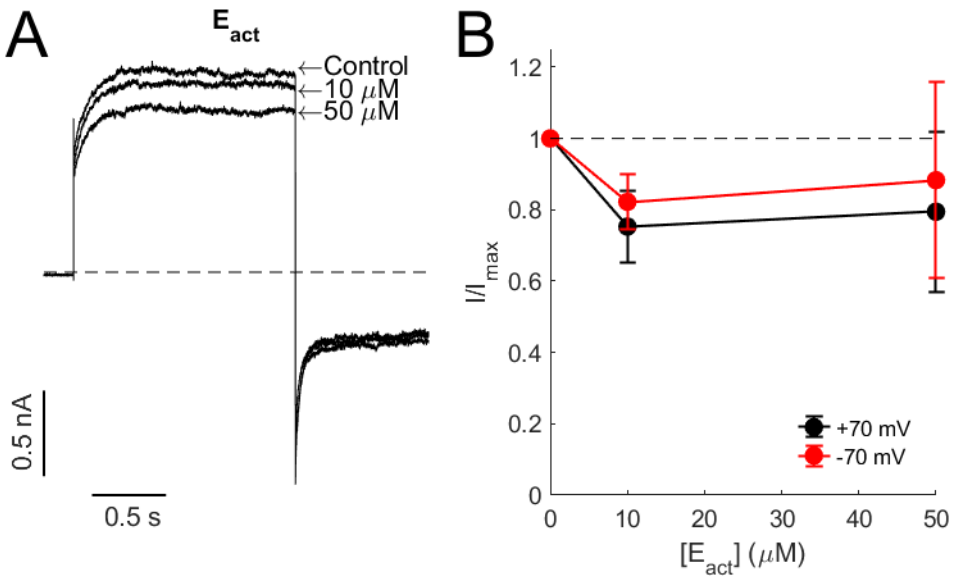


Figure 3.6 The effects of E_{act} on whole-cell TMEM16A currents

(A) Sample whole-cell currents in the absence and presence of E_{act} at the concentrations indicated. Currents were evoked by a 1 s voltage step from a holding potential of 0 to +70 mV and deactivated by a repolarising step to -70 mV. Intracellular solution containing 0.3 µM Ca^{2+} was used for all experiments. (B) Mean current inhibition for [E_{act}], as indicated (n=4).

3.4.3 Biphasic Modulators

Given the lack of activators for TMEM16A, compounds with reported bimodal effect on the channel were studied, in this case A9C (Piper & Greenwood, 2003a; Ta, Adomaviciene, Rorsman, Garnett & Tammaro, 2016) and NFA (Piper, Greenwood & Large, 2002). Understanding the mechanism of TMEM16A channel activation by A9C and NFA could help the future design of compounds that selectively activate the

channel. The effect of NFA was also tested with the rationale that it activates other Cl^- channels such as ClC-K, cation channels such as TRPA (Hu et al., 2010; Picollo, Liantonio, Didonna, Elia, Camerino & Pusch, 2004) and has been shown to activate native CaCC current at negative potentials (Piper, Greenwood & Large, 2002).

A9C was shown to activate the channel to a peak fold change of 1.41 ± 0.10 at 100 µM at +70 mV and 4.79 ± 0.75 at 1 mM at -70 mV. At +70 mV above 100 µM the inhibition component of A9C effect TMEM16A was predominant. The inhibition became the major component of the effect at 1 mM with a maximum inhibition of 0.24 ± 0.06 at 3 mM. At -70 mV inhibition predominated at 3 mM but never fell below a factor of 1 (Fig. 3.7).

NFA was shown to activate the channel to a peak fold change of 1.63 ± 0.08 at 10 µM at +70 mV and 2.58 ± 0.21 at 10 µM at -70 mV. At +70 mV, 30 µM and above the activations was diminished and at 100 µM the block was a factor of 0.62 ± 0.07. At -70 mV the current began to be inhibited at 10 µM again but never fell below a factor of 1 (Fig. 3.7).

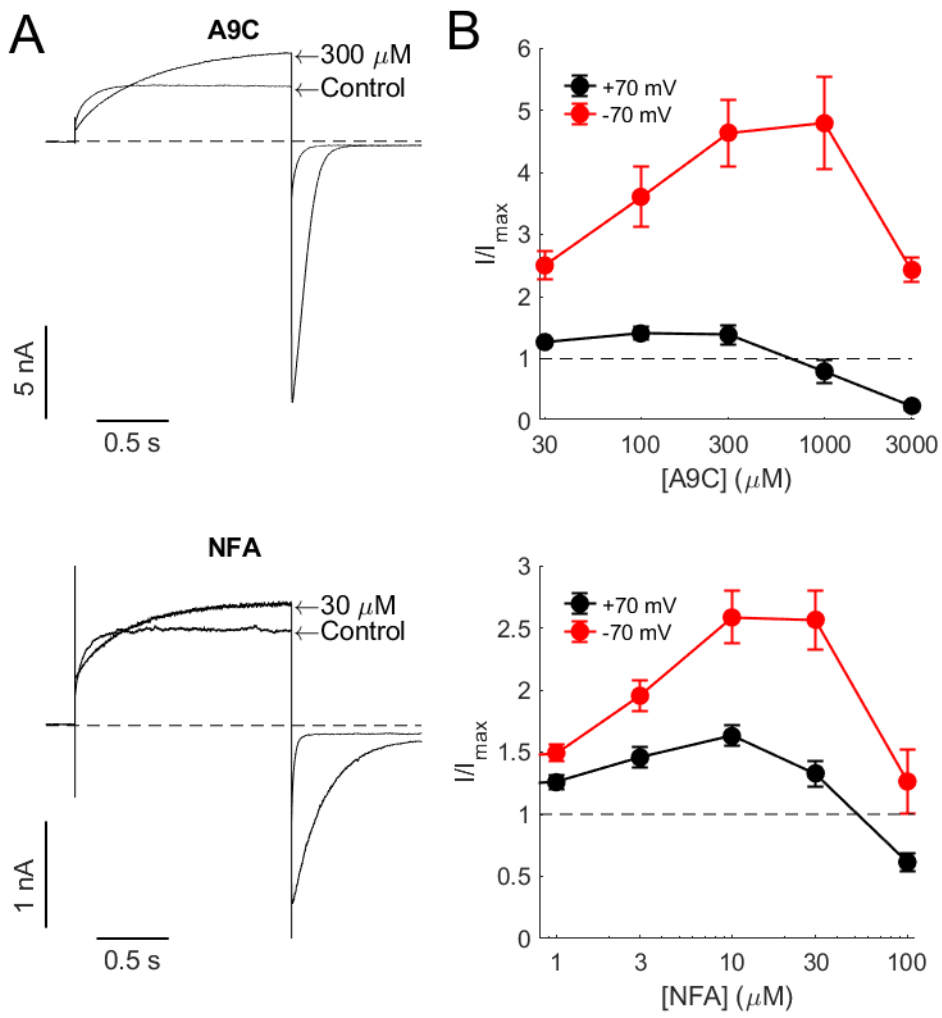


Figure 3.7 The effects of biphasic modulators on whole-cell TMEM16A currents

(A) Whole-cell currents in the absence and presence of blockers at the concentrations indicated. Currents were evoked by a 1 s voltage step from a holding potential of 0 mV to +70 mV and deactivated by a repolarising step to -70 mV. Intracellular solution containing ~0.3 µM $[Ca^{2+}]_i$ was used for all experiments. (B) Concentration-response curves for the inhibition of TMEM16A currents by A9C (n=4) and NFA (n=7) at +70 and -70 mV.

This comprehensive systematic analysis has given us a basic understanding of four test compounds that are used throughout the project: two blockers (Ani9 and MONNA) and two compounds with a bimodal effect (A9C and NFA). E_{act} was not used further as we did not find it to activate TMEM16A and because a recent paper demonstrated that E_{act}

has an indirect effect on the channel (Genovese et al., 2019; Liu, Feng, Luo, Yang, Brett & Hu, 2016). A detailed mechanistic investigation of the mode of action of these four test compounds could shed light on how activation and inhibition can be selectively achieved pharmacologically.

3.5 Effect of MONNA on other TMEM16x family members: TMEM16B and TMEM16F

Next the biophysics and pharmacology of the TMEM16B and TMEM16F channels were studied to understand the selectivity of TMEM16A inhibitors on other TMEM16x family members that are not exclusively CaCCs.

3.5.1 Effect of inhibitors on TMEM16B

The effect of MONNA was studied on TMEM16B analogously to TMEM16A (section 3.4.1). MONNA caused inhibition of TMEM16B whole-cell currents however, the extent of the inhibition was reduced compared to TMEM16A. Fits of data to the Hill equation yielded IC_{50} of 3.5 ± 2.4 µM (n=5) and 7.2 ± 10.5 µM (n=5) at +70 mV and -70 mV, respectively. The maximum inhibition extrapolated from the Hill equation was 65 ± 11 % (n=5) and 40 ± 16 % (n=5) for +70 mV and -70 mV respectively.

Unlike TMEM16A, in the dose response to MONNA on TMEM16B there was a difference in the inhibition at +70 mV and -70 mV suggesting a voltage dependence to the inhibition, therefore the block in TMEM16A and TMEM16B may occur via a different mechanism.

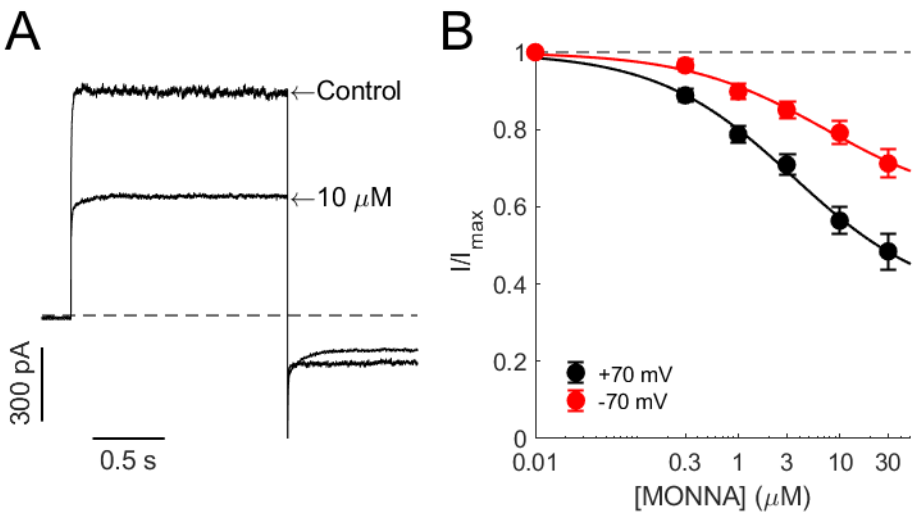


Figure 3.8 The effect of MONNA on whole-cell TMEM16B currents

(A) Whole-cell currents in the absence and presence of blockers at the concentrations indicated. Currents were evoked by a 1 s voltage step from a holding potential of 0 mV to +70 mV and deactivated by a repolarising step to -70 mV. Intracellular solution containing 0.6 µM Ca^{2+} was used for all experiments. (B) Concentration-response curves for the inhibition of TMEM16B currents by MONNA at +70 and -70 mV (n=5). The curves represent fit of the data to the Hill equation.

3.5.2 Effect of inhibitors on TMEM16F

TMEM16F acts both as a CaCC and a phospholipid scramblase (Scudieri et al., 2015). Currently, there are no reported synthetic, small-molecule pharmacological modulators of TMEM16F. Previous work in the group however demonstrates that Ani9 activates TMEM16F currents ~4.7 fold at 10 µM Ani9 (Acheson, 2019).

We therefore tested the modulation of MONNA (10 µM) on TMEM16F to assess the selectivity of MONNA to TMEM16A compared to other family members. MONNA was found to inhibit TMEM16F currents (Fig. 3.9).

Whole-cell TMEM16F currents were elicited using the step protocol in the presence of 78 µM $[Ca^{2+}]_i$. Due to slow TMEM16F activation, as described in section 3.3.2, currents were recorded six minutes after establishing the whole-cell configuration. TMEM16F current was inhibited by 0.71 ± 0.04-fold on application of 10 µM MONNA (n=8) (P<0.05).

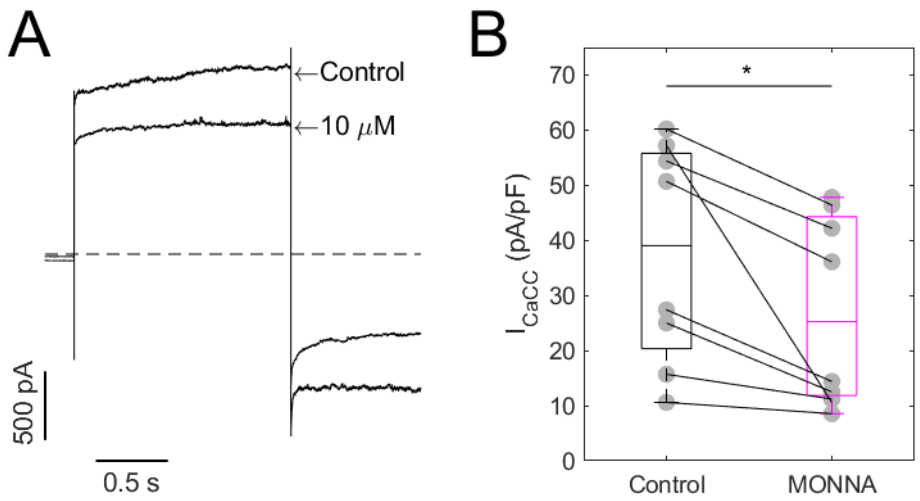


Figure 3.9 The effect of MONNA on whole-cell TMEM16F currents

(A) Whole-cell currents in the absence and presence of blockers at the concentrations indicated. Currents were evoked by a 1 s voltage step from a holding potential of 0 to +70 mV and deactivated by a repolarising step to -70 mV. Intracellular solution containing 78 µM Ca^{2+} was used for all experiments. (B) Box and whisker plot for the inhibition of TMEM16F currents by MONNA (10 µM) at +70 mV. The central mark indicates the median, and the bottom and top edges of the box indicate the 25th and 75th percentiles, respectively. The whiskers extend to the most extreme data points not considered outliers. The lines between points represent the inhibition of each cell (n=5). * p<0.05 using a paired student t test.

3.6 Competition with extracellular Cl^-

The next step of my study was to gain an understanding of the potential site of action of the test compounds. Previous work demonstrated that A9C binds within the pore,

and both activation and inhibition are affected by increasing Cl^- fluxes (Ta, Adomaviciene, Rorsman, Garnett & Tammaro, 2016). A published study of NFA has showed that the extent of TMEM16A modulation was also affected by changes in Cl^- fluxes (Ni, Kuan & Chen, 2014). Thus, I studied whether the permeating ions would also affect the extent of current inhibition provoked by Ani9 and MONNA.

The extent of TMEM16A current inhibition was tested in the presence of high (154 mM) and low (34 mM) extracellular Cl^- concentrations ($[Cl^-]_{ext}$). Currents were elicited in response to the step protocol and the steady state current measured at +70 mV in the absence and presence of concentration of the blocker. In the presence of low $[Cl^-]_{ext}$, application of 0.1 µM $[Ani9]_{ext}$, led to the fractional inhibition of 89.9 ± 1.8 % (n=6), similarly an inhibition of 84.4 ± 2.7 % (n=8) observed in high $[Cl^-]_{ext}$. In the presence of low $[Cl^-]_{ext}$, application of 1.5 µM $[MONNA]_{ext}$, led to the fractional inhibition of 35.5 ± 8.6 % (n=7), this contrasted with an inhibition of 69.1 ± 3.6 % (n=6) observed in high $[Cl^-]_{ext}$.

Thus, changing the extent of Cl^- flux did not alter the degree of Ani9 inhibition, indicating that Ani9 does not compete with the permeating ion. In contrast inhibition by MONNA was enhanced in 34 mM $[Cl^-]_{ext}$ suggesting that MONNA binds in a site within the pore which competes with the permeant ion and is different to that of Ani9. *P<0.05 (ANOVA followed by pairwise comparison with Bonferroni).

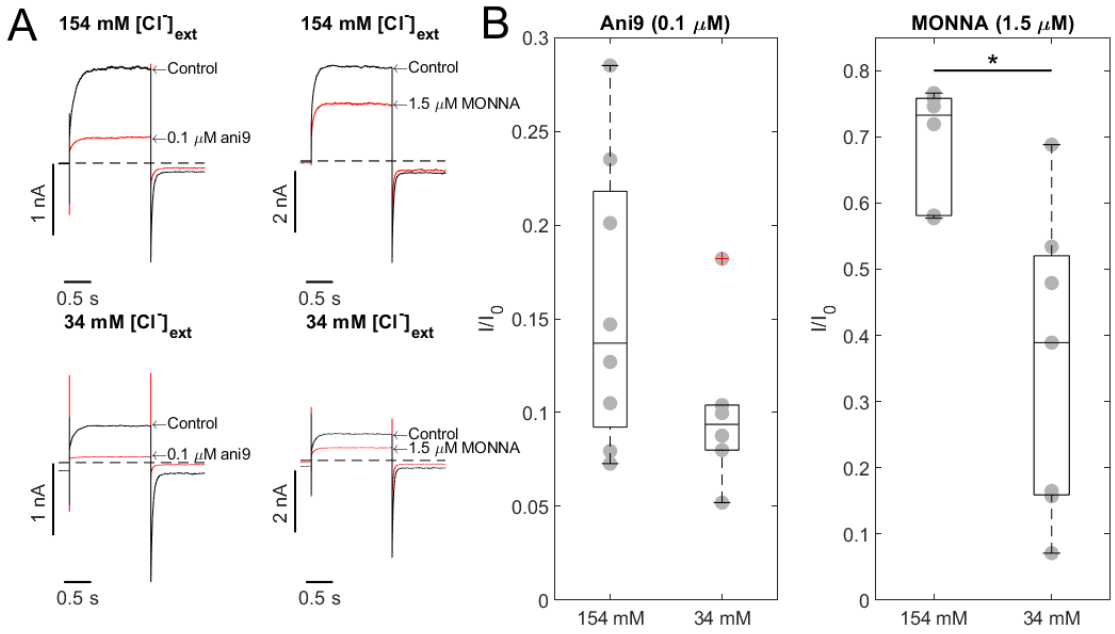


Figure 3.10 The effect of varying $[Cl^-]_{ext}$ on Ani9 and MONNA-mediated inhibition of TMEM16A currents.

(A) Whole-cell currents recorded from HEK-293T cells expressing TMEM16A. Dashed line represents zero current level. Extracellular Ani9 (0.1 µM, left panel) or MONNA (1.5 µM, right panel) was applied as indicated by the solid red line. $[Cl^-]_{ext}$ was 154 mM (top) or 34 mM (bottom). (B) Box and whisker plot of then inhibition of TMEM16A current in response to Ani9 (0.1 µM, n=5, left panel) or MONNA (1.5 µM, n=7, right panel) in low or high $[Cl^-]_{ext}$, as indicated. The central mark indicates the median, and the bottom and top edges of the box indicate the 25th and 75th percentiles, respectively. The whiskers extend to the most extreme data points not considered outliers. *P<0.05 student's t-test.

3.7 Effect of NFA on TMEM16A's single channel current and open probability as examined by noise analysis

As described in Chapter 2, the macroscopic current (I) is the product of the single channel current (i), number of identical and independent channels (N) and the open probability of these channels (P_o):

$$I = iNP_o \qquad [19]$$

Thus, modulation of TMEM16A current could be a result of the change in one of these parameters: I, N or P_o. Modulation of TMEM16A is observed on a sub-millisecond timescale, whereas changes in N involve channel trafficking and expression which takes place on a longer timescale. Thus, a change in N in unlikely to cause current modulation. Noise analysis was carried out to examine whether NFA activation is a product of a change in i or P_o.

Previous work demonstrated that A9C activation is due to an increase in channel open probability (P_o) while the single channel current (i) remains unaltered (Ta, Adomaviciene, Rorsman, Garnett & Tammaro, 2016). To gain an understanding of whether NFA acts in a similar manner, non-stationary noise analysis was performed in the absence (control) and presence of NFA (10 µM). The noise analysis was conducted at negative V_m because it was assumed in that, in analogy with the action of A9C, the compound blocks at positive V_m while at negative V_m the block is relieved and the activation is revealed (Ta, Adomaviciene, Rorsman, Garnett & Tammaro, 2016). Non-stationary noise analysis was performed in the presence of ~0.3 µM $[Ca^{2+}]_i$ during a tail pulse to -70 mV. In the absence of NFA the i of TMEM16A was 0.39 ± 0.05 pA. In the presence of 10 µM $[NFA]_{ext}$ the i was 0.56 ± 0.11 pA. In the absence of NFA the P_o of TMEM16A was 0.18 ± 0.053 pA, however in the presence of 10 µM $[NFA]_{ext}$ the P_o was 0.47 ± 0.05 pA. Extracellular NFA does not affect TMEM16A single channel conductance but alters channel open probability. Thus, noise analysis revealed that NFA, like A9C (Ta, Adomaviciene, Rorsman, Garnett & Tammaro, 2016), acts as a TMEM16A gating modifier which promotes channel gating (Fig. 3.11).

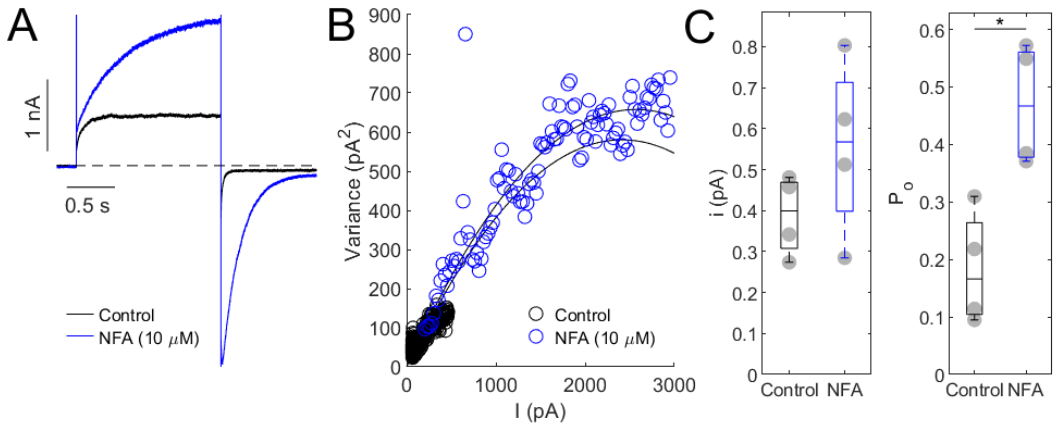


Figure 3.11 Non-stationary noise analysis for whole-cell TMEM16A currents in the presence and absence of NFA activation.

(A) Whole-cell currents recorded from HEK-293T cells expressing TMEM16A in the absence (control) and presence of NFA (10 µM). Dashed line represents zero current level. (B) Current variance plotted against the mean current in the presence and absence of NFA (10 µM), as indicated. The parabolic lines are the best fit of the data using Equation 14. (C) Box and whisker plot of i (left panel) and P_o (right panel) obtained from stationary noise analysis (n=4). The central mark indicates the median, and the bottom and top edges of the box indicate the 25th and 75th percentiles, respectively. The whiskers extend to the most extreme data points not considered outliers. *P<0.05 student's t-test.

3.8 Effect of Ani9 and MONNA on isolated aortic rings

The experiments in this chapter to this point have demonstrated the effect of common CaCC blockers on cloned TMEM16A channels. The understanding of the pharmacology of TMEM16A is still in its infancy so we therefore wanted to test the selectivity of the two most potent and reportedly selective blockers (Ani9 and MONNA). By testing on intact blood vessels and native cells we are further able to understand whether these modulators can act in a physiological system and towards using TMEM16A blockers in a clinical setting.

TMEM16A accounts for the CaCC component in VSMCs and is implicated in agonist induced blood vessel contraction (Matchkov, Boedtkjer & Aalkjaer, 2015; Pedemonte & Galietta, 2014). This section aims to gain an initial understanding of the role of TMEM16A inhibitors on agonist-induced blood vessel contraction, testing Ani9 and MONNA to determine the selectivity to TMEM16A.

Wire-myography was used to study freshly isolated murine aortic rings. The mounting and normalisation procedures for myography experiments is described fully in Chapter 2. Phenylephrine (PE) or potassium methanesulfonate (K-MES) was used as the contractile agonist for these experiments.

Ani9 and MONNA have been demonstrated to be a potent blocker of cloned TMEM16A channels (Fig 3.5), however the selectivity of MONNA has been questioned (Boedtkjer, Kim, Jensen, Matchkov & Andersson, 2015) and there is no detailed report on the selectivity of Ani9. Examining the effects of these inhibitors on isolated aortic rings may offer insight into the selectivity of these compounds in VSM.

Isolated aortic rings were incubated in the presence of Ani9 (1 μM), MONNA (10 μM), or left untreated (control) for 20 minutes, prior to addition of increasing concentrations of PE. These concentrations were selected as they inhibit the cloned TMEM16A channel by ~90 % in each case (Fig 3.5). The tension obtained at various [PE] was normalised for the tension evoked by 50 mM KCl (detailed in section 2.6) and plotted *versus* [PE] (Fig. 3.13). The tension *versus* [PE] experiments were fitted with the Hill equation.

Under control conditions, PE increased aortic constriction in a dose dependent manner, as was seen for both Ani9 and MONNA.

Maximal aortic contraction was significantly reduced in the presence of Ani9 (1 µM) and MONNA (10 µM), with a ~1.8 and ~7.7-fold reduction compared to the control respectively. The difference between the reduction by Ani9 and MONNA. There was no significant change in the EC_{50} under control conditions compared to in the presence of the TMEM16A inhibitors. The more pronounced effect of MONNA may represent the action of MONNA on targets in addition to TMEM16A. Another possibility is that Ani9 acts on another receptor which is enhancing the contractile response, however previous studies done by Kathryn Acheson have shown that Ani9 is selective for TMEM16A in VSMCs, pointing to MONNA being unselective.

Table 3.1 Hill-fit parameters (EC_{50}, max and h) (Eq. 19) for aortic ring tension *versus* [PE] relationships obtained in the absence (control) and presence of Ani9 or MONNA

	EC_{50}	**Max**	**h**	**N**
Control	0.19 ± 0.01	0.69 ± 0.01	1.27 ± 0.06	20
Ani9 (1 µM)	0.29 ± 0.01	0.38 ± 0.01*	1.37 ± 0.07	10
MONNA (10 µM)	0.25 ± 0.00	0.09 ± 0.01*	2.29 ± 0.29*	9

* indicates statistically significant difference from control. ($P < 0.05$ one-way ANVOA followed by pairwise comparison with Bonferroni).

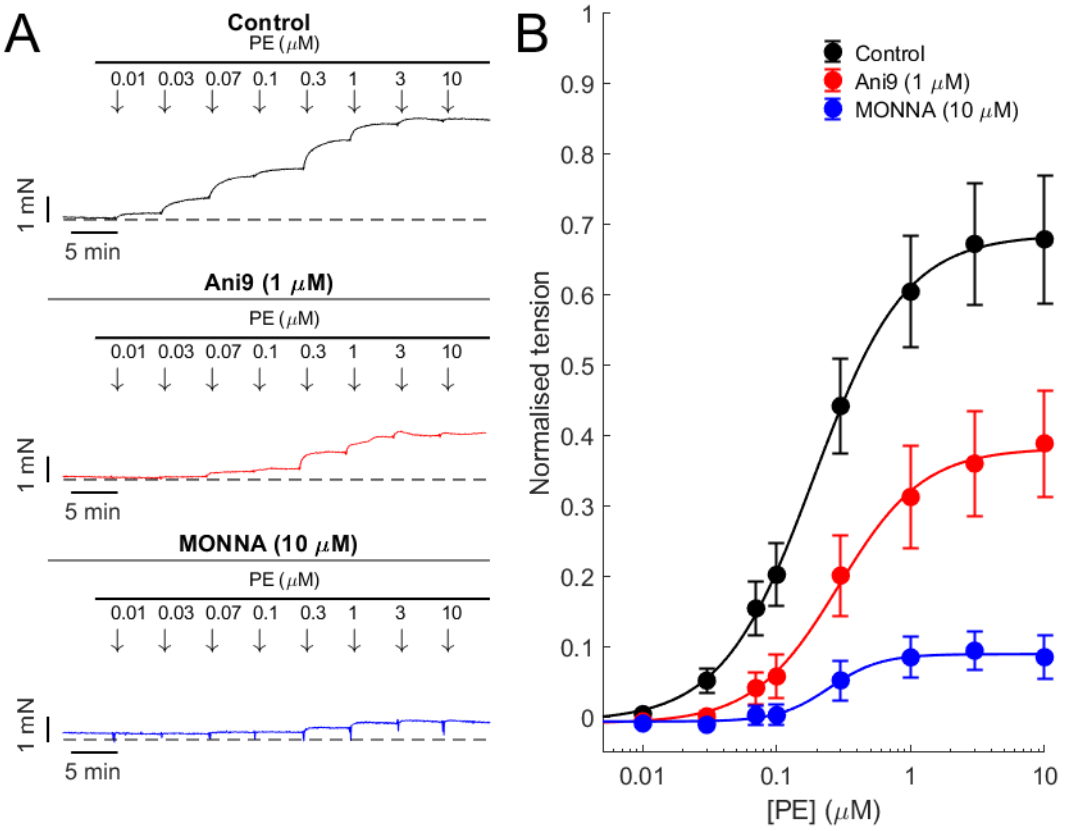


Figure 3.12 PE-mediated contraction of aortic rings in the presence of Ani9 and MONNA.

(A) Isometric tension recordings obtained from isolated aortic rings, exposed to increasing [PE] in the absence (control) or presence TMEM16A blockers MONNA (10 µM) or Ani9 (1 µM). (B) Mean tension *versus* [PE] relationships for isolated aortic rings in the absence (control) or presence of Ani9 or MONNA (n=9-20).

3.8.1 Effect of reducing $[Cl^-]_{ext}$ in VSMCs on isolated aortic rings

The following experiments aimed to define whether TMEM16A has a role in Ani9 and MONNA modulation of blood vessel constriction by increasing the electrochemical gradient for Cl^- in VSMCs. We predict that low $[Cl^-]_{ext}$ will cause aortic contraction, because a shift in E_{Cl} amplifies TMEM16A currents, as described in figure 3.13. If Ani9 and MONNA act via TMEM16A, we expect this low $[Cl^-]_{ext}$-mediated contraction in aortic rings to be reduced in the presence of either modulator.

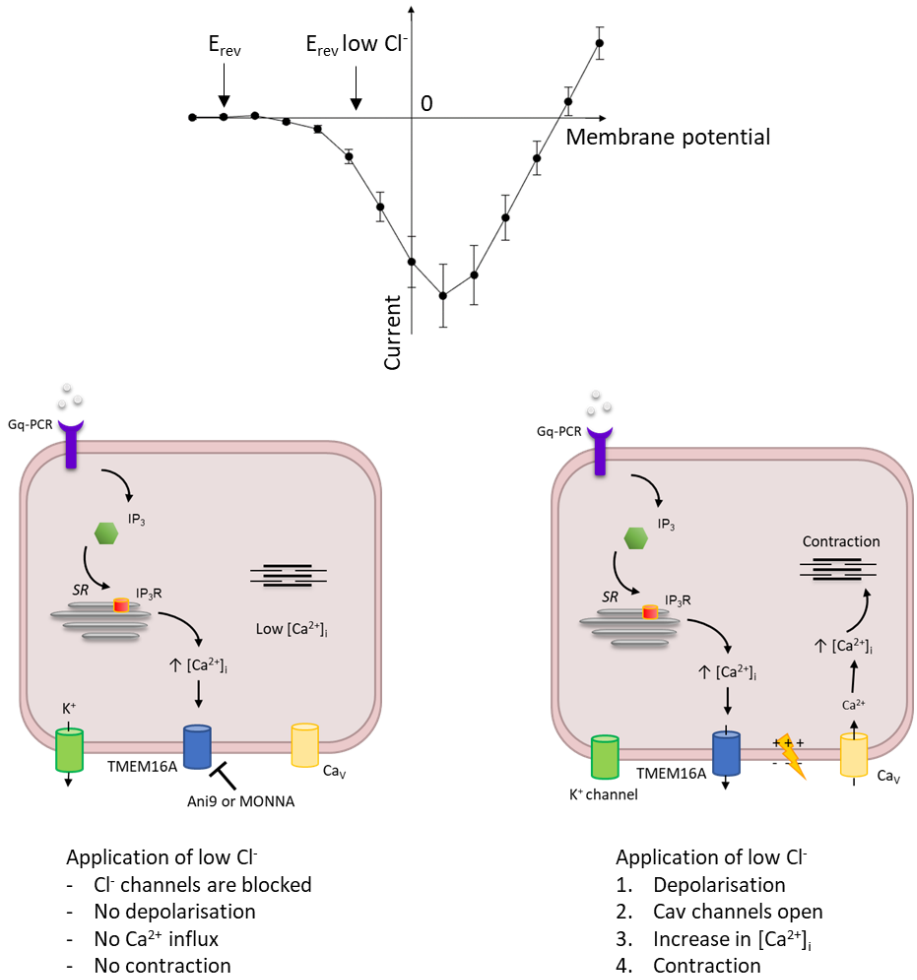


Figure 3.13 Diagram depicting the effect of electrochemical gradient in VSMCs

Black line represents Ca_V current. E_{rev} is shifted to more positive potentials when extracellular solution is exchange for low Cl^- solution. Noradrenaline (NA) binds to α1-adrenoreceptors on the plasma membrane of VSMCs causing activation of G_q-protein coupled receptors (GPCR) and subsequent Ca^{2+} release from the sarcoplasmic reticulum (SR) via the inositol trisphosphate (IP_3) pathway. This rise in $[Ca^{2+}]_i$ is predicted to activate TMEM16A channels (right panel), this activation is blocked by Ani9 or MONNA (left panel). Activation of TMEM16A causes Cl^- efflux and consequently membrane depolarisation and opening of Ca_V channels which leads to cell contraction.

Prior to exchange of standard PSS (Table 2.15) with low Cl^- PSS (Table 2.16), TMEM16A channels were activated by exposure to PE. Different concentrations of PE were

required to elicit the same amount of blood vessel constriction in the absence and presence of Ani9 (1 μM) or MONNA (10 μM). Therefore, based on the data shown in figure 3.12, concentrations of PE were selected that produced a ~20 % activation in all conditions. The concentrations of PE selected for these experiments were 0.1 μM for the control and 1 μM in the presence of Ani9 or MONNA. Isolated aortic rings were incubated in presence of Ani9 (1 μM) or MONNA (10 μM) for 20 minutes or left untreated for the same length of time (control). PE was then added to each aortic ring to activate TMEM16A channels (Fig 3.14). Contraction of the aortic rings in low Cl^- PSS was normalised to the contraction observed in standard PSS. Agonist-induced contraction was significantly reduced in the presence of Ani9 (1 μM) or MONNA (10 μM), with a ~4.1 or ~4.0-fold reduction respectively observed. This suggests that agonist-induced contraction is Cl^- mediated, and that the effect of Ani9 and MONNA on blood vessels is mediated via TMEM16A.

Table 3.2 The effect of TMEM16A inhibitors on aortic contraction in conditions of low $[Cl^-]_{ext}$

	Control	**Ani9 (1 μM)**	**MONNA (10 μM)**
Normalised plateau value	4.98 ± 1.29	1.21 ± 0.11*	1.25 ± 0.04*
n	6	5	4

* indicates statistically significant difference from control. ($P < 0.05$ one-way ANVOA followed by pairwise comparison with Bonferroni).

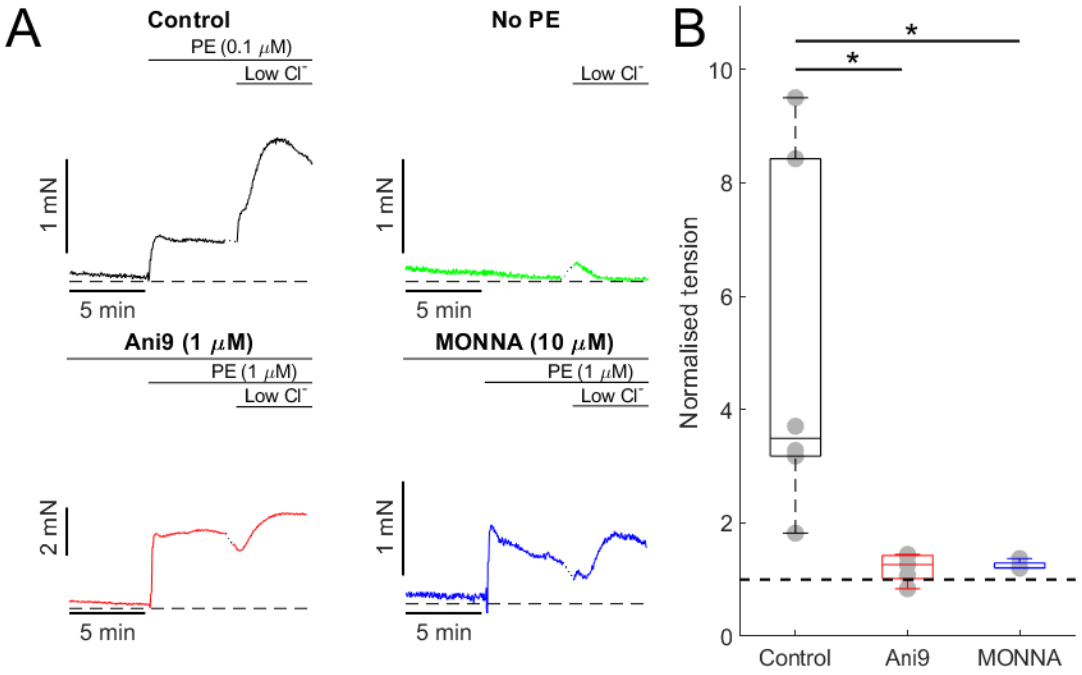


Figure 3.14 PE-mediated contraction of aortic rings in the presence of low $[Cl^-]_{ext}$ and Ani9 or MONNA.

(A) Representative change in isometric tension of aortic rings in response to PE and low $[Cl^-]_{ext}$ conditions, in the presence of PE (0.1 or 1 µM, as indicated) and inhibitors, as indicated. Dotted line represents change of solutions. Dashed lines represent baseline tension. (B) Box and whisker plot showing the fold change on changing solution to low $[Cl^-]_{ext}$, in the absence (control) (N=6), and presence of Ani9 (1 µM, N=5) or MONNA (10 µM, N=4). The central mark indicates the median, and the bottom and top edges of the box indicate the 25th and 75th percentiles, respectively. The whiskers extend to the most extreme data points not considered outliers. *P<0.05 (ANOVA followed by pairwise comparison with Bonferroni).

Myography experiments using altered $[Cl^-]_{ext}$ demonstrated a role for Cl^- channels in this response. Specifically, increasing the Cl^- electrochemical gradient by lowering $[Cl^-]_{ext}$ strongly enhanced contraction of aortic rings, revealing a role for Cl^- channels in this response (Fig. 3.14). However, both Ani9 and MONNA profoundly reduced the effect of low Cl^-.

3.8.2 Effect of Ani9 and MONNA on K^+-mediated depolarisation of aortic rings

The effect of Ani9 and MONNA on aortic ring contraction mediated via a TMEM16A independent manner by elevation of extracellular K^+ concentration ($[K^+]_{ext}$) was studied next. It is well established that increasing $[K^+]_{ext}$ causes depolarisation and contraction of VSMCs (Eid, Abu-Sharib, El-Bassossy, Balamash & Smirnov, 2018; Manoury, Tamuleviciute & Tammaro, 2010; Tammaro, Smith, Hutchings & Smirnov, 2004). Therefore, the depolarising action of TMEM16A would be bypassed in this case, in favour of depolarisation induced by $[K^+]_{ext}$. Specifically, increasing $[K^+]_{ext}$ results in a depolarising shift of the E_K which lead to V_m depolarisation. This activates the L-type Ca_V channels, which causes an increase in $[K^+]_{ext}$, and results in blood vessel contraction (Nelson, Patlak, Worley & Standen, 1990). For this K^+-mediated aortic ring contraction to be independent of changes in $[Cl^-]_{ext}$, K-methanesulfonate was used instead of KCl. Increasing $[K^+]_{ext}$ is expected to cause depolarisation and direct activation of Ca_V channels, in a TMEM16A-independent manner. This is because methanesulfonate does not permeate through Cl^- channels. The rationale for this experiment was that if channels other than TMEM16A are modulated by Ani9 or MONNA, these agents would affect contraction under conditions in which TMEM16A channels are not taking part in the depolarisation of VSMCs.

The isolated aortic rings were incubated in the presence of MONNA (10 μM), Ani9 (1 μM), or alone under identical conditions (control) for 20 minutes, prior to the addition of increasing concentrations of K-methanesulfonate (Fig. 3.15).

In the presence of Ani9 (1 μM) or MONNA (10 μM), aortic contraction induced by 100 mM K-methanesulfonate was reduced by ~1.4 fold ($P>0.05$, Table 3.3). Isolated aortic

ring contraction evoked by K-methanesulfonate was only marginally affected by MONNA and Ani9. It is hypothesised that this could be due to small activation of TMEM16A by the increase in V_m. Overall, this data suggests that Ani9 and MONNA-mediated attenuation of PE-induced contraction requires a modulation of TMEM16A. This is due to the loss of the significant reduction in contraction with MONNA or Ani9 in the absence of TMEM16A-mediated contraction.

Table 3.3 Effect of TMEM16A inhibitors on aortic contraction in the presence of 100 mM K-MES

	Control	**Ani9 (1 μM)**	**MONNA (10 μM)**
100 mM K-methosulphate	1.35 ± 0.08	1.0 ± 0.03*	0.96 ± 0.07*
n	8	6	5

* indicates statistically significant difference from control. ($P < 0.05$ one-way ANVOA followed by pairwise comparison with Bonferroni).

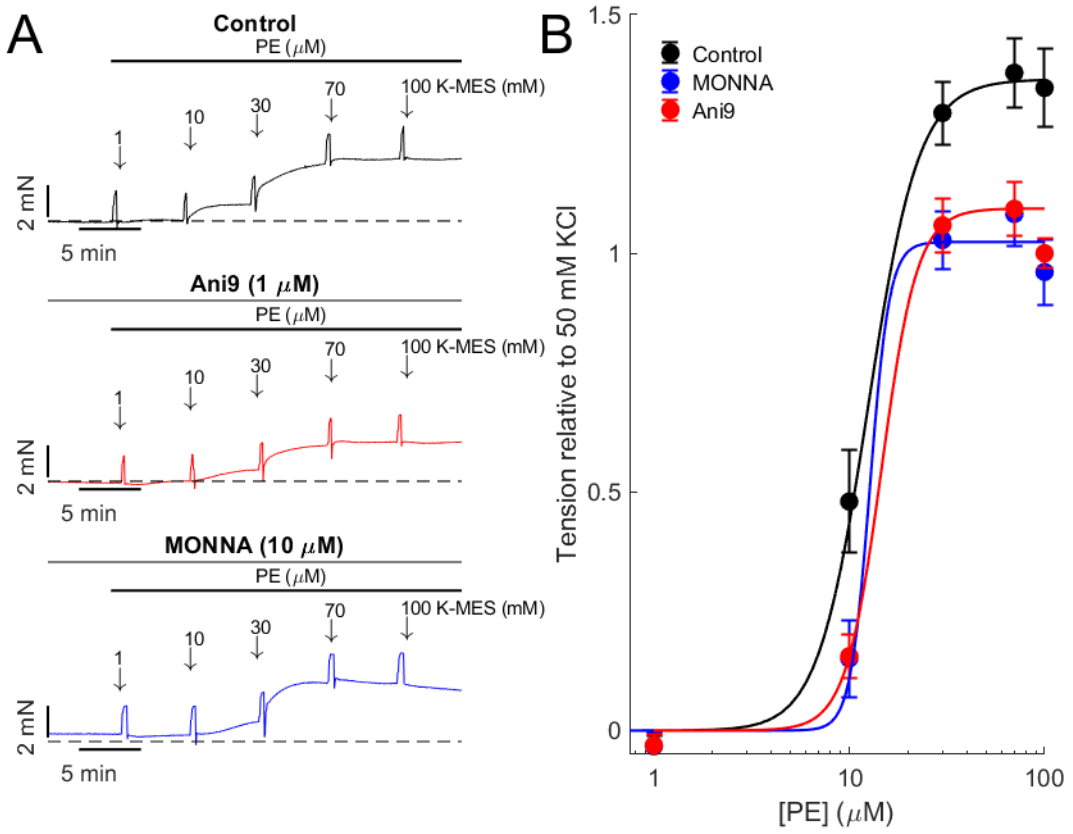


Figure 3.15 K-MES-mediated contraction of aortic rings in the presence of Ani9 and MONNA.

(A) Isometric tension recordings obtained from isolated aortic rings, exposed to increasing [K-MES] in the absence (control) or presence TMEM16A blockers MONNA (10 µM) or Ani9 (1 µM). (B) Mean tension *versus* [K-MES] relationships for isolated aortic rings in the absence (control) or presence of Ani9 or MONNA (n=5-8).

3.9 Native currents in isolated VSMCs

From the previous experiments in this chapter we have confirmed that MONNA and Ani9 act on TMEM16A channels and can mediated agonist induced contraction of blood vessels. In order to further understand this effect and the channels involved in the process we isolated smooth muscle cells from the aorta of 5-8 week old mice. Whole-

cell patch-clamp electrophysiology was used to study global currents within these cells and the effect of the two top blockers.

3.9.1 TMEM16A currents in isolated VSMCs

TMEM16A currents were studied in isolated vascular smooth muscle cells dissociated from mice aorta as described in Chapter 2.

Solutions containing ~0.6 μM $[Ca^{2+}]_i$, and the IV-CaCC protocol was used to elicit whole-cell TMEM16A currents. In the presence of ~0.6 μM $[Ca^{2+}]_i$, hyperpolarising and depolarising steps showed instantaneous TMEM16A currents, followed by time-dependent relaxations towards new steady-state levels. Currents reached a maximum steady-state current density of 34.2 ± 6.1 pA/pF (N=9) at +100 mV. The current density immediately after the voltage changed was measured and represented the instantaneous current component. We observed a nearly linear relationship between the instantaneous current and V_m. However, the relationship between steady-state current and the V_m was outwardly rectifying (Fig. 3.16) analogues to that seen for cloned TMEM16A. The I_{ss}/I_{inst} at +100 mV gives a fraction of 1.8 ± 0.1 (N=9) and the I_{100}/I_{-100} (rectification index) was -3.3 ± 0.3 (N=9) in 0.6 μM $[Ca^{2+}]_i$. The reversal potential for the TMEM16A currents was approximately 0 mV, the estimated Cl^- equilibrium potential for the recording solutions used.

The time of half current was measure as described in section 3.2. As the voltage increased, $\tau_{0.5}$ decreased, equalling 293.4 ± 10.0 ms (N=9) at +40 mV and 171.7 ± 4.7 ms (N=9) at +100 mV ($P<0.05$) (Fig. 3.2). The tail currents measured upon repolarisation to −60 mV were quantified in the same way, $\tau_{0.5}$ did not show a significant change with

voltage over the range of +40 mV to +100 mV (Fig. 3.2). The $\tau_{0.5}$ for the deactivating tail current was 98.0 ± 11.7 ms (N=9) when preceded by a pre-pulse to +40 mV and 94.3 ± 9.2 (N=9) when preceded by a pre-pulse to +100 mV.

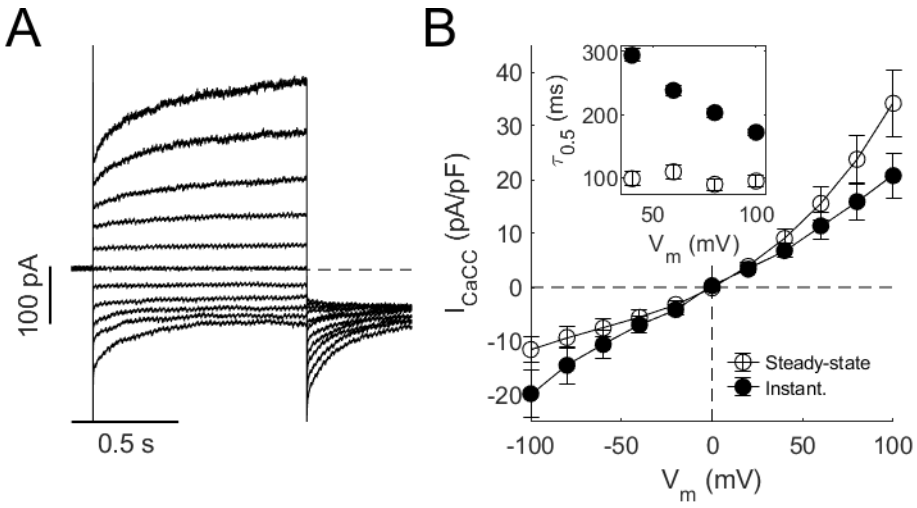


Figure 3.16 Properties of TMEM16A IV-relationship in isolated aortic VSMCs.

Whole-cell current recording from isolated aortic VSMCs and dialysed with 0.6 µM $[Ca^{2+}]_i$. Dotted line represents zero-current level. (B) Mean whole-cell current *versus* V_m relationship, measured at the beginning of the test pulses filled circles and at the end of the test pulses (empty circles) (N=9). Inset in (B) show mean $\tau_{0.5}$ of current activation (filled symbols) and deactivation (open symbols) at various V_m.

3.9.2 Effect on inhibitors on native TMEM16A in VSMCs

Previous experiments demonstrated that MONNA (10 µM) inhibits cloned TMEM16A by ~90 %. Therefore, we next tested whether MONNA can also block TMEM16A currents isolated from aortic SMCs.

Whole-cell currents were recorded from isolated VSMCs using standard CaCC solutions with ~0.6 µM $[Ca^{2+}]_i$, and the IV-ramp protocol (Fig. 3.17). TMEM16A currents were

normalised for the C_m. At -95 mV and +95 mV, addition of MONNA resulted in a ~1.4 fold reduction in TMEM16A current (Fig. 3.17).

This reduction is less pronounced than that seen in cloned TMEM16A currents, this could be due to the presence of additional Cl^- current in aortic smooth muscle that is not blocked by MONNA. Higher concentrations of MONNA are difficult to test due to the low solubility of MONNA above 10 µM.

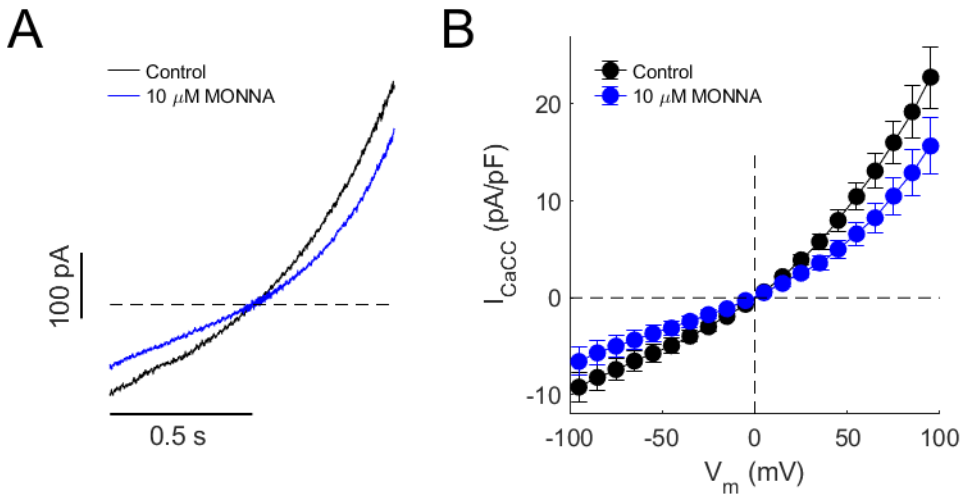


Figure 3.17 MONNA effect on TMEM16A current in VSMCs.

(A) Whole-cell patch-clamp native TMEM16A currents recorded in isolated VSMCs. Solutions contained ~0.6 µM $[Ca^{2+}]_i$, and the IV-ramp protocol was used to elicit TMEM16A currents in the absence (control, shown in black) or presence of MONNA (10 µM, blue). (B) Mean whole-cell current measured from -95 mV to 95 mV in 10 mV increments, in the absence (black, control), or presence of MONNA (10 µM, blue) N=8.

We then assessed the ability of Ani9 to block native TMEM16A currents in isolated aortic SMCs. At -95 mV, addition Ani9 resulted in a ~1.8 fold reduction in TMEM16A current, which increased to a ~2 fold reduction in TMEM16A current at 95 mV (Fig. 3.18). This is

in accordance of work done previously within our lab (data collected alongside Kathryn Acheson).

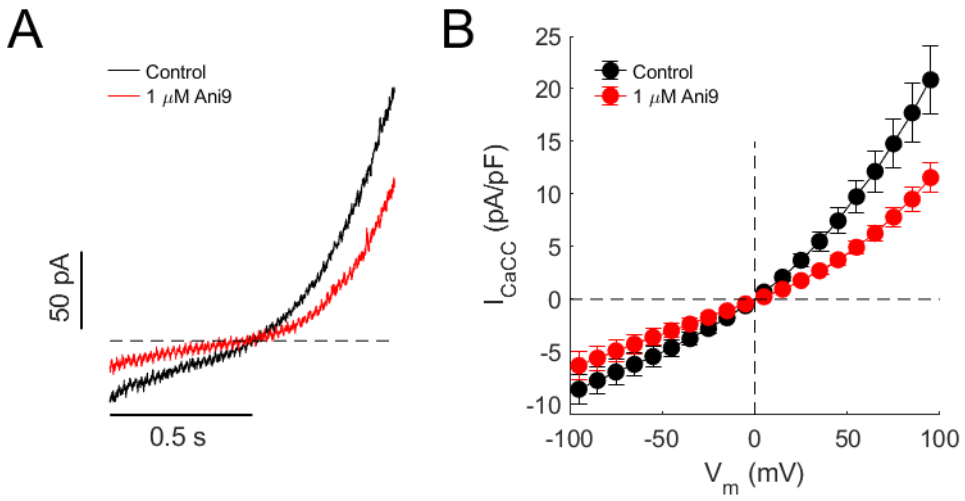


Figure 3.18 Ani9 effect on TMEM16A current in VSMCs.

(A) Whole-cell patch-clamp native TMEM16A currents recorded in isolated VSMCs. Solutions contained 0.6 µM $[Ca^{2+}]_i$, and the IV-ramp protocol was used to elicit TMEM16A currents in the absence (control, shown in black) or presence (red) of Ani9 (1 µM). (B) Mean whole-cell current measured from -95 mV to 95 mV in 10 mV increments, in the absence (black, control), or presence of Ani9 (red) N=10.

3.9.3 Effect of inhibitors on cationic current

Due to previous data reported in section 3.12 demonstrating that Ani9 and MONNA have different effects on isolated aortic rings suggests that the modulators may act on other channels. The selectivity of MONNA has also been reported previously and have been suggested to act in the absence of chloride, and instead target VGCC and K^+ channels (Boedtkjer, Kim, Jensen, Matchkov & Andersson, 2015). Therefore, we examined the possibility that Ani9 or MONNA can modulate other channels in VSMCs.

Whole-cell currents were recorded from isolated VSMCs using cationic solutions and the IV-ramp protocol (Fig. 3.19). Currents were normalised for the C_m and the V_m was held

at -55 mV between sweeps to reduced inactivation of K^+ channels. MONNA (10 µM) was found to increase VSMC currents at depolarising V_m, with an increase by ~4.7 fold at 95 mV. The time course of this effect was defined as the amount of time taken for the modulator effect to plateau in each cell at 100 mV.

Overall, MONNA activated whole-cell VSMC cationic current at positive V_m and therefore modulates other currents which identifies a reason for the change in reduction in contraction of the isolated vessels.

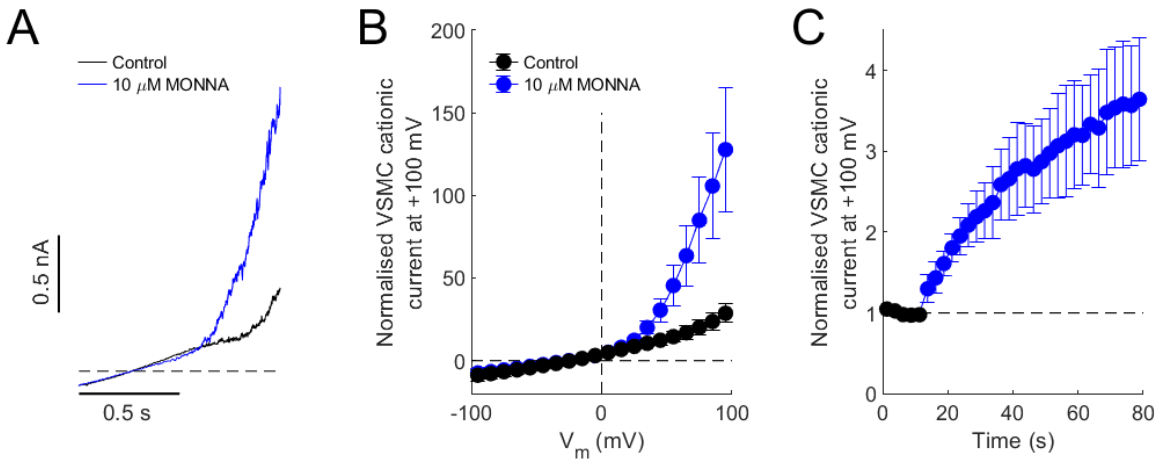


Figure 3.19 Effect of MONNA on cationic currents from isolated VSMCs.

(A) Whole-cell patch-clamp cationic currents recorded from isolated murine aortic SMCs. Cationic solutions and the IV-ramp protocol were used to elicit the currents in the absence (control, black) or presence of MONNA (10 µM, blue). (B) Mean whole-cell current measured from -95 mV to 95 mV in 10 mV increments, in the absence (control, black) N=5, or presence of 10 µM MONNA (10 µM, blue) N=5. (C) Time course for the effect of MONNA (10 µM, blue) on isolated VSMCs cationic current measured at +100 mV. Data was normalised to control currents at +100 mV.

In accordance with previous experiments in the lab Ani9 (1 µM) did not affect VSMC cationic currents at any V_m tested, this suggests Ani9 does not modulate any large-

current cationic ion channels expressed in VSMCs. Data was collected alongside Kathryn Acheson.

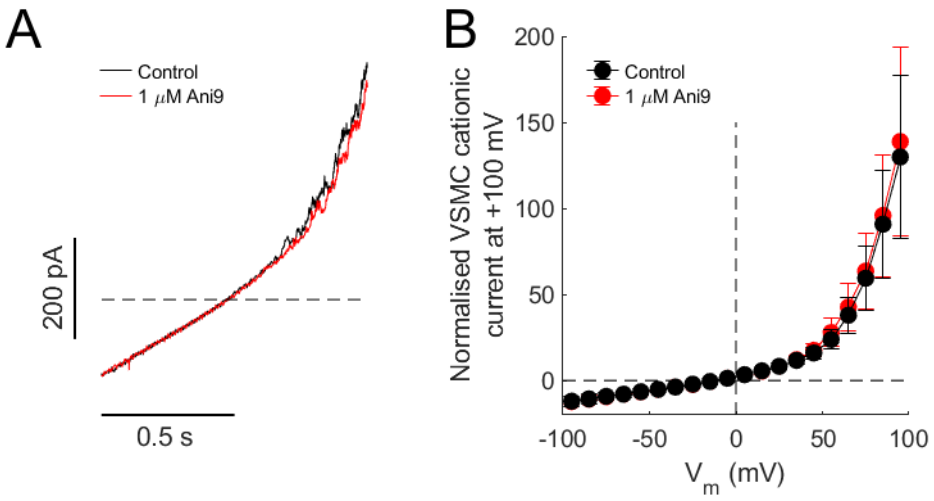


Figure 3.20 Effect of Ani9 on cationic currents from isolated VSMCs.

(A) Whole-cell patch-clamp cationic currents recorded from isolated murine aortic SMCs. Cationic solutions and the IV-ramp protocol were used to elicit the currents in the absence (control, shown in black) or presence (red) of Ani9 (1 µM). (B) Mean whole-cell current measured from -95 mV to 95 mV in 10 mV increments, in the absence (black, control) N=5, or presence of Ani9 (red) N=5.

3.9.4 Exploration of MONNA's modulation of VSMC ion channels

Experiments in figure 3.19 demonstrate that MONNA activates cationic currents in aortic SMCs at positive V_m. Experiments were therefore carried out to determine which of the currents that make up the global cationic current were responsible for this increase. The effect of MONNA on cationic currents was tested in the presence of pharmacological blockers of individual cation currents. TRPM2 channels, K_{ATP} channels and BK_{Ca} channels are the main components of cationic currents in VSMCs therefore blockers of these channels, Clotrimazole, Glibenclamide and Paxilline, were chosen (Hill, McNulty & Randall, 2004; Pompermayer et al., 2005; Zhou & Lingle, 2014).

Concentrations of each blocker was chosen to fully inhibit these channels: Clotrimazole (10 μM), Glibenclamide (10 μM) and Paxilline (1 μM).

Whole-cell currents were recorded from isolated VSMCs using cationic solutions and the IV-ramp protocol (Fig. 3.21). Currents were normalised for the C_m and the V_m was held at -55 mV between sweeps to reduced inactivation of K^+ channels. Current were recorded for 5 sweeps under control conditions, then 10 steps with the pharmacological blocker, and then for the rest of the experiment MONNA (10 μM) was added. The time course of this effect was defined as the amount of time taken for the modulator effect to plateau in each cell at 100 mV.

Clotrimazole (10 μM) was found to have no effect on the whole-cell cationic current in VSMCs and did not affect the increase in current on the application of MONNA (10 μM). At 95 mV, currents were unaffected by clotrimazole (10 μM) but on addition of MONNA (10 μM) the currents increased by ~4 fold (Table 3.4).

Glibenclamide (10 μM) slightly reduced the whole-cell cationic current in VSMCs and did not affect the increase in current on the application of MONNA (10 μM). At 95 mV, currents were unaffected by glibenclamide (10 μM) but on addition of MONNA (10 μM) the currents increased by ~4 fold (Table 3.4).

Paxilline (1 μM) inhibited the VSMC whole-cell VSMC cationic current, and addition of MONNA (10 μM) had no effect on this inhibited current. At 95 mV paxilline (1 μM) blocked the VSMC cationic currents by ~0.69 fold. This block was then not affected by the addition of MONNA (10 μM).

The increase in cationic current by MONNA was unaffected by Clotrimazole and Glibenclamide but blocked by Paxilline. This suggests that MONNA activates BK_{Ca} channels. BK_{Ca} channels are important for membrane depolarisation in agonist-induced contraction of SMCs. Activation of BK_{Ca} channels would tend to hyperpolarize VSMCs, which would deactivate Ca_V channels and would therefore limit VSM contraction (Dopico, Bukiya & Jaggar, 2018; Jackson, 2017).

Table 3.4 Cationic currents evoked in VSMCs in the presence of ion channel blockers and MONNA.

	Control	**Clotrimazole**	**Glibenclamide**	**Paxilline**
Fold increase on addition of MONNA (10 μM) at 95 mV	4.67 ± 1.43	4.21 ± 0.73	3.93 ± 0.77	0.69 ± 0.05*
N	5	5	5	9

* indicates statistically significant difference from control. ($P < 0.05$ one-way ANVOA followed by pairwise comparison with Bonferroni).

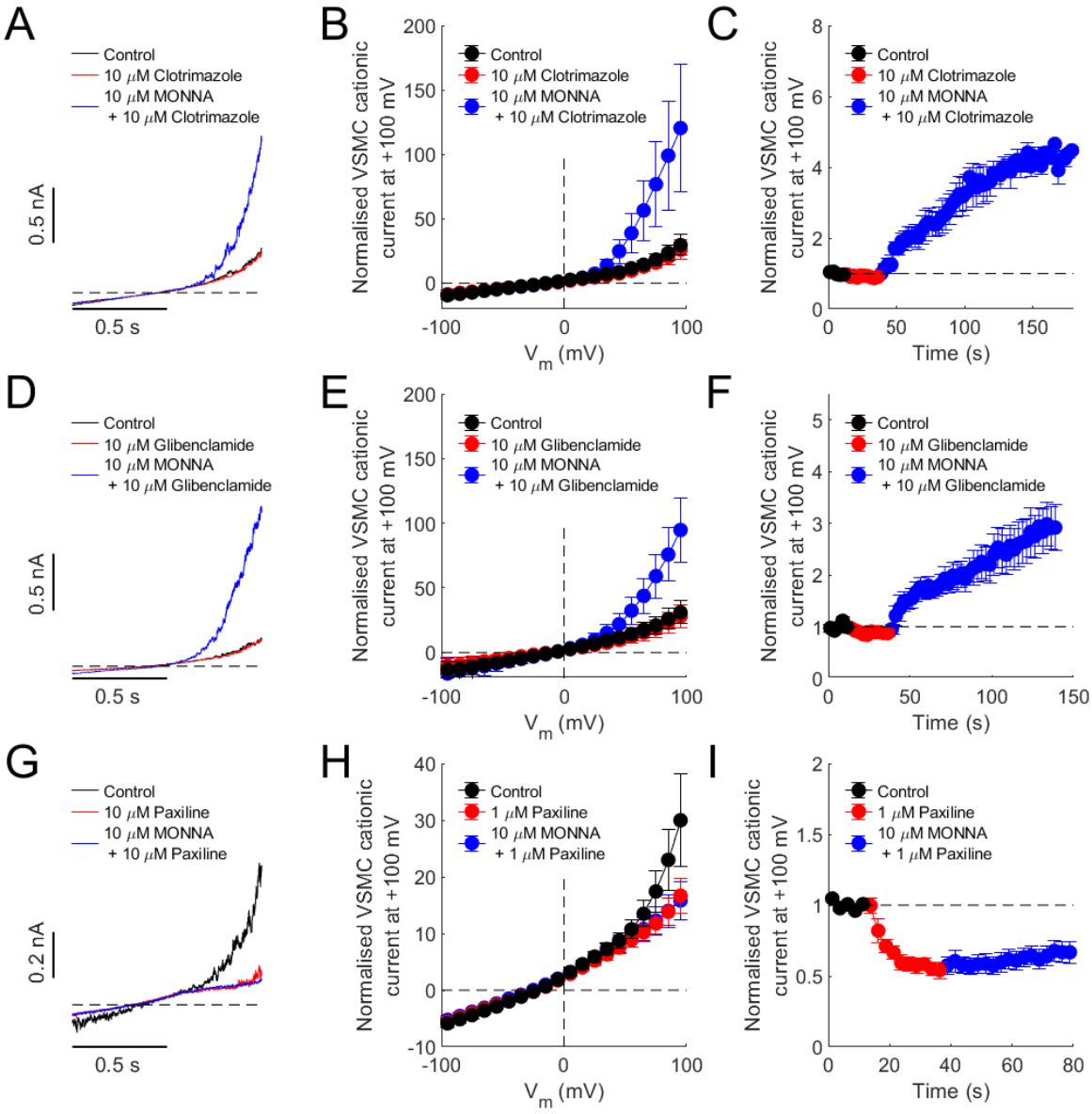


Figure 3.21. Effect of MONNA on isolated VSMCs in the presence of a variety of ion channel blockers.

(A) Whole-cell patch-clamp cationic currents recorded from isolated murine aortic SMCs. Cationic solutions and the IV-ramp protocol were used to elicit the currents in the absence (control), the presence of 10 µM Clotrimazole (red), and presence of 10 µM MONNA and 10 µM Clotrimazole (blue). (B) Mean whole-cell current measured from -95 mV to 95 mV in 10 mV increments, in the absence (control), the presence of 10 µM Clotrimazole (red), and presence of 10 µM MONNA and 10 µM Clotrimazole (blue). (C) Time course for the effect of 10 µM Clotrimazole and 10 µM MONNA on isolated VSMCs cationic current measured at +100 mV. Data was normalised to control currents at +100 mV. (D) Whole-cell patch-clamp cationic currents recorded from isolated murine aortic SMCs.

Cationic solutions and the IV-ramp protocol were used to elicit the currents in the absence (control), the presence of 10 µM Glibenclamide (red), and presence of 10 µM MONNA and 10 µM Glibenclamide (blue). (E) Mean whole-cell current measured from -95 mV to 95 mV in 10 mV increments, in the absence (control), the presence of 10 µM Glibenclamide (red), and presence of 10 µM MONNA and 10 µM Glibenclamide (blue). (F) Time course for the effect of 10 µM Glibenclamide and 10 µM MONNA on isolated VSMCs cationic current measured at +100 mV. Data was normalised to control currents at +100 mV. (G) Whole-cell patch-clamp cationic currents recorded from isolated murine aortic SMCs. Cationic solutions and the IV-ramp protocol were used to elicit the currents in the absence (control), the presence of 1 µM Paxilline (red), and presence of 10 µM MONNA and 1 µM Paxilline (blue). (H) Mean whole-cell current measured from -95 mV to 95 mV in 10 mV increments, in the absence (control), the presence of 1 µM Paxilline (red), and presence of 10 µM MONNA and 1 µM Paxilline (blue). (I) Time course for the effect of 1 µM Paxilline and 10 µM MONNA on isolated VSMCs cationic current measured at +100 mV. Data was normalised to control currents at +100 mV.

3.10 Effect of inhibitors on Ca_V currents in VSMCs

L-type Ca_V channels are reported to be an important aspect of SMC cationic currents, these experiments were therefore used to understand whether Ca_V channels play a role in the MONNA medicated vasorelaxation.

Whole-cell patch-clamp electrophysiology of VSMCs was conducted using Ca_V solutions, and the Ca_V voltage protocol. The peak Ca_V current at each V_m tested was plotted *versus* the V_m. The resulting IV-relationship was characterised by a maximum at 10 mV. In the presence of MONNA (10 µM) the current was reduced by ~3.7 fold at +10 mV.

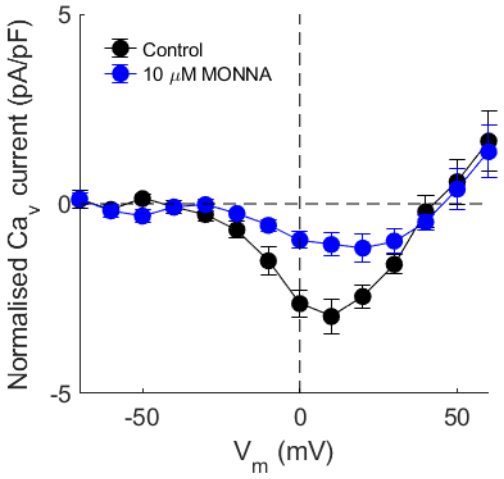


Figure 3.22 Effect of MONNA on Ca_V currents from isolated VSMCs.

Mean whole-cell current measured from -70 mV to 60 mV in 10 mV increments, in the absence (black, control) N=5, or presence of MONNA (blue, 10 µM) N=5.

Whole-cell patch-clamp electrophysiology of VSMCs was conducted using Ca_V solutions, and the Ca_V voltage protocol, in order to record VSMC Ca_V currents in the absence and presence of Ani9. The peak Ca_V current at each V_m tested was plotted *versus* the V_m. The resulting IV-relationship was characterised by a maximum at 10 mV. There was no significant reduction in current at any potential tested in the presence of Ani9 (1 µM).

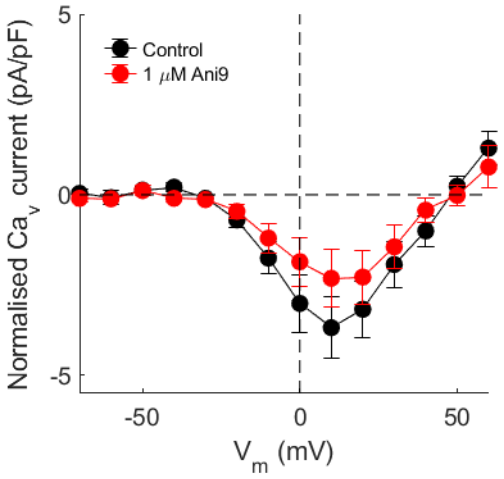


Figure 3.23 Effect of Ani9 on Ca_V currents from isolated VSMCs.

Mean whole-cell current measured from -70 mV to 60 mV in 10 mV increments, in the absence (black, control) N=5, or presence of Ani9 (red) N=5.

3.11 Discussion

In this chapter the key electrophysiological properties of cloned TMEM16A in a heterologous expression system was assessed. In addition, the effects of a range of CaCC blockers were tested on isolated aortic rings during isometric tension recordings. CaCC currents in aortic VSMCs are thought to be primarily mediated by TMEM16A, with low levels of TMEM16B in the aorta (Schreiber et al., 2010). A systematic analysis of potency and selectivity of a range of current Cl^- channel blockers was performed. MONNA, a commonly used TMEM16A blocker, was found to interact with a range of other vascular channels. The lack of selectivity of this compound has implications for the interpretation of published results involving this modulator.

3.11.1 Cloned TMEM16A channels

This chapter included a study of some of the electrophysiological properties of cloned members of the TMEM16x family: TMEM16A, TMEM16B and TMEM16F. This comparative analysis formed the basis for the pharmacological analysis presented in the chapter.

Transfection of TMEM16A and TMEM16B in HEK-293T cells produced outwardly rectifying currents that were both voltage and Ca^{2+}-dependent, closely resembling those recorded for classical CaCCs (Hartzell, Putzier & Arreola, 2005). The large outwardly rectifying TMEM16A and TMEM16B currents were characterised by an instantaneous current following by a time-dependant current component. The instantaneous current is thought to correspond to channels that are open at the holding potential of 0 mV (Manoury, Tamuleviciute & Tammaro, 2010), while the time-dependent component represents channels which are activated in response to depolarising voltage steps. Stepping to -70 mV produced inward tail currents, characteristic of CaCC and represent deactivation of the channels.

3.11.2 Action of inhibitors on TMEM16A and towards identification of binding modality

To date only a few TMEM16A inhibitors have been described and those reported have a low potency and selectivity for TMEM16A. This has hindered a detailed study of the physiological study of the channel.

Oh et al., (2013) used a well-established fluorescence based assay (Galietta, Jayaraman & Verkman, 2001; Oh, Park, Han, Lee, Roh & Lee, 2008) to identify potent inhibitors of TMEM16A, and following an SAR study of identified compounds they reported a new

class of TMEM16A blockers with the most potent blocker being MONNA with a IC_{50} of 0.08 µM. In this study, it was found that other chloride channels such as bestrophin-1, chloride channel protein-2, and cystic fibrosis transmembrane conductance regulator were not appreciably blocked by 10-30 mM MONNA. However in 2015 the selectivity of MONNA was disputed and found that MONNA relaxes rat and mouse mesenteric arteries in the presence and absence of Cl^- therefore raising the question of the selectivity and also questioning the research done using MONNA to dissect TMEM16A contribution in various systems reported in the literature (Boedtkjer, Kim, Jensen, Matchkov & Andersson, 2015).

A novel potent TMEM16A inhibitor, Ani9 has been recently identified with high selectivity for TMEM16A over TMEM16B and was shown not too affect intracellular Ca^{2+} signalling and CFTR channel activity (Seo et al., 2016).

From my study of the dose dependent inhibition of Ani9 and MONNA I found that both compounds inhibited the heterologously expressed TMEM16A channels entirely with an EC_{50} of 0.05 and 0.47 µM, respectively. The effect of the inhibitor appeared not to be influenced by V_m.

By varying the concentration of extracellular chloride, we can alter the chloride flux through the pore and therefore identify whether the inhibitor is binding is the pore. When reducing the extracellular chloride concentration from 154 mM to 34 mM there was no significance difference observed in the inhibition by 0.1 µM Ani9, suggesting that this blocker does not compete with the permeating ion and thus presumably it does not bind within the pore of the channel. However, as the inhibition observed by 1.5 µM was significantly increased from 31 % to 68 % block it suggests that MONNA and Cl^- must

enter the same pore. This data suggests that Ani9 and MONNA inhibit TMEM16A by different mechanisms.

3.11.3 Action of activators on TMEM16A

One of the first TMEM16A activators to be reported is E_{act} which strongly increase native CaCC current even under conditions of low free $[Ca^{2+}]_i$ (Namkung, Yao, Finkbeiner & Verkman, 2011b). A second class of compounds were identified alongside E_{act}, which did not activate TMEM16A in the absence of intracellular Ca^{2+} however did reduce the EC_{50} for Ca^{2+} dependant TMEM16A activation, F_{act} was the most potent compound identified (Namkung, Yao, Finkbeiner & Verkman, 2011b). Interestingly, analogues of E_{act} and F_{act} were identified that fully inhibited TMEM16A current, which they state provides further evidence for direct TMEM16A binding (Namkung, Yao, Finkbeiner & Verkman, 2011a).

The reported activator E_{act} did not activate cloned TMEM16A channels in our hands. However, the original E_{act} study utilised a specific cell line FRT (Fischer rat thyroid) which is obtained from airway epithelial cells (Namkung, Yao, Finkbeiner & Verkman, 2011a). This cell line expresses endogenous CaCCs which may be composed of TMEM16A and potentially other not yet identified auxiliary subunits. It cannot be excluded that E_{act} was acting on a target other than TMEM16A in these cells. The lack of TMEM16A specific activators highlights the need of development in this area.

This is in line with results found in the literature where E_{act} was demonstrated to activate both TRPV1, and therefore elicits pain and itch behaviour as well as increasing intracellular Ca^{2+} (Liu, Feng, Luo, Yang, Brett & Hu, 2016). E_{act} has also been shown to activate TRPV4 and therefore increase intracellular Ca^{2+} which subsequently activated

TMEM16A downstream. Demonstrating that E_{act} does not directly act on TMEM16A in cells not expressing TRPV4. This research is in accordance with the results we gathered as HEK-293T cells do not express TRPV1 or TRPV4 (Genovese et al., 2019).

3.11.4 Action of biphasic modulators on TMEM16A and elucidation of mechanism of action

A9C has previously been shown to have a complex bimodal effect on TMEM16A (Ta, Adomaviciene, Rorsman, Garnett & Tammaro, 2016). Here we can replicate this effect and see that A9C activates TMEM16A tail currents at negative potentials and blocks the steady state current at positive potentials.

We also studied the action of NFA, another commonly used chloride channel blocker, on cloned TMEM16A current and found to have a biphasic effect on the current similar to the effect of A9C. The biphasic effect of A9C was also observed in native currents in isolated PASMCs (Piper, Greenwood & Large, 2002) The compound, however, are poorly selective since they also activate a number of other channels including other channels e.g. CLC-K and TRPA (Hu et al., 2010; Picollo, Liantonio, Didonna, Elia, Camerino & Pusch, 2004). We found that NFA acts in a similar manner to A9C, having a biphasic effect that varies in activation and inhibition based on the concentration of NFA used.

From our non-stationary noise analysis experiments we found that NFA increases the P_o while not affecting single channel conductance, this was the same as seen for A9C, therefore suggesting that NFA activates the channel by affecting the gating of the channel.

Modulators with biphasic effects offer the chance to gain an understanding of both the mechanism of activation and inhibition of the TMEM16A channels.

3.11.5 Modulation of TMEM16x family members by potent TMEM16A inhibitors

We then tested MONNA on other members of the TMEM16x family, specifically TMEM16B and TMEM16F, to understand whether inhibitors of TMEM16A modulate other channels. Previously within the group it was found that Ani9 (1 μM) has no effect on TMEM16B (Acheson, 2019). This is in agreement with published literature where Ani9 is selective for TMEM16A over TMEM16B (Seo et al., 2016). Ani9 was found to activate TMEM16F Cl^- currents, however as these experiments were done in high $[Ca^{2+}]_i$ it was speculated that it would have limited physiological effect (Acheson, 2019).

Our results show that MONNA blocks TMEM16B however the extent of the inhibition is reduced compared to that of TMEM16A. MONNA was also found to block TMEM16F Cl^- currents in high $[Ca^{2+}]_i$. This is the opposite effect to Ani9. This data suggests that Ani9 is a more selective blocker of TMEM16A than MONNA therefore more promising therapeutically. However, as the expression of TMEM16B is low in VSMCs then the off-target effects may be minimal (Davis et al., 2010; Manoury, Tamuleviciute & Tammaro, 2010; Thomas-Gatewood et al., 2011).

3.11.6 TMEM16A in VSMC agonist induced contraction

Two techniques were used to define the role of TMEM16A in agonist induced VSMC contraction. The use of wire myography to study the contraction upon PE induced

stimulation of isolated aortic rings demonstrated that TMEM16A blockers, Ani9 and MONNA, reduces contraction. However, we found there as a difference in the extend of reduction of contraction between the two modulators. MONNA reduced contraction at maximum [PE] by 91 % whereas Ani9 reduced contraction by 62 %.

To confirm whether this was due to Cl^- channels are responsibility for this reduction in contraction solutions with low $[Cl^-]_{ext}$ were used. Under these conditions and on activation by appropriate [PE] aortic contraction increased by ~5 fold, however in the presence of MONNA and Ani9 this was reduced to ~1.3 and ~1.2 fold, respectively. This data supports the hypothesis that Cl^- is a crucial depolarising force in blood vessel contractility, and that MONNA and Ani9 can modulate these currents.

The Cl^- channel impermeable K-methosulphate was then used in place of KCl to provide a depolarising force to the isolated vessel (Lefevre, Lefevre, Coulombe & Coraboeuf, 1996) in a TMEM16A-independent manner. In the experiment outlined in figure 3.15, a reduction in contraction after incubation with MONNA and Ani9 was observed. This can be attributed to some TMEM16A activity remaining at the highest concentrations of K-methanesulfonate tested, due to $[Cl^-]_i$ not being depleted prior to experimentation, and the low Cl^- PSS solution containing some free Cl^-.

3.11.7 TMEM16A in isolated VSMC currents

From our myography studies we found that there was a difference in reduction in aortic contraction between Ani9 and MONNA. We therefore studied the effect of these blockers on currents in isolated smooth muscle cells to define the selectivity.

Ani9 and MONNA were found to block VSMCs CaCC current by ~2 fold and ~1.4 fold respectively at +95 mV. This reduction is lower than seen in cloned currents and could be due to differences in auxiliary units in native CaCCs that are not present in the cloned channels and reducing the effect of Ani9 and MONNA.

Ani9 was not seen to affect isolated cationic currents in SMCs. Whereas MONNA was found to increase global cationic currents by ~4.7 fold at +95 mV and block Ca_V currents by ~3.7 fold at +10 mV. This suggests that Ani9 is selective for TMEM16A in SMCs however MONNA is acting on other channels, specifically BK_{Ca} and Ca_V currents.

This modulation of other channels in the VSMCs explains the change in reduction in aortic contraction of the two blockers. Inhibition of Ca_V currents would prevent the influx of Ca^{2+} into the cell and therefore prevent the stimulation of contraction. Activation of BK_{Ca} channels would tend to hyperpolarize VSMCs, which in turn will deactivate Ca_V channels and further preventing the influx of Ca^{2+} into the cells (Dopico, Bukiya & Jaggar, 2018; Jackson, 2017). The combination of these effects explain why MONNA reduces the contraction of vessels to a greater extent compared to Ani9.

However, when K-MES was used in place of PE to constrict aortic rings there was no significant difference seen between the contraction on pre-incubation with Ani9 or MONNA. If MONNA is activating K^+ channels, as we have seen in the patch-clamp experiments using isolated VSMCs, the increase in K^+ current would lead to hyperpolarisation. This hyperpolarisation would then inactivate Ca_V channels and therefore a smaller increase in $[Ca^{2+}]_i$ leading to a reduction in contraction. However, this not seen when comparing to pre-incubation with Ani9. BK_{Ca} are not the only K^+ channels expressed in the aorta and we have shown MONNA has no effect on K_{ATP}.

Therefore, the activation of BK_{Ca} channels and subsequence hyperpolarisation could not be enough to inactive the Ca_V in the whole tissue and therefore no significant difference between the effect of Ani9 and MONNA.

3.12 Physiological significance

While the pharmacology of TMEM16A is still in its infancy these results provide a further in-depth study of the current inhibitors. These demonstrate Ani9 is a potent and selective blocker of TMEM16A. We have also demonstrated that MONNA is not a selective inhibitor of TMEM16A and acts on other channels found within VSMCs. This is useful information when designing new modulators but also in analysis and interpretation of studies using MONNA to modulate TMEM16A in other tissue level studies. From this knowledge we can look forward to designing new TMEM16A modulators using data collected from this chapter, that can be used for therapeutic benefit.

Chapter 4

Molecular basis of modulation of the TMEM16A channel by A9C and NFA: Insights into channel gating

4 Chapter 4: Molecular basis of modulation of the TMEM16A channel by A9C and NFA: Insights into channel gating

In this chapter we set out to gain mechanistic insights into the action of two biphasic modulators, anthracene-9-carboxylic acid (A9C) and niflumic acid (NFA), of TMEM16A. As outlined in the Introduction, the pharmacology of the TMEM16A channel is still at its infancy. It was argued that defining the mode of action of A9C and NFA, which display both inhibition and activation of the channel, could shed light on the general mechanism of inhibition and allosteric activation of the channel. This could have far reaching implications in understanding the mechanism of action of modulator and therefore forward into drug design.

Specifically, A9C inhibits the channel by acting as a pore blocker, and also allosterically activates the channel by enhancing the channel sensitivity to Ca^{2+} and membrane potential (V_m) (Ta, Adomaviciene, Rorsman, Garnett & Tammaro, 2016). These effects require binding of A9C to site(s) within the pore of the TMEM16A channel (Ta, Adomaviciene, Rorsman, Garnett & Tammaro, 2016). Endogenous ligands such as intracellular Ca^{2+} and plasmalemmal phosphatidylinositol 4,5-bisphospate (PIP_2) are also modifiers of TMEM16A gating (Le, Jia, Chen & Yang, 2019; Ta, Acheson, Rorsman, Jongkind & Tammaro, 2017). Thus, to shed light on the mechanisms of ligand (endogenous or synthetic) modulation on the TMEM16A channel activity, knowledge of the fundamental mechanisms of channel gating and the structural domains involved is required.

The TMEM16A channel is a homodimer encompassing two pores that function independently one another (Jeng, Aggarwal, Yu & Chen, 2016; Lim, Lam & Dutzler,

2016). Each monomer contains two Ca^{2+} binding sites that couple ion binding to channel opening (Dang et al., 2017; Paulino, Kalienkova, Lam, Neldner & Dutzler, 2017). Each pore possesses a steric gate constituted by a portion of the sixth transmembrane helix (TM6). A hinge point formed by glycine at position 640 (G640) enables a conformational change of this intracellular-facing gate in response to Ca^{2+} binding (Paulino, Kalienkova, Lam, Neldner & Dutzler, 2017; Peters et al., 2018) (Fig. 4.1). Alanine substitution of neighbouring amino acids, such as isoleucine and glutamine at position 637 and 645, respectively, stabilises the TM6 in the open state and thus resulted in channels (TMEM16A-Q645A and TMEM16A-I637A) that are open in the absence of intracellular Ca^{2+} (Lam & Dutzler, 2018; Peters et al., 2018) (Fig 4.1). A second gating mechanism, the 'electrostatic gate', is constituted by the Ca^{2+} binding site which encompasses a series of negatively charged residues (Lam & Dutzler, 2018). The vacant Ca^{2+} binding site forms an electrostatic barrier to anion permeation. This electrostatic barrier is removed upon Ca^{2+} binding due to attenuation of the negative charge density of the Ca^{2+}-binding pocket (Lam & Dutzler, 2018).

The afTMEM16 protein is a fungal TMEM16A homologue from *Aspergillus fumigatus* which shares significant structural similarities with the mammalian TMEM16A. afTMEM16A works as a lipid scramblase and it undergoes a structural rearrangement of the outer portion of the pathways for phosphatidylserine scrambling in response to Ca^{2+} binding (Lee, Khelashvili, Falzone, Menon, Weinstein & Accardi, 2018). Whether an analogous gating mechanism occurs in the TMEM16A channel is unknown. Understanding whether gating rearrangements in the outer pore take place in TMEM16A is an important question in the field since gating of the outer pore might

impact on the action of small molecules acting from the extracellular side of the membrane.

Here, we set out to gain mechanistic insights into the action of A9C, a modulator of TMEM16A channel activity that acts exclusively when applied on the outer side of the membrane (Ta, Adomaviciene, Rorsman, Garnett & Tammaro, 2016). We found that constitutively open mutant channels in which the TM6 steric gate is stabilised in the open state, in the absence of intracellular Ca^{2+}, are entirely insensitive to extracellular A9C. However, when intracellular Ca^{2+} was present these mutant channels regained sensitivity to extracellular A9C revealing the unexpected finding that intracellular Ca^{2+} is mandatory for the action of an extracellular modulator. We provide evidence that Ca^{2+} allows the action of A9C on the channel by triggering a conformational change in the outer pore that enables A9C binding/efficacy. Our work may have significant implications for future drug design as it highlights the outer mouth of the channel as a site for pharmacological intervention.

A second biphasic modulator, NFA, was studied in a similar manner to A9C to determine if the two compounds have a similar mechanism of action. Preliminary studies show that NFA modulates TMEM16A via a change in gating, as indicated by noise analysis, however the effect of NFA on constitutively open mutant channels varies from that of A9C at the concentration tested.

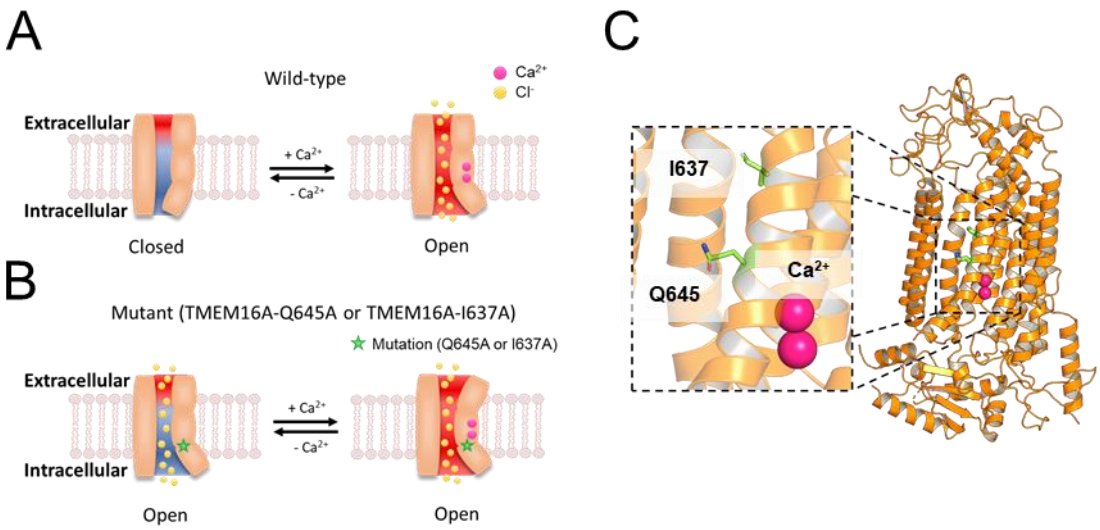


Figure 4.1 Gating mechanisms of wild-type and mutant (TMEM16A-Q645A and TMEM16A-I637A) channels.

(A) Diagrammatic representation of the TMEM16A channel pore and associated gating mechanisms. The movement of the TM6 domain during gating is represented as a tilt on one side of the channel as the result of Ca^{2+} binding. The red background depicts negative electrostatic potential and the blue background depicts positive electrostatic potential in the pore. This represents electrostatic gate/barrier, which is attenuated upon Ca^{2+} binding. (B) Diagrammatic representation of the pore of TMEM16A mutant channels (TMEM16A-Q645A and TMEM16A-I637A) associated with constitutively open TM6 gate. Mutations are indicated by the star symbol. In these mutant channels the electrostatic gate/barrier is presumably intact and can be attenuated upon Ca^{2+} binding. (C) Cryo-EM structure of TMEM16A with bound Ca^{2+} ions shown in pink.

4.1 A9C: TMEM16A modulator with biphasic effect

In Chapter 3 it was shown that A9C and NFA are compounds with a biphasic effect of TMEM16A modulation. Here I further their study of their mode of action by studying the effect of these compounds at a fixed $[Ca^{2+}]_i$ but over a variety of different membrane potentials.

Whole-cell currents were elicited in response to the 'IV-tail' protocol (as described in Chapter 2), which allows examination of the effects of A9C and NFA on current

amplitude and reversal potential. Extracellular A9C induced complex changes in the whole-cell wild-type TMEM16A current (Ta, Adomaviciene, Rorsman, Garnett & Tammaro, 2016). The current measured at the beginning of the tail pulse was significantly potentiated in the presence of 300 µM A9C (by ~7 fold at -100 mV) (Fig. 4.1). In contrast, the current measured at the end of the tail pulse, where the amplitude reached a steady state, was inhibited at positive V_m (by ~0.7 fold at +140 mV) (Fig. 4.2). A9C did not profoundly affect the E_{rev} which was very close to the expected equilibrium potential for Cl^- (E_{Cl}) in our recording conditions (~1 mV) in each case.

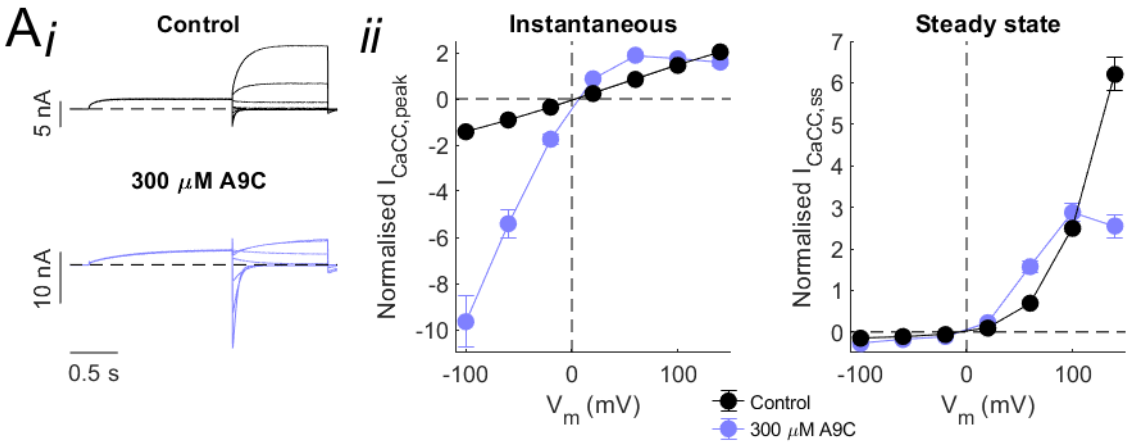


Figure 4.2 Effect of extracellular A9C and NFA on whole-cell TMEM16A current amplitudes.

(Ai) Whole-cell currents recorded from HEK-293T cells expressing TMEM16A channels in the absence (control) or presence of 300 µM $[A9C]_{ext}$. Dashed horizontal line represent the zero-current level. (ii) Left panel: Mean peak whole-cell current density *versus* V_m relationships measured in the absence and presence of 300 µM $[A9C]_{ext}$. Right panel: Mean steady-state whole-cell current density *versus* V_m relationships measured in the absence and presence of 300 µM $[A9C]_{ext}$ (n=9).

4.2 Exploration of constitutively active TMEM16A channels

As described previously the gating of TMEM16A to an open conformation is dependent on both Ca^{2+} and voltage dependant conformational changes. This is sensed by the sixth transmembrane domain (Peters et al., 2018). In order to decouple these two effects and study them in isolation, residues on this domain were screened and mutated to alanine (Peters et al., 2018). From this study mutant channels with enhanced Ca^{2+} sensitivity and therefore could be activated in a Ca^{2+} independent manner was identified.

Q645A and I637A were found to stabilise the first conformational change normally associated with Ca^{2+} binding event. Therefore, opening the channel to the first conductive state by depolarization alone.

4.2.1 Electrophysiological characterisation of constitutively active mutations

A9C acts as an open channel blocker and allosteric activator of the channel sensitivity to intracellular Ca^{2+} at a given V_m (Ta, Adomaviciene, Rorsman, Garnett & Tammaro, 2016). We generated mutant channels that show activity in the absence of intracellular Ca^{2+}, termed TMEM16A-Q645A and TMEM16A-I637A. These point-mutations bias the steric gate (TM6) of the channel towards the open conformation (Lam & Dutzler, 2018; Peters et al., 2018). Thus, these mutant channels enable the study of the inhibitory effect of A9C in the absence of the allosteric activation of Ca^{2+} sensitivity.

We begun by peforming a comparative analysis of the main biophysical propertes of wild-type and mutant channels heterologously expressed in HEK-293T cells. During inside-out patch-clamp recordings at a constant positive V_m (+70 mV), wild-type TMEM16A channels were inactive in nominally Ca^{2+}-free intracellular solution and the current progressively increased as the intracellular Ca^{2+} concentration ($[Ca^{2+}]_i$) was

raised up to ~80 µM (Fig. 4.3). The relationship between $[Ca^{2+}]_i$ and the TMEM16A current at +70 mV was fitted with equation 9 with EC_{50} of 0.7 µM and Hill coefficient (h) of 2.8 (Fig. 4.3, Table 4.1). In contrast, both TMEM16A-Q645A and TMEM16A-I637A channels mediated a significant basal current in nominally 0 $[Ca^{2+}]_i$ (Fig. 4.3). When the patch was exposed to $[Ca^{2+}]_i$ ranging from ~0.05 to ~80 µM, an additional current increase was observed (Fig. 4.3). The fit of the $[Ca^{2+}]_i$-response curves for TMEM16A-Q645A and TMEM16A-I637A with equation 9 gave EC_{50} of 0.17 µM and 0.16 µM and h of 3.8 and 2.9, respectively (Table 4.1). We argued that Ca^{2+} activation of TMEM16A-Q645A and TMEM16A-I637A channels may be due to either (i) disinhibition of the electrostatic gate and/or (ii) Ca^{2+}-dependent activation of additional gating structures.

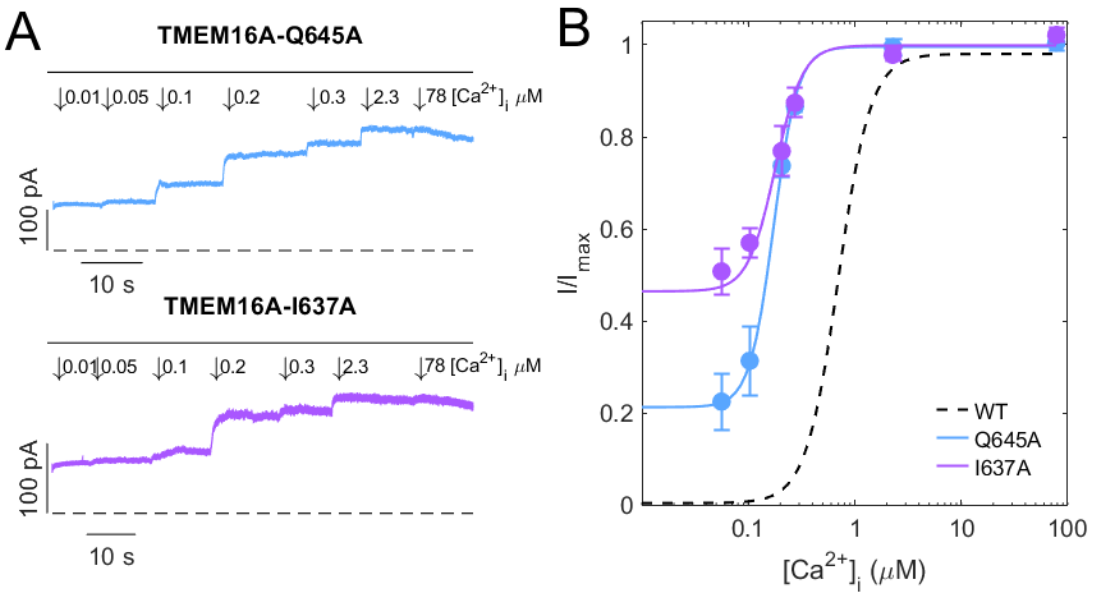


Figure 4.3 Ca^{2+} sensitivity of TMEM16A-Q645A and TMEM16A-I637A channels.

(A) Currents recorded from inside-out patches excised from HEK-293T cells expressing TMEM16A-Q645A or TMEM16A-I637A in response to various $[Ca^{2+}]_i$ (µM), as indicated. The voltage was maintained at +70 mV for the whole duration of the recordings. Dashed line represents the zero-current level. (B) Mean relationships between $[Ca^{2+}]_i$ and the current measured at +70 mV and

normalised to the current measured in the two highest $[Ca^{2+}]_i$ concentrations for TMEM16A-Q645A (n=9) and TMEM16A-I637A (n=5). The smooth curves are best fits of data using equation 9.

Table 4.1 Ca^{2+} sensitivity of TMEM16A-Q645A and TMEM16A-I637A channels.

	EC_{50} (μM)	**h**	**Base**	**n**
TMEM16A	0.70 ± 0.04	2.8 ± 0.07	0.00 ± 0.00	10
TMEM16A-Q645A	0.17 ± 0.01*	3.8 ± 0.5*	0.21 ± 0.06*	9
TMEM16A-I637A	0.18 ± 0.03*	3.3 ± 0.8	0.46 ± 0.05*	5

* indicates statistically significant difference from TMEM16A. ($P < 0.05$ one-way ANVOA followed by pairwise comparison with Bonferroni).

The recordings performed above were conducted at constant V_m. To examine whether TMEM16A-Q645A and TMEM16A-I637A mutations cause an alteration in the response of the channel to V_m, whole-cell currents were recorded in response to the IV-CaCC protocol in cells transfected with either TMEM16A-Q645A or TMEM16A-I637A.

Consistent with the measurement in inside-out patches described above significant TMEM16A-Q645A and TMEM16A-I637A currents were recorded in 0 $[Ca^{2+}]_i$. These currents were activated instantaneously and virtually no time-dependent activation was observed. Thus, the instantaneous current measured at the start of the pulse and the steady state current measured at the end of the pulse essentially coincided. The $\tau_{0.5}$ was difficult to quantify since the small time dependent current activation occurred in less than ~10 ms (Fig. 4.3).

The instantaneous current was still outwardly rectifying while in wild type the IV relationship is linear. This is due to the need for Ca^{2+} binding for the channel to enter the second conductive state, so explaining the lack of slow activating currents and non-ohmic behaviour (Peters et al., 2018).

When $[Ca^{2+}]_i$ was buffered to 0.1 µM to achieve a level of activation comparable to that seen for wild-type TMEM16A channels in 0.3 µM $[Ca^{2+}]_i$, the whole-cell TMEM16A-Q645A and TMEM16A-I637A currents in response to depolarising V_m pulses, reacquired a slow time depended activation similar to that observed for wild-type channels. The instantaneous current *versus* V_m reataionship was near linear while the steady state current *versus* V_m relationship was outwardly rectifying (Fig. 4.3).

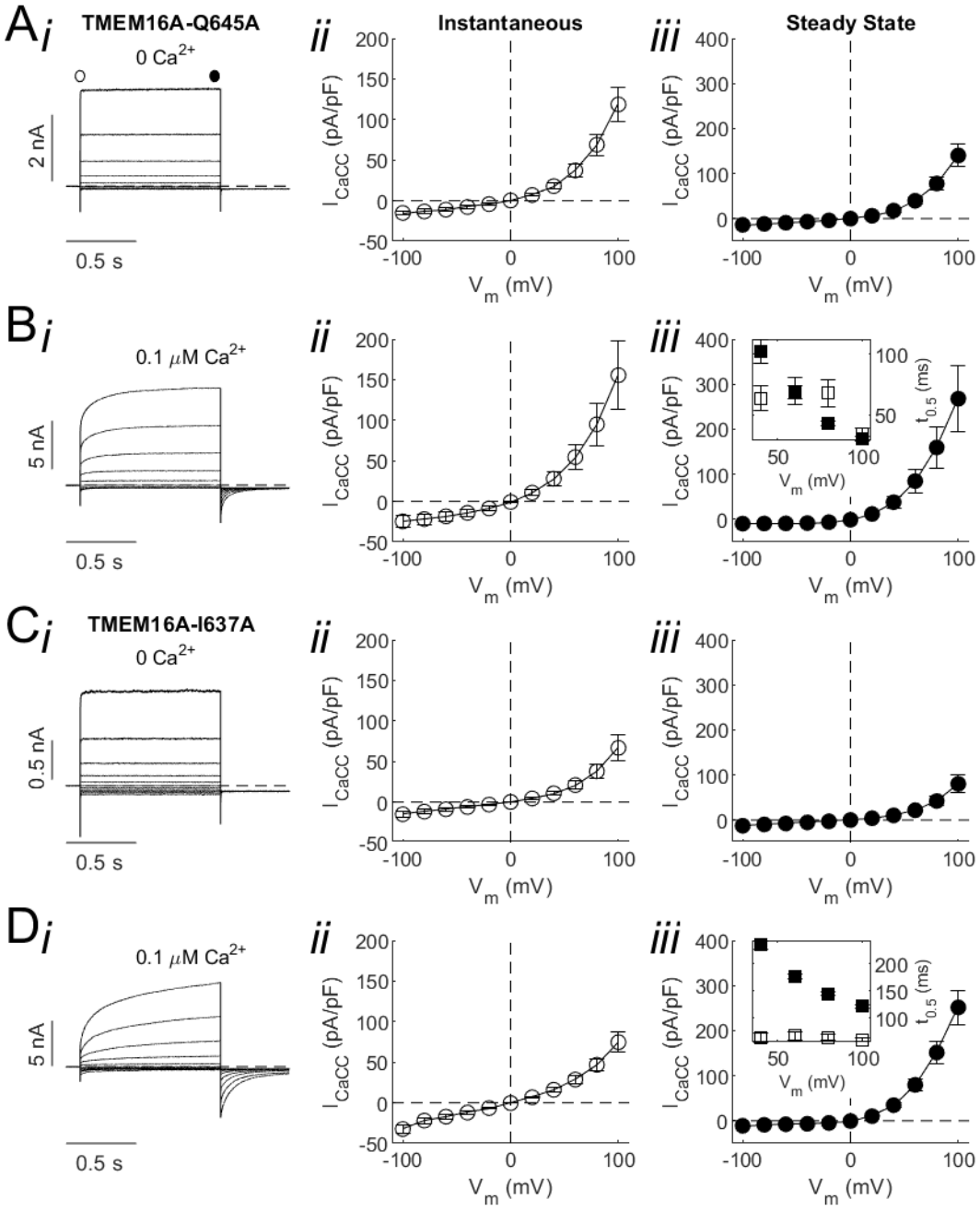


Figure 4.4 Characterisation of IV-relationship of TMEM16A-Q645A and TMEM16A-I637A in the presence or absence of intracellular Ca^{2+}.

(Ai) Whole-cell currents recorded from HEK-293T cells expressing TMEM16A-Q645A channels in the absence of intracellular Ca^{2+}. Dashed line represents zero current. (ii) Mean whole-cell current density *versus* V_m relationship measured at the beginning (Instantaneous) of 1 s V_m pulses from -100 to +100 mV in 20 mV increments. (iii) Mean whole-cell current density *versus* V_m relationship measured at the end (steady state) of the pulses (n=21). (B) Experiments carried out as in (A) with cells expressing TMEM16A-Q645A in the presence of 0.1 µM

$[Ca^{2+}]_i$ (n=14). (C) Experiments carried out as in (A) with cells expressing TMEM16A-I637A in the absence of intracellular Ca^{2+} (n=17). (D) Experiments carried out as in (A) with cells expressing TMEM16A-I637A in the presence of ~0.1 µM $[Ca^{2+}]_i$ (n=16).

4.2.2 A9C effect on constitutively active channels in 0 and ~0.1 µM $[Ca^{2+}]_i$

The effect of extracellular A9C on TMEM16A-Q645A and TMEM16A-I637A channels was next studied. Whole-cell currents were elicited in response to the IV-tail protocol which allows examination of the effects of A9C on current amplitude and reversal potential. Extracellular A9C induced complex changes in the whole-cell wild-type TMEM16A current as described in section 4.1 and consistent with previous work within the Tammaro lab (Ta, Adomaviciene, Rorsman, Garnett & Tammaro, 2016).

To our surprise, the TMEM16A-Q645A and TMEM16A-I637A currents recorded in 0 $[Ca^{2+}]_i$ were entirely insensitive to extracellular A9C at all V_m tested. This indicated that the mutations which favour opening of the intracellular (TM6) gate, have profound influence on the action of extracellularly applied A9C. We also examined the effect of A9C on the mutant channels in the presence of ~0.1 µM $[Ca^{2+}]_i$. Strikingly, the intracellular Ca^{2+} re-conferred these channels the ability to respond to A9C in a manner quantitatively similar to that observed for the wild-type channels. For example, the TMEM16A-Q645A and TMEM16A-I637A currents were activated by ~5 and ~3 fold at -100 mV and inhibited by ~0.5 and ~0.2 fold at +140 mV, respectively.

For both wild-type and mutant (TMEM16A-Q645A, TMEM16A-I637A) channels, A9C did not profoundly affect the E_{rev} which was very close to the expected equilibrium potential for Cl^- (E_{Cl}) in our recording conditions (~1 mV) in each case. Collectively, this set of

experiments demonstrated that intracellular Ca^{2+} is a key regulator of the response of the TMEM16A channel to A9C, an extracellular synthetic small molecule (Fig. 4.5).

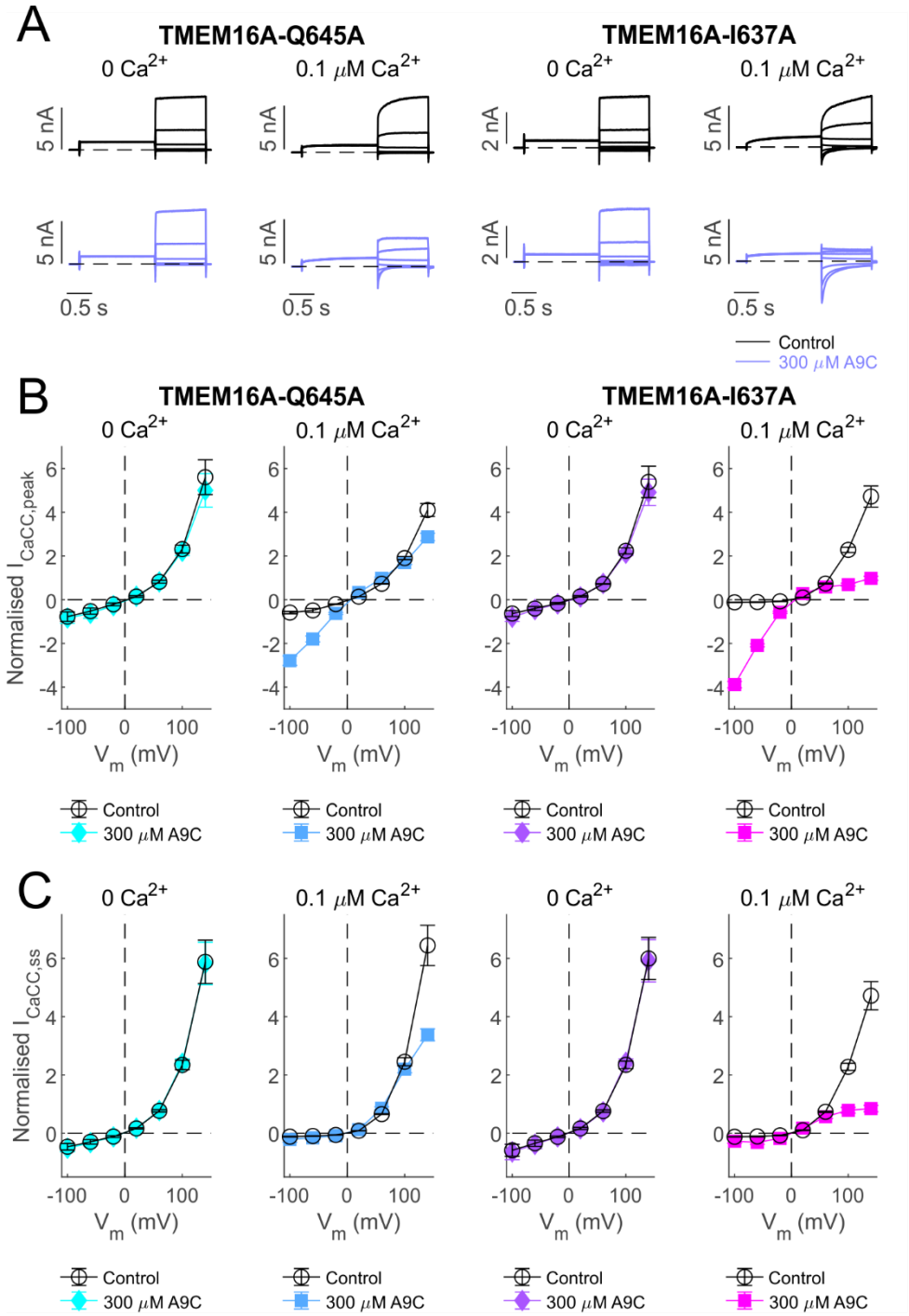


Figure 4.5 Effect of extracellular A9C on whole-cell TMEM16A, TMEM16A-Q645A, and TMEM16A-I637A current amplitudes in the absence or presence of Ca^{2+}.

(A) Whole-cell currents recorded from HEK-293T cells expressing TMEM16A, TMEM16A-Q645A or TMEM16A-I637A channels in the absence (control) or presence of 300 µM $[A9C]_{ext}$ and the indicated $[Ca^{2+}]_i$. Dashed horizontal lines represent the zero-current level. (B) Mean peak whole-cell current density *versus* V_m relationships measured in the presence of 300 µM $[A9C]_{ext}$ and various

$[Ca^{2+}]_i$, as indicated. (C) Mean steady state whole-cell current density *versus* V_m relationships measured in the presence of 300 µM $[A9C]_{ext}$ and various $[Ca^{2+}]_i$, as indicated. The number of experiments was 5 in each case.

To ensure that the lack of sensitivity of the mutant channels is not due to a shift in the dose response to A9C we then assessed the effect of various $[A9C]_{ext}$ (0.1-1 mM) in the absence and presence of intracellular Ca^{2+}. Currents were elicited by a step to +70 mV for 1.5 s followed by a depolarising step to -100 mV for 1 s from a holding potential of 0 mV. TMEM16A-Q645A and TMEM16A-I637A channels remained insensitive to A9C even at much higher concentrations in the absence of $[Ca^{2+}]_i$.

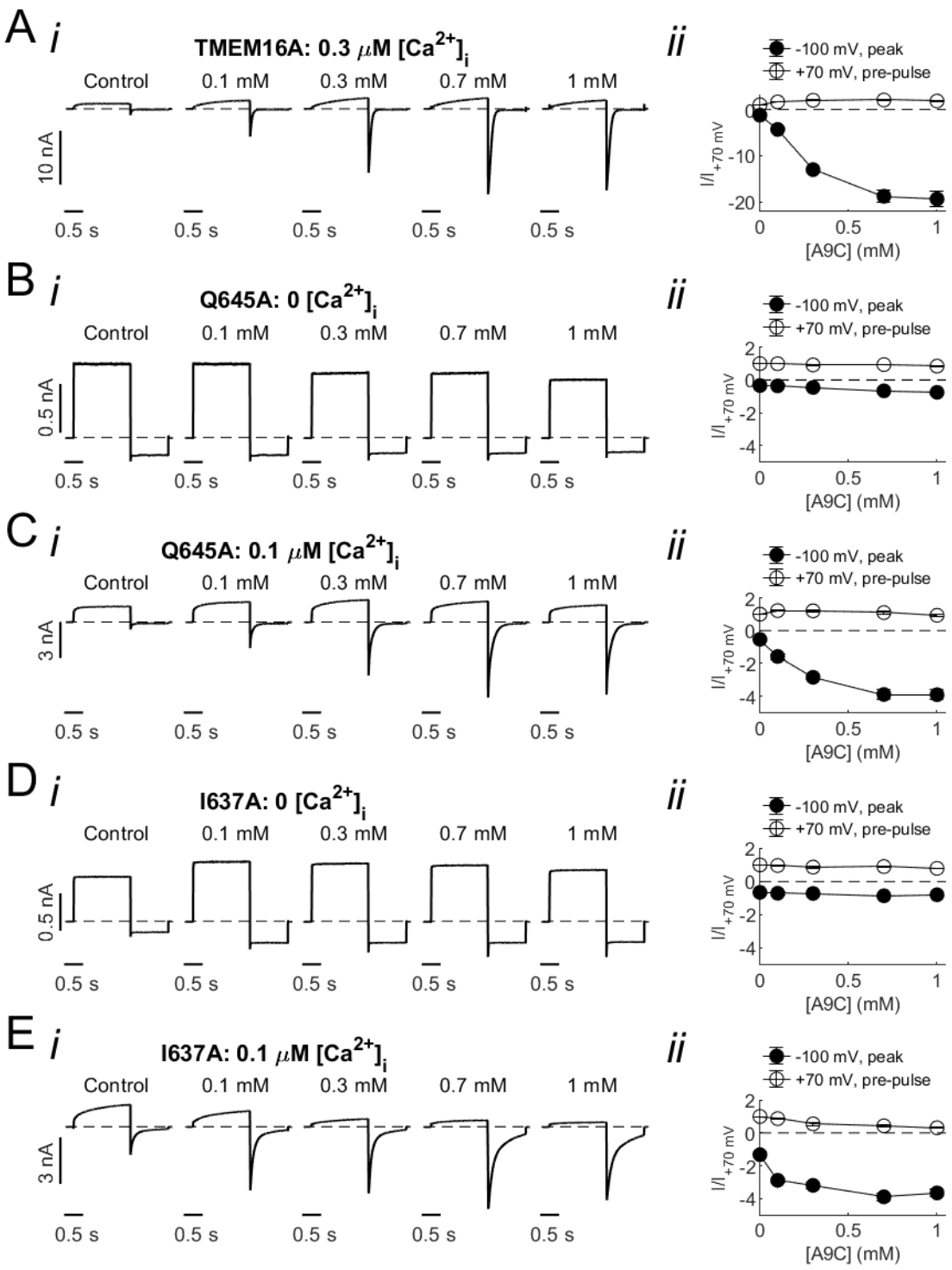


Figure 4.6 Effects of various $[A9C]_{ext}$ on whole-cell TMEM16A, TMEM16A-Q645A and TMEM16A-I637A current amplitude

(Ai) Whole-cell currents recorded from HEK-293T cells expressing TMEM16A in the absence (control) or presence of various $[A9C]_{ext}$, as indicated. $[Ca^{2+}]_i$ was 0.3 μM. Dashed horizontal line indicates the zero-current level. (ii) Mean steady state whole-cell current density measured at +70 mV (open symbols) or mean

peak whole-cell current density measured at -100 mV (filled symbols) *versus* Vm relationships at various $[A9C]_{ext}$ (n=6). (Bi, ii) As described in A, HEK-293T cells expressing TMEM16A-Q645A, $[Ca^{2+}]_i$ was 0 (n=6). (Ci, ii) As described in A, HEK-293T cells expressing TMEM16A-Q645A, $[Ca^{2+}]_i$ was 0.1 µM (n=6). (Di, ii) As described in A, HEK-293T cell expressing TMEM16A-I637A, $[Ca^{2+}]_i$ was 0 (n=7). (Ei, ii) As described in A, HEK-293T cells expressing TMEM16A-I637A, $[Ca^{2+}]_i$ was 0.1 µM (n=7).

4.3 Assessing the influence of the electrostatic gate of the effect of A9C

We argued that in the absence of Ca^{2+}, the unoccupied Ca^{2+} binding pocket, which is characterised by negatively charged residues (such as E650), might electrostatically repel the carboxylate group on the A9C molecule. To test this possibility, we mutated the glutamate at position 650 (E650) to an alanine, since substitutions of this charged residue attenuates the electrostatic gate (Lam & Dutzler, 2018). This allowed us to study the effect of A9C on the TMEM16A channel carrying the E650A in the background of the Q645A (steric gate) mutation in the TM6 (TMEM16A-Q645A-E650A mutant) (Fig. 4.7).

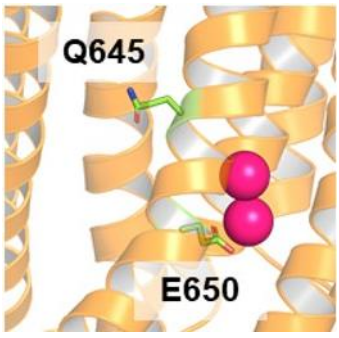


Figure 4.7 TMEM16A structure with Q654 and E650 resides highlighted.

Cryo-EM structure of TMEM16A with Q645A and E650A highlighted and bound Ca^{2+} ions shown in pink.

4.3.1 Ca^{2+} sensitivity of TMEM16A-E650A

We began by testing the Ca^{2+} sensitivity of TMEM16A-Q645A-E650A channels during inside-out recordings at +70 mV. Figure 4.8 shows that TMEM16A-Q645A-E650A is constitutively active in 0 $[Ca^{2+}]_i$. This basal current was 1.8 fold greater than that mediated by TMEM16A-Q645A consistent with the notion that E650A reduced the electrostatic gate (Lam & Dutzler, 2018). Exposure of the intracellular side of the patch to various $[Ca^{2+}]_i$, caused additional activation TMEM16A-Q645A-E650A current. The current *versus* $[Ca^{2+}]_i$ relationship was characterised by an EC_{50} of 0.37 ± 0.09 µM (n=7), which is 2.2 times greater than that for TMEM16A-Q645A channels (Table 4.2), consistent with the fact that E650A mutation reduced the extent of Ca^{2+} binding (Lam & Dutzler, 2018; Peters et al., 2018).

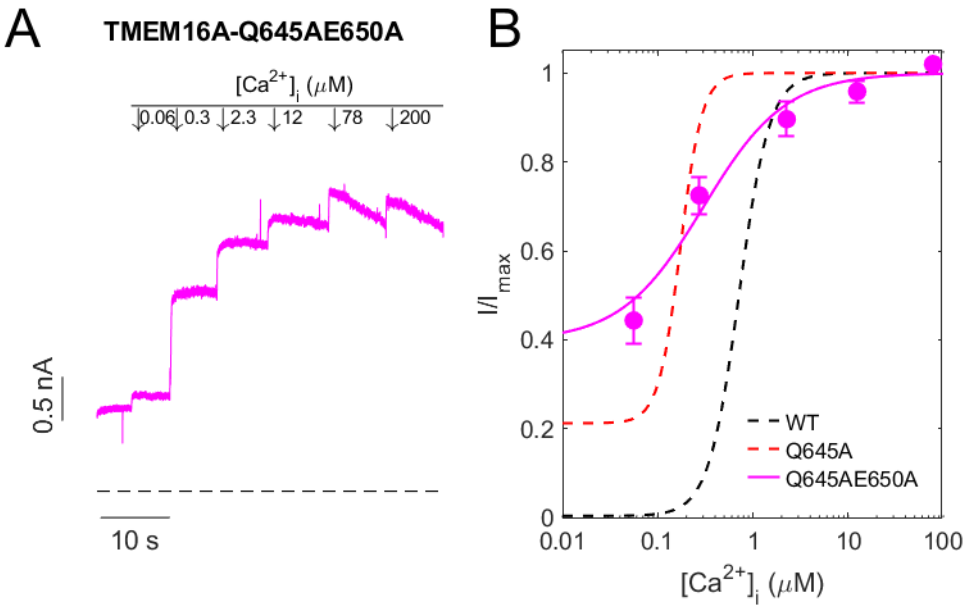


Figure 4.8 Ca^{2+} sensitivity of TMEM16A-Q645AE650A channels.

(A) Currents recorded from inside-out patches excised from HEK-293T cells expressing TMEM16A-Q645AE650A in response to various $[Ca^{2+}]_i$ (µM), as indicated. The voltage was maintained at +70 mV for the whole duration of the recordings. Dashed line represents the zero-current level. (B) Mean relationships

between $[Ca^{2+}]_i$ and the current measured at +70 mV and normalised to the current measured in the two highest $[Ca^{2+}]_i$ concentrations for TMEM16A-Q645A-E650A (n=7). The smooth curves are best fits of data using equation 9.

4.3.2 Assessing the influence of the electrostatic gate on the effect of A9C

Interestingly, whole-cell TMEM16A-Q645A-E650A currents in response to the IV-tail protocol were unaffected by application of extracellular A9C (300 µM) at any V_m tested (Fig. 4.9). Thus, the reduction of the electrostatic gate/barrier due to a charge neutralising mutation in the Ca^{2+} binding site did not confer A9C sensitivity to the channel, suggesting that the electrostatic gate is not a main determinant of A9C action.

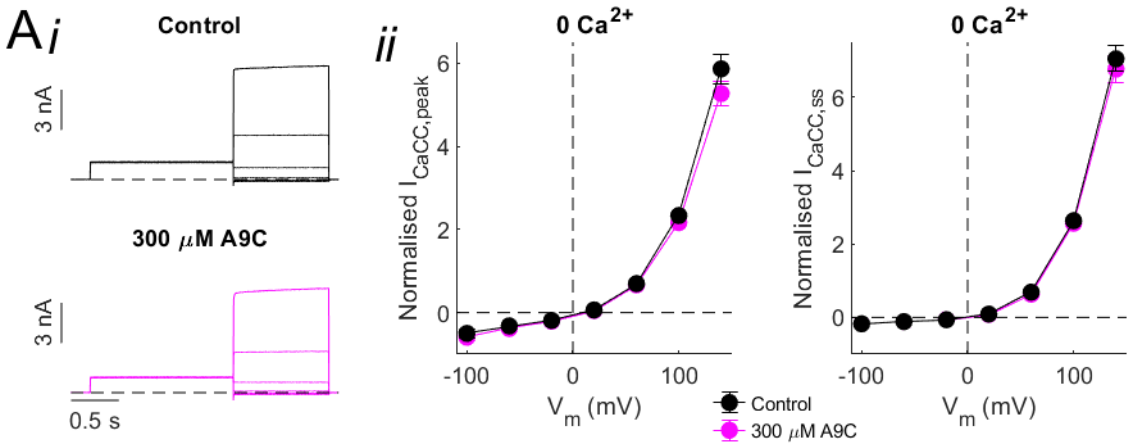


Figure 4.9 Effect of extracellular A9C on whole-cell TMEM16A-Q645A-E650A current amplitudes in the presence or absence of Ca^{2+}

(Ai) Whole-cell currents recorded from HEK-293T cells expressing TMEM16A-Q645A-E650A in the absence (control) and presence of 300 µM $[A9C]_{ext}$, measured in the absence of $[Ca^{2+}]_i$. Dashed horizontal lines represent zero current level. (ii) Left panel: Mean peak whole-cell current density *versus* V_m relationships measured in the absence and presence of 300 µM $[A9C]_{ext}$, measured in the absence of $[Ca^{2+}]_i$. Right panel: Mean steady-state whole-cell current density *versus* V_m relationships measured in the absence and presence of 300 µM $[A9C]_{ext}$, measured in the absence of $[Ca^{2+}]_i$ (n=8).

To test this proposition further, intracellular solutions supplemented with either Mg^{2+} (16 mM) or Gd^{3+} (5 mM). Mg^{2+} acts as a low efficacy ligand that binds in the Ca^{2+} site (this attenuating the electrostatic gate), but is less effective in promoting gating-associated conformational changes in TMEM16A, which would be instead triggered more effectively by Ca^{2+} (Lam & Dutzler, 2018; Ni, Kuan & Chen, 2014). The trivalent Gd^{3+} has been shown to be more efficacious than Ca^{2+} in screening the electrostatic gate (Lam & Dutzler, 2018). Whole-cell currents were measured in response to a constant V_m of +70 mV in the presence of 0 $[Ca^{2+}]_i$, 16 mM $[Mg^{2+}]_i$, 5 mM $[Gd^{3+}]_i$, or 12.5 µM while A9C (300 µM) was rapidly applied to the cell ("concentration jump"). Extracellular A9C did not affect the current amplitude mediated by TMEM16A-Q645AE650A when intracellular Mg^{2+} (16 mM) was present and there was a 23 % or 41 % degree of inhibition in the presence of Gd^{3+} (5 mM) or Ca^{2+} (12.5 µM) ($P<0.05$). Collectively these data suggest that the electrostatic gate has moderate influence on the action of A9C.

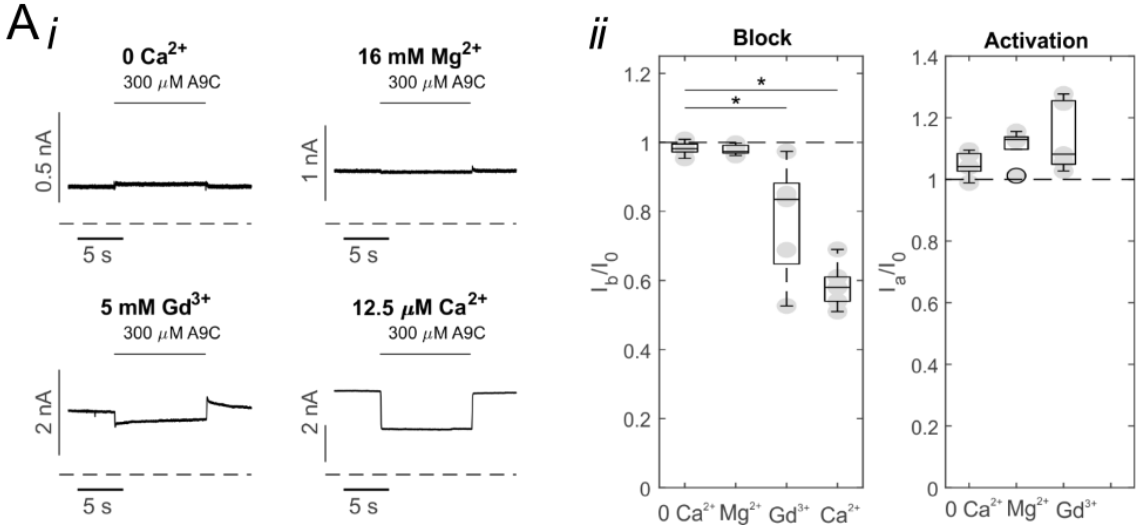


Figure 4.10 Effect of alternative cations on TMEM16A electrostatic gate

(Ai) Whole-cell currents recorded from HEK-293T cells expressing TMEM16A-Q645AE650A channels. V_m was +70 mV and various intracellular solutions, as indicated. Extracellular A9C (300 µM) was applied as indicated by the horizontal

bar via a fast-perfusion system (concentration jump). The dashed horizontal line represents the zero-current level. (ii) Mean current inhibition (I_b/I_0) and activation (I_a/I_0) plotted for each channel types, as indicated. Inhibition (I_b/I_0) and activation (I_a/I_0) plotted for each channel types, as indicated. The central mark indicates the median, with the bottom and top edges of the box indicate the 25th and 75th respectively. The number of experiments was 5 in each case.

4.4 Separation of inhibiting and activating effects of A9C and NFA on TMEM16A using a rapid perfusion system

To isolate the activating effect of A9C from the inhibitory effect, a computer controlled ultra-rapid perfusion system was used. This system allows an ultra-rapid exchange (<50 ms) of solutions (concentration jump). This is required to be able to unveil the blocking component without any activation component.

4.4.1 Effect of 300 µM A9C on TMEM16A, TMEM16A-Q645A and TMEM16A-I637A

To separate the inhibitory and activating effects of A9C on wild-type and mutant TMEM16A channels, whole-cell currents were measured in response to a constant V_m of +70 mV in the absence or presence of $[Ca^{2+}]_i$ while A9C (300 µM) was rapidly applied to the cell ("concentration jump") (Ta, Adomaviciene, Rorsman, Garnett & Tammaro, 2016).

In 0 $[Ca^{2+}]_i$, wild-type TMEM16A channels are closed and extracellular A9C did not cause any increase in current amplitude (not shown) (Ta, Adomaviciene, Rorsman, Garnett & Tammaro, 2016). In 0 $[Ca^{2+}]_i$, the currents mediated by TMEM16A-Q645A or TMEM16A-I637A channels were unaffected by extracellular A9C (300 µM). In the presence of ~0.3 µM $[Ca^{2+}]_i$, when A9C (300 µM) was rapidly applied to the bath solution during the

concentration jump, the TMEM16A current amplitude rapidly declined before increasing to a new steady-state level (Fig. 4.12). As A9C was removed, a dramatic increase in current was observed followed by a rapid return of the current to the level measured in the absence of A9C (Fig. 4.12). A similar complex response was observed when A9C was applied to cells expressing TMEM16A-Q645A or TMEM16A-I637A and in the presence of ~0.1 µM $[Ca^{2+}]_i$. The inhibitory effect of A9C was estimated by back extrapolating the current amplitude (I_b) to the point when the drug was added. The current activation (I_a) was quantified via back extrapolation of the transient spike of current observed upon drug washout (Ta, Adomaviciene, Rorsman, Garnett & Tammaro, 2016). The extent of blockage at each concentration was expressed as I_b/I_0, where I_0 is the current measured in the absence of A9C. The extent of current activation at each $[A9C]_{ext}$ was expressed as I_a/I_0 (Fig. 4.12). The mean I_b/I_0 and I_a/I_0 demonstrate that in the presence $[Ca^{2+}]_i$, wild-type and mutant channels have a similar response to A9C, while in the absence of $[Ca^{2+}]_i$ the channel were insensitive to A9C. The experiments described below aim to test the mechanism(s) by which intracellular Ca^{2+} controls the action of extracellular A9C.

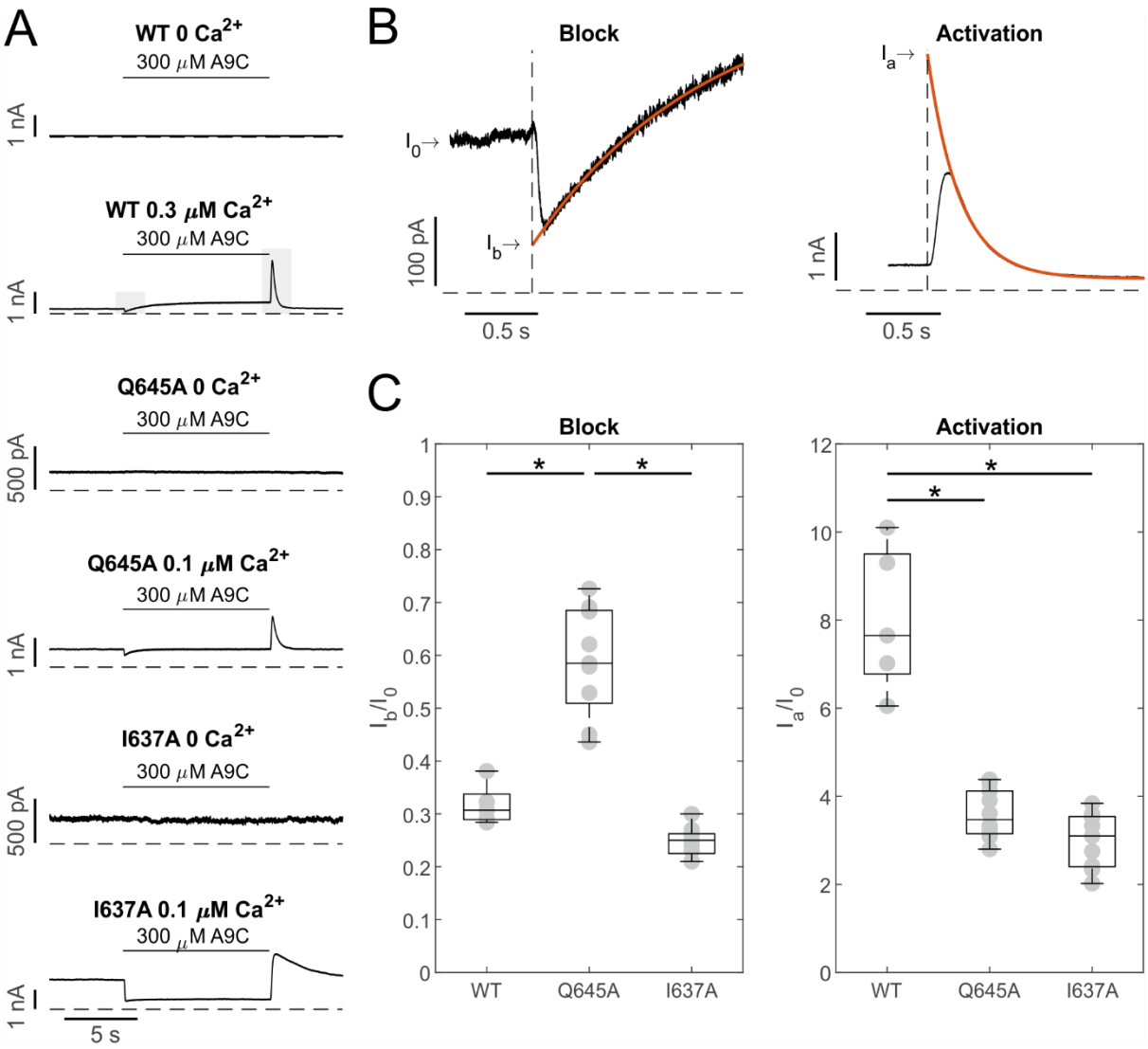


Figure 4.11 Separation of inhibiting and activating effects of A9C on TMEM16A, TMEM16A-Q645A and TMEM16A-I637A channels.

(A) Whole-cell currents recorded from HEK-293T cells expressing TMEM16A, TMEM16A-Q645A or TMEM16A-I637A channels. V_m was +70 mV and $[Ca^{2+}]_i$ was 0, ~0.1 µM or ~0.3 µM, as indicated. Extracellular A9C (300 µM) was applied as indicated by the horizontal bar via a fast-perfusion system (concentration jump). The dashed horizontal line represents the zero-current level. The shaded grey bars indicate regions of the recording that were expanded in B. (B) Expanded view of the currents highlighted by the grey bars shown in A. The continuous red traces represent single exponential fits used to back-extrapolate the currents to obtain I_b (left panel) and I_a (right panel). Dashed horizontal lines represent the zero-current level. (C) Mean current inhibition (I_b/I_0) and activation (I_a/I_0) plotted for each channel types, as indicated. Inhibition (I_b/I_0) and activation (I_a/I_0) plotted for each channel types, as indicated. The central mark indicates the median, with

the bottom and top edges of the box indicate the 25th and 75th respectively. The number of experiments was 6-10 in each case. (*P<0.05, Students t-test).

4.5 Assessing the effect of Ca^{2+} on Cl^- permeation: evidence for a structural rearrangement of the outer pore region

The above experiments indicate that the electrostatic gate unlikely interferes with the action of extracellular modulators. Here we examine whether the intracellular Ca^{2+} triggers a conformation change in the outer pore of TMEM16A which enables A9C binding.

To probe for potential Ca^{2+}-mediated rearrangements into the pore structure, we assessed the apparent affinity of Cl^- for a binding site(s) within the pore in the presence and absence of intracellular Ca^{2+} in the TMEM16A-Q645A channels. In these experiments, intracellular Cl^- was replaced with methanesulphate and strongly depolarising V_m were used to favour unidirectional inward Cl^- fluxes through the pore.

The current was measured in the presence of varying concentrations of extracellular Cl^- ($[Cl^-]_o$). This allows us to assess the relationship between current and $[Cl^-]_o$ at various V_m. The natural logarithm of the apparent $K_{0.5}$ obtained from the Hill fit of these relationships were plotted *versus* of the V_m.

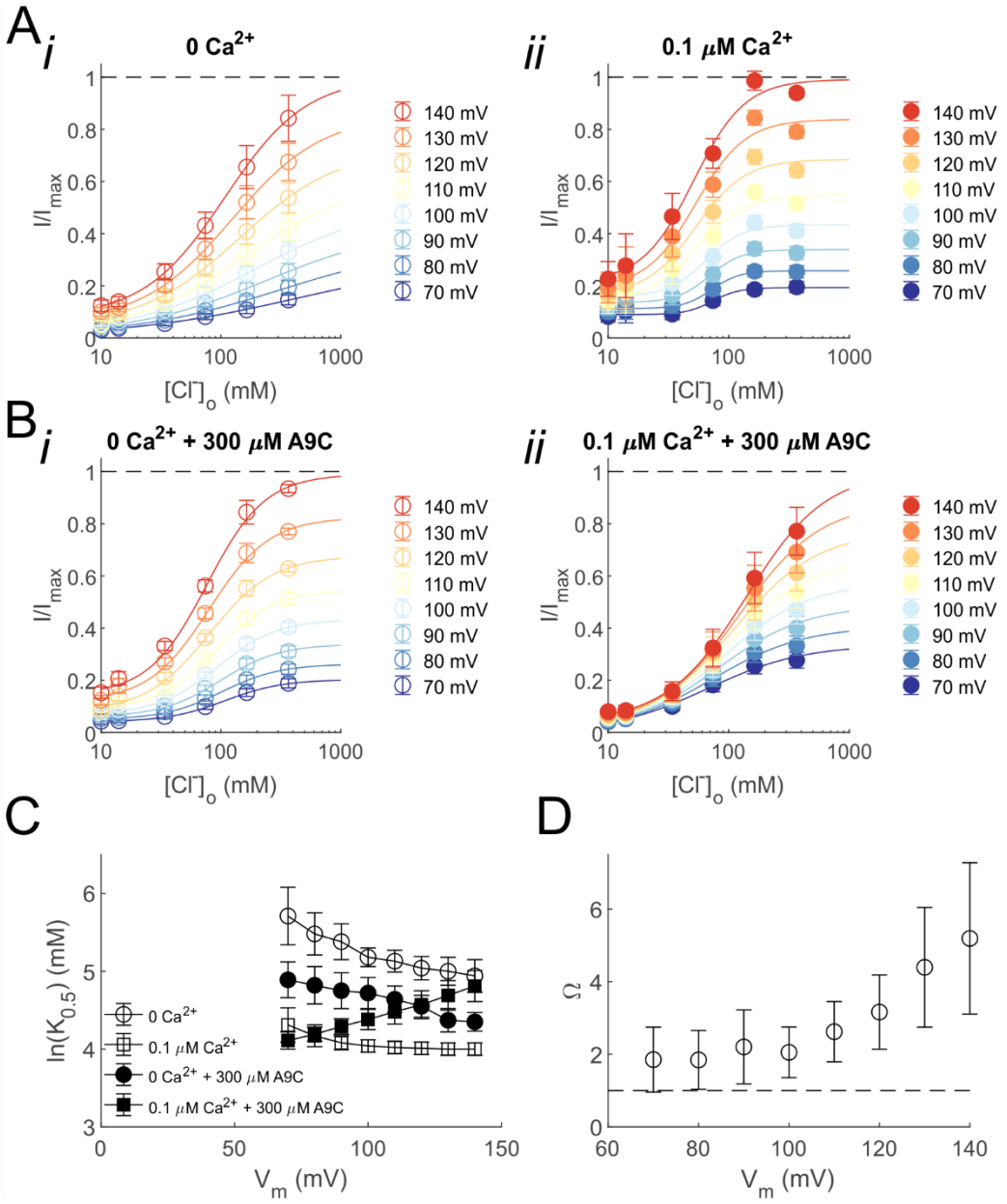


Figure 4.12 Saturation and binding of Cl^- with the TMEM16A-Q645A channel pore.

(A) Mean relationships between $[Cl^-]_o$ and the current measured at various V_m in either (i) 0 or (ii) 0.1 μM $[Ca^{2+}]_i$. The smooth curves are best fits of equation 10 to the data. The number of experiments was 7 in each case. (B) Mean relationships between $[Cl^-]_o$ and the current measured at various V_m in either (i) 0 or (ii) ~0.1 μM $[Ca^{2+}]_i$. The extracellular solution as supplemented with 300 μM A9C. The smooth curves are best fits of equation 7 to the data. The number of experiments was 8-9 in each case. (C) $\ln(K_{0.5})$ *versus* V_m relationships obtained in the absence or presence of intracellular Ca^{2+} and extracellular A9C, as

indicated. The number of experiments was 7-9 in each case. (D) Calculated Ω plotted *versus* V_m.

To investigate the functional interaction between Ca^{2+} and A9C, we calculated the $K_{0.5}$ for Cl^- binding within the pore under conditions in which intracellular Ca^{2+} and extracellular A9C were either absent or present (one at the time or simultaneously). Under our experimental conditions of unidirectional inward Cl^- fluxes, the inward Cl^- flux (J_{Cl}) (in mol/s) is related to $[Cl^-]_o$ following a rectangular hyperbola as:

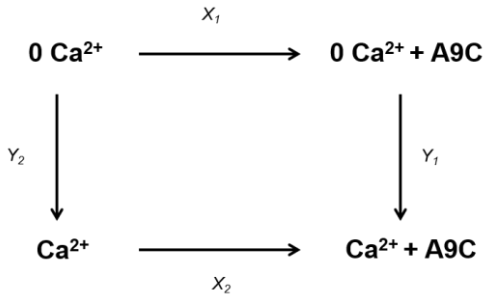
$$J_{Cl} = J_{max} \frac{[Cl]_o}{[Cl]_o + K_{0.5}} \qquad [\ 20\ ]$$

where J_{Cl} max is the maximal flux during saturating $[Cl]_o$ at a given V_m. Multiplication of J_{Cl} with the Faraday constant enables expression of equation 21 in terms of Cl^- current (I_{Cl}) as:

$$I_{Cl} = I_{max} \frac{[Cl]_o}{[Cl]_o + K_{0.5}} \qquad [\ 21\ ]$$

where I_{max} is the maximal current observed in the presence of saturating $[Cl]_o$ at a given V_m. $K_{0.5}$ is the $[Cl]_o$ at which I_{Cl} is half-maximal; thus, it provides an index of Cl^- transport within the pore.

To understanding the cross-influence of Ca^{2+} and A9C on Cl^- binding to the pore, we probed and quantified such interactions using a following thermodynamic cycle.



Each corner of the cycle refers to measurements of $K_{0.5}$ obtained in different conditions: (i) 0 $[Ca^{2+}]_i$ ('0 Ca^{2+}'); (ii) 0 $[Ca^{2+}]_i$ and 300 µM A9C ('0 Ca^{2+}+ A9C'); (iii) ~0.1 µM $[Ca^{2+}]_i$ ('Ca^{2+}') and (iv) ~0.1 µM $[Ca^{2+}]_i$ and 300 µM A9C ('Ca^{2+}+ A9C').

The letters X and Y on each arrow indicate the fold change in $K_{0.5}$ that occurs along the direction of the arrow. For instance, X_1 is equal to $K_{0.5}$(0 Ca^{2+})/ $K_{0.5}$(0 Ca^{2+}+ A9C).

The overall affinity change of going from the '0 Ca^{2+}' condition (top left corner in the diagram of the cycle) to the 'Ca^{2+}+ A9C' condition (bottom right corner) must be the same regardless of the pathway taken; that is:

$$X_1 \times Y_1 = X_2 \times Y_2 \qquad [\ 22\ ]$$

By rearranging equation 23, this leads to the definition of a coupling coefficient, Ω, as:

$$\Omega = \frac{X_1}{X_2} = \frac{Y_2}{Y_1} = \frac{K_{0.5}(0\ Ca^{2+}) \times K_{0.5}(100\ Ca^{2+} + A9C)}{K_{0.5}(100\ Ca^{2+}) \times K_{0.5}(0\ Ca^{2+} + A9C)} \qquad [\ 23\ ]$$

If the two ligands have an independent effect on Cl^- fluxes, Ω will be equal to 1 (i.e. in case A9C alters the $K_{0.5}$ for Cl^- binding by the same extent in the absence or presence of Ca^{2+} this would result in $X_1 = X_2$ and thus Ω =1). If the Ca^{2+} and A9C interact to modulate Cl^- fluxes, then Ω will differ from 1.

In energetic terms, the degree of interaction between Ca^{2+} and A9C ($\Delta\Delta G_{int}$) is given by:

$$\Delta\Delta G = -RTln(\Omega) \quad [24]$$

Our calculation shows that Ω is greater than 1 at each V_m, which correspond to a negative $\Delta\Delta G_{int}$ spanning from ~ -0.4 Kcal/M (a +70 mV) to -1 Kcal/M (at +140 mV).

Collectively, these results indicate that A9C and Ca^{2+} are strongly coupled in their effect on Cl^- transport. This is consistent with the A9C effect on the channel being secondary to a Ca^{2+}-depended gating rearrangement of the outer pore, affecting the action of A9C on the channel. This effect becomes more pronounced as the V_m is increased, possibly because membrane depolarisation favours both (i) binding of intracellular Ca^{2+} and (ii) entry of the negatively charged A9C into the pore.

4.6 Molecular dynamics simulations offer insights into the structural rearrangement of the outer pore region

We next aimed to identify a potential binding site for an A9C molecule in the pore of the TMEM16A channel. This work was done by Tanadet Pipatpolkai and Dr Phillip Stansfeld. The molecular dynamics were done in collaboration to provide confirmation of the electrophysiological experiments as outlined above.

We used molecular modelling and molecular dynamics (MD) to gain insights into the conformational rearrangements that may take place at the outer vestibule of the pore and how Ca^{2+} may induce conformational changes in this region. As there is not yet a structure of a fully open-state of TMEM16A, the structure of TMEM16K (PDB entry: 5OC9) (Bushell et al., 2019) was used to build an initial model of TMEM16A in the conductive conformation. The coordinates of the TMEM16A channel with Ca^{2+}-bound (PDB entry: 5OYB) were structurally aligned with the TMEM16K-based model for

comparison (Paulino, Kalienkova, Lam, Neldner & Dutzler, 2017). The primary difference between the two structures is the position of the TM4 helix. Therefore, coordinates of TM4 from the TMEM16K-based model within the Ca^{2+} bound TMEM16A structure were carefully modelled.

To test whether this model is conductive to solvent, the occupancy of the water molecules within the pore of the open-state model and the closed-state cryo-EM structure (PDB entry: 5OYG) in the last 100 ns of the 200 ns simulations trajectory was compared (Fig 4.16). The open-state model showed water molecules within the outer pore region. In contrast, the closed-state cryo-EM structures showed that the pore is constricted at the outer vestibule, caused by an interaction between V539 (TM4) and I636 (TM6). This prevents permeation of water molecules. Together, this validates that our open-state model is stable and provides a representation of a conductive open-state of the TMEM16A channel .

To identify the role of Ca^{2+} in stabilising the conformational change at the outer pore, the open-state model was simulated with and without bound Ca^{2+} ions. The simulations revealed that the gate remains open and solvated when Ca^{2+} ions are bound. The distance between V539 and I636 was measured to capture TM4-TM6 constriction throughout the 800 ns simulations in three independent simulations. In contrast, the outer pore collapsed in the simulations without Ca^{2+} ions, closing to a narrow ~ 2.5 Å diameter (Fig. 4.16) (n=3).

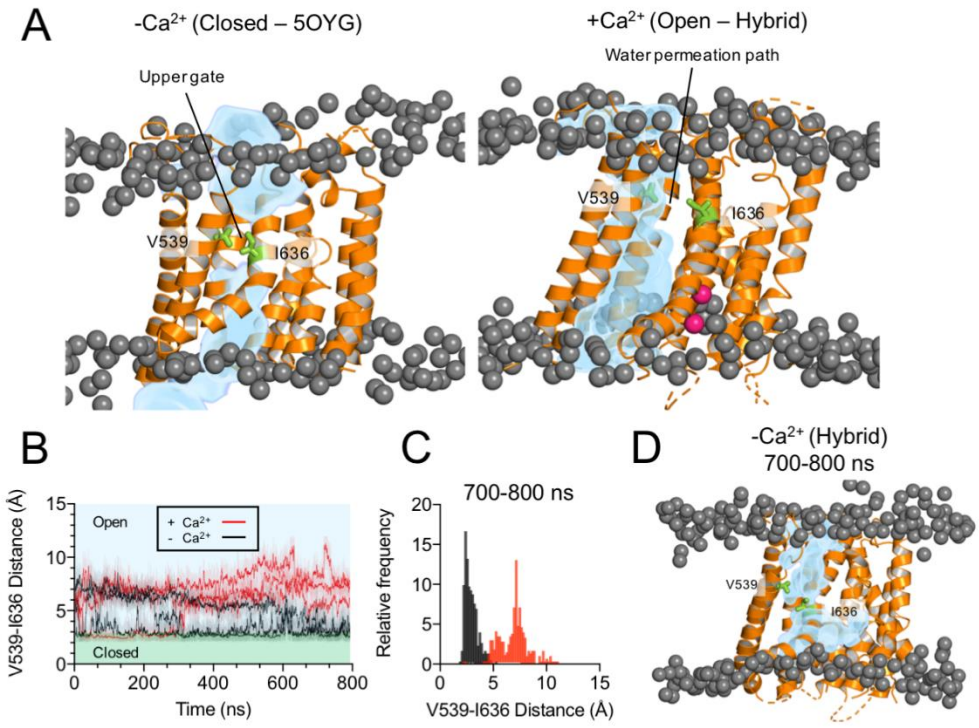


Figure 4.13 Occupancy of water molecules inside the TMEM16A pore.

Created by: Tanadet Pipatpolkai and Dr Phillip Stansfeld.

(A) A representative calculation of the average occupancy of the water molecules inside the pore of the TMEM16A channel over the last 100 ns of a 200 ns simulation. The occupancy of the water molecules is shown in blue. The phosphate headgroups are shown in dark grey sphere, the protein is represented as cartoon in orange, relative position of V539 and I636 in the channel in the modelled Ca^{2+}-bound open state and the Ca^{2+}-free closed state are shown in green (PDB entry: 5OYG). Ca^{2+} ions are shown in pink. (B) Calculated minimum distance between V539 and I636 in the Ca^{2+} bound (red) and the Ca^{2+} (black) free state across 800 ns simulations (n=3). The lighter shaded line shows the distance calculated every 10 ps and the darker line shows running averages over 1 ns. (C) A histogram showing V539-I636 distance in the last 100 ns of the simulation. Two conditions, Ca^{2+} bound (red) and the Ca^{2+} free (black) state, were sampled with the bin size of 0.17 Å and sampled every 1 ns (n=3). (D) Calculations of the average occupancy of the water molecules inside the pore of the TMEM16A channel over the last 100 ns trajectory in the simulation without Ca^{2+} using VolMap. The occupancy of the water molecules is shown in blue. The phosphate headgroups are shown in dark grey sphere, the protein is represented as cartoon in orange, relative position of V539 and I636 in the channel are shown in green.

4.6.1 Identification of the A9C binding site

The A9C molecule was docked in the outer pore of the channel in both the open and closed state. The simulations showed that an A9C molecule can move down into the pore when the channels are in the open-state but not in the close state (Fig 4.17). This was then repeated in the presence and absence of Ca^{2+} to study the effect of Ca^{2+} binding on A9C binding.

Under these conditions, the A9C molecule remained in the outer vestibule and did not move to the centre of the pore because the outer pore shuts rapidly when the Ca^{2+} is removed from the system. Within the pore, A9C reached optimal binding site in the first 100 ns and remained at this site for the entire duration of the simulation. This site was halfway down the channel, and adjacent to the Cl^- binding site. From the final 100 ns of the simulation it was identified residues that were within 4 Å of the A9C molecule for at least half of the time of the simulation. These residues include S513, V539, I636, K641, and Q645. At this site, the carboxyl group of A9C co-ordinate with K641, whilst the aromatic system interacted with hydrophobic side chains, I636 and V539 (Fig. 4.17). Overall, this suggested that a Ca^{2+}-dependent outer pore rearrangement is crucial for an A9C molecule to reach its binding site, consistent with the electrophysiology data shown above.

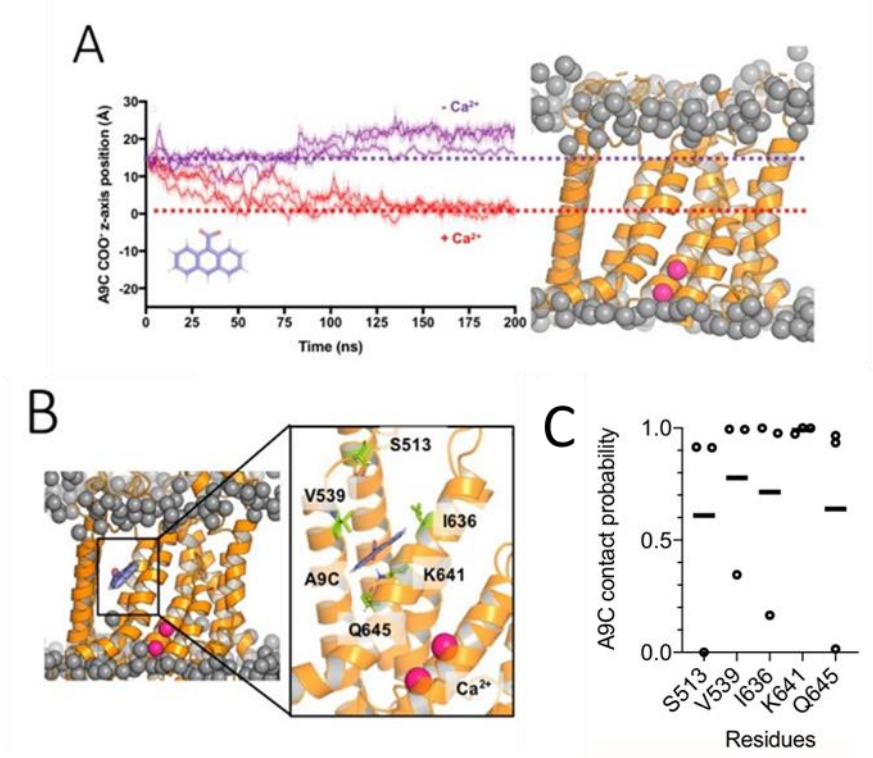


Figure 4.14 Relative position of the A9C molecule in the TMEM16A channel with the presence and absence of Ca^{2+}.

Created by: Tanadet Pipatpolkai and Dr Phillip Stansfeld.

(A) The calculated z-axis position of an A9C molecule in a POPC bilayer where the centre of the bilayer is marked as 0. The positive direction marks the movement of the A9C towards the extracellular side of the pore, and the negative marks the movement towards the cytoplasmic side. The simulations were run in the presence (red) and the absence of Ca^{2+} (purple). An initial position of both simulations is marked with the purple line. The red line shows the relative position of an A9C molecule as it moves downward in the Ca^{2+}-bound TMEM16A channel during simulations. The lighter shaded line shows the distance calculated every 10 ps and the darker line shows running averages over 1 ns (n=3). (B) A representative position of an A9C molecule (blue) after a 200 ns of simulation. The residues presenting contact probability greater than 50% are shown in green. (C) Contact probability across 3 repeats in the last 100 ns of the 200 ns simulation trajectory of residues shown in (A). All individual repeats are shown as individual data points with the mean as a black line.

To test this proposal, we mutated the residues that form the putative binding site (S513, V539, I636, K641, and Q645) one at a time into alanine. The sensitivity of these mutant channels to A9C was tested during concentration jump experiments to enable quantification of the inhibitory and activating effects of A9C during whole-cell patch-clamp in the presence of $[Ca^{2+}]_i$. shows that both the inhibitory (I_b/I_0) and activating (I_a/I_0) effects of A9C were dramatically reduced for all mutant channels. The most significant inhibition was observed in I636 (Fig. 4.18).

TMEM16A-S513A was not studied as HEK-293T cells transfected with this construct did not afford any appreciable level of current.

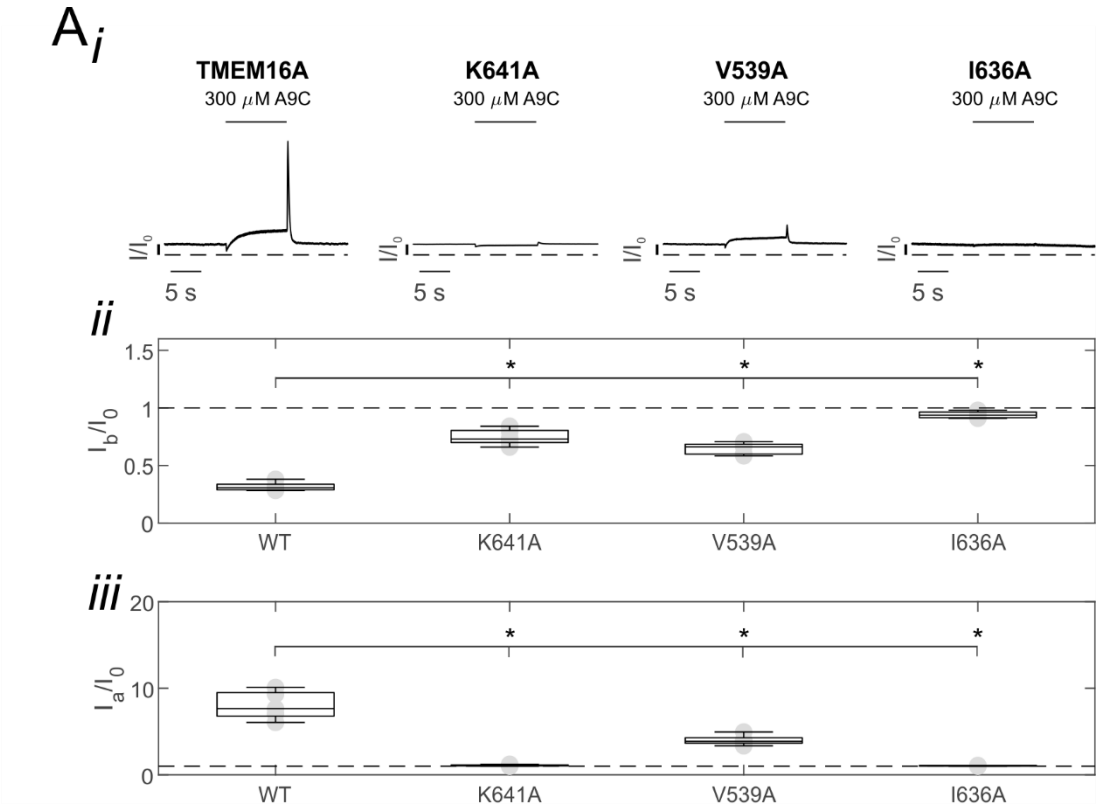


Figure 4.15 Experimental validation of the putative A9C binding site

(Ai) Whole-cell currents recorded from HEK-293T cells expressing TMEM16A, TMEM16A-K641A, TMEM16A-V539A, TMEM16A-I636A or TMEM16A-Q645A

channels, as indicated. Vm was +70 mV and $[Ca^{2+}]_i$ 0.3 µM, except for TMEM16A-Q645A, where $[Ca^{2+}]_i$ was 0.1 µM. Extracellular A9C (300 µM) was applied as indicated by the horizontal bar via a fast-perfusion system ('concentration jump'). Dashed horizontal lines indicates the zero-current level. Vertical bar represents I_0/I_0 (ii) Mean current inhibition (I_b/I_0) plotted for each channel, as indicated. The central mark indicates the median, the bottom and top edges of the box indicates the 25th and 75th percentile, and the whiskers extend to the most extreme data points not considered outliers. The number of experiments was 5-9 in each case. *P<0.05, compared to TMEM16A. (iii) Mean current activation (I_a/I_0) plotted for each channel, as indicated. The central mark indicates the median, the bottom and top edges of the box indicates the 25th and 75th percentile, and the whiskers extend to the most extreme data points not considered outliers. The number of experiments was 5-9 in each case. *P<0.05, compared to TMEM16A.

4.7 Effect of biphasic modulator, NFA, on TMEM16A current

In Chapter 3 it was shown that A9C and NFA are compounds with a biphasic effect of TMEM16A modulation. Here I further their study of their mode of action by studying the effect of these compounds at a fixed $[Ca^{2+}]_i$ but over a variety of different membrane potentials.

Whole-cell currents were elicited in response to the 'IV-tail' protocol (as described in Chapter 2), which allows examination of the effects NFA on current amplitude and reversal potential. NFA has previously been shown to have a biphasic effect on native CaCCs (Piper, Greenwood & Large, 2002) and cloned TMEM16A (Chapter 3).

In contrast to A9C, there was only a mild effect of NFA on the current amplitude, this could be due to the concentration being chosen being too close to the point at which the activation and inhibition effect balance out. The current measured at the beginning of the tail pulse was significantly potentiated in the presence of 30 µM NFA (by ~1.6 fold at -100 mV) (Fig. 4.2). In contrast, the current measured at the end of the tail pulse, where the amplitude reached a steady state, was inhibited at positive V_m (by ~0.6 fold

at +140 mV) (Fig. 4.2). However, there was a change in current kinetics on addition of 30 µM NFA. Therefore, a different protocol is used in section 4.8.2 to separate out the activation and inhibition effects.

NFA did not profoundly affect the E_{rev} which was very close to the expected equilibrium potential for Cl^- (E_{Cl}) in our recording conditions (~1 mV) in each case.

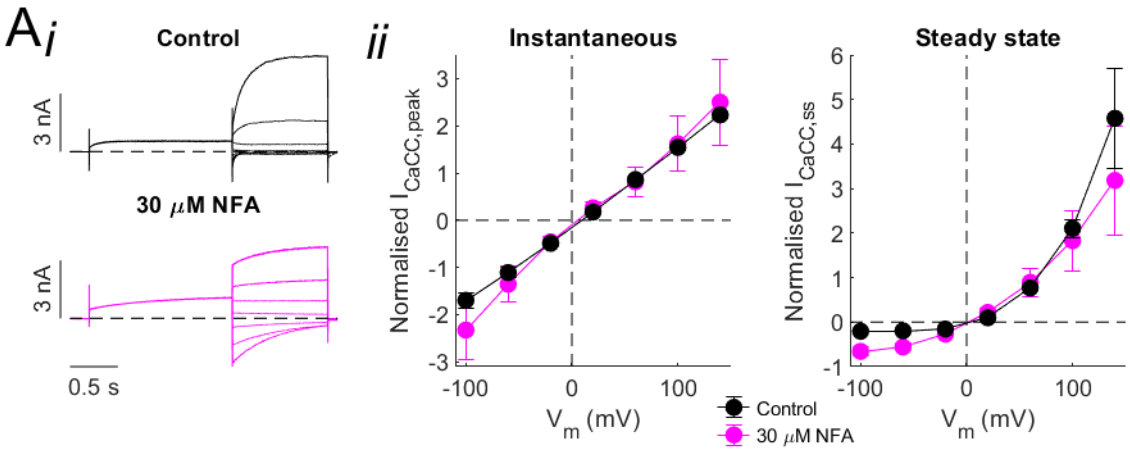


Figure 4.16 Effect of extracellular NFA on whole-cell TMEM16A current amplitudes.

(Ai) Whole-cell currents recorded from HEK-293T cells expressing TMEM16A channels in the absence (control) or presence of 30 µM $[NFA]_{ext}$. Dashed horizontal line represent the zero-current level. (ii) Left panel: Mean peak whole-cell current density *versus* V_m relationships measured in the absence and presence of 30 µM $[NFA]_{ext}$. Right panel: Mean steady-state whole-cell current density *versus* V_m relationships measured in the absence and presence of 30 µM $[NFA]_{ext}$ (n=5).

4.7.1 NFA effect on constitutively active channels in 0 and 0.1 µM $[Ca^{2+}]_i$

To understand whether NFA acts via the same mechanism of action as A9C we studied the effect of NFA on constitutively active mutant channels (TMEM16A-Q645A and TMEM16A-I637A). We did this is an analogous manner to that described in section 4.2.2. Whole-cell currents were elicited in response to the IV-tail protocol which allows

examination of the effects of NFA on current amplitude and reversal potential. Extracellular NFA induced complex changes in the whole-cell wild-type TMEM16A current as described in section 4.1.

To our surprise, the TMEM16A-Q645A and TMEM16A-I637A currents recorded in 0 and 0.1 μM $[Ca^{2+}]_i$ were entirely insensitive to extracellular NFA at all V_m tested. This varied from A9C as there was no modulation by NFA on the addition of intracellular Ca^{2+} (Fig. 4.6).

For both wild-type and mutant (TMEM16A-Q645A, TMEM16A-I637A) channels, NFA did not profoundly affect the E_{rev} which was very close to the expected equilibrium potential for Cl^- (E_{Cl}) in our recording conditions (~1 mV) in each case.

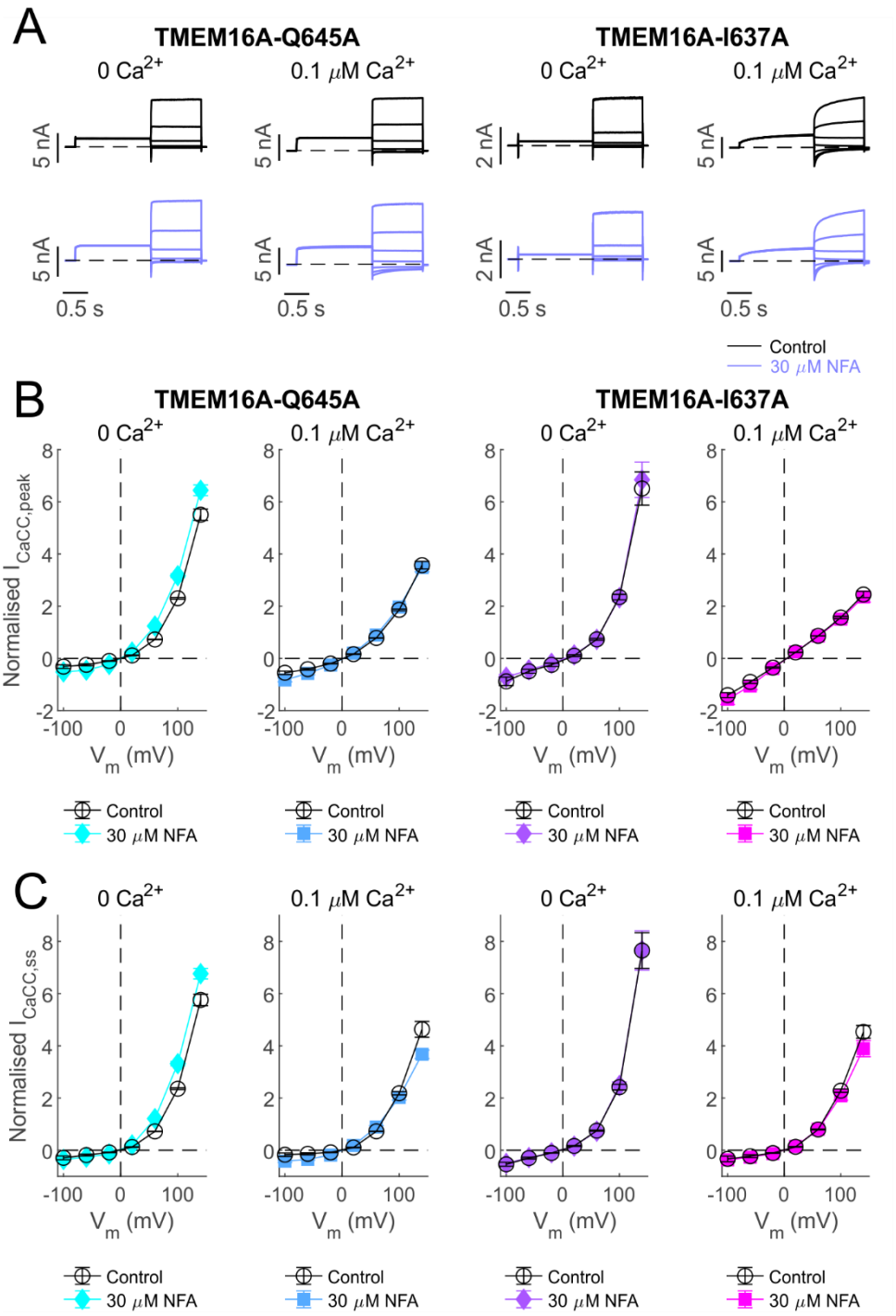


Figure 4.17 Effect of extracellular NFA on whole-cell TMEM16A, TMEM16A-Q645A, and TMEM16A-I637A current amplitudes in the presence or absence of Ca^{2+}.

(A) Whole-cell currents recorded from HEK-293T cells expressing TMEM16A, TMEM16A-Q645A or TMEM16A-I637A channels in the absence (control) or presence of 30 µM $[NFA]_{ext}$ and the indicated $[Ca^{2+}]_i$. Dashed horizontal lines represent the zero-current level. (B) Mean peak whole-cell current density *versus* V_m relationships measured in the presence of 30 µM $[NFA]_{ext}$ and various

$[Ca^{2+}]_i$, as indicated. (C) Mean steady state whole-cell current density *versus* V_m relationships measured in the presence of 30 µM $[NFA]_{ext}$ and various $[Ca^{2+}]_i$, as indicated. The number of experiments was 5 in each case.

4.7.2 Assessing the influence of the electrostatic gate on the effect of NFA

The effect of extracellular NFA, on the TMEM16A-Q645A-E650A channel was also studied (Fig. 4.18). We did this in an analogous manner to that in section 4.1. Whole-cell currents were elicited in response to the IV-tail protocol which allows examination of the effects of NFA on current amplitude and reversal potential. It was found that instantaneous currents unaffected by application of extracellular NFA (30 µM) at any V_m tested in the absence of intracellular Ca^{2+}. In contrast, the inhibition of steady state currents at +140 mV was re-established, suggesting A9C and NFA act via a different mechanism.

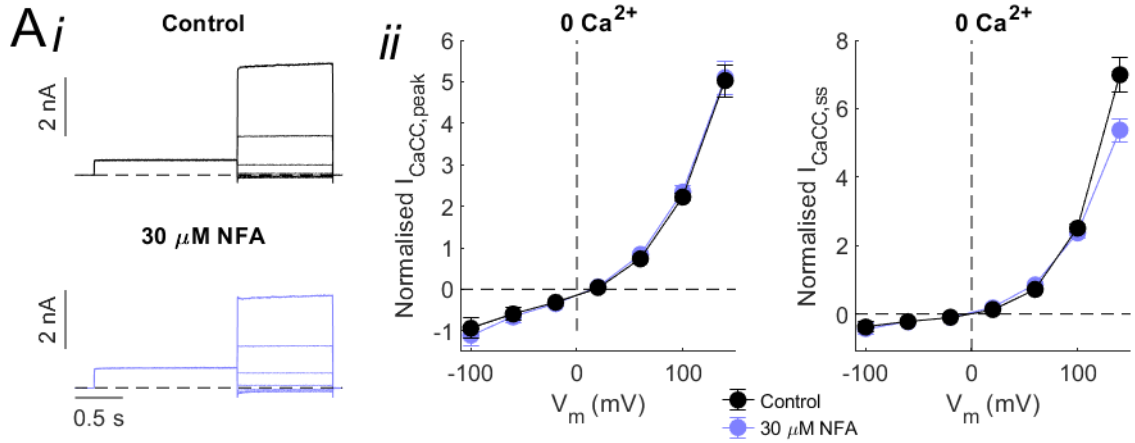


Figure 4.18 Effect of extracellular NFA on whole-cell TMEM16A-Q645A-E650A current amplitudes in the presence or absence of Ca^{2+}.

(Ai) Whole-cell currents recorded from HEK-293T cells expressing TMEM16A-Q645A-E650A in the absence (control) and presence of 30 µM $[NFA]_{ext}$, measured in the absence of $[Ca^{2+}]_i$. Dashed horizontal lines represent zero current level. (ii) Left panel: Mean peak whole-cell current density *versus* V_m relationships measured in the absence and presence of 30 µM $[NFA]_{ext}$, measured in the absence of $[Ca^{2+}]_i$. Right panel: Mean steady-state whole-cell

current density *versus* V_m relationships measured in the absence and presence of 30 µM $[NFA]_{ext}$, measured in the absence of $[Ca^{2+}]_i$ (n=7).

4.7.3 Effect of 30 µM NFA on TMEM16A, TMEM16A-Q645A and TMEM16A-I637A

We then used the rapid perfusion (concentration jump) system to assess the inhibition and activation effect of NFA on TMEM16A, TMEM16A-Q645A and TMEM16A-I637A channels in separation.

In the presence of 0.3 µM $[Ca^{2+}]_i$, when NFA (30 µM) was rapidly applied to the bath solution during the concentration jump, the TMEM16A current displayed the same behaviour as seen in the presence of A9C, a rapid decline in current and then a dramatic increase on removal of NFA (Fig. 4.19). In 0 $[Ca^{2+}]_i$, the currents mediated by TMEM16A-Q645A or TMEM16A-I637A channels were ultimately unaffected by extracellular NFA (30 µM). A small increase in current was observed in TMEM16A-Q645A, in the absence of intracellular Ca^{2+}. This could be due to a change in perfusion speed leading to a slight increase in current. A similar complex response was observed when NFA was applied to cells expressing either mutant channel in the presence of ~0.1 µM $[Ca^{2+}]_i$. The inhibitor and activatory effects were estimated as before. The mean I_b/I_0 and I_a/I_0 demonstrate that in the presence $[Ca^{2+}]_i$, wild-type and mutant channels have a similar response to NFA, just diminished in the magnitude of the effect. However, in the absence of $[Ca^{2+}]_i$ the channels were insensitive to NFA.

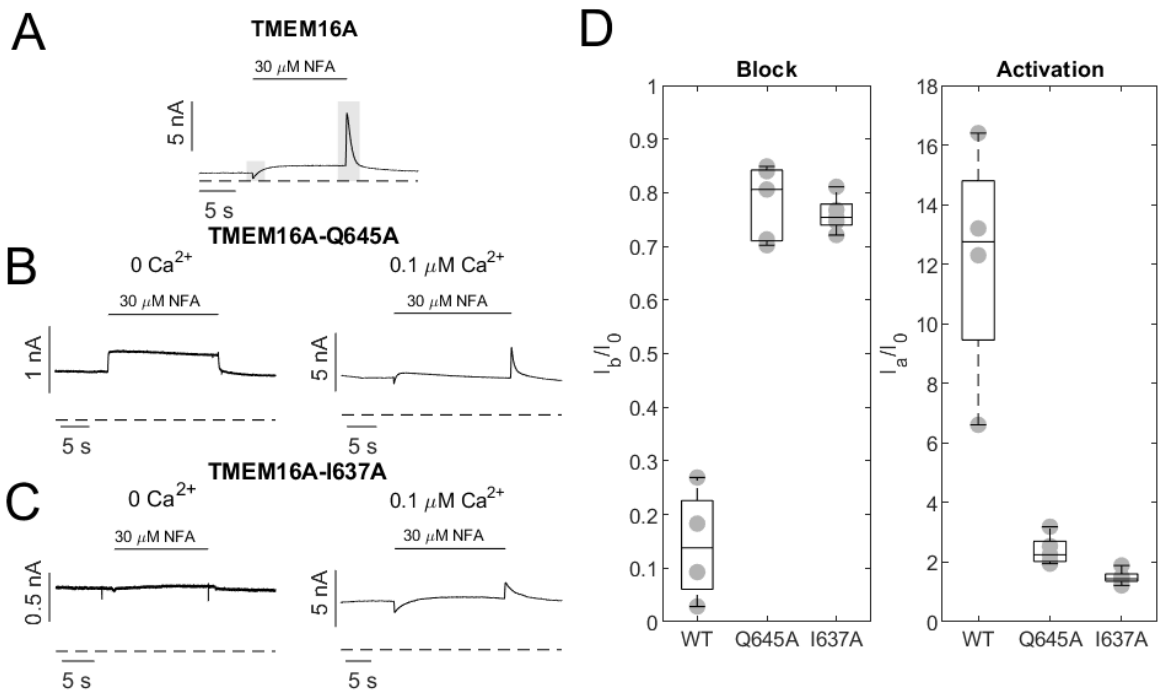


Figure 4.19 Separation of inhibiting and activating effects of NFA on TMEM16A, TMEM16A-Q645A, and TMEM16A-I637A channels.

(A) Whole-cell currents recorded from HEK-293T cells expressing TMEM16A. V_m was +70 mV and $[Ca^{2+}]_i$ was 0.3 µM. Extracellular NFA (30 µM) was applied as indicated by the horizontal bar via a fast-perfusion system (concentration jump). The dashed horizontal line represents the zero-current level. The shaded grey bars indicate regions of the recording that were expanded in D. (B) Experiments were carried out as in A, recorded from HEK-293T cells expressing TMEM16A-Q645A in the absence (control) and presence of 0.1 µM $[Ca^{2+}]_i$. (C) Experiments were carried out as in A, recorded from HEK-293T cells expressing TMEM16A-I637A in the absence (control) and presence of 0.1 µM $[Ca^{2+}]_i$. (D) Mean inhibition (I_b/I_0) and activation (I_a/I_0) plotted for each channel construct, as indicated. The number of experiments was 4-5 in each case.

4.8 Discussion

The key findings of this chapter highlight the link between the action of intracellular Ca^{2+} and extracellular TMEM16A modulators. We used a combination of mutagenesis, electrophysiology, and molecular dynamics to identify the structure-function relationship of TMEM16A using the pharmacological modulation as a probe.

We found that the underlying mechanism is a previously unanticipated Ca^{2+} triggered conformational change at the outer vestibule which allows A9C to reach the centre of the channel. By reaching the centre of the channel it therefore allows the compound to modulate the channel. This ability to reach the centre of the channel is not able to be achieved in the absence of Ca^{2+}.

Guided by the cryo-EM structures of the TMEM16A and TMEM16K proteins, an open state model of the TMEM16A channel was generated by Dr Phillip Stansfeld and Tanadet Pipatpolkai. This model was then used in molecular dynamics simulations and a path for the A9C molecule to access its binding pocket from the extracellular side of the channel. The A9C pocket identified in is in the pore and shown to be partially hydrophobic and shares the same basic residue (K641) required for Cl^- co-ordination.

The identification of this residue as important in the A9C binding site is in accordance with the electrophysiology results. These results demonstrated that mutation of lysine (K) 641 to alanine (A) removed all activation of TMEM16A by A9C.

Comparison of A9C against a second biphasic modulator, NFA, gave insights into the mechanism of activation and inhibition of TMEM16A. These data suggest that there are similarities between the mechanism of action of A9C and NFA. However due to their differing response to constitutively active channels with the electrostatic gate reduced it is suggested that there is a difference in the mechanisms. Further study is required in order to elucidate the action of these two compounds and further understand the pharmacology of TMEM16A.

Our results highlight a potential druggable site at the outer pore of the channel for synthetic small molecules and shed light on a new aspect of Ca^{2+} gating of the TMEM16A channel.

4.8.1 Gating mechanisms of the TMEM16x channels and scramblases

Like some other anion channels, (Last, Kolmakova-Partensky, Shane & Miller, 2016; Miller, 1982) the TMEM16A channel is a homodimer encompassing two pores that function independently from one another (Jeng, Aggarwal, Yu & Chen, 2016; Lim, Lam & Dutzler, 2016).

The binding of Ca^{2+} to the sites in each monomer triggers channel activation (Dang et al., 2017; Paulino, Kalienkova, Lam, Neldner & Dutzler, 2017).

As described in more detail in the introduction, the Ca^{2+} binding promotes the movement at the hinge point on TM6 (G640) which triggers the opening of the "steric gate" on the intracellular vestibule (Paulino, Kalienkova, Lam, Neldner & Dutzler, 2017; Peters et al., 2018). Mutation of these residues opens the channel in the absence of intracellular Ca^{2+} (Lam & Dutzler, 2018; Peters et al., 2018). Run down was observed in the G640P channel was observed, making it difficult to study (Lam & Dutzler, 2018). Mutation of two residues close to G640 to alanine also opens the channel in the absence of intracellular Ca^{2+}, Q645 and I637, however no run down was seen for these channels (Lam & Dutzler, 2018).

An additional gating mechanism of TMEM16A is constituted by the Ca^{2+} binding site where the negatively charged residues near the Ca^{2+} binding site comprise an

'electrostatic gate'. This electrostatic gate is removed on binding of Ca^{2+} to the site (Lam & Dutzler, 2018).

In this chapter we provide evidence of a previously anticipated additional gating component of the channel. The gate being made up by V539 (TM4) and I636 (TM6). Other hydrophobic residues on TM4 (such as I546 and I547) and TM6 (such as I637) have also been shown to form a gate (Lam & Dutzler, 2021; Lam, Rheinberger, Paulino & Dutzler, 2021). This region if like the outer part of the lipid transport pathway in the *Nectria haematocca* TMEM16 scramblase (nhTMEM16).

In nhTMEM16, this portion of the protein undergoes structural rearrangement in response to Ca^{2+} to enable lipid (phosphatidylserine - PS) transport (Lee, Khelashvili, Falzone, Menon, Weinstein & Accardi, 2018).

PS transport in nhTMEM16 requires opening of the outer portion of the lipid permeation pathway, which requires T333 and Y439 moving farther apart by about 4 Å. In the *Aspergillus fumigatus* TMEM16 scramblase (afTMEM16), T333 and Y439 are replaced by T325 and Y432, and on the human scramblase TMEM16K by S363 and T435, respectively.

Thus, for TMEM16 channel and scramblases, the substrate (ions or PS) is blocked by steric hindrance with these residues. This impediment is removed upon Ca^{2+} binding. Here, we have shown that TMEM16 channels and scramblases share a common gating mechanism of the outer pore.

As PS permeates through TMEM16K scramblase, the PS headgroup fully filled up the space inside the TMEM16K cavity/pore. However, permeation of an ion is rather

different to that of lipids. A chloride ion itself doesn't fully fill up a whole pore cavity, but as it would require a water-filled cavity instead as it moves down the pore. This is different as it would not require a direct protein-ion co-ordination throughout its permeation path. Thus, in the same position, it would make sense that V539 and I636 behave as an outer pore hydrophobic gate (water plug) in TMEM16A instead of a chloride interaction site. On the other hand, in the other TMEM16 scramblases, those residues are co-ordinating with the PS in its permeation pathway.

4.8.2 Identification of A9C binding site in the TMEM16A channel

We have previously shown that A9C acts as an open channel blocker and allosteric activator of the channel (Ta, Adomaviciene, Rorsman, Garnett & Tammaro, 2016). The location of the A9C and NFA binding site, however, was unknown. Here, we show that A9C penetrates the channel when the outer gate is open to reach a region composed of 5 amino acids (S513, V539, I636, K641, and Q645). In this way, A9C acts as a voltage dependent open channel blocker. Our work also proposes a potential activatory mechanism by A9C. Given that the A9C binding pocket is adjacent to the Cl^- binding site, the binding of A9C may compete with K641 which is involved in the Cl^- co-ordination. This makes a chloride ion hold on to its binding site less tightly. Together, the binding of A9C may reduce the energy barrier required for the Cl^- to permeate through the pore.

Our results show that A9C binds to a single site and that this produces both inhibition and activation of the channel. This is consistent with our previous work, in which we demonstrated that both effects are dependent on the Cl^- current amplitude, in agreement with a competition between the permeating ion and the A9C (Ta,

Adomaviciene, Rorsman, Garnett & Tammaro, 2016). A9C is a widely used tool compound in Cl^- channel research e.g. (Estévez, Schroeder, Accardi, Jentsch & Pusch, 2003; Ta, Adomaviciene, Rorsman, Garnett & Tammaro, 2016). Our discovery of the A9C binding region on the TMEM16A channel has significant implications for future drug discovery as it may constitute a possible site of action for synthetic modulators of the channel.

Chapter 5

Developing a system to test new small molecules acting on TMEM16A channel

5 Chapter 5: Developing a system to test new small molecules acting on TMEM16A channels

5.1 Creation of TMEM16A stable HEK-293 cell line

The need for TMEM16A modulators was highlighted in the Introduction and previous chapters of this thesis. In order to evaluate compounds that modulate TMEM16A, a rapid and reliable quantitative screening system is required. The patch-clamp technique can study ion channels in significant detail; however, the process is slow and relatively low throughput. Published work describes a high throughput screening methods involving a fluorescence-based cell assay in order to record Cl^- channel activity (Galietta et al., 2001; Galietta, Jayaraman & Verkman, 2001; Namkung, Yao, Finkbeiner & Verkman, 2011a).

The assay uses a mutated green fluorescence protein in which the fluorescence decreases on halide binding (YFP_H148Q/I152L), this provides a read out that can be quantified quickly and easily. The quenching of fluorescence depends on protonation of the chromophore following anion binding (Wachter, Elsliger, Kallio, Hanson & Remington, 1998; Wachter, Yarbrough, Kallio & Remington, 2000). From crystallographic studies of the YFP-H148Q mutant the I^- is found to bind near van der Waals contact to the chromophore imidazolinone carbonyl oxygen, this contact reduces the delocalisation of the phenolate negative charge over the chromophore skeleton (Fig. 5.1) (Wachter, Yarbrough, Kallio & Remington, 2000). The chromophore anion is then destabilised which shifts the pK_a to higher values and making it more likely for the chromophore to be protonated, and on protonation a reduction in fluorescence

(Jayaraman, Haggie, Wachter, Remington & Verkman, 2000; Wachter, Elsliger, Kallio, Hanson & Remington, 1998; Wachter, Yarbrough, Kallio & Remington, 2000).

Iodide is used as a replacement for chloride in the screen since it is typical Cl^- channels have higher permeability for I^- than Cl^- (Adomaviciene, Smith, Garnett & Tammaro, 2013; Evans & Marty, 1986; Franciolini, 1987; Woodbury & Miles, 1973). In contrast, anion exchangers or cotransporters such as AE1 (Cl/HCO_3) and NKCC (Na/K/2Cl) tend to more specifically transport Cl^-. Furthermore, I^- causes substantially greater quenching of molecular and chemical halide sensors compared to Cl^- (Verkman & Jayaraman, 2002).

In order to obtain biosensors with increased I^- selectively a range of mutations have been studied and many of the mutants were found to have a greater affinity to I^- than YFP-H148Q (Galietta, Haggie & Verkman, 2001). The YFP-H148Q/I152L has an anion selectivity sequence of $I^- > NO_3^- > Br^- > Cl^-$, corresponding to a lyotropic sequence which is also found in chloride channels (Smith, Steinle, Meyerhoff & Dawson, 1999; Wright & Diamond, 1977). This suggests that anions with lower dehydration energy ($I^- < Cl^-$) have preferred binding to the sensor. There is a large increase in affinity to I^- in the YFP-H148Q/I152L mutant is probably due to a steric effect in that the change in cavity size means binding the larger anion is preferable (Galietta, Haggie & Verkman, 2001).

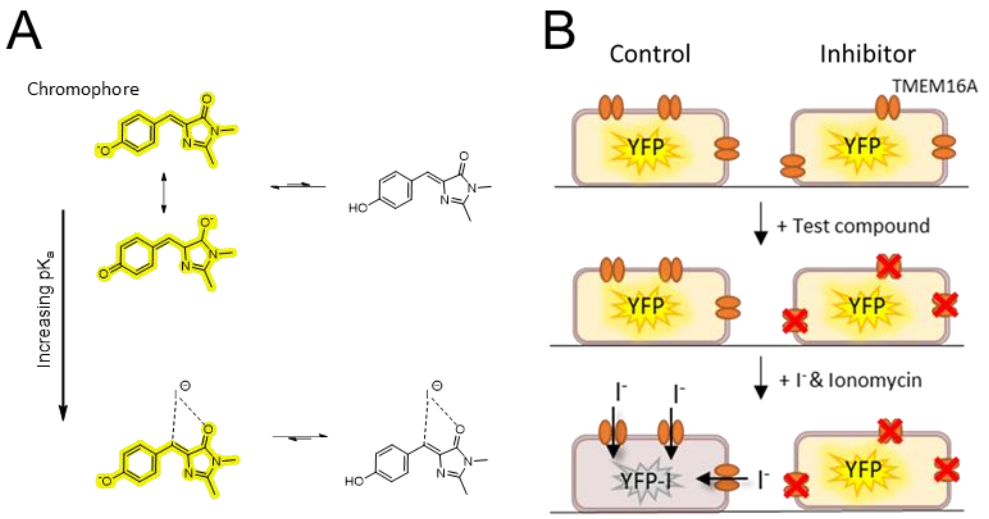


Figure 5.1 Diagrammatic representation of fluorescence quenching assay.

(A) Structural depiction of the chromophore protonation that leads to fluorescence quenching. (B) The orange channels depict TMEM16A. Cells are transfected with the YFP sensor and then incubated in the absence (control) or presence (inhibitor) of test compounds. Fluorescence is measured for 2 seconds and then an I^- and ionomycin extracellular solution, which activates the TMEM16A in control conditions then the I^- will go through the open TMEM16A channels and quench the YFP fluorescence. TMEM16A inhibitors will block the channel and therefore the TMEM16A will not be activated and there will be no quench in fluorescence. Analysis of this quench in fluorescence can select compounds for further study.

The magnitude and electrophysiology characteristics of the whole-cell currents obtained from HEK-293 cells stably transfected with TMEM16A were assessed. Fig.5.2 shows representative traces of TMEM16A currents recorded using intracellular solution containing 0.3 µM free Ca^{2+}. The IV_CaCC protocol was applied in non-transfected HEK-293 cells using 0.3 µM Ca^{2+} intracellular solution and acted as a control. In non-transfected HEK-293 cells, only a small endogenous current was recorded whereas, permanently transfected cells exhibited prominent CaCC currents.

In the presence of 0.3 μM $[Ca^{2+}]_i$, hyperpolarising and depolarising steps showed instantaneous TMEM16A currents, followed by time-dependent relaxations towards new steady-state levels. Currents reached a maximum steady-state current density of 253.8 ± 85.5 pA/pF (n=11) at +100 mV. The current density immediately after the voltage changed was measured and represented the instantaneous current component. We observed a nearly linear relationship between the instantaneous current and V_m. However, the relationship between steady-state current and the V_m was outwardly rectifying (Fig.5.2), like that seen for transiently transfected TMEM16A and native TMEM16A currents. The I_{ss}/I_{inst} at +100 mV gives a fraction of 3.6 ± 0.6 (n=11) and the I_{100}/I_{-100} (rectification index) was -21.9 ± 5.6 (n=11) in ~0.3 μM $[Ca^{2+}]_i$. The reversal potential for the TMEM16A currents was approximately 0 mV, the estimated Cl^- equilibrium potential for the recording solutions used.

The time of half-current was measure as described in section 3.2. As the voltage increased, $\tau_{0.5}$ decreased, equalling 119.4 ± 18.7 ms (n=11) at +40 mV and 49.0 ± 2.9 ms (n=11) at +100 mV (Fig. 5.2). The tail currents measured upon repolarisation to −60 mV were quantified in the same way, $\tau_{0.5}$ did not show a significant change with voltage over the range of +40 mV to +100 mV (Fig. 3.2). The $\tau_{0.5}$ for the deactivating tail current was 4.3 ± 0.6 ms (n=11), when preceded by a pre-pulse to +40 mV and 10.6 ± 1.1 (n=11) when preceded by a pre-pulse to +100 mV ($P<0.05$).

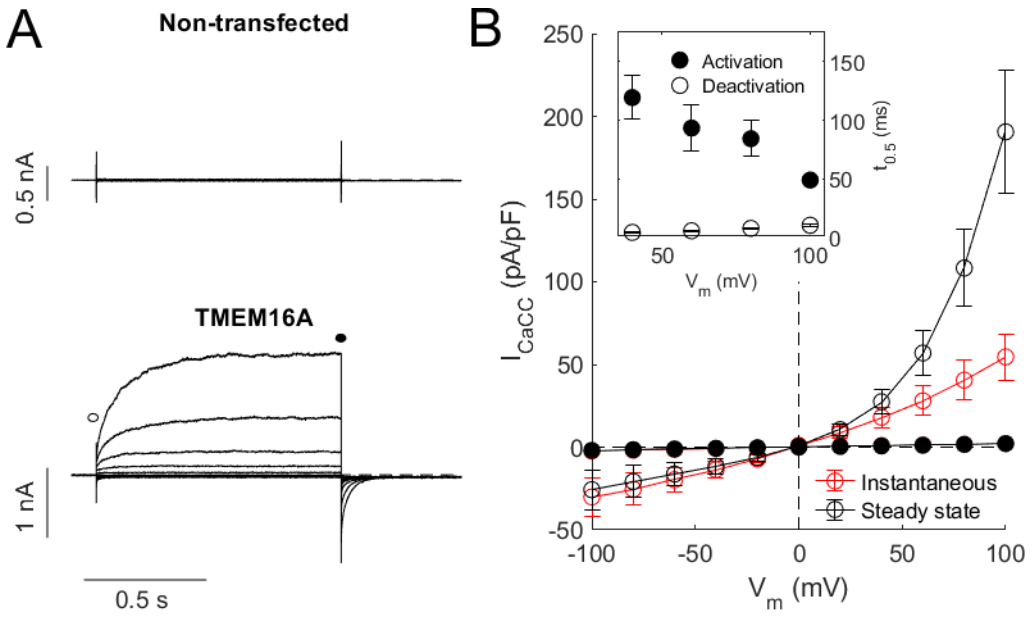


Figure 5.2 IV-relationship of stably transfected TMEM16A HEK-293 cell line

(A) Representative whole-cell currents recorded from non-transfected (NT), and stably transfected TMEM16A HEK-293 cells. Solutions contained ~0.3 µM $[Ca^{2+}]_i$. Currents were recorded using the IV-CaCC voltage protocol. Dashed lines represent the zero-current level. (B) Mean whole-cell current *versus* V_m relationships measured at the beginning (instantaneous) and the end of the test pulses (steady state), as indicated (n=11).

5.2 TMEM16A current response to Ionomycin

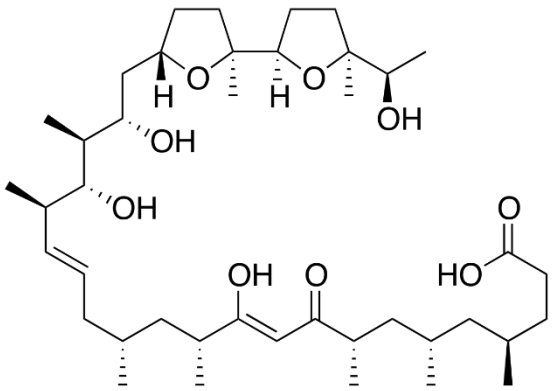


Figure 5.3 Structure of Ionomycin

The optical density of I^- fluxes in the permanently transfected cells requires opening of the TMEM16A channel in the absence of electrophysiological stimuli.

Several modulators have been used to activate both endogenous CaCCs or cloned TMEM16A in intact cells, including the Ca^{2+} ionophores, including ionomycin (Toeplitz, Cohen, Funke, Parker & Gougoutas, 1979), to allow influx of Ca^{2+} from the extracellular membrane to the cell interior. Another method of activation is to increase the intracellular Ca^{2+} concentration by release of Ca^{2+} from the intracellular Ca^{2+} store via activation of the PLC and IP_3 signalling cascade, modulators that have previous been used are ATP (Benedetto et al., 2017), UTP (Namkung, Phuan & Verkman, 2011), and bradykinin (Danielsson et al., 2015). When TMEM16A is expressed in HEK-293T cells there was no increase in current on addition of modulators that increase $[Ca^{2+}]_i$, so it was chosen to use ionomycin in our study to activate TMEM16A by directly increasing the intracellular Ca^{2+} via ionomycin acting as an ionophore.

Whole-cell electrophysiology was used to assess the effect of TMEM16A activation by $[Ca^{2+}]_i$ increase via ionomycin addition. In order to validate the use of ionomycin and select an appropriate concentration to be used in the screen, two intracellular solutions were used. These intracellular solutions only differed in their EGTA concentration. EGTA is the main Ca^{2+} chelating agent in the intracellular solution used in the patch-clamp electrophysiology experiments, therefore low EGTA intracellular CaCC solution was used to prevent complete Ca^{2+} buffering during exposure of the cell to ionomycin and thus to be able to detect the effect of an increase in $[Ca^{2+}]_i$ on the TMEM16A current. Standard intracellular CaCC (high EGTA) solution contained 10 mM EGTA, which is sufficient to quickly buffer the Ca^{2+} that may result from an influx via ionomycin (Naraghi, 1997). We argued that this concentration of EGTA would prevent activation of

TMEM16A by ionomycin and thus enabling us to assess the specific effect of ionomycin on the TMEM16A channel. TMEM16A currents were recorded in the stably transfected TMEM16A HEK-293 cells with the whole-cell patch-clamp configuration, using the IV-ramp protocol.

In non-transfected cells there was no effect of ionomycin on the small endogenous currents, currents recorded were 0.86 ± 0.21 (pA/pF) (n=4) at 95 mV and on application of ionomycin (0.1 μM) the currents were 1.32 ± 0.58 (pA/pF) (n=4) at 95 mV. Therefore, we so not see any current flow from the influx of Ca^{2+} into the cells. This allows us to measure and analyse solely the Cl^- currents.

Control TMEM16A currents were recorded before the addition of ionomycin (0.1 μM). Currents elicited from cells in low intracellular EGTA solutions increased by ~2.5 fold at 95 mV. The current increase reached a maximum after ~7 s exposure to ionomycin. TMEM16A current in the high EGTA solution decreased by ~1.3-fold at 95 mV in response to ionomycin (0.1 μM). TMEM16A currents recorded with high EGTA intracellular solution but in the absence of extracellular increased by ~1.9-fold at 95 mV in response to ionomycin (0.1 μM). This slight increase could be due to residual Ca^{2+} contaminants.

Together this data suggests that ionomycin increases TMEM16A activity via increase in intracellular Ca^{2+} concentration and without affecting conductance's.

Table 5.1 Effect of ionomycin on TMEM16A currents in HEK-293 cells.

	TMEM16A current in low EGTA (pA/pF)		**TMEM16A current in high EGTA (pA/pF)**		**TMEM16A current in low EGTA and 0 $[Ca^{2+}]_e$ (pA/pF)**	
	Control	0.1 µM ionomycin	Control	0.1 µM ionomycin	Control	0.1 µM ionomycin
-95 mV	-8.4 ± 2.0	-145.6 ± 64.0	-14.5 ± 2.9	-12.3±1.5	-6.1 ± 1.1	-9.9 ± 3.1
95 mV	168.0 ± 35.6	416.6 ± 85.2	351.9 ± 74.7	280.4 ± 40.9	77.2 ± 13.1	144.7 ± 44.0
n	5		5		4	

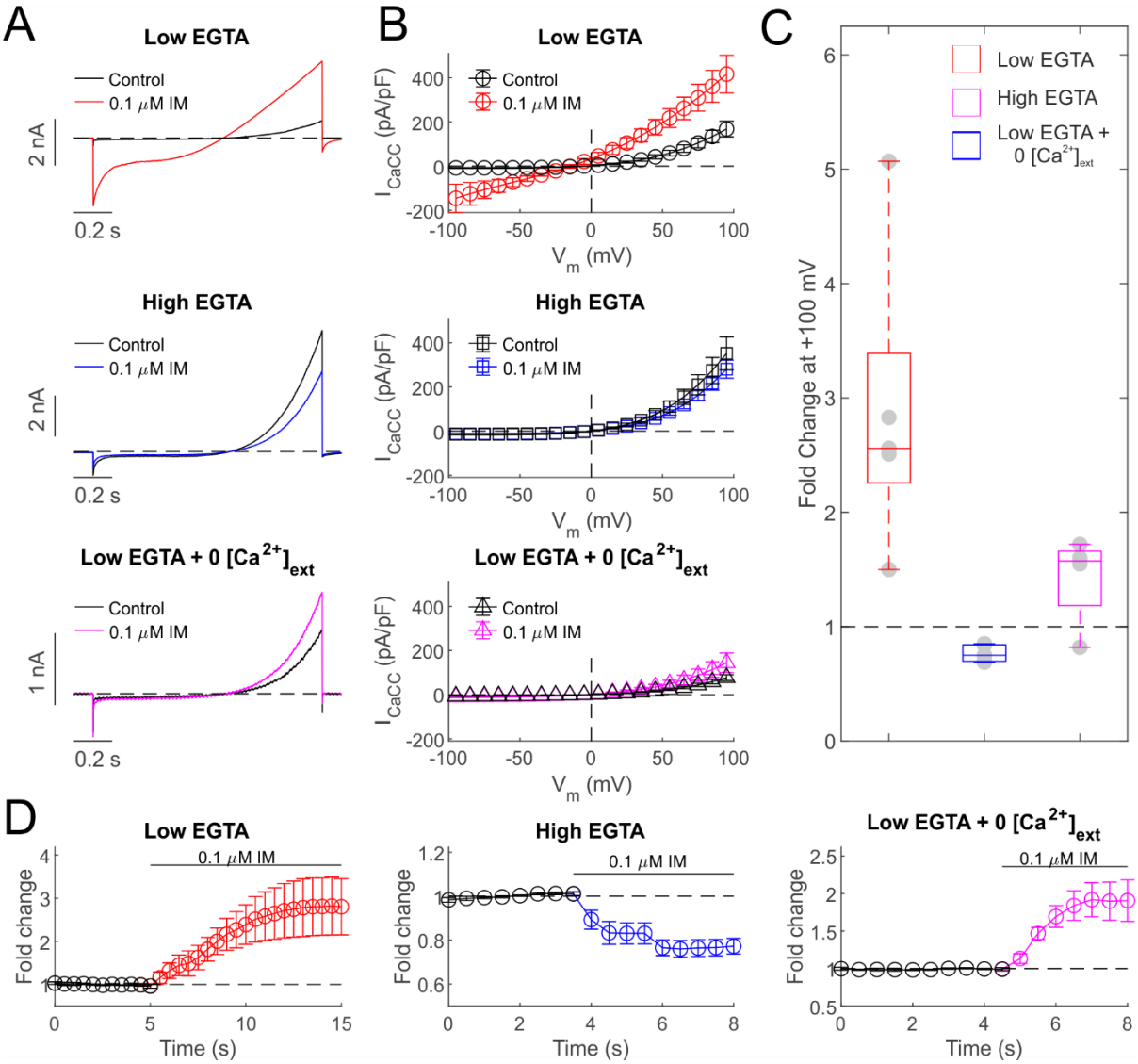


Figure 5.4 Effect of ionomycin on TMEM16A currents in HEK-293 cells.

(A) Whole-cell patch clamp currents recorded from TMEM16A stably transfected HEK-293 cells. TMEM16A current was elicited in response to the IV-ramp voltage protocol, using CaCC solutions containing low intracellular EGTA (n=5), high intracellular EGTA (n=5) or low intracellular EGTA and 0 $[Ca^{2+}]_{ext}$ (n=4) as indicated. 0.1 µM ionomycin was added as indicated. Dashed line indicates zero current level. (B) Mean whole-cell current measured from -95 mV to 95 mV in 10 mV increments, in the absence (control) and presence of ionomycin. Extracellular solutions were low intracellular EGTA (n=5), high intracellular EGTA (n=5) or low intracellular EGTA and 0 $[Ca^{2+}]_{ext}$ (n=4) as indicated. (C) Mean fold change at +100 mV on addition of 0.1 µM ionomycin, plotted for each extracellular solution, as indicated. The central mark indicates the median, with the bottom and top edges of the box indicate the 25th and 75th respectively. The number of experiments was 4-5 in each case. (D) Time course for the effect of 0.1 µM ionomycin on whole-cell TMEM16A currents measured at +100 mV,

extracellular solutions containing low intracellular EGTA (n=5), high intracellular EGTA (n=5) or low intracellular EGTA and 0 $[Ca^{2+}]_{ext}$ (n=4) as indicated. Data was normalised to control currents at +100 mV.

5.2.1 Effect of TMEM16A inhibitors on ionomycin elicited TMEM16A currents

We then tested the ability of TMEM16A inhibitors to block ionomycin elicited TMEM16A currents, to validate the capacity of the system to detected known TMEM16A blockers.

TMEM16A currents were recorded from whole-cell patch-clamp experiments using the IV ramp voltage protocol. Currents were recorded for five sweeps of the voltage protocol under control conditions, followed by ten sweeps in the presence of a TMEM16A inhibitor (Ani9 or MONNA), ionomycin (0.1 µM) was then added for the remaining 15 sweeps. The time course of this effect was defined as the amount of time taken for the ionomycin-induced current increase to reach the steady state value in each cell at 100 mV (Fig. 5.5).

Ani9 (1 µM) and MONNA (10 µM) both inhibited TMEM16A current by ~90 % at 95 mV. We then measured the currents on addition of ionomycin after the channel has been blocked by the inhibitors. On addition of ionomycin (0.1 µM) after Ani9 addition there was an overall ~80 % block of the control currents (n=7). On addition of ionomycin (0.1 µM) after MONNA addition there was an overall ~70 % block of the control currents (n=4).

The set of experiments indicate that the Ani9 and MONNA are still about to block ionomycin elicited TMEM16A currents. Therefore, ionomycin is a suitable compound to use in the screen to activate TMEM16A currents since it does not cause direct channel

modulation and the currents elicited on addition of ionomycin can be blocked by TMEM16A inhibitors, therefore are able to be used as a positive control.

Table 5.2 Effect of inhibitors and ionomycin on TMEM16A currents in HEK-293 cells.

	TMEM16A current (pA/pF)					
	Control	1 µM Ani9	1 µM Ani9 + 0.1 µM ionomycin	Control	10 µM MONNA	10 µM MONNA + 0.1 µM ionomycin
-95 mV	-28.9 ± 10.5	-12.1 ± 4.7	-23.9 ± 7.2	-6.7 ± 1.6	-4.1 ± 1.7	-4.9 ± 1.1
95 mV	268.2 ± 77.0	23.9 ± 7.6	40.5 ± 11.4	146.0 ± 46.2	11.4 ± 2.9	45.4 ± 13.3
n	7			4		

The effect of TMEM16A inhibitors on ionomycin TMEM16A elicited currents recorded at -95 mV and 95 mV.

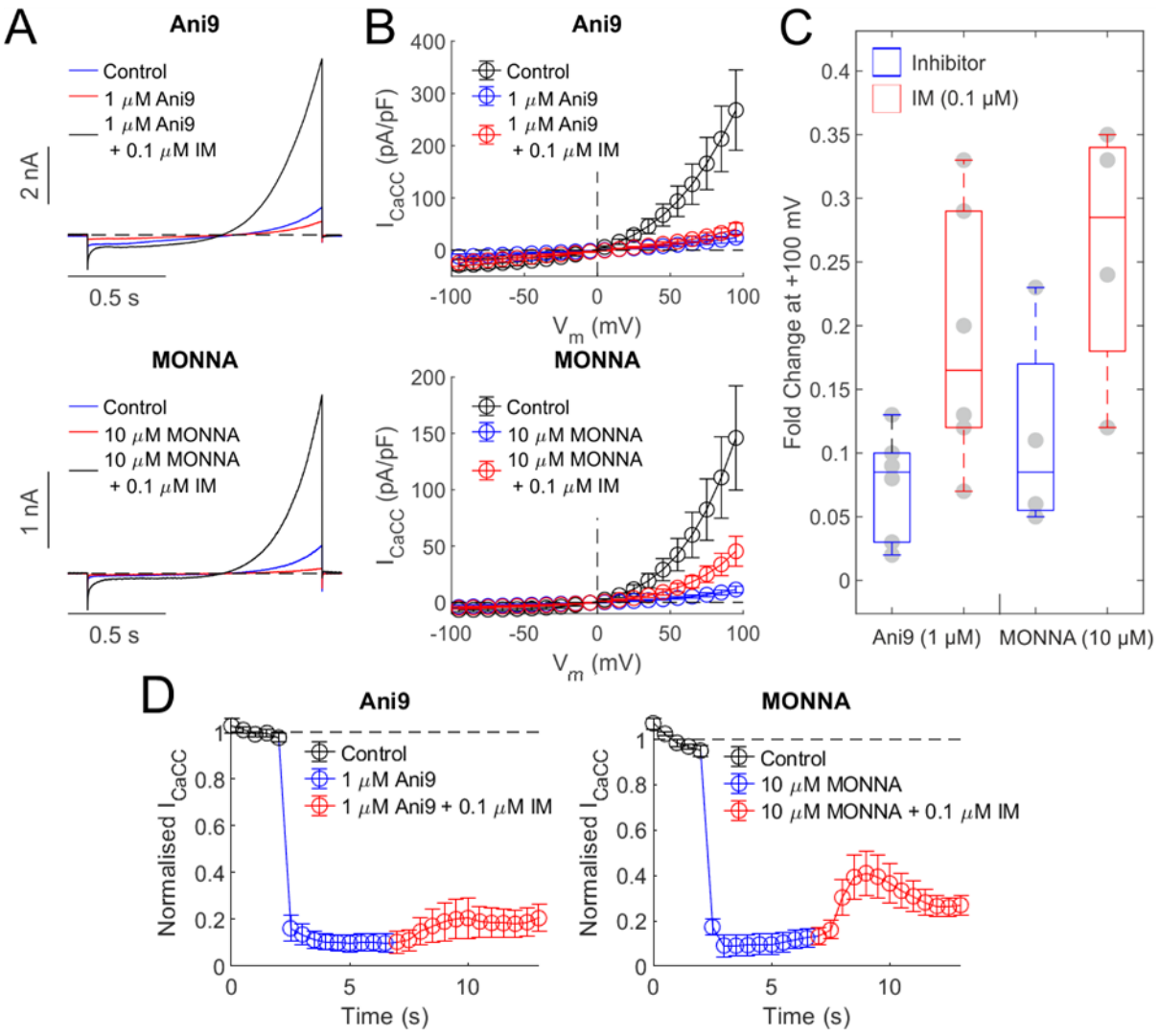


Figure 5.5 Effect of inhibitors and ionomycin on TMEM16A currents in HEK-293 cells.

(A) Whole-cell patch clamp currents recorded from TMEM16A stably transfected HEK-293 cells. TMEM16A current was elicited in response to the IV-ramp voltage protocol, using CaCC solutions containing low intracellular EGTA and the in the absence (control, black), the presence of 1 µM Ani9 or 10 µM MONNA (red), and presence of 1 µM Ani9 or 10 µM MONNA and 100 ionomycin (blue), as indicated. Dashed line indicates zero current level. (B) Mean whole-cell current measured from -95 mV to 95 mV in 10 mV increments, in the absence (control, black), the presence of 1 µM Ani9 or 10 µM MONNA (red), and presence of 1 µM Ani9 or 10 µM MONNA and 100 ionomycin (blue), as indicated. (C) Mean fold change at +100 mV on addition of 1 µM ani9 or 10 µM MONNA (red), and presence of 1 µM Ani9 or 10 µM MONNA and 0.1 µM ionomycin (blue), as indicated. The

central mark indicates the median, with the bottom and top edges of the box indicate the 25th and 75th respectively. The number of experiments was 4-7 in each case. (D) Time course for the effect of 0.1 µM ionomycin and either 1 µM Ani9 or 10 µM MONNA, as indicated, on whole-cell TMEM16A currents measured at +100 mV. Data was normalised to control currents at +100 mV.

5.3 Use of Premo™ Halide Sensor to assess modulation of TMEM16A

The Premo™ Halide Sensor kit was selected as a fast and efficient method to screen TMEM16A modulators in conjunction with the TMEM16A_HEK-293 stable cell line. The cells were transfected with the YFP (Venus) biosensor as described in the Chapter 2, then plated in triplicate and left to settle overnight.

Extracellular solution was then replaced with I^- supplemented CaCC extracellular solution, either in the absence (control) or presence of inhibitor (Ani9 or MONNA). The fluorescence of the YFP (Venus) biosensor treated and non-treated HEK-293 cells were recorded for 2 seconds before injection of ionomycin (final concentrations: 0, 0.5 µM or 1 µM) and 75 mM I^-. Background fluorescence, recorded from non-treated cells, was subtracted. However, low levels of fluorescence beyond the background level was observed.

There was no detectable decrease in fluorescence on injection of 0 ionomycin solution. The fluorescence decreased by 24 % and 29 % on injection of 0.5 µM and 1 µM ionomycin solution, respectively.

However, on preincubation with Ani9 and MONNA the fluorescence also decreased by 30-50% suggesting this is not due to activation of TMEM16A. Also, the reduction in fluorescence on I^- addition is far lower than that seen in previous studies (Galietta,

Jayaraman & Verkman, 2001; Namkung, Phuan & Verkman, 2011; Namkung, Yao, Finkbeiner & Verkman, 2011a).

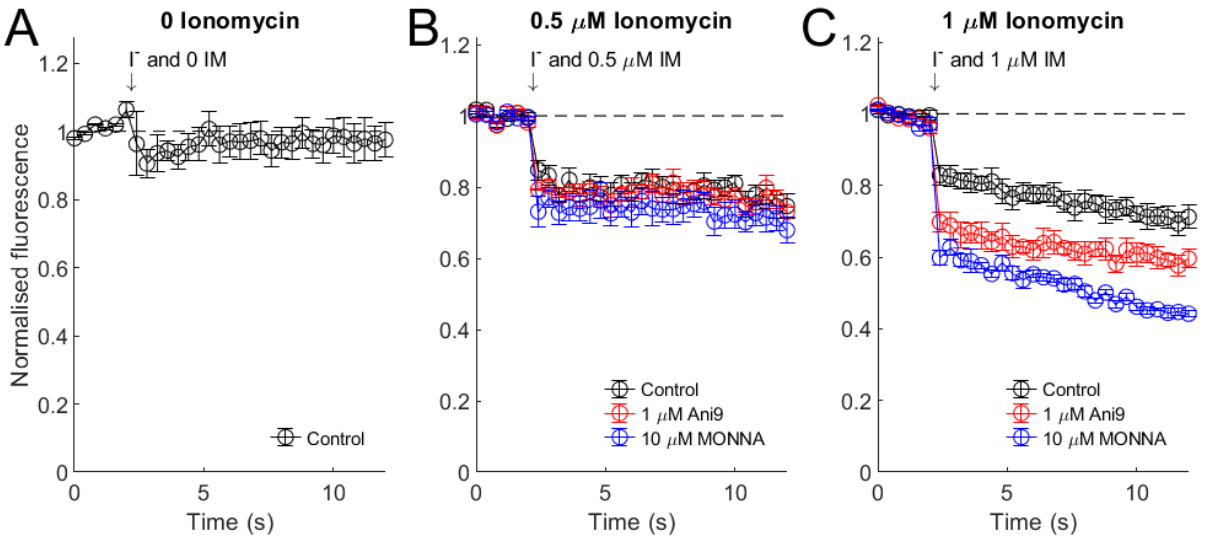


Figure 5.6 Fluorescence assay with I^- supplemented CaCC extracellular solution

(A) Time course for the effect of 0 ionomycin on fluorescence of YFP (Venus) biosensor transfected cells in I^- supplemented CaCC extracellular solution. Data was normalised to fluorescence in the absence of I^- and ionomycin. (B) Time course for the effect of 0.5 µM ionomycin and either 1 µM Ani9 or 10 µM MONNA, as indicated, on fluorescence of YFP (Venus) biosensor transfected cells in I^- supplemented CaCC extracellular solution. Data was fluorescence in the absence of I^- and ionomycin. (C) Time course for the effect of 1 µM ionomycin and either 1 µM Ani9 or 10 µM MONNA, as indicated, on fluorescence of YFP (Venus) biosensor transfected cells in I^- supplemented CaCC extracellular solution. Data was fluorescence in the absence of I^- and ionomycin. Number of experiments was 3 in each case.

5.4 Discussion

To study the modulation of TMEM16A in a fluorescence based assay, a stable cell line, expressing mouse TMEM16A was generated using HEK 293 cells. (Caputo et al., 2008), demonstrated an expected 20-30 % transfection efficiency. Therefore, stable

transfection was selected for this study to ensure that the signal from the group of cells is high enough beyond baseline and the fluorescence is consistent between plates.

Transfection of TMEM16A produced outwardly rectifying currents that were both voltage and Ca^{2+} -dependent, closely resembling those recorded in our transient transfection system (section 3.2) and of CaCC currents in isolated VSMCs (Adomaviciene, Smith, Garnett & Tammaro, 2013; Hartzell, Putzier & Arreola, 2005).

A systematic study of the effect of ionomycin activation of TMEM16A in HEK-293 was carried out. Previous studies have used a stably transfected FRT cell line in analogous assays. TMEM16A is activated via initiation of the IP_3 signalling cascade by ATP and subsequent $[Ca^{2+}]_i$ increase. Within HEK-293 cells ATP is unable to activate this pathway and therefore ionomycin was studied as a receptor independent method to increase $[Ca^{2+}]_i$. This has not previously been studied in the literature however in this thesis we provide evidence to support the use of ionomycin as an indirect receptor independent TMEM16A activator.

In low intracellular EGTA solutions, where Ca^{2+} is not buffered a large increase in CaCC current was observed. This suggests that $[Ca^{2+}]_i$ is increasing and sufficiently activating TMEM16A. In high intracellular EGTA solution where the Ca^{2+} is quickly buffered there is no measurable increase in current, further supporting the conclusion that TMEM16A is being activated by an increase in intracellular Ca^{2+}. The small decrease in current seen on addition of ionomycin, could be due to ionomycin inserting into the membrane and therefore modulating TMEM16A due to the change in rigidity of the membrane (Schreiber et al., 2018). We also found that TMEM16A inhibitors, Ani9 and MONNA, were able to block the currents elicited by ionomycin. On addition to ionomycin after the channels had been blocked by Ani9 and MONNA there was a rise in the current, it is

speculated this is due to the Ca^{2+} and Cl^- flux dependence of the blockers reducing their effect. This suggests ionomycin in conjunction with stably transfected HEK-293 cells are a good model for the fluorescence-based assay, with the use of Ani9 or MONNA as a positive control.

The Premo™ Halide Sensor is a reported to be a highly sensitive, robust, and easy-to-use tool to efficiently screen halide ion channels and transporter modulators in a variety of cellular models. The cells were transfected with the YFP (Venus) biosensor using the BacMam delivery system as described in the Methods. In our hands we saw a small level of fluorescence when transfected with the Premo™ Halide Sensor. On activation of TMEM16A by ionomycin and introduction of I^- in the extracellular solution we also saw no appreciable quenching of fluorescence in either of the solutions tested. This could be due to the cells lifting on injection of the ionomycin and I^- solution. The lifting of the cells would disrupt the measurement of fluorescence and therefore the results. We then recorded in the fluorescence in the presence of extracellular TMEM16A inhibitors. The reduction in fluorescence seen on application of ionomycin was not blocked by either inhibitor.

The next steps in the development of the screen would be to create a stable cell line transfected with both TMEM16A and YFP_QLL which we have obtained from Professor L. Galietta. We could therefore directly compare the use of the commercially available kit and the YFP_QLL transfection to dissect the low fluorescence levels.

The development of this screen can be used in future research within the group to test new compounds for TMEM16A modulation.

Chapter 6

Concluding remarks

6 Chapter 6: Concluding remarks

The overall objectives of this thesis were (i) to study the molecular pharmacology of the TMEM16A channel, (ii) to gain insights into regions of the channel that can be tackled therapeutically and (iii) to explore existing modulators to define their selectivity and potency in isolated blood vessels and isolated vascular SMCs.

Much of the work in this thesis builds on previous research from the Tammaro group, which studied the interesting complex modulation of TMEM16A by A9C (Ta, Adomaviciene, Rorsman, Garnett & Tammaro, 2016) and the selectivity of current blockers on TMEM16A (Acheson, 2019)

TMEM16A had been a proposed drug target for a variety of disorders . However, the current knowledge of the TMEM16A pharmacology is sparse and known modulators have been shown to have low potency or the selectivity of the compounds have been questioned (Boedtkjer, Kim, Jensen, Matchkov & Andersson, 2015; Genovese et al., 2019; Liu, Feng, Luo, Yang, Brett & Hu, 2016). Therefore, the knowledge of the current TMEM16A modulators found by this thesis could help in future drug design for TMEM16A modulators for therapeutic benefit.

A systematic characterisation of the most potent, currently available TMEM16A modulators were studied. This involved examination of the effect of Ani9 and MONNA on cloned and native TMEM16A and also a detailed analysis of these agents on (i) other TMEM16x family members, that have channel function (TMEM16B and TMEM16F) and are also expressed in the vascular system (Manoury, Tamuleviciute & Tammaro, 2010) and (ii) cationic current in aortic SMCs. The effect of these blockers were also studied on isolated aortic rings during stimulation of α1-adrenergic receptors with PE. This

analysis demonstrated that MONNA exhibited a range of other effects. Ani9 was found to be a potent inhibitor of cloned TMEM16A and selective for native TMEM16A in VSMCs, as it did not modulate VSMC cationic currents, including Ca_V currents. Ani9 was then therefore used as a tool to specifically block native TMEM16A. Whereas MONNA was found to be a potent inhibitor of cloned TMEM16A and was found to block TMEM16B and TMEM16F. In addition, MONNA was found to be unselective for native TMEM16A in murine aortic VSMC, alongside inhibiting TMEM16A current it was found to increase cationic current. Using a panel of pharmacological blockers of the dominant cationic currents within smooth muscle cells it was found that MONNA was activating BK_{Ca} current. Study of the effect of MONNA on Ca_V channels showed that MONNA also inhibited Ca_V current.

A key finding of this thesis highlights the link between the action of intracellular Ca^{2+} and A9C, an extracellular modulator, on the TMEM16A channel. A9C has a complex mechanism of TMEM16A modulation which has been well characterised previously (Ta, Adomaviciene, Rorsman, Garnett & Tammaro, 2016). We combined this knowledge with a second biphasic modulator, NFA, to determine the mechanism of action of these compounds. The underlying mechanism is a previously unanticipated Ca^{2+}-triggered conformational change at the outer vestibule which allows A9C to reach the centre of the channel (Fig. 6.1). In collaboration with Tanadet Pipatpolkai and Dr Phillip Stansfeld and guided by the cryo-EM structures of the TMEM16A and TMEM16K proteins, we generated an open state model of the TMEM16A channel. Using MD simulations, we identified a path for the A9C molecule to access its binding pocket inside the pore from the extracellular side of the channel. The A9C binding pocket is partially hydrophobic and shares the same basic residue, K641, required for Cl^- coordination. Our results

highlight a potential druggable site at the outer pore of the channel for synthetic small molecules and shed light on a new aspect of Ca^{2+} gating of the TMEM16A channel.

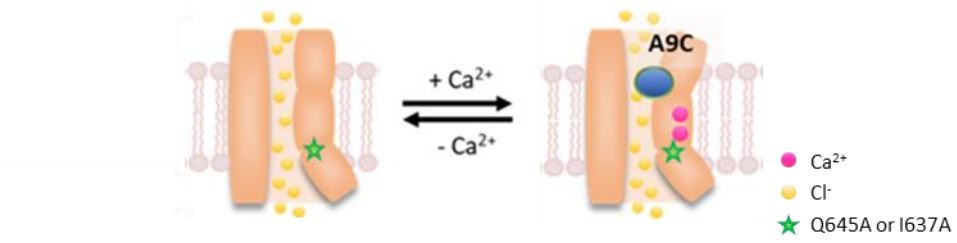


Figure 6.1 Proposed mechanism of Ca^{2+}-dependent gating and A9C modulation of channel activity.

Diagrammatic summary of the key results of our study. The pore of TMEM16A-Q645A channel has a constitutively open TM6 gate. Despite this channel being conductive, A9C does not influence ionic passage. Only when intracellular Ca^{2+} binds to the channel and causes a conformational change in the outer pore, can A9C access its binding site in the centre of the channel, and interfere Cl^- flux.

We also worked towards the development of a fluorescence-based assay to quickly test the effect of compounds on TMEM16A. This was based on previous assays, which were developed to produce a high throughput screening platform able to identify TMEM16A modulators (De La Fuente, Namkung, Mills & Verkman, 2007; Namkung, Yao, Finkbeiner & Verkman, 2011a; Oh et al., 2013; Seo et al., 2016). While we did not get the screen working in the timeframe of this thesis the development of a stable line and the systematic analysis of the activation of ionomycin is useful knowledge for the research community. Discovery of a putative binding site for A9C discovered in Chapter 4 means that compound libraries can be docked into this binding site and compounds identified for future study. This screening system can then be employed to study the TMEM16A activity of compounds and towards the discovery of new and much needed modulators.

Overall, this thesis highlights the complex relationship between the gating and pharmacology of calcium-activated chloride channels. We discovered a new gating mechanism in TMEM16A which is dependent on Ca^{2+} and is crucial for the modulation of A9C. We have identified a putative binding site for A9C which explains both the blocking component and activation of the modulation. This site and the outer gate could therefore be a site for further experiments to identify new modulators of TMEM16A and towards drug design. We have also identified that Ani9 is a selective compound for TMEM16A within isolated aortic VSMCs whereas MONNA has off target effects. MONNA has been shown to activate BK_{Ca} channels and inhibit Ca_V channels. Therefore, previous research using MONNA as a tool pharmacological compound to dissect TMEM16A component of the study and should be re-examined with this knowledge in mind.

The work in this thesis is the basis of future study, towards the design of TMEM16A modulators with therapeutic benefit. Beyond the development of the fluorescence-based assay in future the use of YFP_QLL in place of the kit to set up the assay. This work would be alongside the knowledge of the A9C binding site and outer pore gate to develop new modulators, gives a starting point for computational based drug design.

Publications, presentations, and posters

Publications

Ria L. Dinsdale, Tanadet Pipatpolkai, Angela J. Russell, Phillip J. Stansfeld and Paolo Tammaro: 'An outer pore gate controls the pharmacology of the TMEM16A channel' (under review at PNAS).

Kathryn E. Acheson, **Ria L. Dinsdale**, Lara F. Scofano, and Paolo Tammaro: 'The molecular basis of vascular relaxation by the omega-3 fatty acid DHA: a key role for the TMEM16A channel.' (manuscript in preparation).

Presentations

Ria L. Dinsdale, Angela J. Russell, Phillip J. Stansfeld and Paolo Tammaro: 'Molecular basis of modulation of the TMEM16A channel by anthracene-9-carboxylic acid: insights into channel gating' British Pharmacological Society annual meeting 2019, Edinburgh, UK. British pharmacological society bursary awarded.

Ria L. Dinsdale, Angela J. Russell, Phillip J. Stansfeld and Paolo Tammaro: 'Molecular mechanism of modulation of the TMEM16A channel by anthracene-9-carboxylic acid: implications for channel gating' The Biophysical Society annual meeting 2020, San Diego, USA. 2020 BPS Travel Award awarded.

Ria L. Dinsdale: 'Understanding the molecular pharmacology of vascular calcium activated chloride channels' Paton Prize Talks, Department of Pharmacology, University of Oxford, Oxford, UK.

Poster presentations

Ria L. Dinsdale, Angela J. Russell, Phillip J. Stansfeld and Paolo Tammaro: 'Mechanisms of action of small molecule inhibitors of the vascular TMEM16A chloride channels' 6th BHF Fellows Meeting 2019, Cambridge, UK.

Ria L. Dinsdale, Angela J. Russell, Phillip J. Stansfeld and Paolo Tammaro: 'Mechanisms of action of small molecule inhibitors of the vascular TMEM16A chloride channels' OXION conference 2019, Oxford, UK.

Ria L. Dinsdale, Angela J. Russell, Phillip J. Stansfeld and Paolo Tammaro: 'Mechanisms of action of small molecule inhibitors of the vascular TMEM16A chloride channels' British Heart Foundation Centre of Research Excellence conference 2019, Oxford, UK.

Ria L. Dinsdale, Angela J. Russell, Phillip J. Stansfeld and Paolo Tammaro: 'Targeting chloride channels for diseases of altered blood vessel tone' British Heart Foundation Centre of Research Excellence conference 2018, Oxford, UK.

References

Acheson K (2016). TMEM16F: function from (iso)form. 594**:** 2785-2786.

Acheson K (2019). The role and regulation of TMEM16A in the vascular system. In Cardiovascular Science. University of Oxford, p 297.

Adomaviciene A, Smith KJ, Garnett H, & Tammaro P (2013). Putative pore-loops of TMEM16/anoctamin channels affect channel density in cell membranes. The Journal of Physiology 591**:** 3487-3505.

Amberg GC, & Navedo MF (2013). Calcium dynamics in vascular smooth muscle. Microcirculation 20**:** 281-289.

Archer SL, Weir EK, & Wilkins MR (2010). Basic science of pulmonary arterial hypertension for clinicians: new concepts and experimental therapies. Circulation 121**:** 2045-2066.

Askew Page HR, Dalsgaard T, Baldwin SN, Jepps TA, Povstyan O, Olesen SP*, et al.* (2019). TMEM16A is implicated in the regulation of coronary flow and is altered in hypertension. British Journal of Pharmacology 176**:** 1635-1648.

Ávalos Prado P, Häfner S, Comoglio Y, Wdziekonski B, Duranton C, Attali B*, et al.* (2021). KCNE1 is an auxiliary subunit of two distinct ion channel superfamilies. Cell 184**:** 534-544.e511.

Ayoub C, Wasylyk C, Li Y, Thomas E, Marisa L, Robé A*, et al.* (2010). ANO1 amplification and expression in HNSCC with a high propensity for future distant metastasis and its functions in HNSCC cell lines. British Journal of Cancer 103**:** 715-726.

Bader CR, Bertrand D, & Schwartz EA (1982). Voltage-activated and calcium-activated currents studied in solitary rod inner segments from the salamander retina. J Physiol 331**:** 253-284.

Barish ME (1983). A transient calcium-dependent chloride current in the immature Xenopus oocyte. J Physiol 342**:** 309-325.

Benedetto R, Ousingsawat J, Wanitchakool P, Zhang Y, Holtzman MJ, Amaral M*, et al.* (2017). Epithelial Chloride Transport by CFTR Requires TMEM16A. Scientific Reports 7**:** 12397.

Bers DM (2002). Cardiac excitation–contraction coupling. Nature 415**:** 198-205.

Best L (1997). Glucose and a-ketoisocaproate induce transient inward currents in rat pancreatic beta cells. Diabetologia 40**:** 1-6.

Best L, Brown PD, Sheader EA, & Yates AP (2000). Selective Inhibition of Glucose-Stimulated β-Cell Activity by an Anion Channel Inhibitor. The Journal of Membrane Biology 177**:** 169-175.

Bevan JA, & Laher I (1991). Pressure and flow-dependent vascular tone. FASEB J 5**:** 2267-2273.

Boedtkjer DM, Kim S, Jensen AB, Matchkov VM, & Andersson KE (2015). New selective inhibitors of calcium-activated chloride channels - T16A(inh) -A01, CaCC(inh) -A01 and MONNA - what do they inhibit? Br J Pharmacol 172**:** 4158-4172.

Bradley E, Fedigan S, Webb T, Hollywood MA, Thornbury KD, McHale NG*, et al.* (2014). Pharmacological characterization of TMEM16A currents. 8**:** 308-320.

Britschgi A, Bill A, Brinkhaus H, Rothwell C, Clay I, Duss S*, et al.* (2013). Calcium-activated chloride channel ANO1 promotes breast cancer progression by activating EGFR and CAMK signaling. Proc Natl Acad Sci U S A 110**:** E1026-1034.

Brookfield R (2014). The pharmacology and cardiovascular function of TMEM16A channels. In Faculty of Life Science. University of Manchester, p 201.

Bulley S, & Jaggar JH (2014). Cl^- channels in smooth muscle cells. Pflugers Arch 466**:** 861-872.

Burton AC (1954). Relation of structure to function of the tissues of the wall of blood vessels. Physiol Rev 34**:** 619-642.

Bushell SR, Pike ACW, Falzone ME, Rorsman NJG, Ta CM, Corey RA*, et al.* (2019). The structural basis of lipid scrambling and inactivation in the endoplasmic reticulum scramblase TMEM16K. Nature Communications 10.

Caputo A, Caci E, Ferrera L, Pedemonte N, Barsanti C, Sondo E*, et al.* (2008). TMEM16A, A Membrane Protein Associated with Calcium-Dependent Chloride Channel Activity. Science 322**:** 590-594.

Catterall WA (2011). Voltage-gated calcium channels. Cold Spring Harbor perspectives in biology 3**:** a003947-a003947.

Chai R, Chen Y, Yuan H, Wang X, Guo S, Qi J*, et al.* (2017). Identification of Resveratrol, an Herbal Compound, as an Activator of the Calcium-Activated Chloride Channel, TMEM16A. The Journal of Membrane Biology 250**:** 483-492.

Chipperfield AR, & Harper AA (2000). Chloride in smooth muscle. Prog Biophys Mol Biol 74**:** 175-221.

Contreras-Vite JA, Cruz-Rangel S, De Jesús-Pérez JJ, Figueroa IAA, Rodríguez-Menchaca AA, Pérez-Cornejo P*, et al.* (2016). Revealing the activation pathway for TMEM16A chloride channels from macroscopic currents and kinetic models. Pflügers Archiv - European Journal of Physiology 468**:** 1241-1257.

Criddle DN, de Moura RS, Greenwood IA, & Large WA (1996). Effect of niflumic acid on noradrenaline-induced contractions of the rat aorta. British journal of pharmacology 118**:** 1065-1071.

Criddle DN, de Moura RS, Greenwood IA, & Large WA (1997). Inhibitory action of niflumic acid on noradrenaline- and 5-hydroxytryptamine-induced pressor responses in the isolated mesenteric vascular bed of the rat. British journal of pharmacology 120**:** 813-818.

Cruickshank SF, Baxter LM, & Drummond RM (2003). The Cl(-) channel blocker niflumic acid releases Ca(2+) from an intracellular store in rat pulmonary artery smooth muscle cells. British journal of pharmacology 140**:** 1442-1450.

Cruz-Rangel S, De Jesús-Pérez JJ, Contreras-Vite JA, Pérez-Cornejo P, Hartzell HC, & Arreola J (2015). Gating modes of calcium-activated chloride channels TMEM16A and TMEM16B. 593**:** 5283-5298.

Danahay HL, Lilley S, Fox R, Charlton H, Sabater J, Button B*, et al.* (2020). TMEM16A Potentiation: A Novel Therapeutic Approach for the Treatment of Cystic Fibrosis. Am J Respir Crit Care Med 201**:** 946-954.

Dang S, Feng S, Tien J, Peters CJ, Bulkley D, Lolicato M*, et al.* (2017). Cryo-EM structures of the TMEM16A calcium-activated chloride channel. Nature 552**:** 426-429.

Danielsson J, Perez-Zoghbi J, Bernstein K, Barajas MB, Zhang Y, Kumar S*, et al.* (2015). Antagonists of the TMEM16A calcium-activated chloride channel modulate airway smooth muscle tone and intracellular calcium. Anesthesiology 123**:** 569-581.

Davis AJ, Forrest AS, Jepps TA, Valencik ML, Wiwchar M, Singer CA*, et al.* (2010). Expression profile and protein translation of TMEM16A in murine smooth muscle. Am J Physiol Cell Physiol 299**:** C948-959.

Davis AJ, Shi J, Pritchard HA, Chadha PS, Leblanc N, Vasilikostas G*, et al.* (2013). Potent vasorelaxant activity of the TMEM16A inhibitor T16A inh -A01. 168**:** 773-784.

De La Fuente R, Namkung W, Mills A, & Verkman AS (2007). Small-Molecule Screen Identifies Inhibitors of a Human Intestinal Calcium-Activated Chloride Channel. 73**:** 758-768.

Di A, & Malik AB (2010). TRP channels and the control of vascular function. Current Opinion in Pharmacology 10**:** 127-132.

Dixit R, Kemp C, Kulich S, Seethala R, Chiosea S, Ling S*, et al.* (2015). TMEM16A/ANO1 is differentially expressed in HPV-negative versus HPV-positive head and neck squamous cell carcinoma through promoter methylation. Sci Rep 5**:** 16657.

Dopico AM, Bukiya AN, & Jaggar JH (2018). Calcium- and voltage-gated BK channels in vascular smooth muscle. Pflugers Arch 470**:** 1271-1289.

Doughty JM, Miller AL, & Langton PD (1998). Non-specificity of chloride channel blockers in rat cerebral arteries: block of the L-type calcium channel. The Journal of physiology 507 (Pt 2)**:** 433-439.

Duvvuri U, Shiwarski DJ, Xiao D, Bertrand C, Huang X, Edinger RS*, et al.* (2012). TMEM16A Induces MAPK and Contributes Directly to Tumorigenesis and Cancer Progression. Cancer Research 72**:** 3270-3281.

Earley S (2013). TRPM4 channels in smooth muscle function. Pflugers Arch 465**:** 1223-1231.

Eid BG, Abu-Sharib AT, El-Bassossy HM, Balamash K, & Smirnov SV (2018). Enhanced calcium entry via activation of NOX/PKC underlies increased vasoconstriction induced by methylglyoxal. Biochem Biophys Res Commun 506**:** 1013-1018.

Estévez R, Schroeder BC, Accardi A, Jentsch TJ, & Pusch M (2003). Conservation of Chloride Channel Structure Revealed by an Inhibitor Binding Site in ClC-1. Neuron 38**:** 47-59.

Evans MG, & Marty A (1986). Calcium-dependent chloride currents in isolated cells from rat lacrimal glands. 378**:** 437-460.

Ferrera L, Zegarra-Moran O, & Galietta LJ (2011). Ca2+-activated Cl- channels. Compr Physiol 1**:** 2155-2174.

Forrest AS, Joyce TC, Huebner ML, Ayon RJ, Wiwchar M, Joyce J*, et al.* (2012). Increased TMEM16A-encoded calcium-activated chloride channel activity is associated with pulmonary hypertension. Am J Physiol Cell Physiol 303**:** C1229-1243.

Franciolini F (1987). Anion and cation permeability of a chloride channel in rat hippocampal neurons. 90**:** 453-478.

Furchgott RF, & Zawadzki JV (1980). The obligatory role of endothelial cells in the relaxation of arterial smooth muscle by acetylcholine. Nature 288**:** 373-376.

Galietta LJ (2013). Managing the underlying cause of cystic fibrosis: a future role for potentiators and correctors. Paediatr Drugs 15**:** 393-402.

Galietta LJ, Haggie PM, & Verkman AS (2001). Green fluorescent protein-based halide indicators with improved chloride and iodide affinities. FEBS Lett 499**:** 220-224.

Galietta LJV, Springsteel MF, Eda M, Niedzinski EJ, By K, Haddadin MJ*, et al.* (2001). Novel CFTR Chloride Channel Activators Identified by Screening of Combinatorial Libraries Based on Flavone and Benzoquinolizinium Lead Compounds. Journal of Biological Chemistry 276**:** 19723-19728.

Galietta LV, Jayaraman S, & Verkman AS (2001). Cell-based assay for high-throughput quantitative screening of CFTR chloride transport agonists. Am J Physiol Cell Physiol 281**:** C1734-1742.

Genovese M, Borrelli A, Venturini A, Guidone D, Caci E, Viscido G*, et al.* (2019). TRPV4 and purinergic receptor signalling pathways are separately linked in airway epithelia to CFTR and TMEM16A chloride channels. The Journal of Physiology 597**:** 5859-5878.

Gotts JE, & Matthay MA (2016). Sepsis: pathophysiology and clinical management. BMJ 353**:** i1585.

Green MR, & Sambrook J (2012) *Molecular cloning : a laboratory manual. V. 1 V. 1*. Cold Spring Harbor Laboratory Press: Cold Spring Harbor, N.Y.

Greenwood IA, & Large WA (1998). Properties of a Cl- current activated by cell swelling in rabbit portal vein vascular smooth muscle cells. Am J Physiol 275**:** H1524-1532.

Greger R (1996) *Comprehensive human physiology : from cellular mechanisms to integration 1. 1*. Springer: Berlin.

Gyobu S, Miyata H, Ikawa M, Yamazaki D, Takeshima H, Suzuki J*, et al.* (2016). A Role of TMEM16E Carrying a Scrambling Domain in Sperm Motility. Molecular and Cellular Biology 36**:** 645-659.

Hamill OP, Marty A, Neher E, Sakmann B, & Sigworth FJ (1981). Improved patch-clamp techniques for high-resolution current recording from cells and cell-free membrane patches. Pflügers Archiv - European Journal of Physiology 391**:** 85-100.

Hammer C, Wanitchakool P, Sirianant L, Papiol S, Monnheimer M, Faria D*, et al.* (2015). A Coding Variant of ANO10, Affecting Volume Regulation of Macrophages, Is Associated with Borrelia Seropositivity. Mol Med 21**:** 26-37.

Hanahan D (1983). Studies on transformation of Escherichia coli with plasmids. Journal of Molecular Biology 166**:** 557-580.

Hartzell C, Putzier I, & Arreola J (2005). Calcium-activated chloride channels. Annu Rev Physiol 67**:** 719-758.

Hartzell HC, Yu K, Xiao Q, Chien LT, & Qu Z (2009). Anoctamin/TMEM16 family members are Ca2+-activated Cl- channels. J Physiol 587**:** 2127-2139.

Heinemann SH, & Conti F (1992). Nonstationary noise analysis and application to patch clamp recordings. Methods Enzymol 207**:** 131-148.

Heinze C, Seniuk A, Sokolov MV, Huebner AK, Klementowicz AE, Szijártó IA*, et al.* (2014). Disruption of vascular Ca2+-activated chloride currents lowers blood pressure. 124**:** 675-686.

Henry PJ, & Goldie RG (1990). Beta 1-adrenoceptors mediate smooth muscle relaxation in mouse isolated trachea. Br J Pharmacol 99**:** 131-135.

Herring N, Paterson DJ, & Levick JR (2018) *Levick's introduction to cardiovascular physiology*. 6th edn. CRC Press.

Hill-Eubanks DC, Werner ME, Heppner TJ, & Nelson MT (2011). Calcium signaling in smooth muscle. Cold Spring Harb Perspect Biol 3**:** a004549.

Hill K, McNulty S, & Randall AD (2004). Inhibition of TRPM2 channels by the antifungal agents clotrimazole and econazole. Naunyn Schmiedebergs Arch Pharmacol 370**:** 227-237.

Hille B (2007) *Ion channels of excitable membranes*. Sinauer: Sunderland, Mass.

Hu H, Tian J, Zhu Y, Wang C, Xiao R, Herz JM*, et al.* (2010). Activation of TRPA1 channels by fenamate nonsteroidal anti-inflammatory drugs. Pflügers Archiv - European Journal of Physiology 459**:** 579-592.

Huang CLH, & Keynes RD (2021) *Keynes & Aidley's Nerve and muscle*. Fifth edn. Cambridge University Press: Cambridge.

Huang F, Rock JR, Harfe BD, Cheng T, Huang X, Jan YN*, et al.* (2009). Studies on expression and function of the TMEM16A calcium-activated chloride channel. Proc Natl Acad Sci U S A 106**:** 21413-21418.

Huang X, Godfrey TE, Gooding WE, McCarty KS, Jr., & Gollin SM (2006). Comprehensive genome and transcriptome analysis of the 11q13 amplicon in human oral cancer and synteny to the 7F5 amplicon in murine oral carcinoma. Genes Chromosomes Cancer 45**:** 1058-1069.

Hwang SJ, Blair PJ, Britton FC, O'Driscoll KE, Hennig G, Bayguinov YR*, et al.* (2009). Expression of anoctamin 1/TMEM16A by interstitial cells of Cajal is fundamental for slow wave activity in gastrointestinal muscles. J Physiol 587**:** 4887-4904.

Jackson WF (2000). Ion Channels and Vascular Tone. Hypertension 35**:** 173-178.

Jackson WF (2017). Potassium Channels in Regulation of Vascular Smooth Muscle Contraction and Growth. Adv Pharmacol 78**:** 89-144.

Jacobsen L (2004). FuGENE 6 Transfection Reagent: the gentle power. Methods 33**:** 104-112.

Jayaraman S, Haggie P, Wachter RM, Remington SJ, & Verkman AS (2000). Mechanism and Cellular Applications of a Green Fluorescent Protein-based Halide Sensor. Journal of Biological Chemistry 275**:** 6047-6050.

Jeng G, Aggarwal M, Yu W-P, & Chen T-Y (2016). Independent activation of distinct pores in dimeric TMEM16A channels. 148**:** 393-404.

Johansson B (1989). Myogenic tone and reactivity: definitions based on muscle physiology. J Hypertens Suppl 7**:** S5-8; discussion S9.

Johnson PC (1989). The myogenic response in the microcirculation and its interaction with other control systems. J Hypertens Suppl 7**:** S33-39; discussion S40.

Jones K, Shmygol A, Kupittayanant S, & Wray S (2004). Electrophysiological characterization and functional importance of calcium-activated chloride channel in rat uterine myocytes. Pflugers Arch 448**:** 36-43.

Kashyap MK, Marimuthu A, Kishore CJ, Peri S, Keerthikumar S, Prasad TS*, et al.* (2009). Genomewide mRNA profiling of esophageal squamous cell carcinoma for identification of cancer biomarkers. Cancer Biol Ther 8**:** 36-46.

Klabunde R (2011) *Cardiovascular physiology concepts*. Lippincott Williams & Wilkins.

Knot HJ, & Nelson MT (1998). Regulation of arterial diameter and wall [Ca2+] in cerebral arteries of rat by membrane potential and intravascular pressure. The Journal of physiology 508 (Pt 1)**:** 199-209.

Ko EA, Burg ED, Platoshyn O, Msefya J, Firth AL, & Yuan JX (2007). Functional characterization of voltage-gated K+ channels in mouse pulmonary artery smooth muscle cells. Am J Physiol Cell Physiol 293**:** C928-937.

Kunzelmann K, Ousingsawat J, Cabrita I, Doušová T, Bähr A, Janda M*, et al.* (2019). TMEM16A in Cystic Fibrosis: Activating or Inhibiting? Frontiers in Pharmacology 10.

Kuo IY, & Ehrlich BE (2015). Signaling in muscle contraction. Cold Spring Harbor perspectives in biology 7**:** a006023-a006023.

Lam AKM, & Dutzler R (2018). Calcium-dependent electrostatic control of anion access to the pore of the calcium-activated chloride channel TMEM16A. eLife 7.

Lam AKM, & Dutzler R (2021). Mechanism of pore opening in the calcium-activated chloride channel TMEM16A. Nature Communications 12**:** 786.

Lam AKM, Rheinberger J, Paulino C, & Dutzler R (2021). Gating the pore of the calcium-activated chloride channel TMEM16A. Nature Communications 12**:** 785.

Lamb FS, & Barna TJ (1998). Chloride ion currents contribute functionally to norepinephrine-induced vascular contraction. Am J Physiol 275**:** H151-160.

Lambert M, Capuano V, Boet A, Tesson L, Bertero T, Nakhleh MK*, et al.* (2019). Characterization of Kcnk3-Mutated Rat, a Novel Model of Pulmonary Hypertension. Circulation Research 125**:** 678-695.

Lara J, Acevedo JJ, & Onetti CG (1999). Large-conductance Ca2+-activated potassium channels in secretory neurons. J Neurophysiol 82**:** 1317-1325.

Large WA (2002). Receptor-operated Ca2(+)-permeable nonselective cation channels in vascular smooth muscle: a physiologic perspective. J Cardiovasc Electrophysiol 13**:** 493-501.

Large WA, & Wang Q (1996). Characteristics and physiological role of the Ca(2+)-activated Cl- conductance in smooth muscle. Am J Physiol 271**:** C435-454.

Last NB, Kolmakova-Partensky L, Shane T, & Miller C (2016). Mechanistic signs of double-barreled structure in a fluoride ion channel. 5.

Le SC, Jia Z, Chen J, & Yang H (2019). Molecular basis of PIP2-dependent regulation of the Ca2+-activated chloride channel TMEM16A. Nature Communications 10.

Leblanc N, Ledoux J, Saleh S, Sanguinetti A, Angermann J, O'Driscoll K*, et al.* (2005). Regulation of calcium-activated chloride channels in smooth muscle cells: a complex picture is emerging. Can J Physiol Pharmacol 83**:** 541-556.

Lee B-C, Khelashvili G, Falzone M, Menon AK, Weinstein H, & Accardi A (2018). Gating mechanism of the extracellular entry to the lipid pathway in a TMEM16 scramblase. Nature Communications 9.

Lefevre T, Lefevre IA, Coulombe A, & Coraboeuf E (1996). Effects of chloride ion substitutes and chloride channel blockers on the transient outward current in rat ventricular myocytes. 1273**:** 31-43.

Levitsky DO (2007). Three types of muscles express three sodium-calcium exchanger isoforms. Ann N Y Acad Sci 1099**:** 221-225.

Lim NK, Lam AKM, & Dutzler R (2016). Independent activation of ion conduction pores in the double-barreled calcium-activated chloride channel TMEM16A. Journal of General Physiology 148**:** 375-392.

Lin Y-C, Boone M, Meuris L, Lemmens I, Van Roy N, Soete A*, et al.* (2014). Genome dynamics of the human embryonic kidney 293 lineage in response to cell biology manipulations. Nature Communications 5**:** 4767.

Liu S, Feng J, Luo J, Yang P, Brett TJ, & Hu H (2016). Eact, a small molecule activator of TMEM16A, activates TRPV1 and elicits pain- and itch-related behaviors. n/a-n/a.

Liu W, Lu M, Liu B, Huang Y, & Wang K (2012). Inhibition of Ca(2+)-activated Cl(-) channel ANO1/TMEM16A expression suppresses tumor growth and invasiveness in human prostate carcinoma. Cancer Lett 326**:** 41-51.

Madden JA, Ray DE, Keller PA, & Kleinman JG (2001). Ion exchange activity in pulmonary artery smooth muscle cells: the response to hypoxia. Am J Physiol Lung Cell Mol Physiol 280**:** L264-271.

Malvezzi M, Chalat M, Janjusevic R, Picollo A, Terashima H, Menon AK*, et al.* (2013). Ca2+-dependent phospholipid scrambling by a reconstituted TMEM16 ion channel. Nat Commun 4**:** 2367.

Manoury B, Tamuleviciute A, & Tammaro P (2010). TMEM16A/Anoctamin 1 protein mediates calcium-activated chloride currents in pulmonary arterial smooth muscle cells. The Journal of Physiology 588**:** 2305-2314.

Marks AR (1992). Calcium channels expressed in vascular smooth muscle. Circulation 86**:** III61-67.

Matchkov VV, Aalkjaer C, & Nilsson H (2005). Distribution of cGMP-dependent and cGMP-independent Ca(2+)-activated Cl(-) conductances in smooth muscle cells from different vascular beds and colon. Pflugers Arch 451**:** 371-379.

Matchkov VV, Boedtkjer DM, & Aalkjaer C (2015). The role of Ca2+ activated Cl− channels in blood pressure control. 21**:** 127-137.

Matchkov VV, Secher Dam V, Bødtkjer DMB, & Aalkjær C (2013). Transport and Function of Chloride in Vascular Smooth Muscles. Journal of Vascular Research 50**:** 69-87.

Mazzone A, Eisenman ST, Strege PR, Yao Z, Ordog T, Gibbons SJ*, et al.* (2012). Inhibition of cell proliferation by a selective inhibitor of the Ca(2+)-activated Cl(-) channel, Ano1. Biochem Biophys Res Commun 427**:** 248-253.

McCarron JG, Walsh JV, & Fay FS (1994). Sodium/calcium exchange regulates cytoplasmic calcium in smooth muscle. Pflügers Archiv 426**:** 199-205.

McGuigan JAS, & Stumpff F (2013). Calculated and measured [Ca2+] in buffers used to calibrate Ca2+ macroelectrodes. 436**:** 29-35.

Miledi R (1982). A calcium-dependent transient outward current in Xenopus laevis oocytes. Proc R Soc Lond B Biol Sci 215**:** 491-497.

Miller C (1982). Open-state substructure of single chloride channels from Torpedo electroplax. Philos Trans R Soc Lond B Biol Sci 299**:** 401-411.

Molleman A (2008) *Patch clamping : an introductory guide to patch clamp electrophysiology*. Wiley: Chichester.

Moncada S, & Vane JR (1979). The role of prostacyclin in vascular tissue. Fed Proc 38**:** 66-71.

Montani D, Günther S, Dorfmüller P, Perros F, Girerd B, Garcia G*, et al.* (2013). Pulmonary arterial hypertension. Orphanet J Rare Dis 8**:** 97-97.

Moss RB (2013). Pitfalls of Drug Development: Lessons Learned from Trials of Denufosol in Cystic Fibrosis. 162**:** 676-680.

Mulvany MJ, & Halpern W (1977). Contractile properties of small arterial resistance vessels in spontaneously hypertensive and normotensive rats. Circ Res 41**:** 19-26.

Namkung W, Phuan P-W, & Verkman AS (2011). TMEM16A inhibitors reveal TMEM16A as a minor component of calcium-activated chloride channel conductance in airway and intestinal epithelial cells. J Biol Chem 286**:** 2365-2374.

Namkung W, Thiagarajah JR, Phuan PW, & Verkman AS (2010). Inhibition of Ca2+-activated Cl- channels by gallotannins as a possible molecular basis for health benefits of red wine and green tea. FASEB J 24**:** 4178-4186.

Namkung W, Yao Z, Finkbeiner WE, & Verkman AS (2011a). Small-molecule activators of TMEM16A, a calcium-activated chloride channel, stimulate epithelial chloride secretion and intestinal contraction. FASEB J 25**:** 4048-4062.

Namkung W, Yao Z, Finkbeiner WE, & Verkman AS (2011b). Small-molecule activators of TMEM16A, a calcium-activated chloride channel, stimulate epithelial chloride secretion and intestinal contraction. The FASEB Journal 25**:** 4048-4062.

Naraghi M (1997). T-jump study of calcium binding kinetics of calcium chelators. Cell Calcium 22**:** 255-268.

Nelson MT, Patlak JB, Worley JF, & Standen NB (1990). Calcium channels, potassium channels, and voltage dependence of arterial smooth muscle tone. Am J Physiol 259**:** C3-18.

Nelson MT, & Quayle JM (1995). Physiological roles and properties of potassium channels in arterial smooth muscle. Am J Physiol 268**:** C799-822.

Ni Y-L, Kuan A-S, & Chen T-Y (2014). Activation and Inhibition of TMEM16A Calcium-Activated Chloride Channels. PLoS ONE 9**:** e86734.

Oh S-J, Park JH, Han S, Lee JK, Roh EJ, & Lee CJ (2008). Development of selective blockers for Ca^{2}(+)-activated Cl channel using Xenopus laevis oocytes with an improved drug screening strategy. Mol Brain 1**:** 14-14.

Oh SJ, Hwang SJ, Jung J, Yu K, Kim J, Choi JY*, et al.* (2013). MONNA, a Potent and Selective Blocker for Transmembrane Protein with Unknown Function 16/Anoctamin-1. 84**:** 726-735.

Olschewski A, Veale EL, Nagy BM, Nagaraj C, Kwapiszewska G, Antigny F*, et al.* (2017). TASK-1 (KCNK3) channels in the lung: from cell biology to clinical implications. European Respiratory Journal 50**:** 1700754.

Ousingsawat J, Martins JR, Schreiber R, Rock JR, Harfe BD, & Kunzelmann K (2009). Loss of TMEM16A causes a defect in epithelial Ca2+-dependent chloride transport. J Biol Chem 284**:** 28698-28703.

Palmer RM, Ferrige AG, & Moncada S (1987). Nitric oxide release accounts for the biological activity of endothelium-derived relaxing factor. Nature 327**:** 524-526.

Paulino C, Kalienkova V, Lam AKM, Neldner Y, & Dutzler R (2017). Activation mechanism of the calcium-activated chloride channel TMEM16A revealed by cryo-EM. Nature 552**:** 421-425.

Pedemonte N, & Galietta LJV (2014). Structure and Function of TMEM16 Proteins (Anoctamins). Physiological Reviews 94**:** 419-459.

Peters CJ, Gilchrist JM, Tien J, Bethel NP, Qi L, Chen T*, et al.* (2018). The Sixth Transmembrane Segment Is a Major Gating Component of the TMEM16A Calcium-Activated Chloride Channel. Neuron.

Picollo A, Liantonio A, Didonna MP, Elia L, Camerino DC, & Pusch M (2004). Molecular determinants of differential pore blocking of kidney CLC-K chloride channels. 5**:** 584-589.

Piper AS, & Greenwood IA (2003a). Anomalous effect of anthracene-9-carboxylic acid on calcium-activated chloride currents in rabbit pulmonary artery smooth muscle cells. 138**:** 31-38.

Piper AS, & Greenwood IA (2003b). Anomalous effect of anthracene-9-carboxylic acid on calcium-activated chloride currents in rabbit pulmonary artery smooth muscle cells. British Journal of Pharmacology 138**:** 31-38.

Piper AS, Greenwood IA, & Large WA (2002). Dual effect of blocking agents on Ca 2+ -activated Cl − currents in rabbit pulmonary artery smooth muscle cells. 539**:** 119-131.

Pompermayer K, Souza DG, Lara GG, Silveira KD, Cassali GD, Andrade AA*, et al.* (2005). The ATP-sensitive potassium channel blocker glibenclamide prevents renal ischemia/reperfusion injury in rats. Kidney Int 67**:** 1785-1796.

Putney JW, Steinckwich-Besançon N, Numaga-Tomita T, Davis FM, Desai PN, D'Agostin DM*, et al.* (2017). The functions of store-operated calcium channels. Biochim Biophys Acta Mol Cell Res 1864**:** 900-906.

Quayle JM, Turner MR, Burrell HE, & Kamishima T (2006). Effects of hypoxia, anoxia, and metabolic inhibitors on KATP channels in rat femoral artery myocytes. Am J Physiol Heart Circ Physiol 291**:** H71-80.

Rang HP (2007) *Rang and Dale's pharmacology*. Churchill Livingstone: Edinburgh; Philadelphia.

Ratjen F, Durham T, Navratil T, Schaberg A, Accurso FJ, Wainwright C*, et al.* (2012). Long term effects of denufosol tetrasodium in patients with cystic fibrosis. J Cyst Fibros 11**:** 539-549.

Reimann F, & Ashcroft FM (1999). Inwardly rectifying potassium channels. Current Opinion in Cell Biology 11**:** 503-508.

Rello J, Valenzuela-Sánchez F, Ruiz-Rodriguez M, & Moyano S (2017). Sepsis: A Review of Advances in Management. Advances in Therapy 34**:** 2393-2411.

Rock JR, O'Neal WK, Gabriel SE, Randell SH, Harfe BD, Boucher RC*, et al.* (2009). Transmembrane protein 16A (TMEM16A) is a Ca2+-regulated Cl- secretory channel in mouse airways. J Biol Chem 284**:** 14875-14880.

Rorsman NJG, Ta CM, Garnett H, Swietach P, & Tammaro P (2018). Defining the ionic mechanisms of optogenetic control of vascular tone by channelrhodopsin-2. British Journal of Pharmacology 175**:** 2028-2045.

Ruiz C, Martins JR, Rudin F, Schneider S, Dietsche T, Fischer CA*, et al.* (2012). Enhanced expression of ANO1 in head and neck squamous cell carcinoma causes cell migration and correlates with poor prognosis. PLoS One 7**:** e43265.

Saleh SN, & Greenwood IA (2005). Activation of chloride currents in murine portal vein smooth muscle cells by membrane depolarization involves intracellular calcium release. Am J Physiol Cell Physiol 288**:** C122-131.

Sauter DRP, Novak I, Pedersen SF, Larsen EH, & Hoffmann EK (2015). ANO1 (TMEM16A) in pancreatic ductal adenocarcinoma (PDAC). Pflugers Arch 467**:** 1495-1508.

Schreiber R, Ousingsawat J, Wanitchakool P, Sirianant L, Benedetto R, Reiss K*, et al.* (2018). Regulation of TMEM16A/ANO1 and TMEM16F/ANO6 ion currents and phospholipid scrambling by Ca(2+) and plasma membrane lipid. The Journal of physiology 596**:** 217-229.

Schreiber R, Uliyakina I, Kongsuphol P, Warth R, Mirza M, Martins JR*, et al.* (2010). Expression and function of epithelial anoctamins. J Biol Chem 285**:** 7838-7845.

Schroeder BC, Cheng T, Jan YN, & Jan LY (2008). Expression cloning of TMEM16A as a calcium-activated chloride channel subunit. Cell 134**:** 1019-1029.

Scudieri P, Caci E, Venturini A, Sondo E, Pianigiani G, Marchetti C*, et al.* (2015). Ion channel and lipid scramblase activity associated with expression of TMEM16F/ANO6 isoforms. J Physiol 593**:** 3829-3848.

Scudieri P, Sondo E, Caci E, Ravazzolo R, & Galietta LJ (2013). TMEM16A-TMEM16B chimaeras to investigate the structure-function relationship of calcium-activated chloride channels. Biochem J 452**:** 443-455.

Seo Y, Lee HK, Park J, Jeon D-K, Jo S, Jo M*, et al.* (2016). Ani9, A Novel Potent Small-Molecule ANO1 Inhibitor with Negligible Effect on ANO2. PLOS ONE 11**:** e0155771.

Smith SS, Steinle ED, Meyerhoff ME, & Dawson DC (1999). Cystic Fibrosis Transmembrane Conductance Regulator: Physical Basis for Lyotropic Anion Selectivity Patterns. Journal of General Physiology 114**:** 799-818.

Somlyo AP, & Himpens B (1989). Cell calcium and its regulation in smooth muscle. FASEB J 3**:** 2266-2276.

Stanich JE, Gibbons SJ, Eisenman ST, Bardsley MR, Rock JR, Harfe BD*, et al.* (2011). Ano1 as a regulator of proliferation. Am J Physiol Gastrointest Liver Physiol 301**:** G1044-G1051.

Sui Y, Sun M, Wu F, Yang L, Di W, Zhang G*, et al.* (2014). Inhibition of TMEM16A Expression Suppresses Growth and Invasion in Human Colorectal Cancer Cells. PLOS ONE 9**:** e115443.

Sun H, Xia Y, Paudel O, Yang X-R, & Sham JSK (2012). Chronic hypoxia-induced upregulation of Ca 2+ -activated Cl − channel in pulmonary arterial myocytes: a mechanism contributing to enhanced vasoreactivity. 590**:** 3507-3521.

Suzuki J, Fujii T, Imao T, Ishihara K, Kuba H, & Nagata S (2013). Calcium-dependent phospholipid scramblase activity of TMEM16 protein family members. J Biol Chem 288**:** 13305-13316.

Suzuki J, Umeda M, Sims PJ, & Nagata S (2010). Calcium-dependent phospholipid scrambling by TMEM16F. Nature 468**:** 834-838.

Ta CM, Acheson KE, Rorsman NJG, Jongkind RC, & Tammaro P (2017). Contrasting effects of phosphatidylinositol 4,5-bisphosphate on cloned TMEM16A and TMEM16B channels. British Journal of Pharmacology 174**:** 2984-2999.

Ta CM, Adomaviciene A, Rorsman NJ, Garnett H, & Tammaro P (2016). Mechanism of allosteric activation of TMEM16A/ANO1 channels by a commonly used chloride channel blocker. Br J Pharmacol 173**:** 511-528.

Tammaro P, & Ashcroft FM (2007). A mutation in the ATP-binding site of the Kir6.2 subunit of the K ATP channel alters coupling with the SUR2A subunit. 584**:** 743-753.

Tammaro P, Smirnov SV, & Moran O (2005). Effects of intracellular magnesium on Kv1.5 and Kv2.1 potassium channels. 34**:** 42-51.

Tammaro P, Smith AL, Hutchings SR, & Smirnov SV (2004). Pharmacological evidence for a key role of voltage-gated K + channels in the function of rat aortic smooth muscle cells. 143**:** 303-317.

Teramoto N (2006). Physiological roles of ATP-sensitive K+ channels in smooth muscle. The Journal of physiology 572**:** 617-624.

Thomas-Gatewood C, Neeb ZP, Bulley S, Adebiyi A, Bannister JP, Leo MD*, et al.* (2011). TMEM16A channels generate Ca2+-activated Cl- currents in cerebral artery smooth muscle cells. 301**:** H1819-H1827.

Thorneloe KS, & Nelson MT (2005). Ion channels in smooth muscle: regulators of intracellular calcium and contractility. Can J Physiol Pharmacol 83**:** 215-242.

Tian Y, Schreiber R, & Kunzelmann K (2012). Anoctamins are a family of Ca2+-activated Cl-channels. J Cell Sci 125**:** 4991-4998.

Tien J, Peters CJ, Wong XM, Cheng T, Jan YN, Jan LY*, et al.* (2014). A comprehensive search for calcium binding sites critical for TMEM16A calcium-activated chloride channel activity. eLife 3.

Toeplitz BK, Cohen AI, Funke PT, Parker WL, & Gougoutas JZ (1979). Structure of ionomycin - a novel diacidic polyether antibiotic having high affinity for calcium ions. Journal of the American Chemical Society 101**:** 3344-3353.

Truong EC, Phuan PW, Reggi AL, Ferrera L, Galietta LJV, Levy SE*, et al.* (2017). Substituted 2-Acylaminocycloalkylthiophene-3-carboxylic Acid Arylamides as Inhibitors of the Calcium-Activated Chloride Channel Transmembrane Protein 16A (TMEM16A). J Med Chem 60**:** 4626-4635.

Tsien RW (1983). Calcium Channels in Excitable Cell Membranes. Annual Review of Physiology 45**:** 341-358.

Tuder RM, Marecki JC, Richter A, Fijalkowska I, & Flores S (2007). Pathology of pulmonary hypertension. Clin Chest Med 28**:** 23-vii.

Tykocki NR, Boerman EM, & Jackson WF (2017). Smooth Muscle Ion Channels and Regulation of Vascular Tone in Resistance Arteries and Arterioles. Comprehensive Physiology 7**:** 485-581.

Verkman AS, & Jayaraman S (2002). Fluorescent indicator methods to assay functional CFTR expression in cells. Methods Mol Med 70**:** 187-196.

Wachter RM, Elsliger M-A, Kallio K, Hanson GT, & Remington SJ (1998). Structural basis of spectral shifts in the yellow-emission variants of green fluorescent protein. Structure 6**:** 1267-1277.

Wachter RM, Yarbrough D, Kallio K, & Remington SJ (2000). Crystallographic and energetic analysis of binding of selected anions to the yellow variants of green fluorescent protein 1 1Edited by D. C. Rees. Journal of Molecular Biology 301**:** 157-171.

Wang B, Li C, Huai R, & Qu Z (2015). Overexpression of ANO1/TMEM16A, an arterial Ca2+-activated Cl- channel, contributes to spontaneous hypertension. J Mol Cell Cardiol 82**:** 22-32.

Wang HS, Dixon JE, & McKinnon D (1997). Unexpected and differential effects of Cl- channel blockers on the Kv4.3 and Kv4.2 K+ channels. Implications for the study of the I(to2) current. Circ Res 81**:** 711-718.

Wang M, Yang H, Zheng LY, Zhang Z, Tang YB, Wang GL*, et al.* (2012). Downregulation of TMEM16A calcium-activated chloride channel contributes to cerebrovascular remodeling during hypertension by promoting basilar smooth muscle cell proliferation. Circulation 125**:** 697-707.

Webb RC (2003). Smooth muscle contraction and relaxation. Adv Physiol Educ 27**:** 201-206.

West RB, Corless CL, Chen X, Rubin BP, Subramanian S, Montgomery K*, et al.* (2004). The novel marker, DOG1, is expressed ubiquitously in gastrointestinal stromal tumors irrespective of KIT or PDGFRA mutation status. Am J Pathol 165**:** 107-113.

Wettschureck N, & Offermanns S (2005). Mammalian G proteins and their cell type specific functions. Physiol Rev 85**:** 1159-1204.

Wild PS, Felix JF, Schillert A, Teumer A, Chen MH, Leening MJG*, et al.* (2017). Large-scale genome-wide analysis identifies genetic variants associated with cardiac structure and function. J Clin Invest 127**:** 1798-1812.

Williamson P (2016). Phospholipid Scramblases. Lipid Insights 8**:** 41-44.

Woodbury JW, & Miles PR (1973). Anion Conductance of Frog Muscle Membranes: One Channel, Two Kinds of pH Dependence. Journal of General Physiology 62**:** 324-353.

Wright EM, & Diamond JM (1977). Anion selectivity in biological systems. Physiol Rev 57**:** 109-156.

Xiao Q, Yu K, Perez-Cornejo P, Cui Y, Arreola J, & Hartzell HC (2011). Voltage- and calcium-dependent gating of TMEM16A/Ano1 chloride channels are physically coupled by the first intracellular loop. Proc Natl Acad Sci U S A 108**:** 8891-8896.

Xu WX, Kim SJ, So I, Kang TM, Rhee JC, & Kim KW (1997). Volume-sensitive chloride current activated by hyposmotic swelling in antral gastric myocytes of the guinea-pig. Pflügers Archiv 435**:** 9-19.

Yang H, Kim A, David T, Palmer D, Jin T, Tien J*, et al.* (2012). TMEM16F Forms a Ca2+-Activated Cation Channel Required for Lipid Scrambling in Platelets during Blood Coagulation. 151**:** 111-122.

Yang YD, Cho H, Koo JY, Tak MH, Cho Y, Shim WS*, et al.* (2008). TMEM16A confers receptor-activated calcium-dependent chloride conductance. Nature 455**:** 1210-1215.

Yuan XJ (1997). Role of calcium-activated chloride current in regulating pulmonary vasomotor tone. Am J Physiol 272**:** L959-968.

Zhou Y, & Lingle CJ (2014). Paxilline inhibits BK channels by an almost exclusively closed-channel block mechanism. J Gen Physiol 144**:** 415-440.